

---

# Numerical Studies of Fluid-Particle Dynamics in the Human Respiratory System

A thesis submitted in fulfillment of the requirements for the degree of Doctor of  
Philosophy

---

Qin Jiang Ge

*B. Mech. Eng. (H2A Hons.)*

School of Aerospace, Mechanical and Manufacturing Engineering Science  
Engineering and Technology Portfolio RMIT University  
College of Science Engineering & Health

May 2012

---

To my parents, who have sacrificed and  
given up so much to provide me with  
all my opportunities. Thanks to all their guidance,  
inspiration and encouragement

---

# Author Declaration

I hereby submit the thesis titled “Numerical Studies of Fluid Particle Dynamics in the Human Respiratory System” for the degree of Doctor of Philosophy and certify that the work is my own work and the best of my knowledge it contains no materials previously published or written by another person, nor material which to a substantial extent has been accepted for the award of any other degree or diploma at RMIT or any other educational institution, except where due acknowledgement is made in the thesis. Any contribution made to the research by others, with whom I have worked at RMIT or elsewhere, is explicitly acknowledged in the thesis.

I also declare that the intellectual content of this thesis is the product of my own work, except to the extent that assistance from others in the project’s design and conception or in style, presentation and linguistic expression is acknowledged. I give consent for this copy of my thesis to be made available for loan and photocopying when handed to RMIT University Library for archiving.



.....  
Qinjiang.Ge

May 2012

---

# Acknowledgements

First and foremost, I would like to express my deepest gratitude to my supervisor, Professor Jiyuan Tu of the School of Aerospace, Manufacturing & Mechanical Engineering in RMIT University for his encouragement, organised and patient guidance in every aspect of my research work. The immense influence he presented in shaping my research attitude and approach can never be overestimated.

I would also like to express sincere gratitude to my co-supervisor, Dr. Songlin Ding of the School of Aerospace, Manufacturing & Mechanical Engineering in RMIT University, for the guidance in the Geometry Reconstruction of Computer Programing.

I would also like to express sincere gratitude to my third supervisor, Dr. Kiao Inthavong of the School of Aerospace, Manufacturing & Mechanical Engineering in RMIT University, for the guidance in the Computational Fluid Dynamics, gas-particle flow and scientific writing.

I would also like to thank to my colleagues and friends; Dr. Xiangdong Li, Dr. Sherman Chi-Pok Cheung, Dr. Kai Zhang, Dr. Camby Mei King Se, Pongpat Thavornpattanapong, Hongnan Fan, Jeff Man Chiu Fung, Tian Tu, in the research office who have always provided assistance where necessary.

Finally, a special acknowledgement to my family back in China for their care and encouragement throughout my student years, my mother Qiaofeng Bian for her concern and love, my father Zhiliang Ge for his constant motivation, support and encouragement.

---

# Abstract

This thesis investigates particle inhalation and its deposition in the human respiratory system for therapeutic and toxicology studies. Computational Fluid Dynamics (CFD) techniques including the Lagrangian approach to simulate gas-particle flows based on the domain airflow are used. The Lagrangian approach is used as it tracks each individual particle and determines its fate (e.g deposition location, or escape from computational domain). This has advantages over a Eulerian approach for respiratory inhalation flows as the volume fraction of the second phase can be neglected and a disperse phase for one-way coupling can be used. However, the very first step is to simulate and detail airflow structures.

For the external airflow structures, the heat released from the human body has a significant effect on the airflow micro-environment around it in an indoor environment, which suggests that the transport and inhalation characteristics of aerosol particulates may also be affected since they are entrained by the air and their movement is dependent on the airflow field. Emphasis was put on the effect of human body heat on particle tracks. It was found that body heat causes a significant rising airflow on the downstream side of the body, which transports particles from a lower level into the breathing zone. The importance of body heat decreases with increasing indoor wind speed. Since the rising airflow exists only on the downstream side of an occupant, the occupant-wind orientation plays an important role in particle inhalation. The effect of body heat has to be taken into account when an occupant had his or her back to the wind, and the effect of body heat could be neglected when the occupant is facing the wind.

---

A CFD model that integrates the three aspects of contaminant exposure by including the external room, human occupant with realistic facial features, and the internal nasal-trachea airway is presented. The results from the simulations visualize the flow patterns at different contaminant concentrations. As the particles are inhaled, they are transported through the respiratory airways, where some are deposited onto surrounding mucus walls while others may navigate through the complex geometry and even reach the lung airways, causing deleterious health effects.

The studies in this thesis demonstrated that the transport and deposition of micron sized particles are dominated by its inertial property while submicron and nano sized particles are influenced by diffusion mechanisms. Studies based on an isolated model of the human nasal cavity or tracheobronchial airway tree rely on idealised inlet boundary condition imposed at the nostril or where, were a blunt, parabolic or uniform profile is applied. It is apparent that an integrated model made up of: i) room and ventilation, ii) aspiration efficiency, iii) and particle deposition efficiencies in the respiratory airway is needed. This leads to a more complete and holistic set of results, which can greatly contribute towards new knowledge in identifying preventative measures for health risk exposure assessment.

With regards to the internal airflow structures and particle inhalation, ultrafine particle deposition sites in the human nasal cavity regions often omit the paranasal sinus regions. Because of the highly diffusive nature of nanoparticles, it is conjectured that deposition by diffusion may occur in the paranasal sinuses, which may affect the residual deposition fraction that leaves the nasal cavity. Thus a nasal-sinus model was created for analysis. In general there was little flow passing through the paranasal sinuses. However, flow patterns revealed that some streamlines reached the upper nasal cavity

---

near the olfactory regions. These flow paths promote particle deposition in the sphenoid and ethmoid sinuses. Some differences were discovered in the deposition fractions and patterns for 5 and 10nm particles between the nasal-sinus and the nasal cavity models. This difference is amplified when the flow rate is decreased and at a flow rate of 4L/min the maximum difference was 17%. It is suggested that future evaluations of nanoparticle deposition should consider some deposition occurring in the paranasal sinuses especially if flow rates are of concern.

Inhaled particles with pharmacological agents (e.g. histamine, methacholine) are introduced into the nasal cavity for targeted delivery. Effective nasal drug delivery is highly dependent on the delivery of the drug from the nasal spray device. Atomization of liquid spray occurs through the internal atomizer that can produce many forms of spray patterns and two of these, hollow-cone and full-cone sprays, are evaluated in this study to determine which spray pattern produced greater deposition in the middle regions of the nasal cavity. Past studies of spray particle deposition have ignored the device within the nasal cavity. Experimental measurements from a Particle Droplet Image Analyzer (PDIA) were taken in order to gain confidence to validate the initial particle conditions for the computational models.. Subsequent airflow patterns and its effects on particle deposition, with and without a spray device, are compared. Contours and streamlines of the flow field revealed that the presence of a spray device in the nasal vestibule produced higher levels of disturbed flow, which helped the dispersion of the sprayed particles. Particle deposition was found to be high in the anterior regions of the nasal cavity due to its inertia. Evaluation of the two spray types found that hollow spray cones produced more deposition in the middle regions of the nasal cavity.

---

The major findings from the different computational modeling performed include: 1) the influence of human body heat on particle transport and inhalation which altered both the flow field and the particle transport; 2) while it has been known that micron particles do not reach the maxillary sinuses, it was found that the highly diffusive nature of nanoparticles, allowed deposition by diffusion when the inhalation rate was sufficiently low, e.g. 4L/min and; 3) Inhalation of toxic and sprayed particles in the isolated nasal model which showed that the presence of a nasal spray device altered the inhalation patterns, and that the nasal cavity has preferential deposition regions.



---

# Publications

## Refereed Journal Articles

**Q.J. Ge**, K. Inthavong, J.Y. Tu, (2012) Local Deposition Fractions of Ultrafine Particles in a Human Nasal-Sinus Cavity CFD Model, *Inhalation Toxicology* 24(8):492-505

**Q.J. Ge**, X.D. Li, K. Inthavong, J.Y. Tu, Numerical study of the effects of human body heat on particle transport and inhalation in indoor environment, *Building and Environment* (Available online 8 August 2012)

K. Inthavong, **Q.J. Ge**, Se, C. M. K., Yang, W. and J.Y. Tu, (2011a). Simulation of Sprayed Particle Deposition in a Human Nasal Cavity Including a Nasal Spray Device. *Journal of Aerosol Science* 42:100-113.

K. Inthavong, **Q.J. Ge**, X.D. Li, J.Y. Tu, (2012) Detailed predictions of particle aspiration, affected by respiratory inhalation and indoor air flows, *Atmospheric Environment* 62:107-117

## Refereed conference Papers

**Q.J. Ge**, K. Inthavong, J.Y. Tu, Modelling of Nanoparticle Diffusion in the Paranasal Sinuses, *Proceedings 2011 World Congress on Engineering and Technology*. Pp.430-443 (2011)

K. Inthavong, **Q.J. Ge**, J.Y. Tu, Modelling of Microparticle Transport and Deposition in Respiratory Airway Via Nasal Inhalation, *Proceedings 2011 World Congress on Engineering and Technology*. Pp.27-30 (2011)

---

# Table of Contents

Author Declaration.....	i
Acknowledgements.....	ii
Abstract.....	iii
Publications.....	vii
Table of Contents.....	viii
List of Figures.....	xii
List of Tables.....	xix
Nomenclature.....	xx
Chapter 1 Introduction.....	1
1.1 Motivation.....	1
1.2 Objectives.....	7
1.3 Thesis Structure.....	8
Chapter 2 Literature Review.....	11
2.1 Introduction.....	11
2.2 Human Anatomy of the Respiratory System.....	11
2.2.1 Upper Respiratory Airway.....	13
2.2.1.1 Nose and Nasal Cavity.....	13
2.2.1.2 Pharynx and larynx.....	14
2.2.2 Lower respiratory.....	15
2.2.2.1 Trachea.....	15
2.2.2.2 Bronchi.....	16
2.3 CFD Modeling History.....	17

---

2.4	Fluid Flow Studies in the Respiratory Airway .....	20
2.4.1	Nasal Cavity Model .....	21
2.4.2	Lung Airway Model.....	23
2.5	Particle Deposition Studies for the Human Inhalation.....	26
2.5.1	External Particle.....	26
2.5.2	Internal Particle Deposition Studies.....	28
2.5.3	Spray Particle Drug Delivery Studies .....	29
Chapter 3 Reconstruction of the Respiratory CFD Model .....		32
3.1	Introduction .....	32
3.2	Method.....	34
3.2.1	Image Scanning.....	35
3.2.1.1	Computed Tomography .....	35
3.2.1.2	Magnetic Resonance Imaging (MRI) .....	36
3.2.1.3	Comparison between CT and MRI .....	37
3.2.2	Image Processing and Segmentation .....	39
3.2.3	Geomagic Surface Generation .....	42
3.2.3.1	Stage 1: Point Cloud .....	43
3.2.3.2	Stage 2: Polygon Surface.....	44
3.2.3.3	Stage 3: Surface Refinement.....	44
3.2.3.4	Stage 4: NURBS Surface .....	45
3.2.4	Developing the CFD Model.....	47
3.2.4.1	Mesh Topology.....	47
3.2.4.2	Mesh Quality.....	49
3.2.4.3	Mesh Independence .....	51
3.3	CFD Models .....	51
3.3.1	Nasal Cavity with Sinus Model .....	51
3.3.2	Nasal Cavity with Nasal Spray Device Model .....	53

---

Chapter 4 Numerical Methodology .....	55
4.1 Introduction .....	55
4.2 Gas Phase Modelling.....	55
4.2.1 Governing Equations for Fluid Flow .....	56
4.2.2 Turbulence Modelling.....	56
4.2.2.1 Reynolds Averaged Navier-Stokes Equations (RANS).....	56
4.2.2.2 Re-Normalization Group Model (RNG) .....	58
4.2.2.3 Shear Stress Transport Model (SST) .....	60
4.2.2.4 Transition Shear Stress Transport Model .....	62
4.3 Particle Phase Modelling.....	64
4.3.1 Micron Particles .....	65
4.3.2 Sub-Micron Particles .....	68
4.4 Numerical Solution and Procedure.....	70
4.4.1 Solution Procedure.....	70
4.4.2 Numerical Solution Schemes .....	72
4.4.2.1 Fluid Flow Discretisation .....	72
4.4.2.2 Lagrangian Particle Phase .....	73
Chapter 5 The Effect of Human Thermal Plume on Particle Transport and Inhalation .....	75
5.1 Introduction .....	75
5.2 Numerical Procedure .....	78
5.2.1 Computational Model .....	78
5.2.1 Boundary Conditions .....	80
5.3 Results and Discussion .....	81
5.3.1 Model Validation .....	81
5.3.2 Effects of Thermal Plume on Particle Transport & Inhalation .....	86
5.3.3 Effects of the Human Critical Area .....	91

---

Chapter 6 Integrated Modeling of Room & Human Airway for Inhalation .....	95
6.1 Introduction .....	95
6.2 Numerical Procedure .....	97
6.2.1 Computational Model .....	97
6.2.2 Boundary Condition.....	101
6.3 Results and Discussion .....	103
6.3.1 Validation and Grid Independence .....	103
6.3.2 Influence of Ambient Flow Rate.....	108
6.3.3 Particle Profile and Deposition Pattern.....	111
6.3.3.1 Particle Inhalation Trajectory.....	111
6.3.3.2 Comparison of Critical Area .....	112
6.3.3.3 Particle Deposition Patterns .....	115
6.3.3.4 Particle Deposition Efficiency.....	121
Chapter 7 Particle Deposition in a Human Nasal-Sinus Cavity.....	123
7.1 Introduction .....	123
7.2 Numerical Procedure .....	125
7.2.1 Computational Models.....	125
7.2.2 Boundary Conditions .....	128
7.3 Results and Discussion .....	129
7.3.1 Geometry and Pressure Drop in the Nasal-Sinus Cavity .....	129
7.3.1 Flow Patterns and Streamlines .....	134
7.3.2 Particle Deposition.....	137
Chapter 8 Nasal Drug Delivery with a Nasal Spray Device.....	148
8.1 Introduction .....	148
8.2 Numerical Procedure .....	149
8.2.1 Experimental Setup.....	149
8.2.2 PDIA and Particle Diameters.....	151

---

8.2.3 Computational Boundary conditions .....	152
8.3 Results and Discussion .....	153
8.3.1 Sprayed Particle Characteristics .....	153
8.3.2 Computational Model Validation .....	158
8.3.3 Airflow Field.....	160
8.3.4 Particle Deposition.....	165
8.4 Discussion .....	173
Chapter 9 Conclusion & Recommendation.....	176
9.1 Toxic Particles around the Human Body.....	176
9.1.1 Transportation of Toxic Particles.....	176
9.1.2 Inhalation of Toxic Particles.....	177
9.2 Inhalation of Toxic and Sprayed Particles in the Isolated Nasal Model ....	178
9.2.1 Nasal Cavity with Paransal Sinus .....	178
9.2.2 Nasal Cavity with Spray Device .....	179
9.3 Recommendations for Further Study .....	180
References.....	183
Appendix A Fluid Equations .....	195
Appendix B Published Papers.....	197

---

# List of Figures

FIGURE 2. 1 SCHEMATIC OF THE RESPIRATORY SYSTEM DISPLAYED BY THE UPPER AND LOWER RESPIRATORY TRACT REGION.  
..... 12

FIGURE 2. 2 STRUCTURE OF THE INTERNAL NASAL CAVITY, AND THE ORAL CAVITY. THE NASOPHARYNX, OROPHARYNX, AND  
LARYNGOPHARYNX, THEY ARE THREE MAIN SUBDIVISIONS OF THE PHARYNX..... 13

FIGURE 2. 3 SCHEMATIC OF THE TRACHEOBRONCHIAL AIRWAY SHOWING THE SUBDIVISIONS IN THE FIRST THREE  
GENERATIONS AND WHERE THE BRANCHES LEAD INTO THE SEGMENTS OF THE LUNG, SUBSEQUENTLY CALLED THE  
BRONCHOPULMONARY SEGMENTS. THE RIGHT LUNG HAS THREE LOBES AND APPROXIMATELY TEN SEGMENTS. THE  
LEFT LUNG HAS TWO LOBES AND APPROXIMATELY EIGHT SEGMENTS. .... 17

FIGURE 3. 1 COMPUTATIONAL RECONSTRUCTION METHODOLOGY..... 34

FIGURE 3. 2 CT SCAN AND MRI ..... 38

FIGURE 3. 3 (A) REGION GROW AND (B) THRESHOLD ..... 41

FIGURE 3. 4 MODEL THE GENERATION PROCESS ..... 42

FIGURE 3. 5 UNWANTED DATA LOCATED NEAR MODEL BOUNDARY TO BE REMOVED WITH ‘SELECT OUTLIERS’ FUNCTION . 43

FIGURE 3. 6 (A) SURFACE HOLE. (B) FLAT-FILLING (C) CURVATURE-BASED FILLING ..... 45

FIGURE 3. 7 (A) MANUAL PATCH LAYOUTS (B) INTERSECTING PATCHES (WITH), CONTOUR LINES (ORANGE) AND PATCH LINES  
(BLACK) (C) GRID PERMANENTLY HIGHLIGHTING PROBLEM AREAS ..... 46

FIGURE 3. 8 MESH TOPOLOGY HIERARCHS FROM LOWEST (LEFT) TO THE HIGHEST (RIGHT). .... 48

FIGURE 3. 9 A QUADRILATERAL CELL HAVING MESH SPACING OF  $\Delta x$  AND  $\Delta y$  AND AN ANGLE OF  $\theta$  BETWEEN THE GRID LINES  
OF THE CELL. .... 49

---

FIGURE 3. 10 A TRIANGULAR CELL HAVING AN ANGLE OF $\beta$ BETWEEN THE SURFACES NORMAL TO THE TRIANGULAR PARTS OF THE FACES CONNECTED TO TWO ADJACENT TRIANGLES. ....	50
FIGURE 3. 11 NEAR WALL MESH THAT HAS A 6-PRISM LAYER FOR A NASAL CAVITY WITH SINUS MODEL. ....	52
FIGURE 3. 12 COMPUTATIONAL MODEL INCLUSIVE OF THE NASAL SPRAY DEVICE, HIGHLIGHTED IN RED. (A) EXTERNAL TETRAHEDRAL SURFACE MESH AT THE LEFT NOSTRIL REGION. (B) INTERNAL TETRAHEDRAL SURFACE MESH OF THE NASAL SPRAY DEVICE. THE BLUE ANNULUS REGION REPRESENTS THE SURFACE INLET OPENING SPACE, LEFT OVER FROM THE SPRAY DEVICE PARTIALLY BLOCKING THE OPENING. (C) COMPUTATIONAL MODEL SUBDIVIDED INTO THREE REGIONS. LABELS A, B, C REPRESENT THREE CORONAL SLICES IN THE LEFT NASAL CAVITY CREATED FOR VISUALISATION OF AIRFLOW PATTERNS .....	54
FIGURE 4. 1 FLOW PROCESS OF THE THREE MAIN ELEMENTS WITHIN A CFPD ANALYSIS FRAMEWORK. ....	71
FIGURE 4. 2 OVERVIEW OF THE SEGREGATED SOLVER SOLUTION STEPS .....	72
FIGURE 5. 1 THE COMPUTATIONAL DOMAIN AND HUMAN MANIKINS .....	79
FIGURE 5. 2 REFINED MESHES AROUND THE MANIKIN MODEL.....	80
FIGURE 5. 3 AIRFLOW VELOCITY VECTORS UNDER ISOTHERMAL CONDITIONS .....	84
FIGURE 5. 4 AIRFLOW VELOCITY VECTORS UNDER THE THERMAL CONDITION .....	85
FIGURE 5. 5 TYPICAL TRACKS OF INHALED PARTICLE UNDER FACING-THE-WIND CONDITIONS (0.1 M/S) .....	87
FIGURE 5. 6 PARTICLE INHALATION INTO THE HUMAN .....	89
FIGURE 5. 7 CRITICAL AREAS (BACK-TO-THE-WIND).....	92
FIGURE 5. 8 CENTRAL HEIGHT OF THE CRITICAL AREA VS. WIND SPEED .....	93
FIGURE 5. 9 COMPARISON OF PREDICTED AND EXPERIMENTAL STREAM LINES .....	94



---

FIGURE 6. 1 (A) 3D CAD MODEL INCORPORATING THE EXTERNAL SURROUNDING ROOM, HUMAN OCCUPANT, AND THE INTERNAL NASAL-PHARYNX-LARYNX-TRACHEA RESPIRATORY AIRWAY MODEL. (B) FRONT VIEW SHOWING THE DETAILED FACIAL FEATURES. GEOMETRY DIMENSIONS AND DETAILS OF THE ROOM AND HUMAN OCCUPANT ARE GIVEN IN TABLE 6. 1. ....	98
FIGURE 6. 2 (A) 3D CAD MODEL INCORPORATING THE EXTERNAL SURROUNDING ROOM, HUMAN OCCUPANT, AND THE INTERNAL NASAL-PHARYNX-LARYNX-TRACHEA RESPIRATORY AIRWAY MODEL. (B) FRONT VIEW SHOWING THE DETAILED FACIAL FEATURES. GEOMETRY DIMENSIONS AND DETAILS OF THE ROOM AND HUMAN OCCUPANT ARE GIVEN IN TABLE 6. 1. ....	100
FIGURE 6. 3 MESH INDEPENDENCE FOR TWO VELOCITY PROFILES FROM LINES TAKEN AT THE CROSS-SECTIONS A-A' AND B'B'. ....	104
FIGURE 6. 4 VELOCITY VECTOR PLOTS FOR (A) CFD ORAL INHALATION AND (B) PIV EXPERIMENTAL MEASUREMENTS FROM ANTHONY ET AL. (2005). (C) CFD MOUTH INHALATION. ....	105
FIGURE 6. 5 VELOCITY VECTOR PLOTS FOR (A) CFD ORAL INHALATION AND (B) PIV EXPERIMENTAL MEASUREMENTS FROM ANTHONY ET AL. (2005). (C) CFD MOUTH INHALATION. ....	107
FIGURE 6. 6 INHALATION THROUGH NOSTRILS AT 15LPM. ....	109
FIGURE 6. 7 COMPARISON OF AIRFLOW PATTERN ON THE NOSTRILS WITH DIFFERENT WIND VELOCITY AT 15L/MIN. ....	110
FIGURE 6. 8 TRAJECTORY OF INHALED PARTICLES RELEASED AT 20 CM UPSTREAM FOR DIFFERENT PARTICLE SIZES AND AMBIENT AIR FLOW RATES OF 0.05M/S AND 0.035M/S. THE INHALATION RATE IS 15LPM THROUGH BOTH NOSTRILS. ....	111
FIGURE 6. 9 COMPARISON OF CRITICAL AREA IN INTEGRATED MODEL AT DIFFERENT WIND SPEED. ....	114
FIGURE 6. 10 COMPARISON OF PARTICLE DEPOSITION PATTERN IN INTERGRADE MODEL IN DIFFERENT WIND SPEED AT LIGHT BREATHING (15LPM) (A) THE WIND VELOCITY IS 0.05M/S, (B) THE WIND VELOCITY IS 0.20M/S, (C) THE WIND VELOCITY IS 0.35M/S. ....	120
FIGURE 6. 11 COMPARISON OF DEPOSITION EFFICIENCIES WITH PREVIOUS USING THE INERTIA PARAMETER. ....	122

---

FIGURE 7. 1 CFD GEOMETRIES USED IN THIS STUDY FOR (A) STRAIGHT PIPE (B) 90° BEND PIPE AND (C) NASAL CAVITY WITH SINUS MODEL. ....	126
FIGURE 7. 2 NEAR WALL INTERPOLATION SCHEME APPLIED TO ALL WALL ADJACENT CELLS. ....	129
FIGURE 7. 3 CORONAL SLICES OF THE AIRWAY COMPARING A (A) NASAL CAVITY WITH SINUS MODEL HIGHLIGHTED BY THE MAXILLARY SINUS AND (B) A NASAL CAVITY MODEL WITH THE SINUSES OMITTED. ....	130
FIGURE 7. 4 CORONAL CROSS-SECTIONAL AREAS FROM THE NOSTRILS TO THE POSTERIOR NASOPHARYNX IN A LINEAR AXIAL VECTOR. THE DISTANCE FROM THE NOSTRILS AT X=0CM IS TAKEN AS THE ANTERIOR MOST TIP OF THE NOSTRIL OPENING. ARROW (A) IS AT = 0.0187 CM AND SIGNIFIES THE BEGINNING OF THE FRONTAL SINUS (B) IS AT X = 0.0288 CM SIGNIFYING THE ANTERIOR BEGINNING OF THE MAXILLARY SINUS, AND (C) IS AT X = 0.0566 CM SIGNIFYING THE POSTERIOR END OF THE MAXILLARY SINUS. ....	131
FIGURE 7. 5 COMPARISON OF THE PRESSURE DROP FOR NASAL CAVITY MODEL NCO2 WITHOUT SINUS INCLUSION. ....	133
FIGURE 7. 6 STREAMLINES PASSING THROUGH THE NASAL CAVITY THAT ORIGINATE FROM THE (A) LEFT AND (B) RIGHT NOSTRILS AT 10L/MIN. MAGNIFIED INSET HIGHLIGHTS THE FLOW STREAMLINES THAT REACH THE SPHENOID AND ETHMOID SINUS REGIONS. ....	135
FIGURE 7. 7 STREAMLINES PASSING THROUGH THE NASAL CAVITY THAT ORIGINATES FROM THE (A) LEFT AND (B) RIGHT NOSTRILS AT 10L/MIN. ....	136
FIGURE 7. 8 VELOCITY MAGNITUDE CONTOURS AT 10L/MIN. ....	137
FIGURE 7. 9 COMPARISON OF DEPOSITION EFFICIENCY RESULTS USING THE EULERIAN SPECIES MODEL, BROWNIAN MODEL-FLUENT 6.3, AND BROWNIAN MODEL- FLUENT 12.1 IN (A) STRAIGHT PIPE 10L/MIN, AND A (B) 90° BEND PIPE. ....	139
FIGURE 7. 10 COMPARISON SIMULATION DATA FOR NASAL WITHOUT SINUS DEPOSITION EFFICIENCY FOR 10L/MIN BREATHING RATES. ....	140
FIGURE 7. 11 COMPARISON SIMULATION DATA FOR NASAL WITHOUT SINUS DEPOSITION EFFICIENCY FOR 4L/MIN AND 10L/MIN BREATHING RATES. ....	142

---

FIGURE 7. 12 NP DEPOSITION PATTERN IN THE NASAL-SINUS CAVITY FOR (A) 1NM - RESULTING IN 98% DEPOSITION AND (B) 10NM - RESULTING IN 29.8% DEPOSITION. PARTICLES ARE COLOURED BY TRAJECTORY TIME WITHIN THE NASAL CAVITY BEFORE IMPACTING ONTO THE SURFACES AT 10L/MIN.....	144
FIGURE 7. 13 FRONTAL VIEW SHOWING THE NP DEPOSITION IN THE MAXILLARY OSTIUM AND SINUS FOR THE (A) RIGHT NASAL CAVITY, AND (B) THE LEFT NASAL CAVITY AT 10L/MIN. DIFFERENT SIZED PARTICLES ARE COLOURED AS FOLLOWS: 1NM RED CIRCLE; 10NM BLUE SQUARE; 40NM BLACK TRIANGLE. ....	146
FIGURE 8. 1 SCHEMATIC OF THE EXPERIMENTAL SETUP FOR SPRAY PARTICLE MEASUREMENTS.....	151
FIGURE 8. 2 (A) MICROSCOPE SCAN OF THE INTERNAL SPRAY ATOMISER NOZZLE.(B) INSTANTANEOUS IMAGES WITH FIELD OF VIEW (FOV) OF 3.853-MM X 3.082-MM OF THE EXTERNAL SPRAY CHARACTERISTICS TAKEN AT TEN LOCATIONS AND COLLATED TOGETHER (C) TWO SETS OF IMAGES SEPARATED BY IN TIME SHOWING THE SPRAY PARTICLE FORMATION AT THE NEAR-NOZZLE REGION AND AT THE LIGAMENT BREAKUP REGION .....	156
FIGURE 8. 3 SAUTER MEAN DIAMETER $D_{32}$ , TAKEN FOR EACH FOV SECTION OR THE FOURTH ( $y = 7.705$ MM) AND FIFTH ROWS ( $y = 10.787$ MM) AS DEPICTED IN FIGURE 8. 7B.....	157
FIGURE 8. 4 FLOW RATE THROUGH THE NASAL CAVITY AS A FUNCTION OF A PRESSURE DROP BETWEEN THE NOSTRIL AND THE NASOPHARYNX .....	159
FIGURE 8. 5 INERTIAL DEPOSITION EFFICIENCY FOR MICRON PARTICLES IN THE LEFT CAVITY SIDE OF A HUMAN NASAL CAVITY COMPARED WITH REPORTED DATA.....	160
FIGURE 8. 6 FLOW RATE DISTRIBUTION BETWEEN THE LEFT AND RIGHT NASAL CHAMBER. COMPARISON IS ALSO MADE WITH THE PRESENCE OF THE NASAL SPRAY DEVICE. WHITE SYMBOLS –MODEL WITHOUT THE SPRAY DEVICE; BLACK SYMBOLS –MODEL INCLUSIVE OF THE SPRAY DEVICE; TRIANGLES – LEFT CAVITY; CIRCLE – RIGHT CAVITY. ....	161
FIGURE 8. 7 PATH STREAMLINES IN THE ANTERIOR REGION OF THE NASAL CAVITY AFFECTED BY THE PRESENCE OF THE NASAL SPRAY DEVICE. ....	162
FIGURE 8. 8 CROSSFLOW STREAMLINES SUPERIMPOSED ONTO CONTOURS OF VELOCITY MAGNITUDES AT DIFFERENT CORONAL CROSS-SECTIONS AS DEFINED IN FIGURE 3. 12.....	164

---

FIGURE 8. 9 SPRAYED PARTICLE DEPOSITION FROM A HOLLOW AND A SOLID SPRAY CONE. THE X-AXIS LABELS, A, M, P REPRESENT ANTERIOR, MIDDLE, AND POSTERIOR REGIONS RESPECTIVELY.....	166
FIGURE 8. 10 DEPOSITION PATTERN OF 5 $\mu$ M IN THE NASAL CAVITY FOR A SOLID AND HOLLOW SPRAY CONE. THE PARTICLE TRAJECTORIES ARE COLOURED BY RESIDENCE TIME. ....	167
FIGURE 8. 11 DEPOSITION OF 15 $\mu$ M IN THE NASAL CAVITY. THE PARTICLE TRAJECTORIES ARE COLOURED BY RESIDENCE TIME. .....	168
FIGURE 8. 12 EFFECT OF THE SWIRL FRACTION ON THE DEPOSITION OF 15 $\mu$ M IN THE NASAL CAVITY WITH A HOLLOW CONE SPRAY WITH A CONE ANGLE OF 30 $^{\circ}$ . THE PARTICLE TRAJECTORIES ARE COLOURED BY RESIDENCE TIME .....	171
FIGURE 8. 13 EFFECT OF THE SWIRL FRACTION ON THE DEPOSITION OF 15 $\mu$ M IN THE NASAL CAVITY WITH A HOLLOW CONE SPRAY WITH A SWIRL FRACTION OF 0.5. THE PARTICLE TRAJECTORIES ARE COLOURED BY RESIDENCE TIME .....	172

---

# List of Tables

TABLE 3. 1 BENEFIT COMPARISON OF CT AND MRI SCANNING .....	37
TABLE 3. 2 PERFORMANCE COMPARISON OF CT AND MRI SCANNING .....	39
TABLE 5. 1 EXPERIMENTAL CONDITIONS AND BOUNDARY CONDITIONS OF VALIDATION COMPUTATIONS .....	82
TABLE 6. 1 MODEL GEOMETRY AND FLOW CONDITION DETAILS.....	97
TABLE 6. 2 INHALATION AND ROOM FLOW DETAILS .....	102
TABLE 7. 1 DIMENSIONS AND DETAILS OF THE GEOMETRIES CONSIDERED IN THIS STUDY .....	127
TABLE 7. 2 SUMMARY OF GEOMETRIC CHARACTERISTICS OF THE NASAL CAVITY. ....	127

---

# Nomenclature

$A$	Area
$C_D$	Drag coefficient
$C_\mu$	Turbulent viscosity relationship
$d_p$	Particle diameter
$D$	Diffusivity
$E$	Energy term
$F_D$	Drag force
$F_g$	Gravity force
$I$	Inertial parameter
$k$	Turbulent kinetic energy
$P$	Pressure
$Pr$	Prandtl number
$Q$	Air flow rate
$S$	Strouhal number

---

$St$	Stokes number
$T$	Temperature
$T_L$	Fluid Lagrangian integral time
<b>Greek Letters</b>	
$\alpha$	Womersley number, or insertion angle
$\beta$	Spray angle
$\Gamma$	Diffusion coefficient of the scalar
$\varepsilon$	Dissipation rate of turbulent kinetic energy
$\emptyset$	Governing scalar variable
$\kappa$	Turbulent kinetic energy
$\mu$	Dynamic viscosity
$\nu$	Kinematic viscosity
$\rho$	Density
$\tau_p$	Particle relaxation time
$\lambda$	Swirl fraction
$\omega$	Breathing frequency
$\zeta$	Normally distributed random number

---

# Chapter 1

## Introduction

### 1.1 Motivation

This thesis presents the reconstruction of the complex three-dimensional models from biomedical images and based on these models, investigates the airflow and inhalation of particles in the human respiratory system using CFD. CFD technology is the science of predicting fluid flow, heat transfer, mass transfer, chemical reactions, and related phenomena by solving the mathematical equations which govern these processes using a numerical methodology. CFD analysis complements testing and experimentation and reduces the total effort required in the laboratory. Simulations are relatively economical, with costs likely to decrease as computers become more powerful, can be executed in a short period of time, and provide the ability to theoretically simulate any physical condition. This technology is a powerful predictive tool, which has developed over the last 30 years. Nowadays, many researchers in a wide variety of research areas have been using CFD technology to great effect. Through advances in science and technology, numerical simulations have appeared due to the increase of such techniques. Studies of air and particle flow in the human respiratory airway have significant importance in many fields of study and applications, ranging from therapeutic drug delivery to toxicology of inhaled particles (micro or nano), especially in indoor environments.



---

Particle transport characterization is especially important in hospitals or densely populated areas during infectious disease outbreaks, for instance, the epidemic outbreak of influenza such as bird flu and SARS, and the H1N1-swine flu. During the H1N1 outbreak during March and April of 2009, international air travelers departing from Mexico were unknowingly transporting a novel influenza A (H1N1) virus to cities around the world (Green 2004). Characterizing the particle transport within the indoor cabin environment during the flight can help identify passengers at risk due to the spread of pathogens from an infected passenger.

The transport characteristics of aerosol particles within indoor environments and their inhalational patterns by human occupants has great relevance to improving health outcomes as people spend approximately 90% of their time indoors and a number of health problems have been found to be associated with particle inhalation (Inthavong et al. 2009a). For instance, cigarette smoke, which is a common indoor pollutant in a room is dangerous to people who have ever smoked, but who live with partners who smoke, as they are at increased risk of a range of tobacco-related diseases, since passive smoking is a serious health risk for both smokers and nonsmokers (Robinson et al. 2006).

Over the past few decades, numerous experimental and numerical investigations have been conducted under various conditions and many important conclusions have been reported. This includes work by Hinds et al. (1998) and Anthony and Flynn (2006) which investigated particle aspiration at the low air velocities typical of occupational settings whose results help to understand aerosol particle behaviour. It is generally accepted nowadays that the particle inhalation by a human occupant is determined by many factors such as the particle size, ambient wind speed, airflow pattern in the

---

breathing zone, inhalation rate, mouth inhalation or nasal inhalation, and even the human facial features (Li et al. 2012).

A human body is continually exchanging energy with its environment. The average thermal energy generated by a human body with an ordinary activity level and at moderate room temperatures was found to be up to 100 Watts (Gowadia and Settles 2001). Due to this heat, a temperature gradient is formed and drives a buoyant free-convection with upward velocity in the vicinity of the human body. This is especially true for fine and ultrafine particles as their transport is mostly controlled by the indoor flow field (Zhang et al. 2009a). This effect, however, has been rarely investigated quantitatively except for a few experimental measurements (Rim and Novoselac 2009a) conducted in quiescent or quasi-quiescent indoor environments, whose conclusions may be not applicable to realistic situations where ventilation systems are operating and the orientation of an occupant relative to the wind may be random.

During human respiration, the inhaled air, which often contains foreign particles, is transported through the respiratory airways. Particles are deposited onto surrounding surfaces while some may navigate through the complex geometry and may even reach deep into the lung parenchyma, causing deleterious health effects. The inhalation of particulate matter (PM) is a major health and safety concern. Generally, particles in the ambient air can be categorised by their size as micron or sub-micron. For example 1-1000nm particles include diesel fumes, asbestos fibres and general dust; 1-1000  $\mu\text{m}$  particles include glass fibres and general dust (Lide 1994). These particles can be modelled by using CFD simulation to track and predict their transport in the large enclosed indoor environments and small human respiratory airways. CFD simulations

---

are an ideal method to predict the risks of contamination of particles and gases since particle transport and dispersion is highly associated with airflow motion and its turbulence. In addition, it is an inexpensive method in comparison to experimental measurements. A number of studies (Bogdanffy and Sarangapani 2003; Oberdörster 2000) have provided information in relation to toxicity and health effects, however these studies are based on an isolated model of the human nasal cavity or tracheo-bronchial airway tree and as such, the inlet boundary condition imposed at the nostril or trachea inlets are unknown and instead a blunt, parabolic or uniform profile is applied (Jayarajua et al. 2008).

When some particle types are reduced to nanoscales they have demonstrated novel and enhanced properties (e.g. significant increase in strength, greater chemical reactivity and enhanced colours). This has led to an exponential increase in the production of engineered nanoparticles, posing a significant health risk through exposure to these substances in the workplace and in our daily life. For example the presence of nanoscale titanium dioxide ( $\text{TiO}_2$ ) is massively produced and widely used in paints, printing ink, paper, cosmetics, car materials, and cleaning products because of its inherent advantages of anticorrosion and enhanced photocatalysis. Toxicity studies of  $\text{TiO}_2$  performed on rodents have shown potential for its translocation into the central nervous system via the olfactory pathway (Oberdörster et al. 2004). In the past, there has been extensive research involving inhalation of ultrafine and particulate air pollution. These studies often use cast replica models or computational models of separate organs of the respiratory system (i.e. nasal cavity, lung airways) to predict local deposition (Cheng et al. 1995; Xi and Longest 2008a). Because of the highly diffusive nature of nanoparticles, it is conjectured that deposition by diffusion may

---

occur in the paranasal sinuses which may affect the residual deposition fraction that leaves the nasal cavity.

Delivery of drugs through aerosol particles has been used extensively to apply medication to the nasal area of patients. It is an effective way to treat a variety of respiratory ailments, particularly for members of the population who are of allergic constitution. Nasal delivery of medication has become a viable alternative to an oral or intravenous route of systemic drug therapy for a variety of diseases. The advantages of using the nasal cavity are its rapid action, improvement of patient compliance and bypassing of metabolic decomposition that orally taken drugs in the digestive system must undergo. These benefits have led to the medical industry pushing forward into researching and developing new drugs that can be delivered nasally. In fact, a marketing report shows that the U.S. market of advanced drug delivery systems was over \$54.2 billion in 2004 and in 2005 it reached \$64.1 billion. It was predicted that over 5 years, this market will continue to grow at an average annual growth rate (AAGR) of 15.6% to reach \$153.5 billion by 2011 (Mandal and Mandal 2010). The efficiency of such products is measured by the amount of particles that deposit on the highly vascular mucous walls. More intimate knowledge of particle flow dynamics can help assess the likelihood of the therapeutic effects caused by the inhalation of the drug particle type and its targeted deposition location. Furthermore a major advantage of significance to the medical and pharmaceutical industries is the ability to simulate fluid-particle flows that are difficult to reproduce experimentally. Now, many researchers are using CFD technology in their research studies (Chen et al. 2010; Inthavong et al. 2011a; Longest and Oldham 2006; Schmehl et al. 1999; Zhao et al. 2003).

---

The human respiratory system is complex and the anatomical system that introduces respiratory air to the interior and performs air exchange includes the nasal cavity, pharynx, larynx, trachea and lung. With regards to the historical development and evolution of airway models, the first physical nasal cavity model was created and experimental measurements were made in 1951 (Proetz 1951). After nearly 40 years, the first CFD nasal models began to appear. The earliest realistic CFD model was developed by Keyhani et al. (1995). The nasal cavity is the first region where the air enters the respiratory system and plays a critical role in breathing; however its modeling can be complicated. The paranasal sinuses around the nasal cavity include the maxillary, sphenoid, ethmoid and frontal sinuses; which are air filled spaces that are connected to the nasal cavity by narrow passageways call the ostium. Each paranasal sinus is lined with the same respiratory mucosa found in the main nasal passage and therefore has the same heating and air conditioning capabilities. The paranasal sinuses do not have an influence on airflow (Xiong et al. 2008b), but may allow sub-micron particles to deposit on them. Particles can also be trapped by the mucous secretions produced in the sinuses, which continually flow into the nose by the ciliated surface. In addition, blowing of the nose helps to drain the sinuses. CFD studies of the nasal cavity are important in establishing the effects of airway geometry on the airflow. Furthermore understanding the flow dynamics caused by geometrical differences, in particular anatomical and pathological anomalies leads to better clinical appraisals and improved and informed decision-making on surgical procedures.

This thesis intends to reconstruct a realistic respiratory airway from CT images. Reconstruction of 3D geometries can be performed rapidly and efficiently through CAD (Computer Aided Drawing) software for human respiratory airway models. The reconstruction is based on reverse engineering CAD technique from scans of the

---

respiratory organs via CT or MRI. The biomedical images can provide very detailed information to enable realistic airway geometry to be produced in comparison to cast models. With the numerical simulations, using CFD, a wider scope of studies based on realistic computational models can be applied. However, CFD technology has a drawback, which is the reliability of its results. This is attributed to the numerical set up, which includes mesh generation, discretization scheme, turbulence models, and boundary condition specifications. Therefore, this thesis investigates the many issues that relate to CFD modeling of inhalation of air and particles through the respiratory airway.

## **1.2 Objectives**

This thesis uses practical and efficient CFD technical approaches to investigate airflow patterns, particle deposition region and deposition efficiency in the human respiratory system. The objectives can be divided into four parts: i) reconstruct 3D simulation models ii) analyse airflow patterns iii) track toxic particles and iv) drug application. Because the respiratory system is a complex structure, air flow patterns are difficult to measure. CFD simulations can provide detailed data that are normally difficult to produce through experiments, due to interventional and clinical risks for the volunteer. The studies are aimed to:

- present airflow patterns around a 3D manikin model in an indoor environment.
- analyse particle transport around a thermal manikin during inhalation.
- identify major micron size particle deposition in the human respiratory from the external ambient air.

- 
- identify nano size particle deposition regions in the nasal cavity model and nasal sinus cavity model.
  - compare the deposition patterns caused by different particle morphologies.
  - simulate medical application of a nasal spray device.

The research is aimed at contributing to knowledge of particle deposition patterns and to assist in risk analysis of exposure to harmful particles in industry.

### **1.3 Thesis Structure**

The rationale for conducting this research, the scope and outlines of this thesis are explained in Chapter 1.

Chapter 2 provides a review of the background for this research. It begins with an introduction to the anatomy of the human respiratory airway. This is followed by a literature review of previous studies related to this thesis including fluid flow, particle transport and particle deposition studies. This chapter aims to provide the framework and context of where the current research has developed.

Chapter 3 presents the method in which the 3D models are reconstructed from CT scans. There are four main stages: extracting CT data, image processing, surface reconstruction and mesh generation. The different types of CFD models include the nasal cavity, nasal cavity with sinuses, and integrated respiratory airway.

Chapter 4 presents the mathematical and numerical methodology for airflow and gas particle flows. CFD is fundamentally based on the governing equations of fluid dynamics. The different turbulence models used and related equations that are solved are discussed. Following this there is description of the Lagrangian particle tracking model.

---

Chapter 5 is the beginning of the main body of this thesis. It describes the airflow structures and particle tracking around the thermal human body in an indoor area. The effects of body heat on particle transport and inhalation are synthetically investigated with special consideration of various indoor wind speeds and the occupant-wind orientation.

Chapter 6 extends the analysis from outside the human to the human inhalation into the respiratory airway. A CFD model simulation integrating the three aspects of contaminant exposure by including the external room, a human occupant with realistic facial features, and the internal nasal-trachea airway is produced. This leads to a more holistic set of results, which can greatly contribute towards new knowledge in identifying preventative measures for health risk exposure assessment.

Chapter 7 investigates the flow patterns in the nasal cavity, in the paranasal ostium and its corresponding sinus, and uptake of ultrafine particles with a focus on the ostium region that may cause occlusion and contribute to sinusitis. Different sizes of the particles (micron and sub-micron) were modeled under three breathing conditions. The numerical results showed that a percentage of particles deposited within the maxillary sinuses.

Chapter 8 moves into the simulation of drug application sprays. Effective nasal drug delivery is highly dependent on the delivery of drug from the nasal spray device. Particle deposition was found to be high in the anterior regions of the nasal cavity due to the spray's inertia. Evaluation of two spray types found that hollow spray cones produced more deposition in the middle regions of the nasal cavity.



---

Chapter 9 summarises significant outcomes from each research section between Chapters five to eight. The final section of this chapter highlights the potential clinical significance of this study and provides recommendations for further study.

---

# Chapter 2

## Literature Review

### 2.1 Introduction

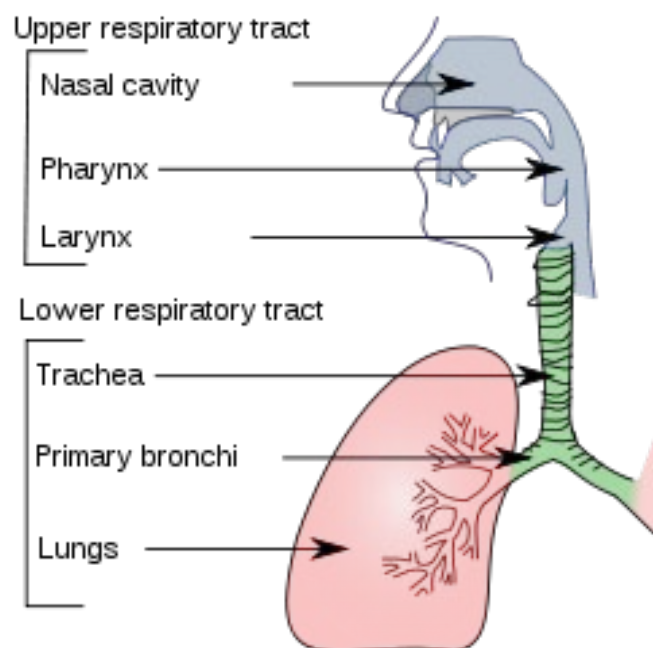
Before moving into the computational methods of reconstructing the respiratory models and CFD simulation, this chapter provides the fundamentals of the anatomy and physiology the respiratory system and CFD simulation background in this field. Firstly, this chapter discusses the anatomy and naming conventions of the respiratory system in order to establish a base of knowledge for decision-making when reconstructing the model. Following this, the use of CFD technology in the respiratory system is investigated, which includes fluid flow and particle deposition studies. The primary aims are to summarise the important features of respiration to help with developing the CFD simulation settings, and how it will all be incorporated into the computational models.

### 2.2 Human Anatomy of the Respiratory System

The human respiratory system divides into two main anatomical parts, the upper respiratory tract and the lower respiratory tract. Their main function is to give humans a space for exchanging oxygen and carbon dioxide gases between the air and our blood. This occurs with each breath we take, where oxygen first enters the nose or mouth during inhalation. The air passes through the larynx and the trachea, which then splits

---

into two bronchi and numerous branches of bronchioles until it reaches the alveoli, the endpoint where gas exchange occurs. Exhalation begins after gas exchange and the air containing CO<sub>2</sub> begins the return journey through the bronchial pathways and back out to the external environment through the nose or mouth. Secondary functions of the respiratory system include filtering, warming and humidifying the inhaled air. Other functions include sound production via the vocal cords in the larynx, control of body pH levels via the lungs, and smell via the olfactory bulbs in the nose.



*Figure 2. 1 Schematic of the respiratory system displayed by the upper and lower respiratory tract region.*

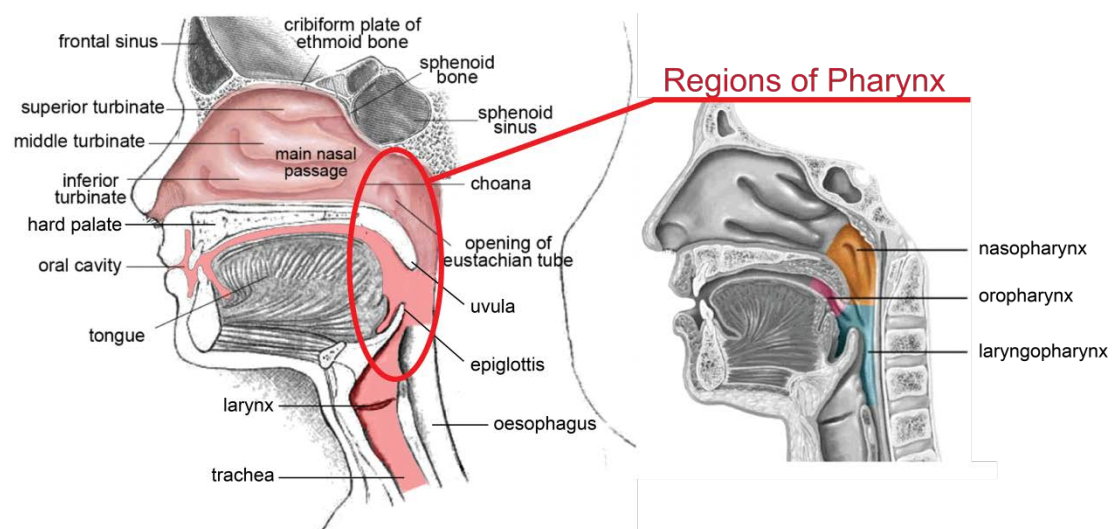
The respiratory system can be separated into regions based on function or anatomy (Figure 2. 1). The upper respiratory tract includes the organs located outside of the chest cavity (thorax) area (i.e. nose, pharynx, larynx), whereas the lower respiratory tract includes the organs located almost entirely within it (i.e. trachea, bronchi, bronchioles).

---

## 2.2.1 Upper Respiratory Airway

### 2.2.1.1 Nose and Nasal Cavity

The anatomy and morphology of the human nose are different amongst different ethnic groups. However, in general all human nose structures are for the large part synonymous. Air passes through the nostrils and the vestibules to enter the nasal cavity. The two nostril openings and consequently the two vestibules leading to two nasal chambers or cavities are separated by the septum. The top of the nasal cavity is divided from the anterior cranial cavity by the cribriform plate of the ethmoid bone, and the sphenoid bone (see Figure 2. 2). The cribriform plate is perforated with many small openings that allow the olfactory nerve branches that are responsible for the sense of smell to extend through to the brain.



*Figure 2. 2 Structure of the internal nasal cavity, and the oral cavity. The nasopharynx, oropharynx, and laryngopharynx, they are three main subdivisions of the pharynx.*

The lateral walls abut on either side with the maxillary bones, and the floor of the nasal cavity is separated from the top of the mouth by the palatal bones. From the vestibule the air passes through a constricted cross-sectional area which has been termed the

---

anterior nasal valve, before entering the main nasal passage. In each cavity there are three passageways within the main nasal passage, formed by three corresponding curled bony plates that project medially into the main passage way from the septum wall, called the superior, middle and inferior nasal turbinate (see Figure 2. 2).

Surrounding the nasal passageways are the paranasal sinuses, which are four pairs of empty air spaces that open or drain into the nasal cavity. They are located in the frontal, sphenoid, ethmoid, and maxillary bones and as such their names are taken from where they are located (see Figure 2. 2). The frontal sinuses are located just above the orbit. The maxillary, the largest of the sinuses extends laterally on either side of the nose. The sphenoid sinus lies in the body of the sphenoid bone, deep in the face just behind the nose. The ethmoid sinuses are not single large cavities but rather a collection of small air pockets, located around the area of the bridge of the nose. At the posterior end of the main nasal passage are the oval-shaped orifices of the posterior nares, approximately 1.5-3.0 cm in diameter. The choanae are openings that allow air to pass from the main nasal passage, into the pharynx (see Figure 2. 1). Once air has passed through the posterior nares, it has left the nasal cavity and enters the next major segment of the upper respiratory tract – the pharynx.

### **2.2.1.2 Pharynx and larynx**

The pharynx is a tube-like structure about 12.5cm long that connects the posterior nasal and oral cavities to the larynx and oesophagus. It extends from the base of the skull to the level of the sixth cervical vertebrae. Structurally, the pharynx can be divided into three anatomical parts according to its location, as shown in Figure 2. 2; these are the nasopharynx (posterior to the nasal chambers), the oropharynx (posterior to the mouth), and the laryngopharynx (posterior to the pharynx). The nasopharynx is located between

---

the internal nares and the soft palate and lies superior to the oral cavity. At the base of the nasopharynx are the soft palate and the uvula. In the walls of the nasopharynx are the auditory (Eustachian) tubes connected to the middle ear. The oropharynx is located posterior to the mouth, inferior from the soft palate, and superior to the level of the hyoid bone. At this location the mouth leads into the oropharynx and both food and inhaled air pass through it. The laryngopharynx extends from the hyoid bone to the oesophagus. It is inferior to the epiglottis and superior to the junction where the airway splits between the larynx and the oesophagus. The larynx is commonly known as the voice box as it houses the vocal folds that are responsible for sound production. It serves as a sphincter in transmitting air from the oropharynx to the trachea and also in creating sounds for speech. It is found in the anterior neck, connecting the hypopharynx with the trachea, which extends vertically from the tip of the epiglottis to the inferior border of the cricoid cartilage. At the top of the larynx is the epiglottis which acts as a flap that closes off the trachea during the act of swallowing to direct food into the oesophagus instead of the trachea. The laryngeal skeleton consists of nine cartilages, three single (thyroid, cricoid, and epiglottis) and three paired (arytenoid, corniculate, and cuneiform), connected by membranes and ligaments. The hyoid bone is connected to the larynx but is not considered part of the larynx.

## **2.2.2 Lower respiratory**

### **2.2.2.1 Trachea**

The trachea is a hollow tube about 11-14cm long connecting the cricoid cartilage in the larynx to the primary bronchi of the lungs. Its cross-sectional diameter in normal human adults is 1.3-2.5cm in the coronal plane and 1.3-2.7cm in the sagittal plane, while for females the diameters are slightly smaller (Liu et al. 2009a). The variation in the trachea

---

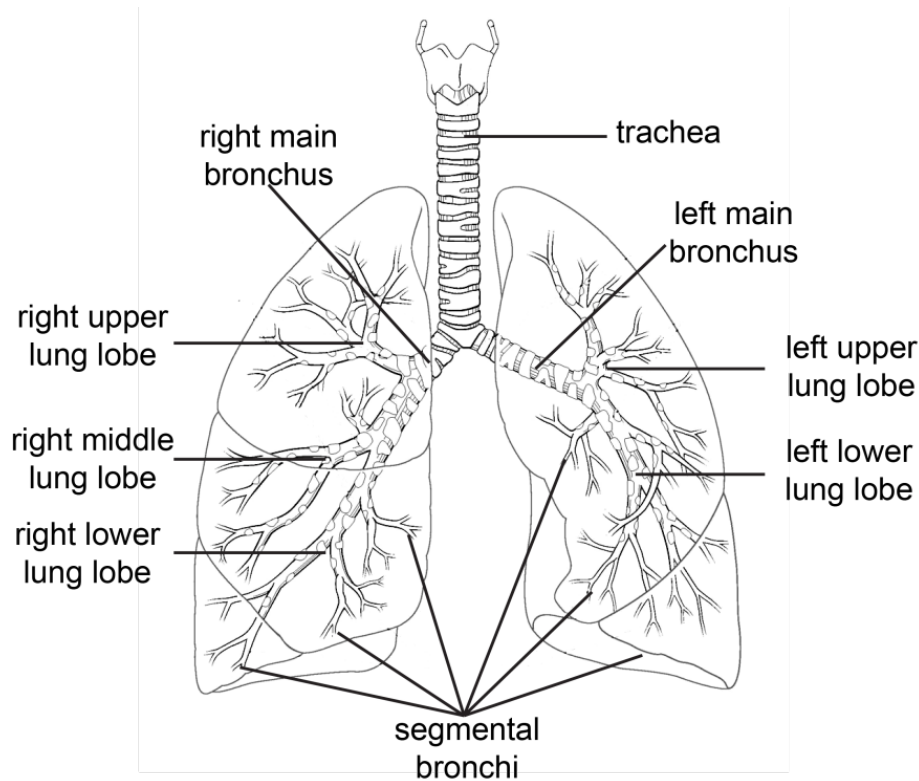
cross-section between the coronal and sagittal plane is due to its shape being a horse-shoe where the anterior side is made up of C-shaped cartilaginous rings, and posteriorly by a flat band of muscle and connective tissue called the posterior tracheal membrane, closing the C-shaped rings. There are 16 to 20 tracheal rings that hold and support the trachea, preventing it from collapsing in on itself, but also providing some flexible movement for any neck movement. Further downstream, along subsequent bronchi, the cartilage support becomes progressively smaller and less complete. The tracheal mucosa consists of pseudo-stratified, ciliated columnar epithelium, while its submucosa contains cartilage, smooth muscle, and seromucous glands.

#### **2.2.2.2 Bronchi**

The trachea divides into the main bronchi at the carina, with the right bronchus wider, shorter and more vertical than the left bronchus (mean lengths of ~2.2cm and ~5cm respectively) (Smith et al. 2001). This leads to increased chances of inhaled foreign particles depositing within the right bronchus. The right main bronchus bifurcates posterior and inferiorly into the right upper lobe bronchus and an intermediate bronchus. This bifurcation occurs earlier on the right than on the left lung in all models. The left bronchus passes inferolaterally at a greater angle from the vertical axis than the right bronchus. It is located anterior to the oesophagus and thoracic aorta and inferior to the aortic arch. Each main bronchi leads to the lung of its respective side (Figure 2. 3). The right main bronchus subdivides into three lobar bronchi (right upper lobe bronchus, right middle lobe bronchus, and right lower lobe bronchus) while the left main bronchus divides into two (left upper lobe bronchus and left lower lobe bronchus). Each lobar bronchus serves as the airway to a specific lobe of the lung. The lobar bronchi further divide into segmental bronchi, which supply the bronchopulmonary segments of

---

each lobe. A bronchopulmonary segment may be defined as an area of distribution of any bronchus (Comte et al. 2008). Technically there are ten bronchopulmonary segments in each lung, however in the left lung some of these segments fuse and there can be as few as eight bronchopulmonary segments.



*Figure 2. 3 Schematic of the tracheobronchial airway showing the subdivisions in the first three generations and where the branches lead into the segments of the lung, subsequently called the bronchopulmonary segments. The right lung has three lobes and approximately ten segments. The left lung has two lobes and approximately eight segments.*

## **2.3 CFD Modeling History**

For the last 30 years, researchers have been using simple geometrical models for CFD simulations. These models were created from graphics software and their dimensions such as the geometric shape, perimeter, and cross-sectional area were estimated from literature data such as Weibel's model (1963). The problem in advancing was how to get a truly realistic model. With the development of computer technology, leading to



---

advanced biomedical imaging more researchers were able to develop realistic geometrical models reconstructed from CT and MRI images.

In order to convert CT images into a 3D computational model, a process called segmentation needs to be applied, more details in chapter 3. In the segmentation of CT images, several methods have been published in the literature; many of them use pixel based segmentation approaches, such as grey-level threshold (Pal and Pal 1993), region-growing (Tschirren et al. 2005), or watershed algorithms (Beare 2006). Many studies concerning the reconstruction of human organs have been performed based on the data obtained from CT. this includes human nasal cavity(Garcia et al. 2007; Inthavong et al. 2008c; Keyhani et al. 1995; Liu et al. 2009b; Zhao et al. 2004) and lung airway (de Rochefort et al. 2007; Nanduri et al. 2009; Tippe et al. 1999). Furthermore some commercial software packages have recently become available in the market for the reconstruction of bronchi. However, there are many problems in the geometries generated by these packages such surface overlap, small gap between two surfaces, miss surface data. The models generated from Segmentation Programs cannot be utilized in CFD study directly. Thus, extensive work must be done modify these models to satisfy a CFD simulation.

The parallel development and availability of both software and hardware have enabled the application of CFD to study of the respiratory tract. The earliest studies focused on characterizing transport and uptake. As described by Elad et al (1993), the three dimensional simulations were conducted using a trapezoidal geometry to approximate the human nasal cavity.

In another study, tracings of human nasal airways from CT scans were used by Keyhani and colleagues (Keyhani et al. 1995) to construct the first anatomically accurate three

---

dimensional CFD model of airflow in one side of the nose. Three dimensional airflow in the pharynx was studied using CFD methods by Shome et al. (1998), while a CFD model of a human nasal, oral , orinasal, laryngeal and tracheal airways based on casts of a medical teaching model was described by Yu et al. (1998).

Recently, there has been an increase in the number of CFD simulations involving realistic nasal cavities, Kelly et al (2000) created a model of a nasal cavity slices from CT scan images captured in parallel slices spaced 1 mm apart. Lindemann et al (2004) created a three-dimensional model of the two nasal cavities, with CT slice thickness of 1.3mm and an increment of 0.6mm. For more recently, Xu et al (2006) created an upper airway model, of three infant reconstructed from magnetic resonance images (MRI) obtained during quiet tidal breathing. The model is including nasal cavity and nasopharynx regions. Xiong et al (2008a) created two nasal cavity models, that include the maxillary sinuses, from CT scans selected from thirty scans of healthy adults. The influence of surface smoothing on the 3D models was investigated by Schroeter et al (2011), who was generated three models with different smoother surfaces from MRI scans of one healthy adults.

The lung model is distinct from the nasal cavity model where most experimental and numerical studies in the literature on flows in the human airways have been based on simplified and idealised, the airway models extracted from the early morphological studies by Weibel (1963) and Horsfield et al(1971), where was a symmetric lung model with three-generation created by Gradon et al (1990), while an early realistic lung model was reconstructed from CT scans by Perzl (1996). Calay et al (2002) made a three-dimensional asymmetric bifurcation model of the central airway based on morphological data. Two lung airway models including lower sub-segmental

---

bronchus was presented which have been present by Vial et al (2005), one is normal with no apparent morphological alterations, while the other is Li et al (2007b) created two ideal models of the features are out-of-plane configurations and cartilaginous rings in the trachea. A 17 generation model, including both central and lower tracheobronchial airways was created by Gemci et al (2008) A five-generation airway extracted from the trachea to segmental bronchi of a 60-year-old Chinese male patient was created by Luo et al (2008). A later study by Sandeau et al (2010) using CT scans extended CFD modelling in the respiratory tract included the pharynx and larynx.

In summary, many of the respiratory airway regions have been reconstructed from CT or MRI images to create a realistic model. However, most of the models in the earlier studies only presented individual regions of the respiratory airway, and just a few were of the upper respiratory tract, lower respiratory tract or full respiratory tract. An integrated CFD model has not yet been developed, which integrates the upper respiratory region such as the nasal cavity, pharynx, larynx and the upper trachea bronchial airway tree.

## **2.4 Fluid Flow Studies in the Respiratory Airway**

The CFD models described above were developed to study the effects of respiratory tract airflow patterns, on nasal uptake or deposition of particles and tissue response patterns in humans. The flow patterns can provide more detailed data that are relevant to the prediction of gas particle flows in inhaled air. Several early simplified model studies focused on the uptake of inhaled airflow. Tarabichi and Fanous (1993) studied the effects of the inferior rim of the pyriform aperture on airflow patterns near the nasal valve which showed an uneven distribution of airflow through the valve with most of the flow occurring in the ventral segment. The results show removal of flow would

---

result in a more even distribution of flow across the valve. Elad et al (1993) conducted airflow simulations with and without nasal turbinates in the nasal cavity, developing a simplified nose-like computational model, where the cross-section was trapezoidal. The turbinates were represented by curved plates that emerge from the lateral walls. The results showed that in the steady and laminar conditions, the turbinates and the trapezoidal shape of the cavity force more air flux towards the olfactory organs at the top of the cavity. Martonen et al (1993) reported an original theory, which presented the simulation of laryngeal and tracheobronchial fluid dynamics under various breathing conditions. The result showed that the fluid dynamics patterns are heterogeneous in the airway system, which may promote particle deposition in the larynx and tracheobronchial airways.

### **2.4.1 Nasal Cavity Model**

From 1995 onwards, the two earliest realistic CFD studies of the nasal cavity were reported by Keyhani et al (1995),(1997). These two papers individually determined the laminar airflow patterns in the half nasal cavity at light breathing flow rates and the airflow effects on odorant transport in a nasal passage. Subramaniam et al (1998) created a 3D human nasal cavity that included the nasopharynx and investigated regional disposition of inhaled acidic vapours. The study steady-state and the airflow were streamlined in the main nasal passages, which complex flow patterns were found in the vestibule and nasopharynx. Swirling air currents and recirculating flow were predicted in the nasal vestibule, and the expansion at the nasopharynx gave rise to two downward, counter current, spiralling vortices. This significant lateral flow was observed mainly in the middle lateral meatus. In the same year, another 3D human nasal cavity with nasopharynx model was conducted by Shome et al (1998). In this study,

---

sleep apnoea treatment therapies were modelled and the pharynx walls were assumed to be passive and rigid in order to find a pressure drop in these models. The pressure drop in the pharynx lies in the range 200-500Pa and the airflow in the pharynx lies in the laminar-to-turbulence transitional flow regime. This kind of change caused by treatment therapies can significantly affect the airflow characteristics in patients suffering from sleep apnoea.

Van Reimersdahl et al (2001) reported the flow field and compared with experimental data, for inspiration and expiration in a model of the human nasal cavity. A steady-state CFD simulation showing temperature distribution in the human nasal cavity is given in Lindemann et al (2004), which report relationship between airflow patterns and heating of inspired air. Zhao et al (2004) simulate the inspiratory and expiratory airflow with odorants in the nasal cavity model with the results showing airflow patterns and odorant transport affected by geometric shape, especially in the olfactory region and the nasal valve region. Understanding the olfactory region may provide important guidance for treatments for nasal-sinus disease. Lindeman et al (2005) reported the airflow in a nasal cavity that included the paranasal sinuses after radical sinus surgery during inspiration. Zhao et al (2006) were simulated the turbulent airflow in the nasal cavity where the inhalation flow rate is between 300ml/s and up to 1000ml/s at each nostril. The results presented no difference in predicted olfactory odorant flux for turbulent versus laminar flow while the differences resistance between the mucosal nasal airway wall and the air phase, showed some with technology, models are becoming more advance. Croce et al (2006) reported the pressure-flow relationships measured in a human nasal cavity including the maxillary sinuses. The results showed that the major total pressure drop was localized in the nasal valve region. At the same time, the results provided good agreement between measured and

---

numerically computed total pressure drops observed up to a flow rate of 15L/min which is an important step for validating the ability of CFD software to describe flow in a physiologically realistic nasal model. Xiong et al (2008b) investigated airflow velocity, trace, distribution, and air pressure, as well as the airflow exchange between the nasal cavity and paranasal sinus. The significant results were that there was little pressure difference and flow difference exchange between the inner and outer aspects of the paranasal sinus and the nasal cavity during stable airflow. The flow force is strongest at the front end of the inferior and middle turbinate and uncinated process. In 2008, Wen et al (Wen et al. 2008a) developed a numerical simulation adopting a laminar steady flow for flow rates of 7.5 and 15 L/min to get a better understanding of the physiology of the nose. The general agreement of gross flow features that were found included high velocities in the constrictive nasal valve area region, high flow close to the septum walls, and vortex formations posterior to the nasal valve and olfactory regions. More recently Zhu et al (2011) evaluated and compared the effects of differences of nasal morphology among three healthy male subjects from Caucasian, Chinese and Indian ethnic groups on nasal airflow patterns.

## **2.4.2 Lung Airway Model**

For the lung airway models, early studies of airflow in the lung airways include the experimental work by Proetz (1951) and Schroter et al (1969). Most experimental and numerical human airway flow studies have been based on idealised airway models extracted from the early morphological studies by Weibel (1963) and Horsfield et al (1971). Experimental studies include (Chang and El Masry 1982; Isabey and Chang 1981; Isabey and Chang 1982) which produced a model of the central airway down to the third generation of the bifurcation, and presented few velocity profiles and flow

---

patterns Ferron et al (1991) simulated airflows in combination with heat and water vapour transport in 2D human lung bifurcation. The results show that CFD analysis is a possible tool to determine airflows. The first realistic lung model for CFD studies of airflow patterns and particle transport was by Perzl (1996).

In CFD simulations, Calay et al (2002) studied the unsteady respiratory airflow dynamics within a human lung model of Horsfield et al. (1971). Liu et al(2002) studied three-dimensional air flow features for steady airflow in the 5th–7th generation ideal model of Weibel (1963). The same authors, extended their work to deal with asymmetric airway extracted from the 5th - 11th branches in order to more appropriately model more of the human air passage(Liu et al. 2003). The results showed relations between the Reynolds number and overall flow patterns and pressure drop in the airway model.

Van Ertbruggen (2005) studied gas flow and particle deposition in a realistic three-dimensional (3D) model of the bronchial tree, extending from the trachea to the segmental bronchi and reported flow simulations of non-fully developed flows in the branches due to their relative short lengths. Lin et al (2007) reported airflow modelling, that considered both upper and intra-thoracic airway geometry. They created two geometries of the human upper respiratory tract model. Their integrated model included a mouthpiece, the mouth, the oropharynx, the larynx, and the intra-thoracic airways up to six generations. The results showed that a curved sheet-like turbulent laryngeal jet is observed only in the integrated model with turbulence intensity in the trachea varying from 10% to 20%. They concluded that turbulence induced by the laryngeal jet could significantly affect airway flow patterns as well as tracheal wall shear stress. More recently, airflow simulation was performed using a realistic lung model. Nagels et al

---

(2009) where a using large eddy simulation (LES) method was used to determine transitional and turbulent flow within an asymmetric bifurcating model of the upper airway. The computational model of a human tracheobronchial airway using a normal breathing cycle (inspiratory and expiratory) to flow distribution was performed by Inthavong et al (2010). The human inhalation results showed velocity contours and secondary flow vectors with vortex formation downstream of the bifurcations that enhanced particle deposition.

In summary, the respiratory flow has been treated as a steady or quasisteady condition based on the Womersley parameter for normal breathing in these studies (Womersley 1955). The Womersley parameter is defined as:

$$\alpha = R \left( \frac{\omega}{\nu} \right)^{\frac{1}{2}} = R \left( \frac{\omega \rho}{\mu} \right)^{\frac{1}{2}} \quad 2.1$$

where  $R$  is an appropriate length scale,  $\omega$  is the angular frequency of the oscillations and  $\nu$ ,  $\rho$ ,  $\mu$  are the kinematic viscosity, density, and dynamic viscosity of the fluid.

Two other important parameters that influence the deposition pattern include the local geometry of the tracheobronchial (TB) tree, and the inhalation patterns. The numerical simulations have become a vital tool in understanding the nature of pulmonary airflow in the human respiratory model. They are able to identify vortices from in the nasal cavity, down to the bronchial airways and the end of the acinar regions. Furthermore CFD has shown airflow acceleration; flow in to the olfactory region, detailed airflow in the middle airways, and acceleration/deceleration in the laryngopharynx. Overall, almost all of the models above are of isolated regions of the human respiratory system, with only a few researchers using a more complex integrated model. The geometrical structure and detail of the respiratory airway are crucial factors that can affect airflow.



---

There have been no integrated CFD models that include the external room, human occupant with realistic facial features, and the internal nasal-trachea airway.

## **2.5 Particle Deposition Studies for the Human Inhalation**

Foreign particles that pass through the respiratory airway during human respiration can cause many respiratory diseases, including serious conditions like lung cancer. At the same time, the respiratory pathway can be a route for nasal/oral drug delivery. However, the nature of particle deposition from a source into a human airway will affect the pattern of deposition, a fact that cannot be neglected for both toxicology and drug delivery. The transport characteristics of particles and human inhalation characteristics by occupants in indoor environments have great importance attached to them.

### **2.5.1 External Particle**

Particle transport around a human manikin has been studied by in vivo measurements and numerical simulations (Anthony and Flynn 2006; Anthony et al. 2005; Baldwin and Maynard 1998; Bird 2005; Hinds et al. 1998; Kato and Yang 2008; Kennedy and Hinds 2002; Mihaescu et al. 2008; Zhu et al. 2005). An early study was performed by Holmberg et al (1998) which determined the flow fields and particle distributions around a standing person using CFD simulations. They reported that the particle distribution pattern from a downstream point source is strongly dependent on the ventilation air supply rate. Aitken et al (1999) improved the non-thermal manikins to thermal manikins, in order to predict the inhalability of particles of varying aerodynamic diameters in low air movement environments by experimental simulation. The results obtained indicate that human inhalability in low air movement

---

environments may be significantly greater than that in moving air conditions with a maximum bias of 48% being measured.

Later Kennedy et al (2002) used experiments to better define particle inhalability by determining the number of particles entering either the mouth or nose during breathing at 14, 20 and 37L/min, and producing the fraction of airborne particles that are inhaled as a function of particle size. The result showed wind velocity and breathing pattern had little effect on inhalability for the range of conditions examined. Orientation-averaged inhalability for nose breathing dropped quickly with particle size reaching less than 10% at 60 $\mu$ m. Facing-the-wind nose inhalability was slightly increased for particles smaller than 60 $\mu$ m compared to orientation averaged inhalability for nose breathing.

Gao et al (2004) used experiments and CFD simulation to define micro-environment around seated thermal human manikin with and without personalized ventilation system. The results showed the personalized airflow rate is from 0 to 3l/s; the best inhaled air quality is achieved at the airflow rate of 0.8l/s by the experiments. The CFD simulation results showed detailed analysis of interaction between thermal plume around human body and personalized airflow, that it is clearer understands the mechanism of inhalation process.

More recently, Anthony et al (2006) used CFD to investigate particle (0.3–116 $\mu$ m) aspiration at low air velocities typical of occupational settings. The simulation showed a realistic representation of a human head on a simpler geometric torso that was positioned facing wind at 0.2 or 0.4m/s, and breathing was simulated using constant inhalation of 1.8 or 4.3m/s. Results from the 0.4m/s free stream and 4.3m/s inhalation rate compared well with results from the previous literature for smaller particles. For

---

particles  $\geq 68\mu\text{m}$ , simulations yielded smaller aspiration efficiencies than reported in experiments.

## **2.5.2 Internal Particle Deposition Studies**

Internal particle transport studies by experiment and numerical simulations have recorded the particle deposition in a human respiratory airway (Cai and Yu 1988; Heyder and Rudolf 1977; Hounam et al. 1971; Inthavong et al. 2006; Kelly et al. 2004a; Kim and Fisher 1999; Kim et al. 1994; Kleinstreuer and Zhang 2010; Longest and Xi 2007; Pattle 1961; Shi et al. 2006; Wiesmiller et al. 2003; Zhang and Finlay 2005). An early study by Swift et al (1991) determined micron particle ( $1\text{-}4\mu\text{m}$ ) deposition in an adult and infant nasal cavity at both laminar and turbulent steady-state conditions. The experimental results show deposition in the child nasal passage was greater than the adult at the same flow rate, but was similar in efficiency for equivalent states of rest or exercise breathing. Guilmette et al (1994) rebuilt two replicas of the nasal airway based on the Swift's MRI data. Deposition efficiency of the replicas was measured for particle diameters between  $0.005$  and  $0.15\mu\text{m}$  and constant inspiratory flow rates of 10 and 20L/min. Cheng et al (1999) studied nine different sizes of particles in the range of  $0.93 \pm 30\mu\text{m}$  at a constant inspiratory flow rate of 15, 30 and 60L/min in the oral airway region. The airway replica included the oral cavity, pharynx, larynx, trachea, and 3 generations of bronchi.

Hofmann et al (2003) studied inspiratory deposition efficiency of ultrafine particles in a physiologically realistic bronchial airway bifurcation model. The model had approximately 3-4 airway generations and the simulation involved different particle sizes, ranging. from 1 to 500nm. The inhalation flow was under three different flow conditions, representing resting up to heavy exercise breathing conditions. Kelly et al

---

(2004a) investigated the impact of differently manufactured nasal replicas on micron and nano size particle deposition efficiencies. The simulation of nanoparticle deposition was also performed by Zamankhan et al (2006) under steady laminar conditions, where diffusion was the dominant deposition mechanism for the smallest range of particles (1-20nm). Based on the simulated results, a semi-empirical equation for the capture efficiency of the nasal passage for nano size particles was fitted in terms of Peclet number. Zhang et al (2009b) created a representative human tracheobronchial tree that was geometrically represented with adjustable triple-bifurcation units (TBUs) in order to effectively simulate local and global micron particle depositions. It is the first comprehensive attempt to compute micron-particle transport in a (Weibel Type A) 16-generation model with realistic inlet conditions. The CFD model predictions were compared to experimental observations as well as analytical modelling results.

### **2.5.3 Spray Particle Drug Delivery Studies**

In terms of spray particle deposition for drug delivery applications, various studies adopting human subjects or nasal cavity replicas have found relationships for particle deposition efficiencies with nasal spray parameters such as spray cone angle and the particle size distribution produced (Cheng et al. 2001; Inthavong et al. 2006; Suman et al. 2002). Kimbell et al (2004) simulated particle deposition by releasing particles from different planes in order to imitate nasal spray delivery. Another study by the same authors Kimbell et al (2007) showed particles were released from different locations of the nostrils to characterise the deposition efficiencies and patterns from nasal sprays. However the particles were released passively into the nasal cavity and the effects of the particles' boundary conditions caused by the atomisation of the drug was not included.

---

Inthavong et al (2008a) performed experiments using particle/droplet image analyser (PDIA) and particle image velocimetry (PIV) imaging techniques. The experimental visualisation and results showed particle formation from a nasal spray device and this determined critical parameters for the CFD studies and aid in the design of effective nasal drug delivery devices. The reported critical parameters were particle size, diameter of spray cone at a break-up length and a spray cone angle to assist the pharmaceutical industry to improve and help guide the design of the nasal spray devices.

The literature findings indicate that the experimental and numerical studies showed that a human's inhalability is strongly influenced by factors such as transport characteristics of particles, airflow velocity in the breathing region, breathing conditions, and the ambient environment. Specifically these factors as follows: particle size, ambient wind speed, inhalation rate, and even the human facial features. However, the human thermal plume is also an important factor so one must include human body heat to the calculation. Heat affects the airflow pattern around a human body and may intensify inhalation particle transport. The influence of particle size is attributed to its aerodynamics flight, governed by forces acting on the particle. Micron sized particles are predominately affected by its inertial property while submicron and nano sized particles are influenced by diffusion mechanisms.

In the reviewed studies, an isolated model of the nasal cavity or oral cavity or airway tree is used. In these isolated studies, the uptake of the ultrafine particles within the nasal-sinus model is not present. Along with this, the inlet boundary condition imposed in all previous studies is unknown and instead a blunt, parabolic or uniform profile is applied. This leads to some loss in achieving a holistic set of results that may be better

---

achieved with an integrated model. In the pharmaceutical industry, particle deposition from nasal spray devices has been investigated. Nasal spray parameters, such as spray cone angle and particle size and their effect on deposition were reported. These studies of spray particle deposition have ignored the presence of the device within the nasal cavity. Further investigations are needed to provide and establish more realistic drug delivery simulations.

---

# Chapter 3

## Reconstruction of the Respiratory CFD Model

### 3.1 Introduction

In this thesis, the research object is in gas air and gas-particles studies of the human respiratory model through the use of numerical simulations. Building realistic and reliable three-dimensional models is imperative due to the inherent health risks volunteer subjects would be exposed to in an experimental setting.

Experimental simulations can give valuable descriptive and quantitative information on air flow patterns and deposition rates in the respiratory system, but the methods are time consuming and expensive. The resolution of the measurements can also be poor because of the small size of the cast model and therefore scaled-up physical models are required. Conversely, numerical simulations are repeatable, can have a larger number of tests and give fine detailed solutions and greater control of variables at low cost and quick turnaround times.

In 1951, Proetz was able to create a plastic replica cast model of the nasal cavity displaying simple inferior and middle turbinates. It was the first comprehensive experiments to demonstrate the streamlined field of inspiration and expiration. (Proetz

---

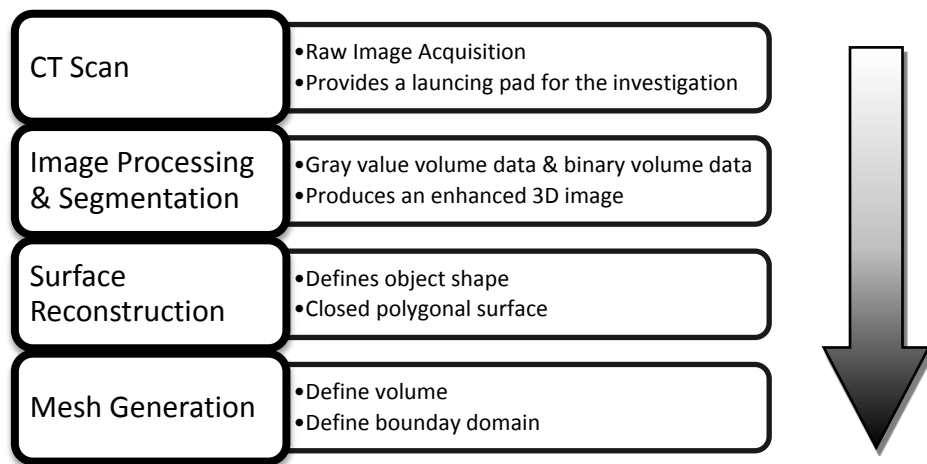
1951). The earliest simple nasal CFD model was created by Elad et al (1993) which was one half of the cavity. The nose-like cavity was constructed as a trapezoidal shape with a base of about 1 cm at the nasal floor and a width of 0.1-0.3 cm at the top. In addition, the results analyzed the processes of heat and water transport. Keyhani et al (1995) built on early realistic CFD model from CT scan segments using imaging software called VIDA (Cardiothoracic Imaging Research Section, University of Pennsylvania), where the model is contained 76,950 elements and 89,152 nodal points. In 2006, Inthavong et al (2006) created a realistic model and used an unstructured mesh for the nasal model. The model had a mesh size of 586,000 elements. In 2008, Doorly et al (2008) created the first whole face model, which connected facial features with the nasal cavity and presented evidence that structures outside the nasal cavity itself affect the flow dynamics within it. For lower airway models, the earliest lung airway CFD model was built by Weibel (1963). The model was a very simple pipe model with 2 generations of bronchioles. In the 2002, an early oral CFD model was constructed by Zhang et al (2002) in which the diameter and length scale values of the oral cavity, pharynx, larynx, and trachea were based on a human cast from Cheng et al (1999). In 2007, a realistic model of the oral cavity combined with the trachea and lung has been rebuilt by Lin et al (2007). It is evident that in the near last 20 years, the evolution of the computational model has undergone a qualitative, and quantitation change in terms of realistic shape, grid number and reconstruction efficiency. Numerical simulations are very practical and helpful for many researchers to solve problems in their project field. This chapter contains a description of geometric reconstruction methods using the CT scans of human volunteers.



---

## 3.2 Method

The design and construction of a computer generated human respiratory model includes image acquisition and processing of the CT scan and geometry, surface and mesh generation. There are a series of processes involved in the model design and development, which must be completed prior to a CFD model being created. The construction of the computational model can be divided into four stages (Figure 3. 1): image acquisition, segmentation, surface reconstruction and mesh generation.



*Figure 3. 1 Computational reconstruction methodology*

In biomedical research, due to the complexity of the human respiratory system, it is impractical to design a model using Computer Aided Drafting (CAD). It would be a very time consuming exercise and the end result would most likely be an over-simplification of the intended design. Recent technological advancements and increasing interest in biomedical research have seen the development of software capable of building 3D models from medical images. From there, medical imaging processes using CT or MRI are implemented which provide a more viable and appropriate method of development towards a realistic model. The development of a computational model of the human respiratory system begins with taking data from

---

medical imaging of a human volunteer. The data comes in the form of a 3D matrix or a series of 2D matrices of volume elements, in which structures are differentiated from one another by brightness or grey scale differences. The two main imaging techniques are MRI and CT, with each technique having its own advantages and disadvantages.

### **3.2.1 Image Scanning**

#### **3.2.1.1 Computed Tomography**

Computed tomography, first made commercially viable in 1972 by Sir Godfrey Hounsfield (2004), is a medical imaging medium that allows doctors to scan multiple cross-sections of patients in order to view internal organs and structures and assist in diagnosing pathology. Different tissues within the human body have different levels of X-ray absorption and transmissivity. Thus, by applying a high sensitivity instrument to measure the beams of radiation, the CT machine is able to obtain measurement data that is inputted into a computer for processing.

The CT scanning process involves moving a patient through the gantry (a donut-shaped device), which houses an X-ray tube and detector array. An X-ray focuses beams of radiation onto the patient to determine its internal shape and structure. Unlike a typical x-ray, which uses a stationary machine to direct the beams, the CT scan is unique in that the x-ray tube rotates around the object, producing an image in cross section. The CT machine releases X-rays that scan a certain thickness level of the human body and are subsequently detected by a probe, which translates the X-rays into visible light. The photoelectric data is then converted into electrical signals, and then through a digital converter into numbers that are inputted to the computer. The scanned data is put through computer calculation, which obtains information of each individual

---

element of X-ray attenuation coefficient or X-ray absorption coefficient and arranges it in a matrix (digital matrix). Using a digital/analog converter, each number is assigned to a colour ranging in shade from black to white as small squares called pixels, which all together constitute a CT image.

Different CT machines have its own settings producing a diverse size and number of the image pixels. The range in size can be  $1.0 \times 1.0\text{mm}$  or  $0.5 \times 0.5\text{mm}$ ; the number from  $256 \times 256$  or  $512 \times 512$ . Obviously, a smaller number produces more pixels resulting in an image with higher resolution.

CT is widely used in a clinical setting due to its diagnostic value. However, CT equipment is relatively inexpensive and examination fees are on the high side. However, CT scanning has some diagnostic limitations, especially qualitative diagnosis, and also exposes patients to relatively high levels of ionizing radiation compared to other imaging mediums. As a result, it is important to only use CT examination judiciously and only when there is a defined purpose for it.

### **3.2.1.2 Magnetic Resonance Imaging (MRI)**

MRI is a relatively new type of high-tech imaging examination method and has been applied to diagnostic medical clinical imaging since the early 1980's (Riederer 2004). It has no ionizing radiation damage, no bone artefacts, more direction (such as transverse, coronal and sagittal plane) and multi-parameter imaging and provides high resolution of soft tissue.

During an MRI scan, the machine uses generates a powerful magnetic field to align the atomic nuclei in the body and then radio frequency fields to alter the alignment of this magnetization. The scanner is then able to detect the rotating magnetic field produced

---

by the nuclei and convert this data into accurate images. MRI is able to obtain very clear and precise images that they greatly improve the efficiency of the doctor's diagnosis. MRI can be used on any part of the body, and with its graphic imaging and high resolution, it can be more objective and more specific in showing the anatomy of the human body tissues and its relationship to adjacent structures.

### 3.2.1.3 Comparison between CT and MRI

A comparison of the two imaging techniques is show in Table 3. 1 and the performance comparison of the two images techniques is shown in Table 3. 2. An example of an MRI and CT scanned images is shown in Figure 3. 2. The scanned images are viewed as a series of stacked two-dimensional pixels, and they have an associated depth, or slice of thickness.

*Table 3. 1 Benefit comparison of CT and MRI scanning*

Benefit comparison		
	Pros	Cons
<b>MRI</b>	<ul style="list-style-type: none"> <li>• No radiation</li> <li>• Higher resolution</li> </ul>	<ul style="list-style-type: none"> <li>• High equipment costs</li> <li>• High usage costs</li> <li>• Less contrast, lower prevalence rates</li> </ul>
<b>CT</b>	<ul style="list-style-type: none"> <li>• Lower equipment costs</li> <li>• Lower usage costs</li> <li>• Higher prevalence rates, more contrast</li> </ul>	<ul style="list-style-type: none"> <li>• Radiation occurs</li> <li>• Lower resolution</li> </ul>

---

---

Furthermore, CT images produce a matrix of CT image grey-scale values resolved by the voxel. Because different tissues have different attenuation characteristics, the resulting image distinguishes between different tissues using grey scale. This allows good detection of bone structure, which is an advantage over MRI.



CT image

MRI image

*Figure 3. 2 CT scan and MRI*

However, dental and metallic equipment pose a problem with CT scan quality. These devices can cause considerable streaks or blurring products in the nasal sinus anatomy. MRI is able to differentiate the nasal cavity from nasal membrane structures well, although the cartilage locations must be concluded from their surrounding mucosa, because the actual bone structures may not be visible.

Table 3. 2 Performance comparison of CT and MRI scanning

Performance comparison		
Capability feature	MRI	CT
<b>Semantide</b>	NMR(Nuclear magnetic resonance) signal	Through the organization of x-rays
<b>Electromagnetic wave</b>	Radio wave	Continuation x-rays
<b>Electromagnetic wave frequency</b>	Less than 100MHz	$3 \times 10^{10}$ - $3 \times 10^{14}$ MHz
<b>Magnetic</b>	Static magnetic field and magnetic field gradient of superposition	NA
<b>Fault trend</b>	Any direction	Perpendicular to the body axis
<b>Each level imaging time</b>	Dependent on scanning sequence	Around 1 second

### 3.2.2 Image Processing and Segmentation

The scanned images obtained from CT and MRI, are series of cross sectional images which contain different grey scale information. Materialise's Interactive Medical Image Control System (MIMICS) (Materialise 2008) is an interactive tool for the visualization and segmentation of CT images as well as MRI images and 3D rendering of objects. Mimics forms an interface between scanned data and rapid prototyping, STL file format, CAD, Finite Element analysis, and CFD analysis. It allows for automated and semi-automated segmentation, however extensive manual clean-up is still required, which is a time consuming and tedious process. This research field is highly active (Aykac et al. 2003; Pal and Pal 1993) and a lot of manufacturing companies are waiting for researchers to create an automated algorithm. In relation to the human respiratory airway, the complexities the anatomy and imperfect images created by

---

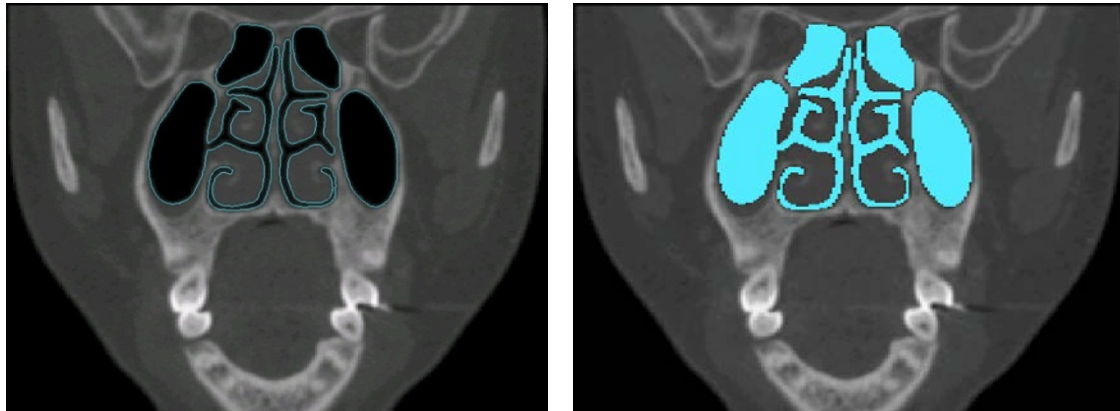
medical imaging, it is a very difficult task for automation. A system that could achieve this would allow the extraction of the airway from the CT scan with minimal cleaning up required by the user.

The original CT images are created as DICOM (Digital Imaging and Communications in Medicine) format and must be converted into STL format to ensure it is compatible with Mimics. The image processing begins by extracting a new volume from the initial image to reduce noise (undesirable regions) from the airway, (Figure 3. 3a). This action lessens the burden on computational resources by minimizing the number of calculations required to further process the image. Additional background noise is removed via 3D convolution, which acts as a smoothing technique. Filtering also provides smoothing of the image volume by alleviating the inherent discontinuities present due to the numerous slices and subsequent discrepancies. Segmentation of the image involves partitioning the digital image into multiple sets of pixels, in effect creating a simpler, more manageable representation (Shapiro 2001). It is used to locate boundaries (airway walls) by segmenting each slice one at a time. The segmentation process allocates each and every pixel with a label which denotes its visual characteristic. Data is able to be exported as a point cloud, which is a log containing the co-ordinate points for the nasal airway boundaries. Additionally the data distinguishes between the inside and outside of the nasal airway walls effectively defining its volume.

A 2D segmentation is used to detect and extract, slice by slice, the walls of the airway. For the segmentation process, both the region growing and threshold algorithms used in this study are shown in Figure 3. 3. Some global threshold selection algorithms include Howarth et al (2001), which obtains the threshold values using an image histogram.

---

The region growing method found in Mimics is based on the Mumford-Shah algorithm (Mumford and Shah 1989).



(a) region grow

(b) threshold

*Figure 3. 3 (a) region grow and (b) threshold*

Regional segmentation was applied as it allows the tracking only of the domains of interest, even in the presence of noise. A first regional segmentation with a greater number of partitioning regions than necessary is performed on each single slice. This allows the algorithm to detect the walls even in severely disturbed images. Another algorithm is applied in order to remove sub-regions unrelated to the airway, which typically present a lower intensity value with respect to the signal due to the relatively low density of gas compared to other tissues.

In this study, the threshold was empirically chosen and represents 85% of the maximum grey-level value of the study. The airway repository system model should exhibit some irregularities due to the image discretions, such as sinus, jet and harsh corners. They can cause severe distortion in the flow field values during CFD simulation. In order to avoid this, a moving average is applied to the space between all airway cavities. The number of average operations ( $n$ ) is imposed by the user, so that the function executes  $n$ -times



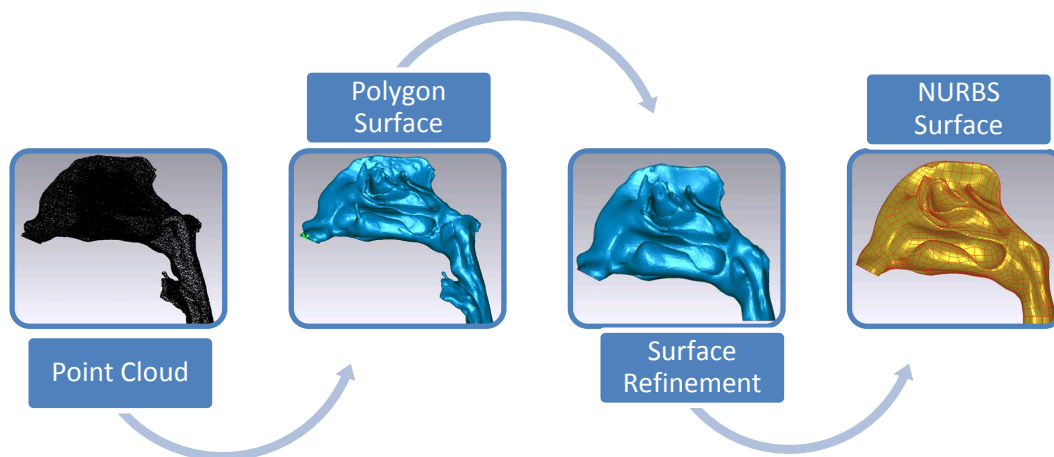
---

the computations. As an optimal trade-off between removing contour irregularities and preserving a suitable spatial resolution, a moving average step was applied twice.

### 3.2.3 Geomagic Surface Generation

Converting a cloud point model into a realistic 3D polygonal model that can satisfy modelling and visualization demands is an extensive and problematic process (Fabio 2003). Geomagic Studio software (2005) is a reverse engineering package used to transform 3D scan data and polygon meshes into accurate 3D digital models. Detailed below are the four key phases concerned, which are shown in Figure 3. 4.

- Stage 1 – Point Cloud
- Stage 2 – Polygon Surface
- Stage 3 – Surface Refinement
- Stage 4 – NURBS Surface

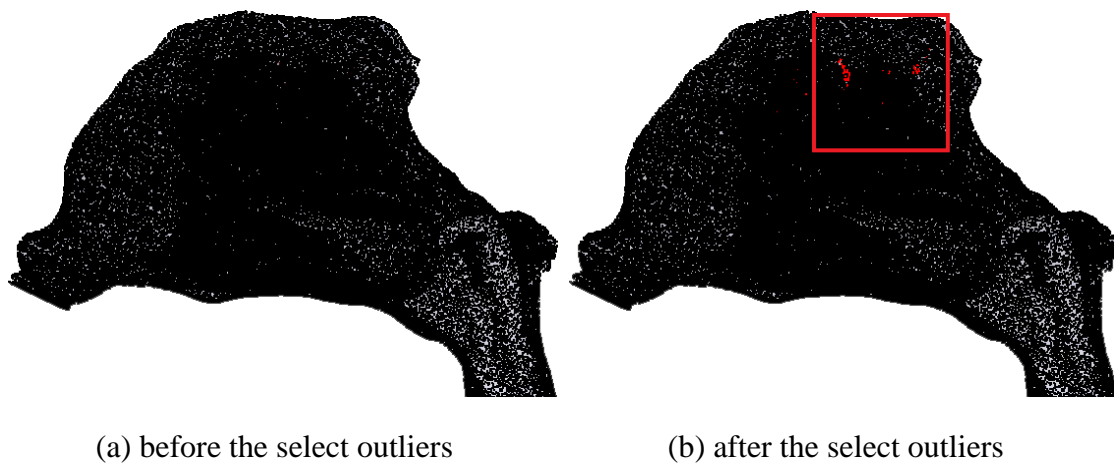


*Figure 3. 4 Model the generation process*

---

### 3.2.3.1 Stage 1: Point Cloud

The point cloud model was exported from Mimics and opened in Geomagic (Figure 3. 4). As Mimics is unable to specify the exact location of the nostrils, this selection of block data was required to be transferred into Geomagic. The nostrils are more easily identified. The block must be manually removed to reveal the outline of the nostrils and surrounding area. To make this process is easier; the shading can be alternated between point cloud and polygon phases to gain a better view of proceedings. Surrounding the basic model is an assortment of small isolated data points. This unwanted ‘noise’ (Red dots in Figure 3. 5b) can be immediately removed as they are deemed as outliers, and not a part of the actual geometry. Unwanted data can also exist so close to the main cloud caused by reflections or inadvertent background surfaces and need to be manually removed. Because these points are located so close to the nasal cavity model, care must be taken to ensure no vital sections of the airway are deleted. A brief recall of the human nasal cavity anatomy will ensure only the unwanted data is removed.



*Figure 3. 5 Unwanted data located near model boundary to be removed with ‘Select Outliers’ function*

To further eliminate unwanted excess data uniform sampling is applied. This removes intersecting (common) points and ensures the data points are uniformly distributed. It is

---

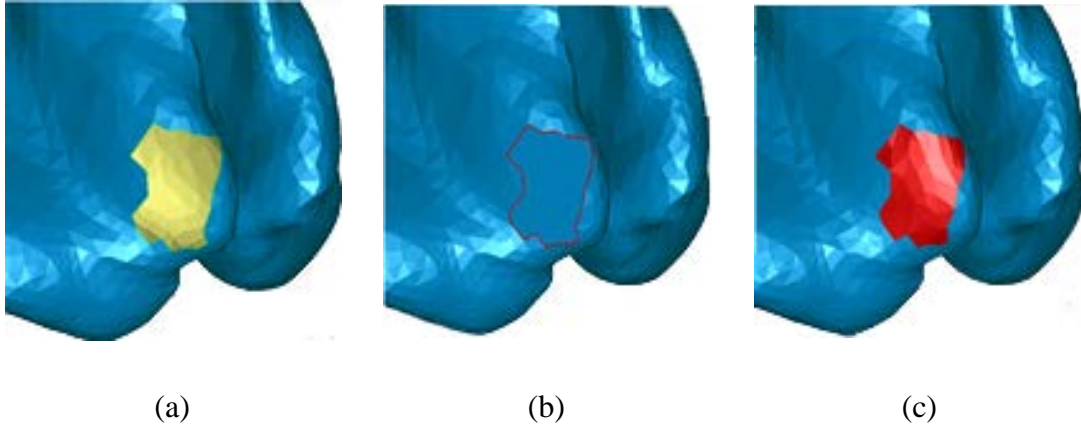
still possible to retain excess points in areas of high curvature to maintain adequate geometry. Furthermore, the removing of unnecessary data streamlines the computational operation performance by optimizing resources including power, memory and overall speed.

### **3.2.3.2 Stage 2: Polygon Surface**

After the completion of the cloud point data, the next stage is to produce a polygon surface. The polygon surface is as a triangle, which is a closed plane formed by three line segments that do not intersect except at vertices. A polygon object consists of polygons arranged in a complex mesh. The cloud points are create as a meshed surface based on the different mathematical algorithms such as Unorganized point clouds, Structured point clouds, Surface oriented and so on(Fabio 2003). Alternatively there is the option to modify the required surface quality and triangle count, which also determines the complexity and subsequent performance of the mesh. The visually disorganized exterior of the cloud points is transformed into a relatively smooth surface (Figure 3. 4b). However, the next step involves the refinement of this surface.

### **3.2.3.3 Stage 3: Surface Refinement**

The subsequent the surface, many holes of varying sizes and shapes and can appear randomly placed on the model. Holes are filled either as curvature-based filling or flat-filling based on adjacent edge. Due to the complex and highly curved form of the model curvature-based filling is ideally suited as it blends the hole to suit the surrounding area, as shown in Figure 3. 6.

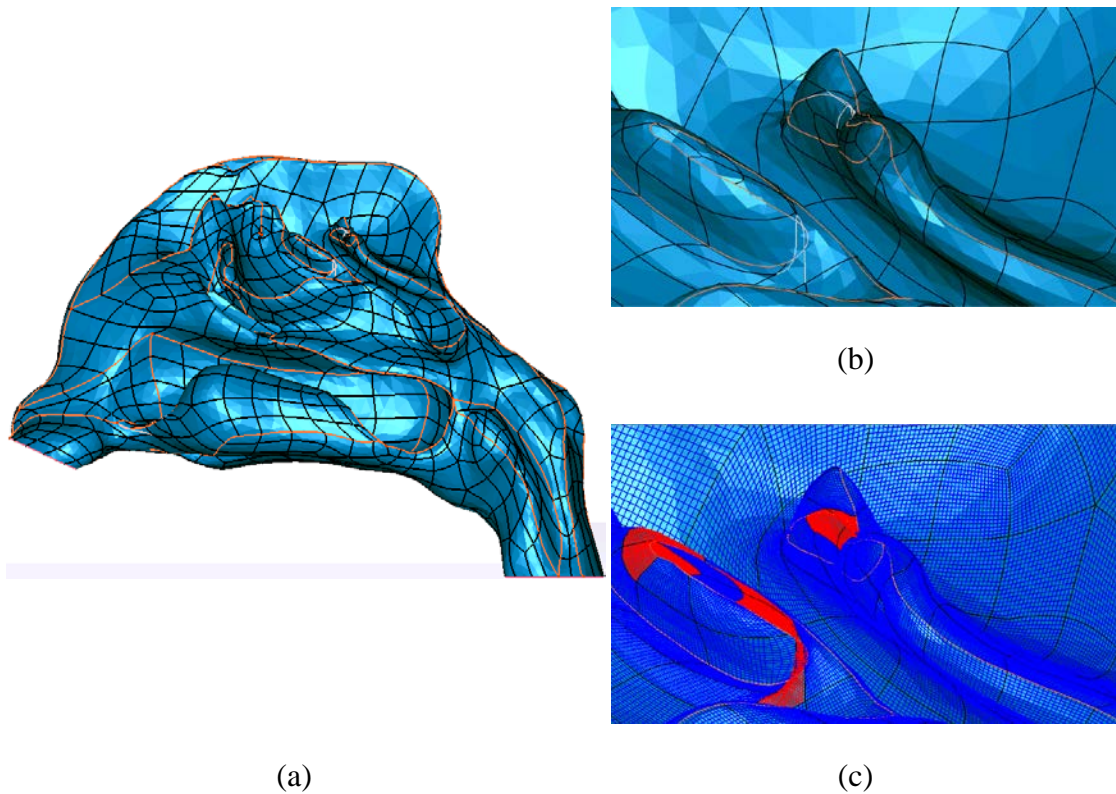


*Figure 3. 6 (a) surface hole. (b) flat-filling (c) curvature-based filling*

However, usually when dealing with large holes, the surrounding geometry is too complicated for a smooth filling to be created automatically. This requires the manual editing in the adjacent area of each individual hole by recognizing abnormal shaped polygons and either deleting them to smooth the surface. Modification of the model should be kept to a minimum to ensure the fundamental shape is kept intact and credible. Upon completion of filling the large holes, small holes remain. For very small holes flat filling is adequate. The nasal cavity model is used as a base model to create one without sinuses. The relevant sinuses were removed and the operations described above were used to fill the gaps and refine the model.

#### **3.2.3.4 Stage 4: NURBS Surface**

The final stage of the surface generation is to generate a NURBS (Non-Uniform Rational B-Splines) surface (Piegl and Tiller 1995). Firstly a series of panels on which the patches lie needs to be formed to cover the entire outside surface of the model. The panels and patches are applied to the no sinus model initially as it has a simpler geometry. The number of patches, in the form of triangles are applied automatically, or a user-defined specified amount.



*Figure 3. 7 (a) manual patch layouts (b) Intersecting patches (with), contour lines (orange) and patch lines (black) (c) Grid permanently highlighting problem areas*

The number of patches must be increased manually until the entire model is covered sufficiently, as in Figure 3. 7a. The large amount of patches can improve the surface properties. It will also aid in the application of the mesh by reducing errors, if not eradicating them entirely. The computational resources available must be taken into account, as the larger the patch quantity on a complex model, the more need for a powerful computer. The key is to make a cautious balance between the two parameters. A later inconvenience of the complex model of the nasal airways is the existence of numerous intersecting patches, which must be repaired, as seen in Figure 3. 7b. Manual rearranging of patches is still required and is a repetitive and time consuming exercise, especially in the sinus model. The model is due to the complex and bunched nature of the geometry; and it is difficult to eradicate all the intersecting patches. When the patch is repositioned, the remaining highlighted problem areas can become invisible. To

---

alleviate this, the grid can be constructed in a manner that permanently highlights the patches that need modifying, as shown in Figure 3. 7c. The manual construction of the patch layout is occasionally required. Completion of a sufficient patch layout occurs when patches are evenly spread across the model and the grid construction exhibits no intersecting patches. The model is then ready for the application of the NURBS (Non-Uniform Rational B-Splines) (Piegl and Tiller 1995) surface shown in Figure 3. 4d, which is based on the grids that lie in patches that lie on panels. The models are now ready to be imported into ANSYS ICEM. (Ansys 2007)

### **3.2.4 Developing the CFD Model**

In computing CFD simulations, the mesh generation is a significant setup for attaining accurate computational results. For this thesis, the ICEM (ANSYS) was used. The reconstructed model is exported as an IGES format, from Geomagic, and is imported into ICEM where the surfaces generated are detected as faces. Generating a quality mesh requires technical knowledge as well as originality. For different flow problems, different techniques and strategies can be applied to generate a high quality mesh. This includes the importance of developing a coarse mesh to begin with for initial flow field testing, and implementing mesh independence test to ensure an optimum mesh has been used.

#### **3.2.4.1 Mesh Topology**

A computational mesh topology has a hierarchical system whereby higher topology assumes the existence of the topologies underneath (Figure 3. 8). The hierarchy for a mesh element from the lowest to highest topology is points, lines, faces, and then

volumes. The different type of mesh element used (or its combination of) determines whether the mesh can be set up as a structured or unstructured mesh.

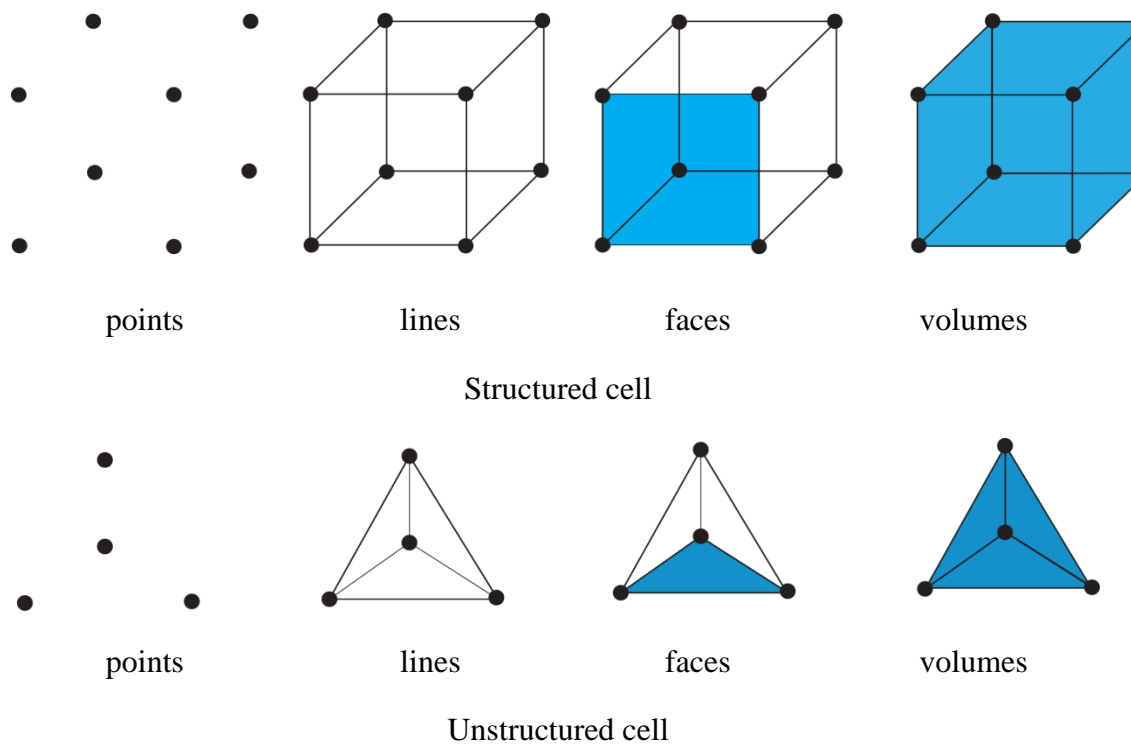


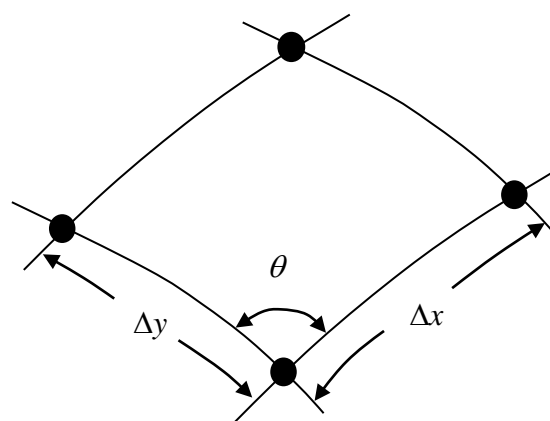
Figure 3. 8 Mesh topology hierarchys from lowest (left) to the highest (right).

The benefits of a structured grid are the small computing memory and a better solution of convergence, but it is hard to apply on complicated geometric shapes such as the respiratory organs. Conversely, the unstructured grid has the ability to comply with complicated geometries, but it requires significantly more computing memory, because of the increased number of adjacent nodes to each individual node. For example, the human respiratory model is a complicated geometry that includes the nasal and oral cavities, pharynx, larynx, trachea and bronchi. For this kind of realistic model, it is more suitable to apply an unstructured mesh, whereas it would be impossible to achieve a computational model with a structured one.

---

### 3.2.4.2 Mesh Quality

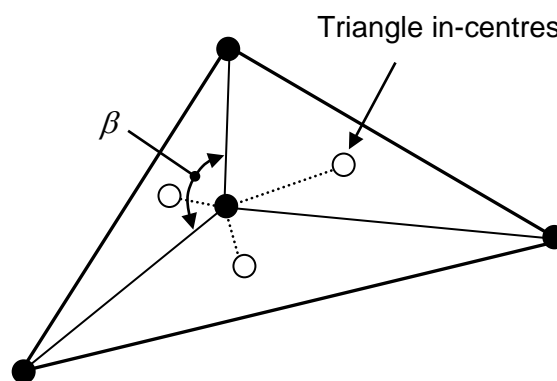
Generating a quality mesh is not a trivial exercise. The quality of a cell depends on factors in the grid shape, such as aspect ratio, skewness, and warp angle. The grid shape can be in the form of a structured or unstructured mesh as shown in Figure 3. 9 and Figure 3. 10. The grid aspect ratio of the cell is defined as  $AR = \Delta y / \Delta x$ . In the first boundary layer mesh, to help keep the solution accurate, this ratio should be small to make an AR within a suitable range. In addition, large ratios should always be avoided in significant flow regions inside the computation domain because they are prone to producing poor iterative convergence and reduce the solution accuracy in the computational flow solver during the numerical computations. Mesh skewness is measured by determining the angle  $\theta$  between the mesh lines (Figure 3. 9). For minimal distortion, it is most desirable for the mesh lines to be at an angle  $\theta$  of approximately 90 degrees (orthogonal). If the angle is  $\theta < 45$  degrees or  $\theta > 135$  degrees, the mesh becomes skewed and often exhibits deterioration in the computational results or leads to numerical instabilities.



*Figure 3. 9 A quadrilateral cell having mesh spacing of  $\Delta x$  and  $\Delta y$  and an angle of  $\theta$  between the grid lines of the cell.*



For an unstructured mesh, special care needs to be taken to ensure that the warp angles measuring between the surfaces' normal to the triangular parts of the faces are not greater than 75 degrees as indicated by the angle  $\beta$  in Figure 3. 10. Cells with large deviations from the co-planar faces can lead to serious convergence problems. In many grid generation packages, the problem can be overcome by a grid smoothing algorithm to improve the element warp angles. Whenever possible, the use of tetrahedral elements should be avoided in wall boundary layers. Prismatic or hexahedral cells are preferred because of their regular shape. A prism grid is often used to close the thin wall flow in the boundary layer. The first grid element, which is a thin layer behind the wall, then other grid elements above the first element until its layers cover the distance of the boundary layer. This allows maximum flexibility in matching appropriate cells with boundary surfaces and allocating cells of various element types in other parts of the complex flow regions. In this thesis, an unstructured mesh is used for all the models and a prism mesh for the boundary layer.



*Figure 3. 10 A triangular cell having an angle of  $\beta$  between the surfaces normal to the triangular parts of the faces connected to two adjacent triangles.*

---

### **3.2.4.3 Mesh Independence**

Mesh independence is performed to analyze the suitability of the mesh and to yield an estimate of the numerical errors in the computational simulation. In addition it is used to determine the minimum mesh resolution required to generate a solution that becomes independent of the mesh size that is used. In this thesis, each model is made with at least three significantly different grid resolutions, where each subsequent mesh is approximately doubled in each direction. A flow field variable should be checked at each mesh to monitor its value or profile. The mesh is considered independent when the flow variable does not change with an increase in the mesh size. This leads to a mesh that has been optimised and hence is grid independent for the flow field where a compromise between computational resources and accuracy has been made.

## **3.3 CFD Models**

### **3.3.1 Nasal Cavity with Sinus Model**

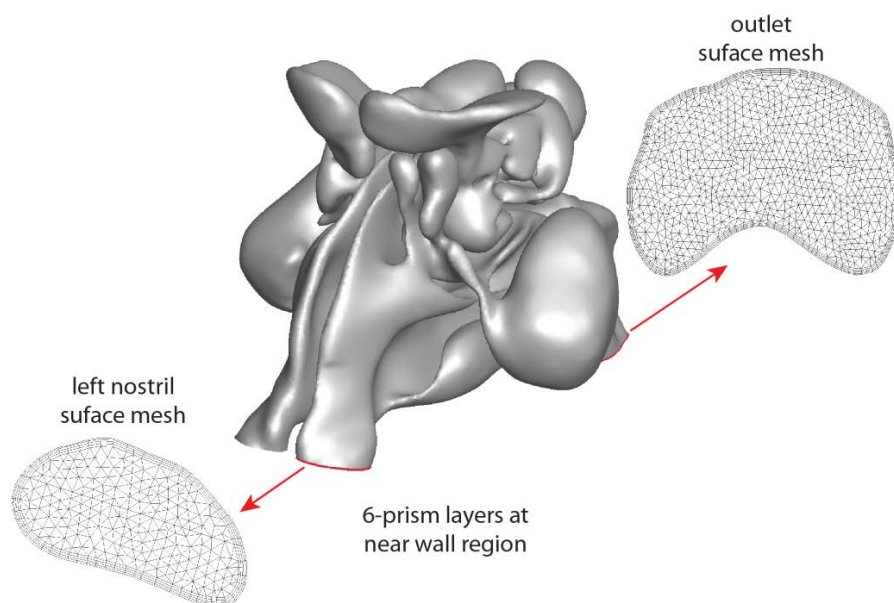
For the nasal cavity, CT scans of a healthy nose from a 51-year-old Asian male, were obtained. The outline of the model was segmented from the CT-scans and a computational mesh for CFD analysis was applied. Two nasal cavity models were reconstructed from the same CT scans, and are labelled as NC02 (nasal cavity without paranasal sinuses) and NC02-S (nasal cavity with paranasal sinuses), noting that the difference in the labels is the character S to denote the addition of the sinuses.

The influence of computational smoothing on airflow resistance and particle deposition has been discussed by Schroeter et al (2011). The developed model underwent 5% level of smoothing to ensure that any artificial residual artefacts persisting from the scanned images were omitted from the final computational model. Given that images

---

obtained from CT-scans are more prone to artefacts than other conventional radiographs, the level of smoothing applied allowed a compromise between retention of real geometry artefacts (e.g. overlying mucus) to artificially created artefacts caused by CT-scans and its segmentation (e.g. streaking, distortion and shading due to inconsistency and inaccuracy of scanner, patient movement or the presence of metallic materials in or on the patient) and CAD file interpretations.

The meshing scheme used a hybrid mesh that included six-prismatic layers with an inner tetrahedral core. Grid independence based on velocity profiles at the outlet was performed where the optimum number of cells for each geometry mesh was 3million for NC02 and 4million for NC02-S. This means that the geometries showed less than 1% change in velocity profiles when the mesh was further refined. As discussed earlier, the mesh should change slowly and smoothly away from the domain boundary. Figure 3. 12 shows the application of a hybrid mesh that contains tetrahedral elements inside the domain and prism layers along the surface or domain boundaries.



*Figure 3. 11 Near wall mesh that has a 6-prism layer for a nasal cavity with sinus model.*

---

### 3.3.2 Nasal Cavity with Nasal Spray Device Model

An existing computational model of the nasal cavity is used and for brevity, the details of its model construction, and verification can be found by Inthavong et al (2009b), and is labelled as NC01 (nasal cavity without paranasal sinuses). In earlier studies, Inthavong et al(2006) along with others in the literature (Kleinstreuer and Zhang 2003; Li et al. 2007a; Straatsma et al. 1999), the number of cells making up the mesh in the computational model of the nasal cavity was limited by the available computing power.

Now with increased computing power (HPxw6600 Workstation 16GB Ram, 16 Processors), a nasal cavity with 3.5 million cells (193Mb in computational memory size) was developed using unstructured tetrahedral cells with mesh refinements at the near wall regions and high curvature geometric features. The finer mesh, especially near the wall boundaries, allows better modelling of the sharp gradients found in the boundary layer. In addition the maximum  $y^+$  value in any cell of the model needed to be in the order of 1, ( $y^+_{\max} = 0.78$ ) to resolve the near wall region for the low Reynolds number  $k-\omega$  turbulence model. Grid independence was achieved for a mesh size of 1 million cells (Inthavong 2006), however it was found that a small percentage of adjacent wall cells had a  $y^+$  value greater than 1, which was addressed in the final model.

Based on this nasal cavity model, a second model was created to include the presence of a nasal spray device inside the left nostril. The spray device has a head diameter of 7mm inserted at an angle of  $10^\circ$  from vertical. The computational model with nose spray is depicted in Figure 3. 12 and consists of 3 regions, namely Anterior Region (nasal vestibules), Middle Region (olfactory and turbinates) and Posterior Region (nasopharynx), and is labelled as NC01S (nasal cavity with spray drive)

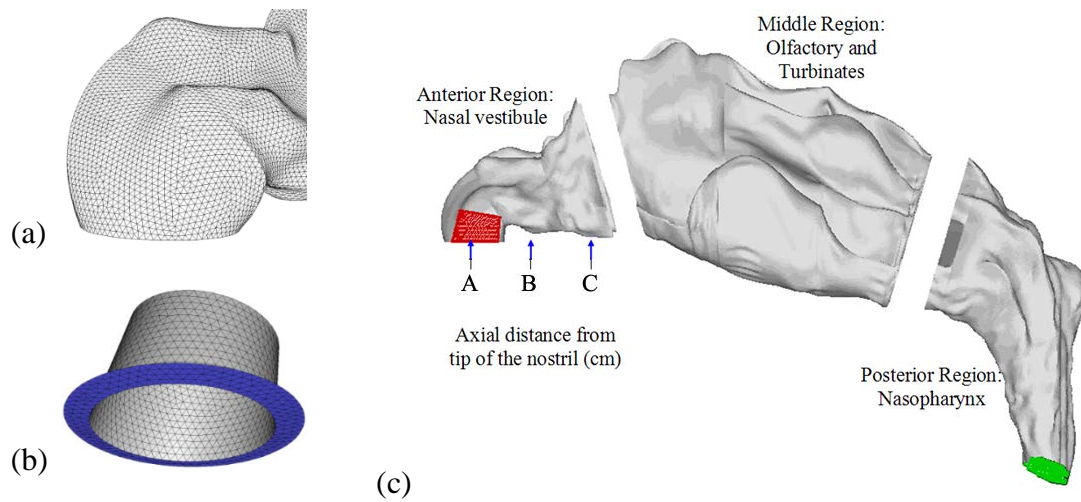


Figure 3.12 Computational model inclusive of the nasal spray device, highlighted in red. (a) External tetrahedral surface mesh at the left nostril region. (b) Internal tetrahedral surface mesh of the nasal spray device. The blue annulus region represents the surface inlet opening space, left over from the spray device partially blocking the opening. (c) Computational model subdivided into three regions. Labels A, B, C represent three coronal slices in the left nasal cavity created for visualisation of airflow patterns

---

# Chapter 4

## Numerical Methodology

### 4.1 Introduction

In this chapter, the general numerical models and mathematical equations used for the numerical simulations in this thesis are provided. The turbulent models,  $k$ - $\epsilon$  and Shear Stress Transport (SST) models, that are in the framework of Reynolds averaged Navier-Stokes (RANS) model, are used to describe the gas phase modelling. For the particle phase modelling, the numerical models used the Lagrangian particle tracking and Eulerian diffusion model. For different sized the particle, used different modelling methods are needed and this is discussed in the separate chapters (chapter 5, 6 and 7).

### 4.2 Gas Phase Modelling

The governing equation of fluid flow is represented through infinitesimal small control volume to conserve mass and energy from the basic conservation principles. It can be shown that these equations conform to a generic transport equation. Fundamentally the transport equation describes the inertial movement by the local acceleration and convection of a fluid variable, which is opposed by the diffusion which acts against the flow of the fluid variable.

---

## 4.2.1 Governing Equations for Fluid Flow

CFD is fundamentally based on the governing equations of fluid flow, and heat transfer which are the conservation laws of physics. The equations are:

- Continuity equation
- Three momentum equations, and
- Energy equation

which are solved numerically for the incompressible gas phase flow in the computational domain. These equations form what is called the full Navier-Stokes equations. The full set of equations can be found in Appendix A.

## 4.2.2 Turbulence Modelling

### 4.2.2.1 Reynolds Averaged Navier-Stokes Equations (RANS)

The Reynolds Averaged Navier Stokes (RANS) based turbulence models gets its name from the decomposition of the flow variables into the average and fluctuating components within the governing equations resulting in time averaged equations with the turbulent features encapsulated by the Reynolds stress. This is achieved by adopting a suitable time-averaging operation on the momentum equations to yield the RANS equations as:

$$\frac{\partial(\rho_g \bar{u}_j^g)}{\partial x_j} = 0 \quad 4.7$$

$$\frac{\partial(\rho_g \bar{u}_i^g)}{\partial t} + \frac{\partial(\rho_g \bar{u}_j^g \bar{u}_i^g)}{\partial x_j} = \frac{\partial}{\partial x_j} \left( \mu_g \frac{\partial \bar{u}_i^g}{\partial x_j} \right) - \frac{\partial \bar{p}_g}{\partial x_i} - \frac{\partial(\rho_g \overline{u'_i u'_j})}{\partial x_j} + \frac{\partial \bar{\tau}_{ij}}{\partial x_j} \quad 4.8$$

where  $\bar{u}_i^g$  and  $u_i'$  are gas phase mean velocity and gas phase fluctuating velocity, respectively. The  $\bar{\tau}_{ij}$  is the mean viscous stress tensor component:

$$\bar{\tau}_{ij} = \mu_g \left( \frac{\partial \bar{u}_i^g}{\partial x_j} + \frac{\partial \bar{u}_j^g}{\partial x_i} \right) \quad 4.9$$

The time-averaged equations can be solved if the unknown Reynolds stresses,  $\overline{\rho_g u_i' u_j'}$  in Equation (4.8) can be related to the mean flow quantities. It was proposed that the Reynolds stresses could be linked to the mean rates of deformation (Hinze, 1975):

$$\rho_g \overline{u_i' u_j'} = \mu_{g,t} \left( \frac{\partial \bar{u}_i^g}{\partial x_j} + \frac{\partial \bar{u}_j^g}{\partial x_i} \right) - \frac{2}{3} \rho_g \sigma_{ij} k_g \quad 4.10$$

where  $\mu_{g,t}$  is the eddy viscosity or turbulent viscosity. Since the complexity of turbulence in most engineering flow problems precludes the use of any simple formulae, it is possible to develop similar transport equations to accommodate the turbulent quantity  $k_g$  and other turbulent quantities such as the rate of dissipation of turbulent energy  $\varepsilon_g$ . Here,  $k_g$  and  $\varepsilon_g$  can be defined and expressed in Cartesian tensor notation as:

$$k_g = \frac{1}{2} \overline{u_i' u_i'} \quad \text{and} \quad \varepsilon_g = \frac{\mu_{g,t}}{\rho_g} \left( \frac{\partial u_i'}{\partial x_j} \right) \left( \frac{\partial u_i'}{\partial x_j} \right) \quad 4.11$$

From the local values of  $k_g$  and  $\varepsilon_g$ , a local turbulent viscosity  $\mu_{g,t}$  can be evaluated as:

$$\mu_{g,t} = \frac{C_\mu \rho_g k_g^2}{\varepsilon_g} \quad 4.12$$

By substituting the Reynolds stress expressions in Equation (4.10) into the governing Equation (4.7) and (4.8), and removing the overbar that is indicating the time-averaged quantities, one obtains the following equations can be obtained.



$$\frac{\partial(\rho_g u_j^g)}{\partial x_j} = 0 \quad 4.13$$

$$\frac{\partial(\rho_g u_i^g)}{\partial t} + \frac{\partial}{\partial x_j} \left( \rho_g u_i^g u_j^g - (\mu_{g,t} + \mu_g) \left( \frac{\partial u_i^g}{\partial x_j} + \frac{\partial u_j^g}{\partial x_i} \right) \right) = -\frac{\partial p_g}{\partial x_i} \quad 4.14$$

#### 4.2.2.2 Re-Normalization Group Model (RNG)

In the 1984, Yakhot and Orszag (1984) developed Re-Normalization Group model (RNG), the kinetic energy ( $k$ ) and dissipation ( $\varepsilon$ ) are solved by two additional differential equations, are obtained from the following transport equation:

$$\frac{\partial(\rho_g k_g)}{\partial t} + \frac{\partial(\rho_g u_j^g k_g)}{\partial x_j} = \frac{\partial}{\partial x_j} \left( \sigma_k \mu_{eff} \frac{\partial k_g}{\partial x_j} \right) - \rho_g \overline{u_i' u_j'} \frac{\partial u_i^g}{\partial x_j} + \beta g_i \frac{\mu_i \partial T}{Pr_t \partial x_i} - \rho_g \varepsilon_g \quad 4.15$$

$$\begin{aligned} \frac{\partial(\rho_g \varepsilon_g)}{\partial t} + \frac{\partial(\rho_g u_j^g \varepsilon_g)}{\partial x_j} = \\ \frac{\partial}{\partial x_j} \left( \sigma_\varepsilon \mu_{eff} \frac{\partial \varepsilon_g}{\partial x_j} \right) - C_{1\varepsilon} \left( -\rho_g \overline{u_i' u_j'} \frac{\partial u_i^g}{\partial x_j} + C_{3\varepsilon} \beta g_i \frac{\mu_i \partial T}{Pr_t \partial x_i} \right) - \rho_g C_{2\varepsilon} \frac{\varepsilon_g^2}{k_g} - R \end{aligned} \quad 4.16$$

The coefficient of thermal expansion,  $\beta$ , is defined as

$$\beta = -\frac{1}{\rho} \left( \frac{\partial \rho}{\partial T} \right)_p \quad 4.17$$

The degree to which  $\varepsilon$  is affected by the buoyancy is determined by the constant  $C_{3\varepsilon}$ .

In ANSYS FLUENT is not specified, but  $C_{3\varepsilon}$  is instead calculated according to the following relation:

$$C_{3\varepsilon} = \tanh \left| \frac{v}{u} \right| \quad 4.18$$

Where  $v$  is the component of the flow velocity parallel to the gravitational vector and  $u$  is the component for the flow velocity perpendicular to the gravitational vector. The

Prandtl number ( $Pr_t$ ) is the turbulent Prandtl number for energy and  $g_j$  is the component for the gravitational vector in the  $i$  th direction,  $Pr_t$  is  $1/\alpha$ , where  $\alpha$  is given by equation:

$$\left| \frac{\alpha - 1.3929}{\alpha_0 - 1.3929} \right|^{0.6321} \left| \frac{\alpha + 2.3929}{\alpha_0 + 2.3929} \right|^{0.3679} = \frac{\mu_{mol}}{\mu_{eff}} \quad 4.19$$

$\alpha_0=1.0$ . in the high Reynolds number limit ( $\mu_{mol}/\mu_{eff} \ll 1$ ),  $\alpha k = \alpha \varepsilon \approx 1.393$ . The RNG turbulence model is the turbulent viscosity. The scale elimination procedure in RNG theory results in a differential equation for turbulent viscosity  $\mu_{eff}$  :

$$d \left( \frac{\rho_g^2 k_g}{\sqrt{\varepsilon_g \mu_g}} \right) = 1.72 \frac{\hat{v}}{\sqrt{\hat{v}^3 - 1 + C_v}} d \hat{v} \quad 4.20$$

where  $\hat{v} = \mu_{eff} / \mu_g$  and  $C_v=100$ .

The RNG k- $\varepsilon$  model includes an additional strain rate term R in the  $\varepsilon$ -equation (4.18) for the RNG k- $\varepsilon$  model. The term is modelled as:

$$R = \frac{C_\mu \eta^3 (1 - \eta/\eta_o) \varepsilon_g^2}{1 + \beta \eta^3} \frac{1}{k_g} \quad 4.21$$

Here,  $\beta$  and  $\eta_o$  are constants with values of 0.015 and 4.38. The significance of the inclusion of this term is its responsiveness towards the effects of rapid rate strain and streamlines curvature, which cannot be properly represented by the standard k- $\varepsilon$  model. According to the RNG theory (Yakhot and Orszag 1986), the constants in the turbulent transport equations are given as:

$$\sigma k = 0.718, \sigma \varepsilon = 0.718, C1\varepsilon = 1.42 \text{ and } C2\varepsilon = 1.68 \quad C\mu = 0.09,$$

### 4.2.2.3 Shear Stress Transport Model (SST)

The shear-stress transport (SST)  $k$ - $\omega$  model was developed by Menter (1994) to accommodate for a wider class of flows. The modifications include the addition of a cross diffusion term in the  $\omega$  equation and a blending function to ensure that the model equations behave appropriately in both the near wall and far field zones. To achieve this, the  $k$ - $\omega$ -SST model is converted into a  $k$ - $\omega$ -SST formulation. The  $k$ - $\omega$ -SST model is similar to the standard  $k$ - $\omega$  model, which are obtained from the following transport equation:

$$\frac{\partial(\rho_g k_g)}{\partial t} + \frac{\partial(\rho_g k_g u_j^g)}{\partial x_j} = \frac{\partial}{\partial x_j} \left( \left( \mu + \frac{\frac{1}{\max\left[\frac{1}{\alpha^*}, \frac{SF_2}{a_1 \omega}\right]} \frac{\rho k}{\omega}}{\sigma_k} \right) \frac{\partial k}{\partial x_j} \right) + \min(-\rho_g \overline{u_i' u_j'} \frac{\partial u_i^g}{\partial x_j}, 10 \rho \beta_i^* [1 + 1.5F(M_i)] k \omega) - \rho \beta_i^* [1 + 1.5F(M_i)] k \omega \quad 4.22$$

$$\frac{\partial(\rho_g \omega_g)}{\partial t} + \frac{\partial(\rho_g \omega_g u_j^g)}{\partial x_j} = \frac{\partial}{\partial x_j} \left( \left( \mu + \frac{\frac{1}{\max\left[\frac{1}{\alpha^*}, \frac{SF_2}{a_1 \omega}\right]} \frac{\rho k}{\omega}}{\sigma_\omega} \right) \frac{\partial \omega}{\partial x_j} \right) - \frac{\alpha}{\nu_i} \rho_g \overline{u_i' u_j'} \frac{\partial u_i^g}{\partial x_j} - \rho(F_1 \beta_{i,1} + (1 - F_1) \beta_{i,2}) \omega^2 + 2(1 - F_1) \rho \sigma_\omega \frac{1}{\omega} \frac{\partial k}{\partial x_j} \frac{\partial \omega}{\partial x_j} \quad 4.23$$

The coefficient  $\alpha^*$  and  $\alpha$  damps the turbulent viscosity. For a in a low-Reynolds-number flow axis given by:

$$\alpha = \frac{\alpha_\infty}{\alpha^*} \left( \left( \frac{\frac{\rho k}{\alpha_0 + \frac{\mu \omega}{R_\omega}}}{1 + \frac{\mu \omega}{R_\omega}} \right) \right) \quad \text{and} \quad \alpha^* = \alpha_\infty^* \left( \frac{\frac{\beta_i}{3} + \frac{\mu \omega}{R_k}}{1 + \frac{\mu \omega}{R_k}} \right) \quad 4.24$$

There are same components for the dissipation of  $k$  and  $\omega$ ; in dissipation of  $k$

$$\beta_i^* = \beta_\infty^* \left( \frac{\left( \frac{4}{15} + \left( \frac{\rho k}{\mu \omega} \right) / R_\beta \right)^4}{1 + \left( \frac{\rho k}{\mu \omega} \right) / R_\beta} \right)^4 \quad \text{and} \quad f_\beta = \begin{cases} \frac{1}{1+680\chi_k^2} & \chi_k \leq 0 \\ \frac{1}{1+400\chi_k^2} & \chi_k > 0 \end{cases} \quad \text{and} \quad \chi_k \equiv \frac{1}{\omega^3} \frac{\partial k}{\partial x_j} \frac{\partial \omega}{\partial x_j} \quad 4.25$$

in dissipation of  $\omega$

$$f_\beta = \frac{1+70\chi_\omega}{1+80\chi_\omega} \quad \chi_\omega = \left| \frac{\Omega_{ij} \Omega_{jk} S_{ki}}{(0.09\omega)^3} \right| \quad s \equiv \sqrt{2\Omega_{ij} \Omega_{ij}} \quad \text{and} \quad \Omega_{ij} = 0.5 \left( \frac{\partial u_i}{\partial x_j} - \frac{\partial u_j}{\partial x_i} \right) \quad 4.26$$

where S is the strain rate magnitude in 4.23 and 4.24 and

$$\sigma_k = \frac{1}{F_1/\sigma_{k,1} + (1-F_1)/\sigma_{k,2}} \quad 4.27$$

$$\sigma_\omega = \frac{1}{F_1/\sigma_{\omega,1} + (1-F_1)/\sigma_{\omega,2}} \quad 4.28$$

the blending functions, F1 and F2, are given by

$$F_1 = \tanh \left( \left( \min \left[ \max \left( \frac{\sqrt{k}}{0.09\omega y}, \frac{500\mu}{\rho y^2 \omega} \right), \frac{4\rho k}{\sigma_{\omega,2} D_\omega^+ y^2} \right] \right)^4 \right) \quad 4.29$$

$$F_2 = \tanh \left( \left( \max \left[ 2 \frac{\sqrt{k}}{0.09\omega y}, \frac{500\mu}{\rho y^2 \omega} \right] \right)^2 \right) \quad 4.30$$

where y is the distance to the next surface and  $D_\omega^+$  is the positive portion of the cross diffusion term.

$$\alpha_\infty = F_1 \left( \frac{\beta_{i,1}}{\beta_\infty^*} - \frac{\kappa^2}{\sigma_{\omega,1} \sqrt{\beta_\infty^*}} \right) + (1-F_1) \left( \frac{\beta_{i,2}}{\beta_\infty^*} - \frac{\kappa^2}{\sigma_{\omega,2} \sqrt{\beta_\infty^*}} \right) \quad 4.31$$

According to the theory,  $F(Mt)$  is the compressibility function, the constants in the turbulent transport equations are given:

$$\alpha_{k,1} = 1.176 \quad \alpha_{\omega,1} = 2 \quad \alpha_{k,2} = 1 \quad \alpha_{\omega,2} = 1.168 \quad a_1 = 0.31 \quad \beta_{i,1} = 0.075 \quad \beta_{i,2} = 0.0828 \quad \kappa = 0.41$$

$$\alpha_{\infty}^* = 1 \quad \alpha_{\infty} = 0.52 \quad \alpha_0 = \frac{1}{9} \quad \beta_{\infty}^* = 0.09 \quad \beta_i = 0.072 \quad R_{\beta} = 8 \quad R_k = 6 \quad R_{\omega} = 2.95 \quad \sigma_k = 2 \quad \sigma_{\omega} = 2$$

#### 4.2.2.4 Transition Shear Stress Transport Model

The transition SST model is based on the coupling of the SST  $k$ - $\omega$  transport equations with two other transport equations, one for the intermittency and one for the transition onset criteria, in terms of momentum-thickness Reynolds number. Langtry and Menter (2006) have been developed the model to cover standard bypass transition as well as flows in low free-stream turbulence environments. The transport equation for the intermittency  $\gamma$  is defined as

$$\frac{\partial(\rho\gamma)}{\partial t} + \frac{\partial(\rho U_j \gamma)}{\partial x_j} = P_{\gamma 1} - E_{\gamma 1} + P_{\gamma 2} - E_{\gamma 2} + \frac{\partial}{\partial x_j} \left[ \left( \mu + \frac{\mu_t}{\sigma_y} \right) \frac{\partial \gamma}{\partial x_j} \right] \quad 4.32$$

The transition sources are defined as follows:

$$P_{\gamma 1} = 2F_{length} \rho S [\gamma F_{onset}]^{c_{\gamma 3}}$$

$$E_{\gamma 1} = P_{\gamma 1} \gamma \quad 4.33$$

where  $S$  is the strain rate magnitude.  $F_{length}$  is an empirical correlation that controls the length of the transition region. The destruction/relaminarization sources are defined as follows:

$$P_{\gamma 2} = (2c_{\gamma 1}) \rho \Omega \gamma F_{turb}$$

$$E_{\gamma 2} = c_{\gamma 2} P_{\gamma 2} \gamma \quad 4.34$$

where  $\Omega$  is the vorticity magnitude. The transition onset is controlled by the following functions:

$$\text{Re}_V = \frac{\rho y^2 S}{\mu} \quad \text{and} \quad R_T = \frac{\rho k}{\mu \omega} \quad 4.35$$

$$F_{onset1} = \frac{\text{Re}_V}{2.193 \text{Re}_{\theta c}} \quad \text{and} \quad F_{onset2} = \min\left(\max\left(F_{onset1}, F_{onset1}^4\right), 2.0\right) \quad 4.36$$

$$F_{onset3} = \max\left(1 - \left(\frac{R_T}{2.5}\right)^3, 0\right), \quad F_{onset} = \max\left(F_{onset2} - F_{onset3}, 0\right) \quad \text{and} \quad F_{turb} = e^{-\left(\frac{R_T}{4}\right)^4} \quad 4.37$$

$\text{Re}_{\theta c}$  is the critical Reynolds number where the intermittency first starts to increase in the boundary layer. This occurs upstream of the transition Reynolds number  $\tilde{\text{Re}}_{\theta t}$  and the difference between the two must be obtained from an empirical correlation. Both the  $\tilde{\text{Re}}_{\theta t}$  and  $F_{length}$  correlations are functions of  $\text{Re}_{\theta c}$ . The constants for the intermittency equation are:

$$c_{\gamma 1} = 0.03 \quad ; \quad c_{\gamma 2} = 50 \quad ; \quad c_{\gamma 3} = 0.5 \quad ; \quad \sigma_{\gamma} = 1.0$$

Coupling of the transition model to the SST transport equation occurs as follows:

$$\frac{\partial}{\partial t}(\rho k) + \frac{\partial}{\partial \chi_j}(\rho u_j k) = \overline{P}_k - \overline{D}_k + \frac{\partial}{\partial \chi_j} \left( (\mu + \sigma_k \mu_t) \frac{\partial k}{\partial \chi_j} \right) \quad 4.38$$

$$\overline{P}_k = \gamma_{eff} P_k \quad 4.39$$

$$\overline{D}_k = \min\left(\max\left(\gamma_{eff}, 0.1\right), 1.0\right) D_k \quad 4.40$$

$$R_y = \frac{\rho y \sqrt{k}}{\mu} \quad 4.41$$

---


$$F_3 = e^{-\left(\frac{R_y}{120}\right)^3} \quad 4.42$$

$$F_t = \max\left(F_{1orig}, F_3\right) \quad 4.43$$

Where  $P_k$  and  $D_k$  are the original production and destruction terms for the SST model and  $F_{1orig}$  is the original SST blending function. Note that the production term in the  $\omega$ -equation is not modified. The rationale behind the above model formulation is given in detail in Menter et al (2003). In order to capture the laminar and transitional boundary layers correctly, the mesh must have a  $y^+$  of approximately one. If the  $y^+$  is too large (i.e.  $> 5$ ), then the transition onset location moves upstream with increasing  $y^+$ . It is recommended to use the bounded second order upwind based discretization for the mean flow, turbulence and transition equations.

### 4.3 Particle Phase Modelling

Particle dynamics, its motion transport and deposition in a flow domain can be described in either the Lagrangian or Eulerian perspective. This selection has a significant influence on the modelling requirements and the results produced. For example in the Lagrangian method, individual particle deposition can be visualised, while in the Eulerian, an approach volume fraction or concentration representing the particle phase in each cell on the surface walls is used to describe the particle phase deposition. This difference in perspectives leads to different coupling approaches of the particle equations to the governing equations of fluid flow. In this research, only the Eulerian-Lagrangian and Eulerian species (or component) model is used.

---

### 4.3.1 Micron Particles

A Lagrangian formulated micron particle equation of motion is solved using FLUENT (used in chapter 5, 6 and 8). The trajectory of a discrete particle phase is determined by integrating the force balance on the particle. This force balance equates the particle inertia with the forces acting on the particle. Appropriate forces such as the drag and gravitational forces are incorporated into the equation of motion. Particles are individually tracked under the Lagrangian approach by integrating the force balance equations on the particle as follows:

$$\frac{du_p}{dt} = F_D(u_g - u_p) + \frac{g(\rho_p - \rho_g)}{\rho_p} + F_s \quad 4.44$$

where  $F_s$  is other possible forces such as virtual mass force, Basset force and pressure gradient force, which are not applicable for micron particles with  $\rho_p \gg \rho_g$ .

$F_D(u_g - u_p)$  is the drag force per unit particles mass, and  $F_D$  is given by:

$$F_D = \frac{18\mu_g C_D \text{Re}_p}{\rho_p d_p^2} \frac{1}{24} \quad 4.45$$

where  $\rho_p$  denotes the density of particle material and  $d_p$  is the particle diameter.  $u_p$

presents the particle velocity.  $\text{Re}_p$  is the relative Reynolds number defined as:

$$\text{Re}_p = \frac{\rho_p d_p |u_p - u_g|}{\mu_g} \quad 4.46$$

$C_D$  is drag coefficient as correlated as a function of the  $\text{Re}_p$ :

$$C_D = a_1 + \frac{a_2}{\text{Re}_p} + \frac{a_3}{\text{Re}_p^2} \quad 4.47$$



---

The treatment of one-way turbulent particle dispersions can be performed through a stochastic methodology. The simplest approach and the one available in FLUENT is the eddy-interaction model (EIM), which is also called the discrete or discontinuous random walk model, (DRW). The DRW model is widely used in turbulent particle flows for its conceptual simplicity and uncomplicated reconstruction of the local eddies whose scales are deduced from local mean flow quantities. The fluid velocity in the particle motion equation (Equation 4.44) becomes  $u_g = \bar{u} + u'$  where  $\bar{u}$  is the mean velocity and  $u'$  is the fluctuating velocity component. The flow field is then assumed to consist of random discrete eddies, each of which are defined by a lifetime, length, and velocity scale. From the model of Gosman and Ioannides (1981) the eddy scales for homogeneous isotropic stationary turbulence are determined from the fluid turbulence model as:

$$L_e = (C_\mu)^{3/4} \frac{k^{3/2}}{\varepsilon} \quad \tau_e = \frac{L_e}{(2k/3)^{0.5}} = \sqrt{3/2} (C_\mu)^{3/4} \frac{k}{\varepsilon} \quad \text{and} \quad u_e = (2k/3)^{0.5} \quad 4.48$$

Graham and James (1996), suggests that these same representative scales should be doubled for non-homogeneous turbulence as the length and time scales is expected to under-estimate particle dispersion. The fluctuating velocity components  $u'_i$  that prevail during the lifetime of the turbulent eddy are sampled by assuming that they obey a Gaussian probability distribution. The fluctuating velocity is then:

$$u'_i = \zeta \sqrt{u_i'^2} \quad 4.49$$

where  $\zeta$  is a normally distributed random number. Assume the local root mean square (RMS) velocity fluctuation is isotropy, it can be obtained by:

---


$$\sqrt{u_i'^2} = \sqrt{2\kappa_g/3} \quad 4.50$$

The interaction time between the particles and eddies is smaller of the eddy lifetime  $\tau_e$  and the particle eddy a crossing time  $\tau_{cross}$ . The characteristic lifetime of the eddy is defined as:

$$\tau_e = -T_L \log(r) \text{ in which } T_L \approx \frac{0.15}{\omega} \quad 4.51$$

$$t_{cross} = -\tau \ln \left[ 1 - \left( \frac{L_e}{\tau |u_g - u_p|} \right) \right] \quad 4.52$$

$$\tau = \frac{\rho_g \rho_p d_p^2}{18 \rho_g \mu_g} \quad 4.53$$

The particle interacts with the fluid eddy over the interaction time. When the eddy lifetime is reached, a new value of the instantaneous velocity is obtained by applying a new value of  $\zeta$  in 4.49. Small micron particles have been shown to be sensitive to the near wall anisotropy. When using a RANS turbulence model such as the  $k-\omega$  model that is based on the isotropic assumption ( $u' = v' = w' = (2k/3)^{0.5}$ ), the deposition of the micron particles (1-10 $\mu\text{m}$ ) is overpredicted. The overprediction is primarily caused by  $v'$  which is much smaller in comparison with the other fluctuating components,  $u'$  and  $w'$ . This can be accounted for through a damping function (Matida et al. 2004; Wang and James 1999) applied in the near wall region of  $y^+ < 60$  given as:

$$k_{new} = [1 - \exp(-0.02y^+)] k_{simulated} \quad \text{for } y^+ < 60 \quad 4.54$$

---

### 4.3.2 Sub-Micron Particles

For sub-micron particles, the effects of Brownian random force generated by the impact of gas molecules on the particle can be included as an additional force term and included as part of  $F_s$  in the particle equation of motion given by Equation (4.44):

For submicron particles,  $F_D$  takes the form of Stokes' drag law (Ounis et al. 1991) that

is  $C_D = \frac{24}{Re}$ , convert it with Equ4.47 becomes:

$$F_D = \frac{18\mu}{d_p^2 \rho_p C_c} \quad 4.55$$

where  $C_c$  is the Cunningham correction factor to Stokes' drag law, which can be calculated from,

$$C_c = 1 + \frac{2\lambda}{d_p} \left( 1.257 + 0.4e^{-(1.1d_p/2\lambda)} \right) \quad 4.56$$

$\lambda$  is the mean free path of air, assumed to be 65 nm. Amplitudes of the Brownian force components are of the form,

$$F_B = \zeta \sqrt{\frac{\pi S_0}{\Delta t}} \quad 4.57$$

where  $\zeta$  is a zero mean, unit variance independent Gaussian random numbers.  $\Delta t$  is the time-step for particle integration, and  $S_0$  is a spectral intensity function,

$$S_0 = \frac{216\nu k_B T}{\pi^2 \rho d_p^5 \left( \frac{\rho_p}{\rho} \right)^2 C_c} \quad 4.58$$

which is directly related to the diffusion coefficient.

---

Saffman's lift force, or lift due to shear (Li and Ahmadi 1992), is a generalisation of the expression originally provided by (Saffman 1965) and is applied here as:

$$F_L = \frac{2Kv^{1/2}\rho d_{ij}}{\rho_p d_p (d_{ik}d_{kl})^{1/4}} (\vec{v} - \vec{v}_p) \quad 4.59$$

$K$  is a constant and is equal to 2.594 while  $d_{ij}$  is the deformation tensor. This form of the lift force is intended for small particle Reynolds numbers. Also, the particle Reynolds number based on the slip velocity must be smaller than the square root of the particle Reynolds number based on the shear field.

Small particles suspended in a gas that exhibits a temperature gradient experiences a thermophoretic force in the direction opposite to that of the gradient. This effect is included in the thermophoretic force term,

$$F_T = -D_T \frac{1}{m_p T} \frac{\partial T}{\partial i} \quad 4.60$$

where  $D_T$  is the thermophoretic coefficient given by Talbot et al (1980).

An alternative for the Lagrangian approach in nanoparticle modelling is to use the Eulerian species approach. This involves modelling the nanoparticle diffusion with a single mixture component fluid with the nanoparticles treated as a chemical component or species. A scalar  $c$ , representing the concentration of the nanoparticles is applied to the transport equation as:

$$\frac{\partial(u_j c)}{\partial x_j} = \frac{\partial}{\partial x_j} \left[ \left( \tilde{D} + \frac{\nu_T}{S} \right) \frac{\partial c}{\partial x_j} \right] \quad 4.61$$

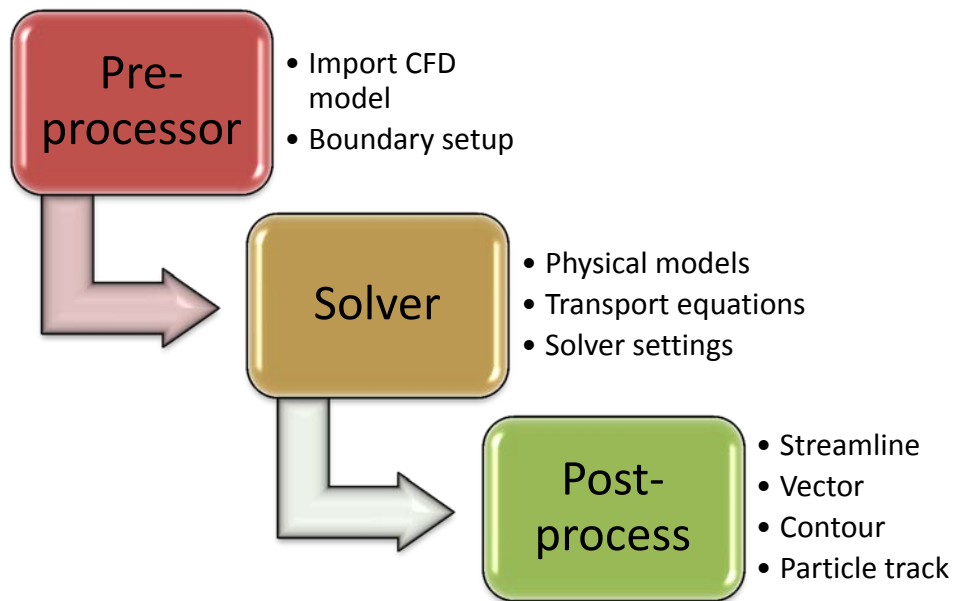
which neglects the effects of particle inertia. Longest et al (2007) showed that the effects of particle inertia plays a minor role in ultrafine aerosol deposition.

---

## 4.4 Numerical Solution and Procedure

### 4.4.1 Solution Procedure

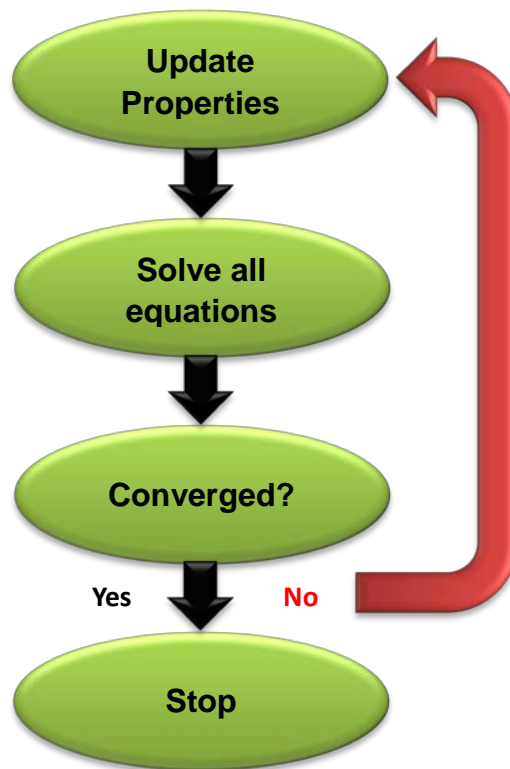
To summarise the CFD solution process, Figure 4. 1 shows the interconnections of the three main elements of a CFD analysis (Ansys 2007). In the Pre-processor stage, geometry for analysis and defining the computation domain, the fluid properties and physics, is needed. This stage determines the analysis type that can be steady flow or transient flow, and at laminar or turbulent state. The transport of heat may be included into the analysis if it contributes significantly to the fluid flow process. The three heat transfer modes are conduction, convection and radiation. In terms of modelling the particle phase, there are two methods that can be used: Lagrangian discrete phase, and a fully coupled Eulerian multiphase. The complex nature of the fluid flow behaviour has important implications in which boundary conditions are prescribed for the flow problem. The appropriate conditions selected need to mimic real physical representation of the fluid flow. At inflow and outflow boundaries of the flow domain, suitable fluid flow boundary conditions are required to accommodate the fluid behavior entering and leaving the flow domain. The flow domain may also be bounded by open boundaries. Appropriate boundary conditions are also required to be assigned for external stationary solid wall boundaries that bound the flow geometry and the surrounding walls of possible internal obstacles within the flow domain.



*Figure 4. 1 Flow process of the three main elements within a CFPD analysis framework.*

The numerical methods and solution is the basis of the second main element of a CFD simulation. The selection of an appropriate numerical solution method is imperative to obtain reliable results. These methods include discretisation schemes (equations applied onto the mesh), pressure-velocity coupling schemes, particle tracking schemes, and convergence criteria.

The steps in a solver can be shown in Figure 4. 2. Values of flow properties such as the velocity, pressure, temperature and other transport parameters of interest are defined at every computational cell before calculations can begin. During the actual numerical calculations the user should undertake solution monitoring which involves checking for convergence of the iterative process and performing grid independence. The last step is Post-processing, which involves the conversion of raw data into meaningful results. CFD has the ability to produce colourful graphics, and precise detailed data such as streamline, contour, and vector plots as well as particle tracking.



*Figure 4. 2 Overview of the segregated solver solution steps*

## **4.4.2 Numerical Solution Schemes**

### **4.4.2.1 Fluid Flow Discretisation**

Almost all commercial CFD codes adopt the finite volume discretisation of the Navier-Stokes equation with different schemes to obtain numerical solutions. There a number of fluid flow discretisation schemes, which can be categorised by their accuracy. The first order scheme is the least accurate, and is susceptible in producing incorrect results. The second order accurate upwind schemes reduce some of the errors found in first order schemes, and accounts for upstream flow effects by taking, the value of a cell face to equal to the value at the upstream node. Furthermore, the effect of a mesh refinement is far more influential under a second-order scheme in comparison to a fist-order scheme. The third order accurate Quadratic Upstream

---

Interpolation for Convective Kinetics (QUICK) scheme, that uses a quadratic approximation across two variable points at the upstream and one at the downstream and it was based on a weighted average of upwind and central interpolation of the variables. This provides accuracy for a larger range of flows, over the first order and Upwind schemes, although it can be difficult to obtain a converged solution if the CFD problem is complicated.

A popular scheme for pressure-velocity coupling for an incompressible flow is typically iterative methods, which is embodied in a scheme called SIMPLE. It is a widely used scheme developed by Patankar (1980) and can be found in nearly all CFD codes. The SIMPLE scheme provides a method of calculating the pressure and velocities for an incompressible flow. When coupled with other governing variables, the calculation needs to be performed sequentially since it is an iterative process.

When the CFD model has highly skewed cells or the physical problem is complicated, the discretised equations may encounter difficulties in converging, and in fact can diverge, and the solution is not achieved. The under-relaxation factor is a value between 0 and 1 which aims to reduce large changes in the variable which can help reduce the likelihood of divergence in the solution. However the value should not be set too small as this will slow down the solution. Therefore there is an optimal value that is low enough to prevent divergence in the solution but still high enough to provide rapid convergence. The selection of a suitable under-relaxation factor is flow dependent and different for each case, and so a single value cannot be used.

#### **4.4.2.2 Lagrangian Particle Phase**

The particle tracking equation is in the form of an ODE. Solution methods to the ODE include implicit, analytic, trapezoidal and runge-kutta. The first two methods are low



---

order schemes, while the latter two methods are high order scheme. The implicit method and analytic method use different integration (implicit Euler integration and analytic integration) at same equation (Equation 4. 44). The implicit method is unconditionally stable for all particle relaxation times. Instead, the analytical integration method is force held constant during the integration. The analytic method is very efficient; however it can become inaccurate for large steps and in situations where the particles are not in hydrodynamic equilibrium with the continuous flow. In the high order scheme, the trapezoidal method uses a semi-implicit trapezoidal integration as a fourth order scheme. The runge-kutta method is fifth order scheme and it derived by Cash et al (1990). The runge-kutta scheme is suggested of non-drag force changes along a particle integration step.

---

# Chapter 5

## The Effect of Human Thermal Plume on Particle Transport and Inhalation

### 5.1 Introduction

The transport characteristics of aerosol particles and their inhalation characteristics by human occupants in indoor environments have had a great deal of importance attached to them as people spend approximately 90% of their time indoors and a number of health problems have been found to be associated with particle inhalation (Inthavong et al. 2009a). During the past decades, numerous experimental and numerical investigations (Aitken et al. 1999; Anthony and Flynn 2006; Anthony et al. 2005; Hinds et al. 1998; Hsu and Swift 1999; King Se et al. 2010) have been conducted under various conditions and many important conclusions have been reported. It is generally accepted nowadays that the particle inhalability by a human occupant is subjected to many factors such as the particle size, ambient wind speed, airflow pattern in the breathing zone, inhalation rate, inhalation pattern (mouth or nasal inhalation), and even human facial features.

---

However, most of the previous investigations on particle inhalation failed to take into account the effects of the metabolic heat released from a human body. In fact, a human body is continually exchanging energy with its environment. The average thermal energy generated by a human body with an ordinary activity level and at moderate room temperatures was found to be up to 100Watts (Gowadia and Settles 2001). Due to this heat, a temperature gradient is formed and drives a buoyant free-convection with upward velocity in the vicinity of the human body, which is known as the human thermal plume (Craven and Settles 2006). Homma et al (1988) measured the free convection around a person standing in quiescent air using smoke wire photography and hot-wire anemometry. It was found that the thermal boundary layer was approximately 50mm thick at the face level and its velocity was up to 0.25m/s. Using a laser Doppler anemometer, Johnson et al (1996) measured the airflow around a human body standing with its back towards the free stream (0.2m/s). A significant upward airflow was observed in the downstream of the human body and the upward velocity was found to be approximately 0.19m/s at the nose level. A synthetic literature survey demonstrated that the human thermal plume can produce vertical air velocities of 0.1 to 0.25m/s in the breathing zone (Craven and Settles 2006; Homma and Yakiyama 1988; Johnson et al. 1996; Rim and Novoselac 2009b) This vertical velocity induced by body heat is roughly equal to the average wind speed in most indoor environments (0.05~0.25m/s according to Baldwin et al (1998) and Schmees et al (2008), it is therefore reasonable to expect that the buoyancy-driven convection may significantly change the airflow pattern and play an important role in transporting aerosol particles in the vicinity of a human body. This is especially true for fine and ultrafine particles as their transport is mostly controlled by the indoor flow field (Longest and Kleinstreuer 2004).

---

During the past years, the effects of human thermal plume on aerosol particle transport and inhalation have been investigated by few researchers in quiescent air. For example, using a sedentary thermal manikin (the surface area was  $1.5\text{m}^2$  and the total heating power was  $85\text{W}$ ), Rim et al (2009b) investigated experimentally the effects of human thermal plume on the inhalability of fine/ultrafine particles (0.03, 0.77 and 3.2 microns in diameter) in stratified indoor air. It was found that when the particle source was at floor level and in near proximity to an occupant, the inhaled particle concentration by the manikin was up to 4 times higher than the ambient concentration. This implies that the thermal plume plays an important role in transporting pollutants and particles from the floor level to the breathing zone. However, the conclusions based on quiescent or quasi-quiescent indoor air conditions may not be quantitatively applicable to realistic situations where ventilation is operating and the orientation of an occupant relative to the free stream may be random. Therefore, for the purpose of accurate description of the effects of human metabolic heat on particle transport and inhalation, some important factors including the wind speed and the occupant orientation have to be taken into account. In fact, few experimental investigations have been conducted to study the human thermal plume under low-speed wind conditions. For example, Heist et al (2003) measured the airflow around a child-size thermal manikin (80cm in height, facing to or back to the free stream, and with a constant surface temperature of  $33^\circ\text{C}$ ) in a wind tunnel. It was found that the presence of body heat dramatically changed the airflow pattern by causing an upward airflow on the downstream side of the manikin, which was believed to be capable of transporting particulates into the breathing zone form near the floor. This is especially true when the occupant was downstream facing. Unfortunately, the authors only measured the airflow field but failed to include particles in the experimental measurements. To the best of our knowledge, the effects

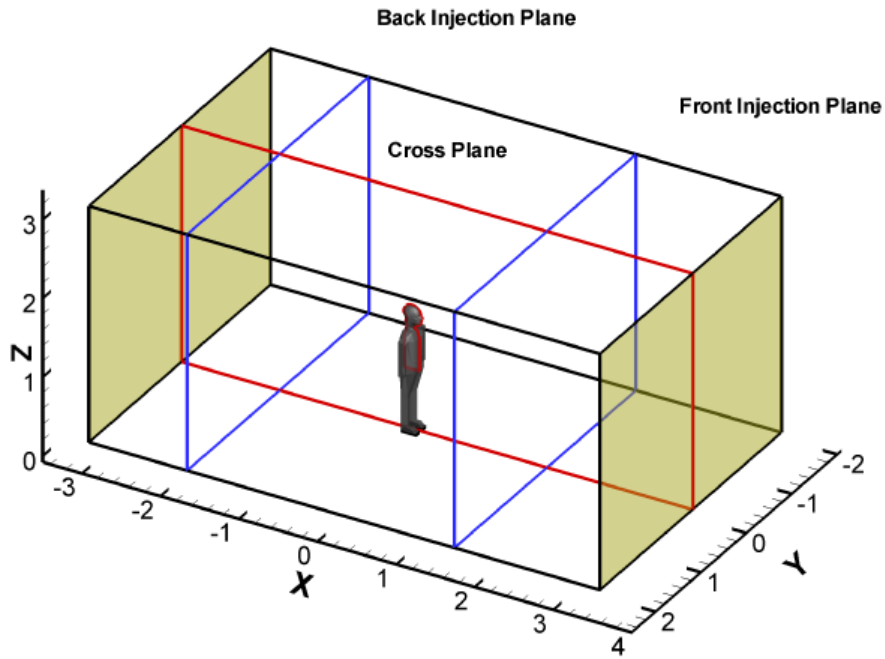
---

of human metabolic heat on particle transport and inhalation in a realistic indoor environment have rarely been investigated. Therefore in this chapter, the effects of human metabolic heat on particle transport and inhalation are synthetically investigated using CFD, with special consideration of various indoor wind speeds and the occupant-wind orientation.

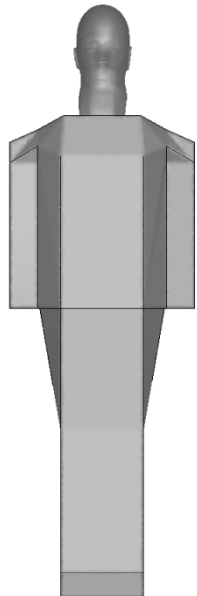
## **5.2 Numerical Procedure**

### **5.2.1 Computational Model**

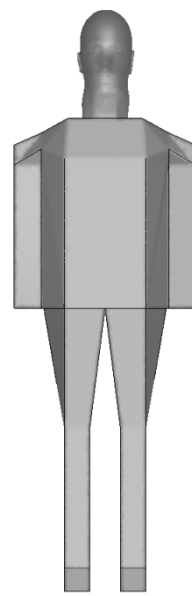
The computational domain of this study was a rectangular wind tunnel containing a 1.65m tall human manikin standing in its middle plane, as illustrated in Figure 5. 1a. The dimensions of the wind tunnel (4m-width×7m-depth×3m-height) were created large enough so that the flow field near the manikin was free from the effects of the no-slip condition of the stationary surrounding walls. Two slightly different manikin models were created in this study, namely one with its legs closed (Figure 5. 1b) and the other with its legs open (Figure 5. 1c). The former was used for model validation and the latter stood for more realistic situations. In order that the detailed airflow pattern and particle transport characteristics in the breathing zone could be captured, the manikin head was carefully built in terms of the anthropometric data of Tilley (1993) to represent the 50<sup>th</sup> percentile of a human male aged between 20 and 65 years.



(a) Layout of the computational domain



(b) Manikin model No. 1



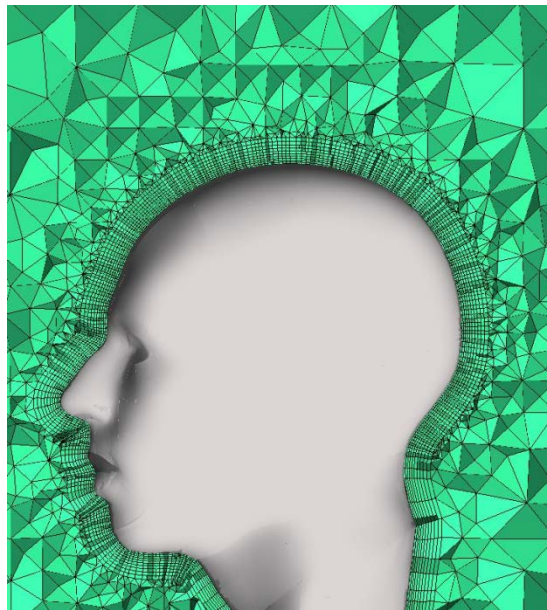
(c) Manikin model No. 2

*Figure 5. 1 The computational domain and human manikins*

Unstructured tetrahedral and prism meshes were adopted to discretise the computational domain, with fine meshes around the manikin to capture the geometric

---

features of the manikin and the effects of human thermal plume, as illustrated in Figure 5. 2. The grid sensitivity test proved that the mesh independence was achieved at 4.0 million cells, with the skewness of the cells and  $y^+$  value on the walls dropping below 0.8 and 0.78 respectively.



*Figure 5. 2 Refined meshes around the manikin model*

### **5.2.1 Boundary Conditions**

This manikin-wind orientation effect was taken into account in this study by applying an evenly distributed air inflow at the either tunnel end and a zero pressure boundary condition at the other end, which thereby produced a facing-the-wind and back-to-wind situation, respectively. The free stream velocity at the tunnel inlet was chosen to be in the range of 0.05 to 0.25m/s, which represents the typical indoor wind speeds (Schmees et al. 2008). The periodic respiration activities of the human body were neglected and the inhalation was assumed to be steady according to Horschler et al. (2010). A constant inhalation rate of 15 liters per minute (L/min) representing light human breathing at light activity conditions (Mihaescu et al. 2008; Snyer 1975) was equally applied at the

---

manikin nostrils, namely 7.5 L/min for each nostril. For heat transfer modelling, a constant free stream temperature of 26°C, which is a typical air-conditioning ventilation temperature in summer seasons, was applied at the tunnel inlet and a constant temperature of 31°C was applied at the manikin surface, as recommended by Gao et al. (2004). Particles with density of 1000kg/m<sup>3</sup> were released in a circular plane with a diameter of 1.6m and located 1.5m upstream of the manikin. The particle size was chosen to be small enough, (at 1.0µm), so that the effect of gravitational settling could be safely neglected and the transport of particles was mostly controlled by the airflow field (Jiang and Zhao 2010). A uniform particle concentration assumption to satisfy the “negligible bluff-off effects” criteria was used which is in line with the work by Chung et al (1994). This is achieved by releasing particles at the same velocity as that of the free stream. The assumption is needed to ensure consistent results regardless of the particle source location and to have a well-mixed condition. Finally, computations were also conducted using the isothermal conditions for the purpose of comparison. Sensitivity analysis proved that when the number of particle tracks turned over 100,000, the numerical results were independent of the particle track number.

## **5.3 Results and Discussion**

### **5.3.1 Model Validation**

The predicted air flow field was validated using Heist et al’s (2003) experimental data. In their experiments, they investigated the airflow pattern around a child-size manikin (80cm in height, leeward, without breathing) standing with its back towards the coming free stream in a wind tunnel using laser Doppler anemometry. Particle transport was not included in the experiments; therefore, only airflow equations were solved in the validation computations. The airflow visualization experiments were conducted under



isothermal and thermal conditions, respectively. In the isothermal condition, both the free stream and the manikin had the same temperature (21°C) while in thermal conditions, the temperatures of the free stream and the manikin surface were maintained at 21°C and 33°C, respectively, as listed in Table 5. 1. In order to achieve hydrodynamic and thermodynamic similarities with the experimental setup, the manikin model with its legs closed (Figure 5. 1b) was employed and the boundary conditions of the CFD model were carefully chosen to produce an equal Reynolds number for the isothermal case and an equal Richardson number for the thermal case, respectively, as listed in Table 1 as well. The Richardson number is defined by,

$$Ri = \frac{Gr}{Re^2} = \frac{g\beta(T_s - T_{ref})H}{u^2} \quad 5.1$$

where, Gr and Re are the Grashof number and Reynolds number, respectively.  $T_s$  is the manikin surface temperature and  $T_{ref}$  is the reference temperature, which takes the value of the free stream temperature (21°C).  $H$  is the manikin height and  $u$  is the velocity of the free stream.

*Table 5. 1 Experimental conditions and boundary conditions of validation computations*

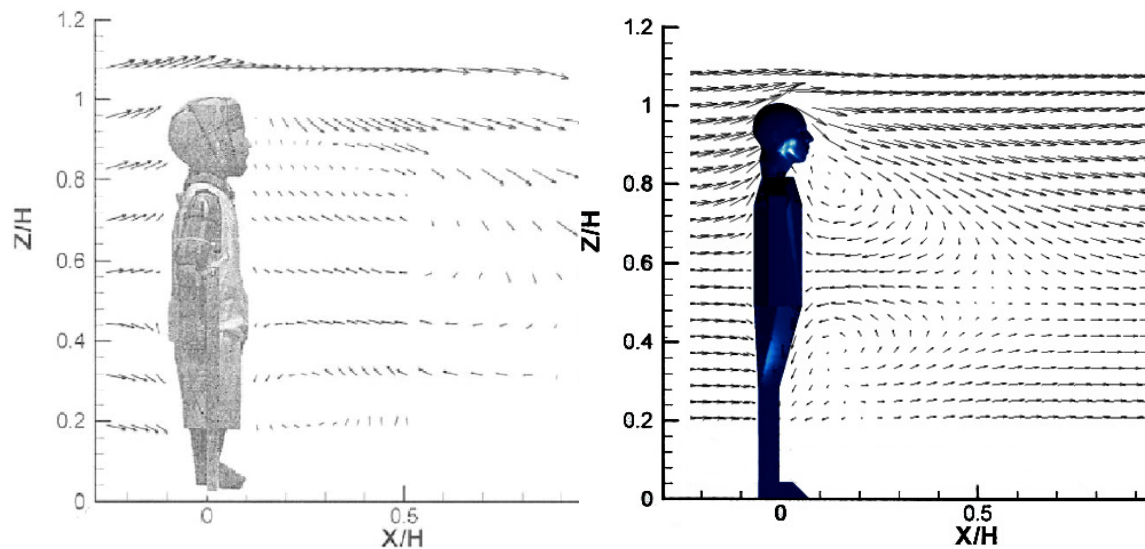
	$u$ (m/s)	$T_{ref}$ (°C)	$T_s$ (°C)	H (m)	Re	Ri
Experiment-Isothermal	0.1	21	21	0.8	5481	--
Simulation-Isothermal	0.051	21	21	1.6	5481	--
Experiment-Thermal	0.1	21	33	0.8	--	1.27
Simulation-Thermal	0.051	21	22.6	1.6	--	1.27

The predicted airflow fields around the manikin under the isothermal and thermal conditions are compared against the experimental results in Figure 5. 3 and Figure 5. 4. For the convenience of comparison, the coordinates in the figures are normalized with

---

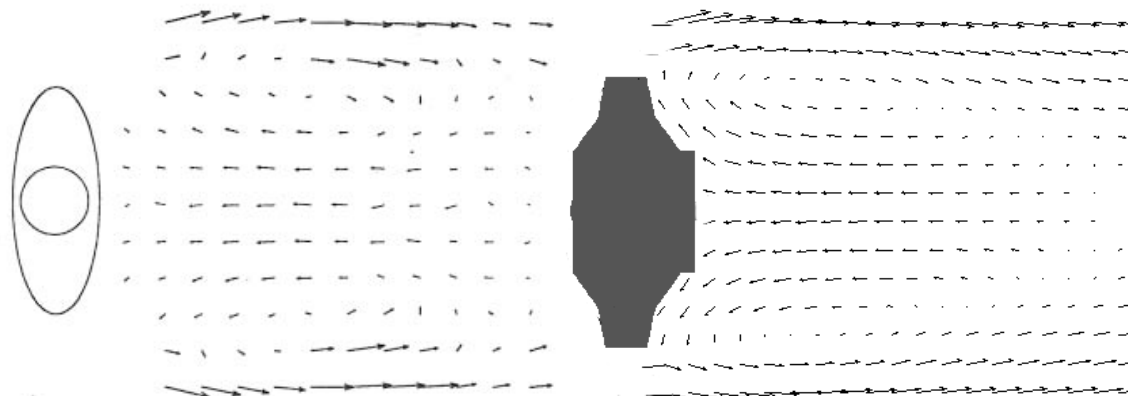
the manikin height (H). It was found that the simulated airflow fields generally agree well with the experimental results. The difference in the local vector distributions may be due to the different geometric shape of the manikins.

Figure 5. 3a and Figure 5. 3b are shown under the isothermal conditions, with a wake region containing two counter-rotating vortexes forming on the downstream side of the manikin. One of the vortexes is located near the breathing zone while the other is located at a lower height (near the legs). The former vortex entrains air flowing around the head into the breathing zone. This suggests that the air and contaminants that may be inhaled by an occupant are released from a source located at a height of the breathing zone. In addition, vortexes are also observed in horizontal planes. Figure 5. 3c and Figure 5. 3d show the airflow vectors in the horizontal plane of  $Z/H=0.6$ , where two counter-rotating elliptic vortexes are distributed symmetrically on the downstream side of the manikin. However, both the experiments and the numerical simulations using the thermal conditions present a totally different figure of the airflow pattern.



(a) Experiment

(b) Simulation

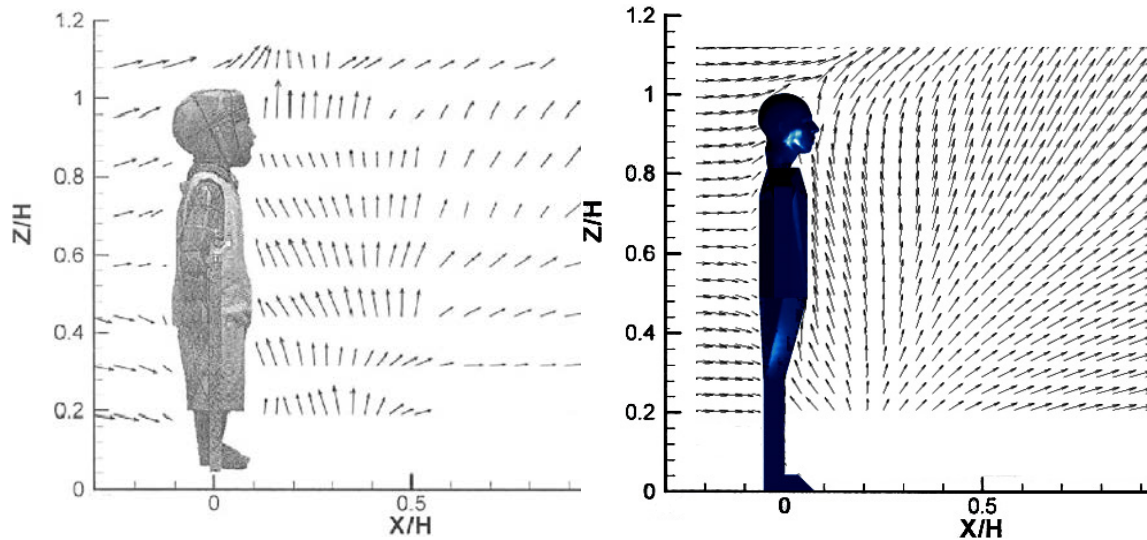


(c) Experiment,  $Z/H = 0.6$

(d) Simulation,  $Z/H = 0.6$

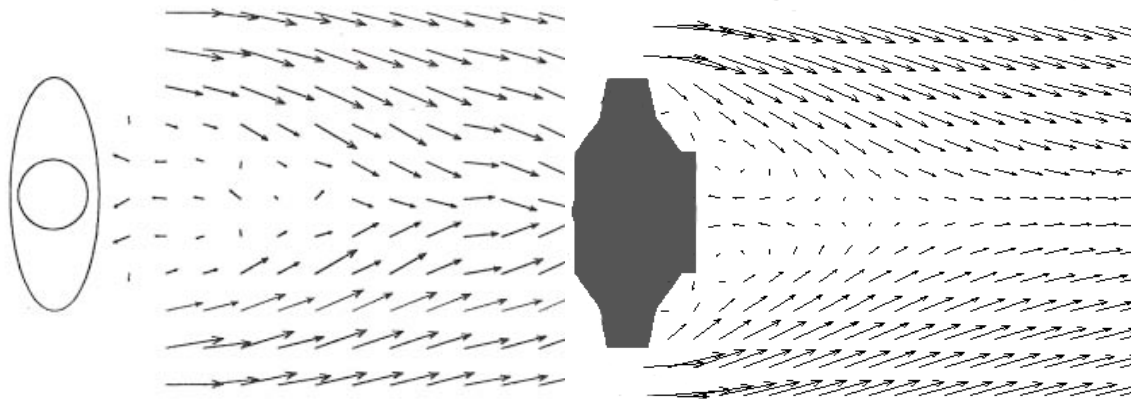
*Figure 5. 3 Airflow velocity vectors under isothermal conditions*

In Figure 5. 4a and Figure 5. 4b, when heat transfer between the manikin and the air is included, the vortex region on the downstream side of the manikin (Figure 5. 3a and Figure 5. 3b) is replaced by an upward rising airflow. Because of this rising airflow, the air in the breathing zone was observed to come from a lower height, especially from near the floor level, which indicates that the air and contaminants that may be inhaled are released from a source located near the floor. Furthermore, the counter-rotating vortexes in the horizontal plane of  $Z/H=0.6$  (Figure 5. 3c and Figure 5. 3d) are significantly suppressed, as shown in Figure 5. 4c and Figure 5. 4d.



(a) Experiment

(b) Simulation



(c) Experiment,  $Z/H = 0.6$

(d) Simulation,  $Z/H = 0.6$

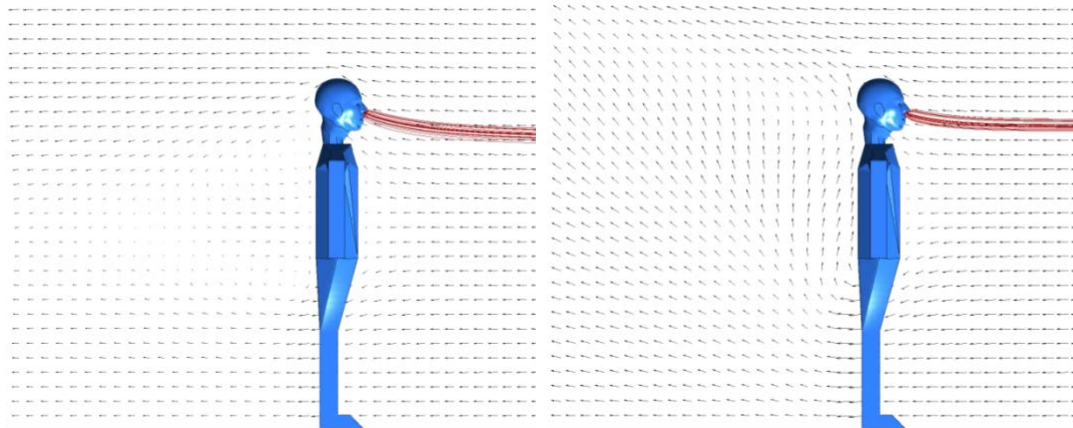
Figure 5. 4 Airflow velocity vectors under the thermal condition

It is clear that due to the heat transfer between a human body and its surroundings, there actually exists a distinct upward rising airflow (the human thermal plume) on the downstream side of the body. Because of this rising airflow, air and particulate contaminants in the breathing zone that may be inhaled by a human occupant actually come from a lower level than the breathing zone. Therefore, for the purpose of effective assessment of particle transport and inhalation, the effect of human body heat has to be taken into account, which will be discussed in the following sections.

---

### **5.3.2 Effects of Thermal Plume on Particle Transport & Inhalation**

Further simulations were conducted with various boundary conditions to investigate the effects of human body heat on particle transport and inhalation. In the following simulations, a more realistic manikin model that is open legs in Figure 5. 1c representing a human occupant standing with its legs open was employed. In addition, as demonstrated in the above paragraph, the airflow field on the downstream side of the manikin is significantly changed by its body heat while that on the upstream side is invisibly affected. This indicates that the inhalation characteristics of particles may be different with varying orientation of the manikin relative to the free stream. As illustrated previously, due to the obstacle of the manikin, the affected region is located at the downstream side of it. This indicates that when the manikin is facing the wind, the effect of body heat on particle inhalation is not significant since the airflow field in the breathing zone is not obviously changed. Figure 5. 5 shows that for the facing-the-wind cases, despite the total different airflow field on the downstream side of the manikin, the tracks of inhaled particles are almost the same for both the isothermal and the thermal conditions.

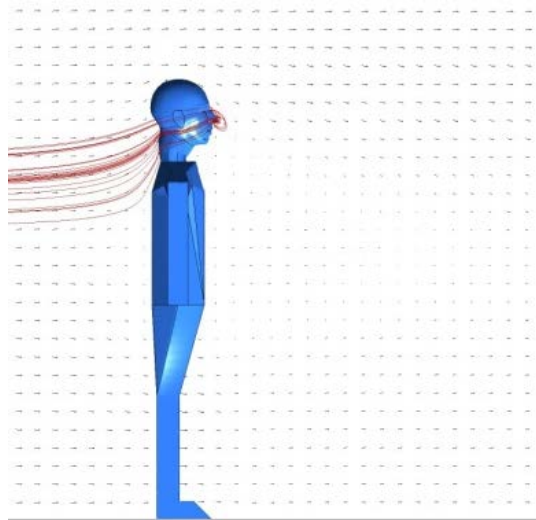


(a) Isothermal

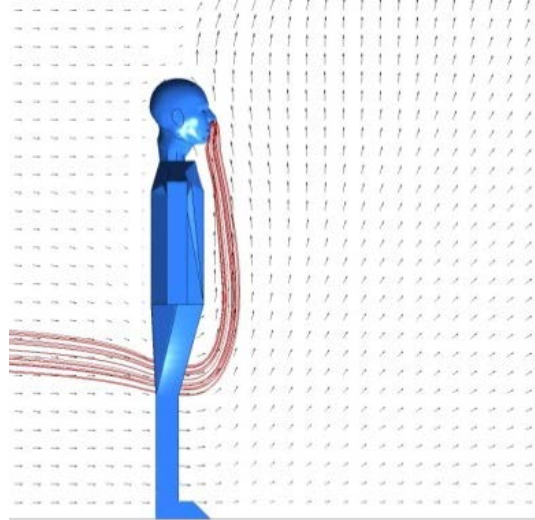
(b) Thermal

*Figure 5. 5 Typical tracks of inhaled particle under facing-the-wind conditions (0.1 m/s)*

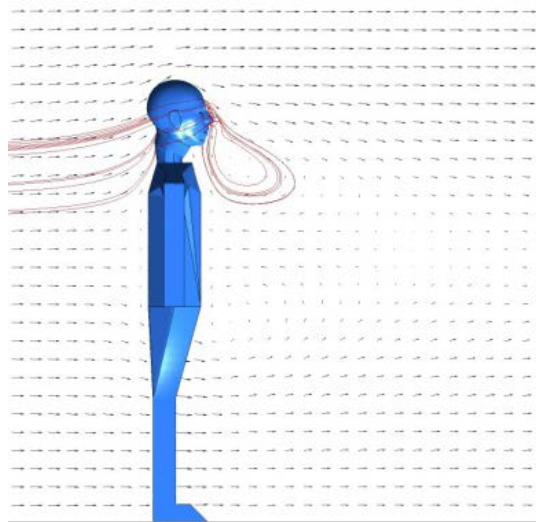
However, computations using the back-to-the-wind conditions produced a completely different picture. The images on the left side of Figure 5. 6 show the airflow field around the manikin and the inhaled particle tracks under the back-to-the-wind situation. Firstly, it was found that the airflow field on the downstream side of the manikin was significantly affected by body heat. However, due to the gap between the open legs which allows air flowing through, the size of the affected region is smaller than that in the closed-legs situation (See Figure 5. 3(b) and Figure 5. 4(b)). Similar to what has been discussed in the validation part, a vortex region containing two counter-rotating vortices was predicted using the isothermal conditions and a significant upward airflow velocity was predicted using the thermal conditions in Figure 5. 6.



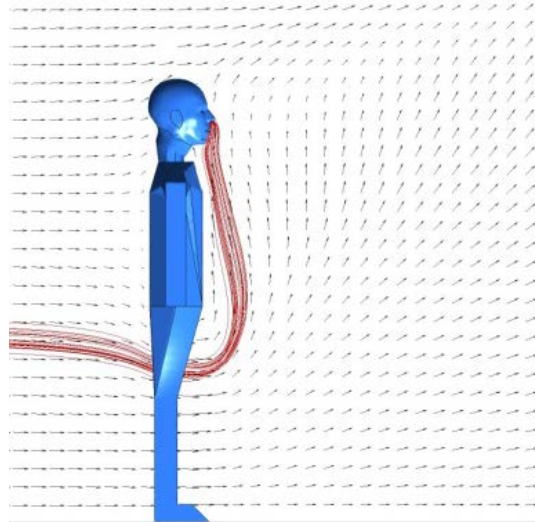
(a) 0.05 m/s Isothermal Condition



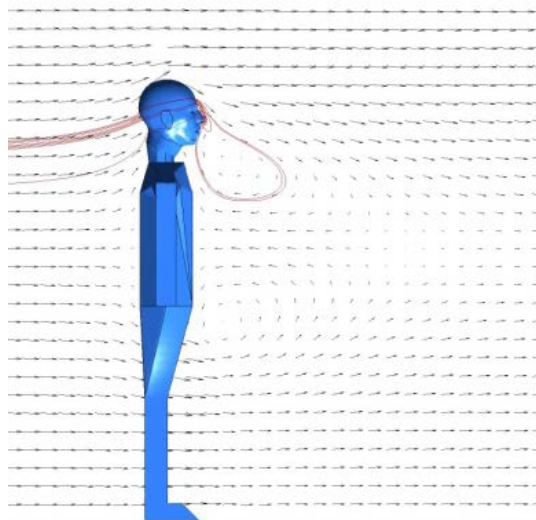
(f) 0.05 m/s Thermal Condition



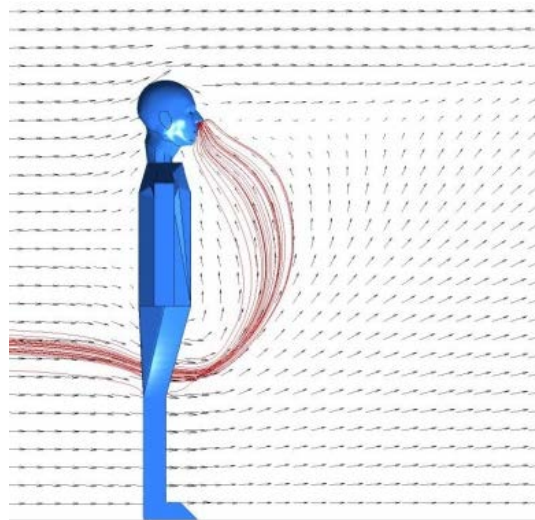
(b) 0.10 m/s Isothermal Condition



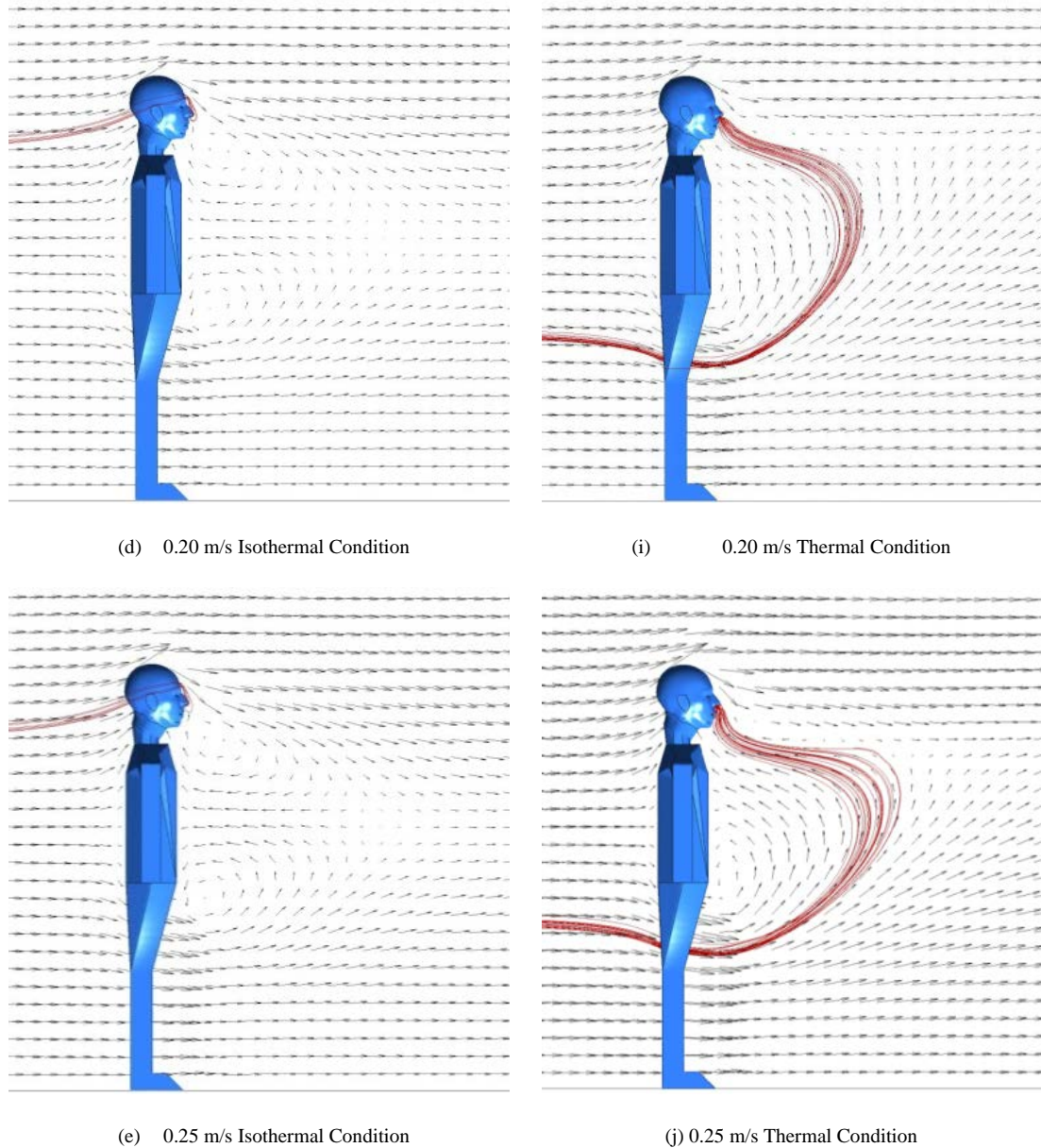
(g) 0.10 m/s Thermal Condition



(c) 0.15 m/s Isothermal Condition



(h) 0.15 m/s Thermal Condition



*Figure 5. 6 particle inhalation into the human*

For the isothermal condition, the vortex region was elongated with increasing free stream speed. The airflow field on the downstream side of the manikin was found to be significantly affected by body heat. However, due to the gap between the open legs which allows air flowing through, the size of the affected region is smaller than that in the closed-legs situation. Similar to what has been discussed in the validation part, a vortex region containing two counter-rotating vortices was predicted using the isothermal conditions and a significant upward airflow velocity was predicted using the



---

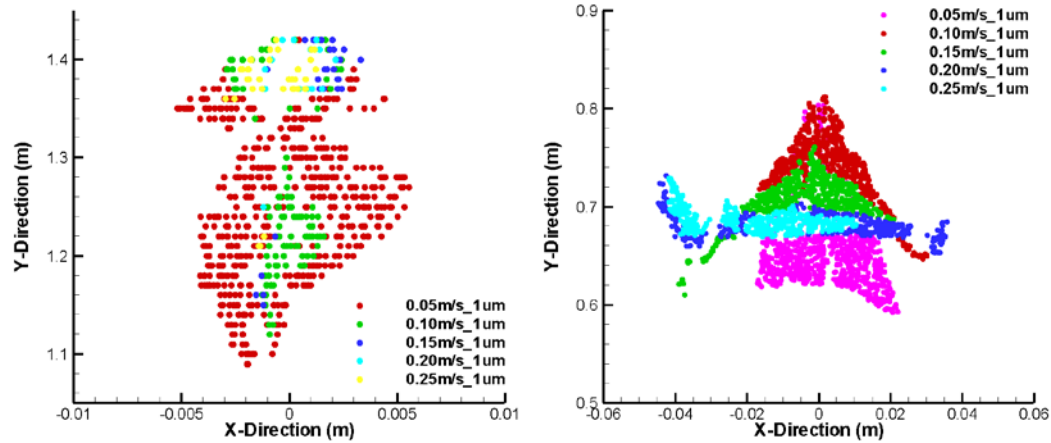
thermal conditions. For the isothermal condition, the vortex region was elongated with increasing free stream speed. However, for the thermal condition, the upward airflow velocity was gradually suppressed with increasing free stream speed and a big vortex was formed on the downstream side of the manikin (Figure 5. 6h). Similar to that of the isothermal situation, the size of the vortex was also elongated with increasing free stream speed (Figure 5. 6i and Figure 5. 6j).

The comparison is in Figure 5. 6, that the most significant difference between the thermal and isothermal situations exists in the tracks of inhaled particles. When the body heat is not considered, the inhaled particles come from a higher level, which is slightly lower than that of nose. The images on the left side of Figure 5. 6 illustrate that the particles are elevated to avoid the obstacle when approaching the manikin and some particles going around the manikin head are inhaled. The number of inhaled particles decreases with increasing free stream speed. However, the inhaled particles have totally different tracks when body heat is included in the computations. As shown in the images on the right side of Figure 5. 6, due to the rising airflow on the downstream side of the manikin, the inhaled particles come from a lower level than that in the isothermal situation. In particular, the air flowing through the leg gap entrains particles into the breathing zone. With increasing wind speed and vortex region size (Figure 5. 6g to Figure 5. 6j); particles go a further distance before being inhaled. The comparison demonstrates that taking body heat into account in the computations would lead to a totally different prediction of the tracks of inhaled particles. When the pollution sources are located at different height levels, the inhaled particles may be different due to this effect. Therefore, it is critical to consider the effects of body heat when modelling particle transport around a human body and its inhalation by a human occupant.

---

### 5.3.3 Effects of the Human Critical Area

Further analysis was conducted to quantify the effects of body heat on particle inhalation. Figure 5. 7 shows the so-called “critical area”, which is defined by Anthony et al (2006) as a finite area upstream of the breathing person where particles are inhaled. For this study, the critical area is located in the plane of particle injection (1.5 m upstream of the manikin). It is found that the critical area shrinks with increasing wind speed under both the isothermal and thermal conditions. In Figure 5. 7a, the shape of critical area s not many rules can be found at isothermal condition and the particle trajectory is around the head into the nostril, since the area form is based on the human head shapes. On the other hand, the critical area shape is delta at a low wind velocity of 0.05m/s to 0.15m/s. At high wind velocity, the delta shape turns into a flat disc. However, the critical areas of the isothermal cases are located much higher than those of the thermal cases. The height range of the critical area is 1.08m to 1.42m and 0.58m to 0.82m, and they are split between isothermal and thermal conditions. In addition, it is also interesting to find that the critical area is a vertical narrow region. In the isothermal condition, it is more obvious as the width of smallest narrow region is less than 0.005m.



(a) Open leg Isothermal condition      (b) Open leg Thermal condition

*Figure 5. 7 Critical areas (back-to-the-wind)*

For the purpose of further comparison, the central heights of the critical areas under various conditions, including thermal and isothermal, as well as facing-the-wind and back-to-the-wind cases, are shown in Figure 5. 8. It is found that when the manikin is facing-the-wind and heat transfer is not included in the model, the wind speed has no effect on the central height of critical areas. When heat transfer is included in the facing-the-wind computations, the central height of the critical area decreases gradually with increasing wind speed and finally approaches that of the isothermal cases. This is in a good agreement with the experimental observation of Vincent et al (2008), who found that for a thermal manikin in a low-speed wind tunnel, the rising airflow caused by the body heat reaches the channel top and then causes a vortex flow (in the red circle in Figure 5. 9). This vortex suppresses the oncoming airflow and causes a downward velocity. As a result, the stream lines upstream of the vortex are observed to descend. This vortex is gradually suppressed with increasing free stream speed and the central height of critical area is therefore observed to decrease.

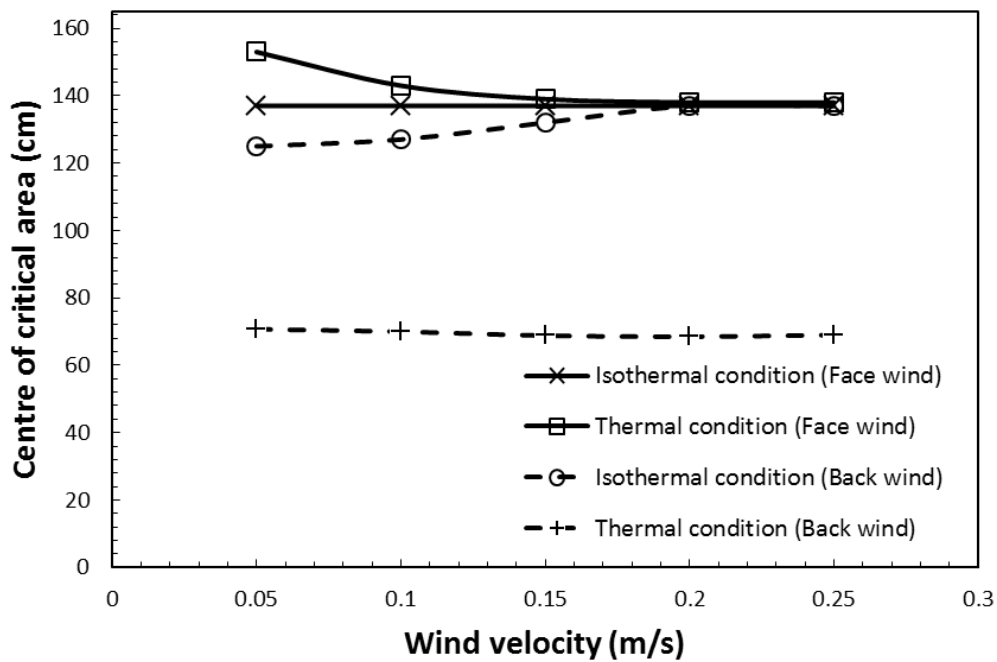
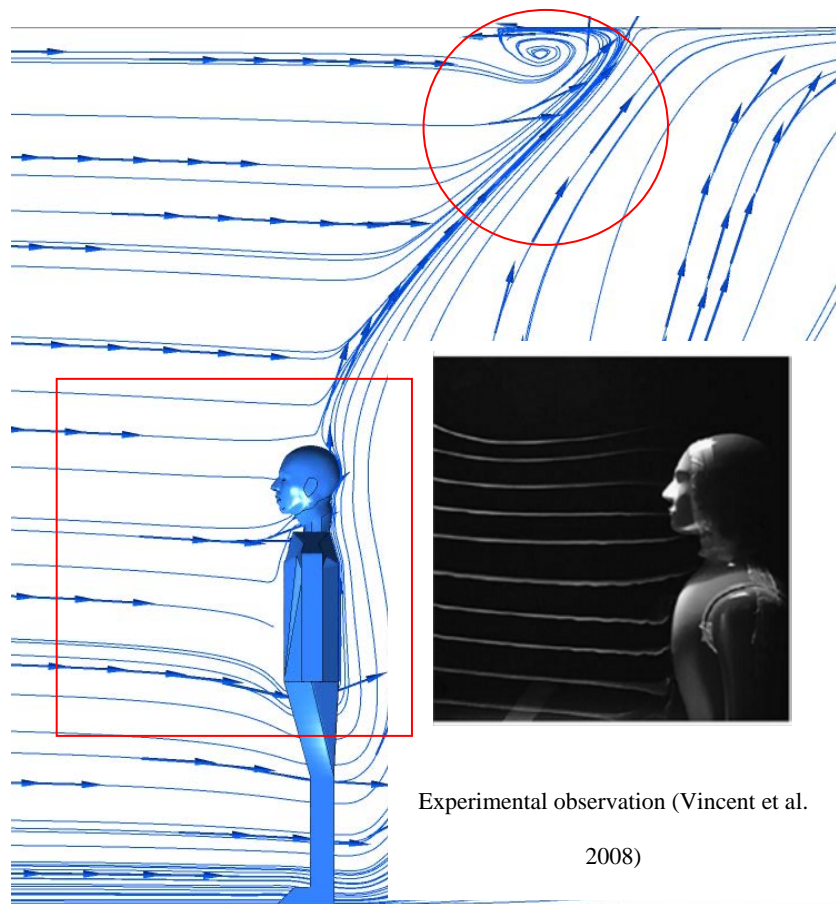


Figure 5. 8 Central height of the critical area vs. wind speed

When the manikin is back-to-the-wind and heat transfer is not considered, the predicted central height of critical area is still around the nose level. The central height of critical area increases with the increasing wind speed. This is because increasing wind speed increases the particle inertia, which makes particles from lower levels unable to be inhaled so only particles passing around the manikin head could be inhaled, as shown in Figure 5. 6. However, when heat transfer is included in the computational model, the predicted central height of the critical area is much lower and also decreases with increasing wind speed. This further demonstrates that the body heat plays an important role in transporting particles into the breathing zone from a lower level. Therefore, for an indoor human occupant standing with its back to the wind, it is critical to take into account its body heat when modelling particle transport and inhalation.



*Figure 5. 9 Comparison of predicted and experimental stream lines*

---

# Chapter 6

## Integrated Modeling of Room & Human Airway for Inhalation

### 6.1 Introduction

Following chapter 5, this chapter studies particle transport and inhalation into the internal airway from the external room. The study of exposure to airborne particles is an important problem in the interest of public and occupational health. The particles are mainly transported by the ventilated space, and its transport and dispersion within a room is important for understanding exposure risk as well as determining optimal ventilation designs. Recently CFD simulations have been performed to investigate and visualize the flow patterns and contaminant concentrations, with all the studies based on an isolated model such as the human nasal cavity or tracheobronchial airway tree.

Studies have shown that localised concentrations and preferential flow regions are primarily caused by the room geometry (Gao and Niu 2006; Tian et al. 2008b), and ventilation systems (Longest et al. 2008). Other CFD studies have incorporated a human figure into the room Popiolek et al (2006) which is a step towards a more integrated and realistic modeling approach to particulate exposure. Khoo et al (1998) placed a human occupant in a room to show the effects of contaminant inhalation, although the human face was simplified. However it has been shown that the actual

---

inhalation of particles from the external surroundings, referred to as the aspiration efficiency is influenced by facial features (Anthony et al. 2005; Mihaescu et al. 2008) and that it is recommended that CFD simulations should incorporate the complex features of the human face to adequately account for particle aspiration in low velocity environments. As the particles are inhaled, the particles are transported through the respiratory airways where some are deposited onto surrounding surfaces while others may navigate through the complex geometry and may even reach the lung airways, causing deleterious health effects. Internal respiratory studies have been previously by (Inthavong et al. 2011b; Ishikawa et al. 2009) and (Liu et al. 2007; Schroeter et al. 2006) which has found that the transport and deposition of micron sized particles are dominated by its inertial property while submicron and nano sized particles are influenced by diffusion mechanisms.

Therefore this chapter presents an integrated CFD model simulation that integrates the three aspects of contaminant exposure by including the external room, human occupant with realistic facial features, and the internal nasal-trachea airway. Air and particle flow patterns in the free stream and proximal to the nostrils are shown. Identification of upstream airborne particle locations that are likely to be inhaled (aspiration efficiency) are found. Results for the inhalation and particle profile at the nostrils are presented with its corresponding curve-fit equation. These results may be applied to CFD studies of the nasal cavity that neglect the surrounding environment.

## 6.2 Numerical Procedure

### 6.2.1 Computational Model

A CT scan of the upper respiratory airway consisting of the nasal cavity, pharynx, larynx, and upper trachea from a 51 year old non smoking Asian male provided the basis for reconstruction of a computational model. Segmentation of the desired airway was performed to extract a contiguous airway path from the nostril inlets to the upper trachea. In addition to the nostrils, a partial region of the external nose, proximal to the nostrils was included.

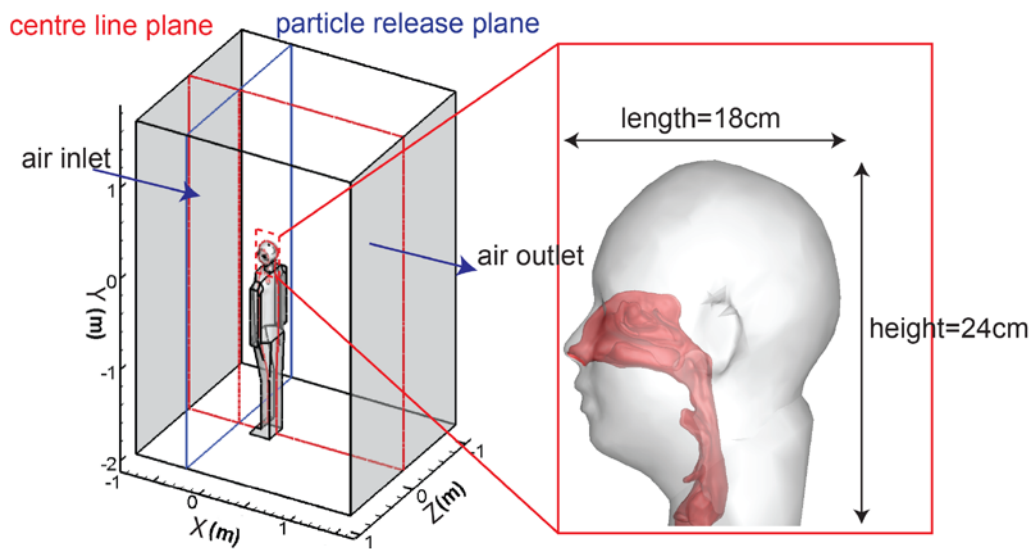
*Table 6. 1 Model geometry and flow condition details*

<b>Human occupant details</b>			<b>Facial details</b>		
Dimension	Present study	50 <sup>th</sup> % man Huston (2008)	Dimension	Present study	50 <sup>th</sup> % man Zhuang et al (2010)
occupant height	170.0	175.9	<b>head length</b>	18.3	19.5
mid shoulder height	139.7	144.4	<b>head circumference</b>	56.3	56.8
head width	13.5	15.5	<b>face length</b>	9.1	11.8
head depth	18.3	19.6	<b>face width</b>	13.5	14.1
top of head to chin	19.2	22.1	<b>nose length</b>	4.13	5.0
top of head to mouth centre	15.2	18.0	<b>nose protrusion</b>	1.56	2.1
top of head to eyes	9.2	11.5	<b>nose breadth</b>	3.79	3.4

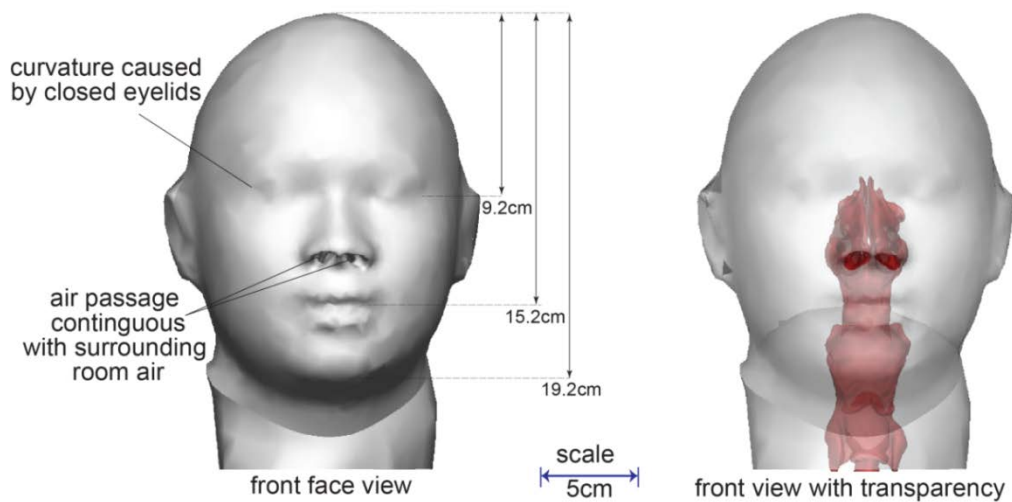
The three-dimensional (3D) head contained detailed facial features, such as shaped eyes, nose, mouth, and ears. Details of the facial features are given in Table 6. 1 and is compared with the 50<sup>th</sup> percentile of a caucasian male as described in the literature. The



comparisons show that the CFD model used in this study is slightly smaller than the 50<sup>th</sup> percentile for caucasian males. The realistic head was placed onto a simple human body shape, and this model was placed into an empty room to simulate the ambient air. The three submodels (respiratory airway, human body, and surrounding room) were combined by importing the models into a CAD (Computer Aided Design) software modelling program and merged together. The final CAD model is shown in Figure 6. 1.



(a)



(b)

Figure 6. 1 (a) 3D CAD model incorporating the external surrounding room, human occupant, and the internal nasal-pharynx-larynx-trachea respiratory airway model. (b) Front view showing the

---

*detailed facial features. Geometry dimensions and details of the room and human occupant are given in Table 6. 1.*

It is apparent that the model geometry spans over multiple length scales from metre lengths of the room down to millimetre lengths within the airway bronchi. This presents a challenge when it comes to producing a quality computational mesh for CFD analysis. This step was also the most exhaustive stage in the CFD simulation process. Meshing the model involved isolating the internal respiratory airway from the external surroundings. Prism layers were applied to the boundary respiratory walls and a tetrahedral unstructured mesh filled the airway passage. The respiratory airway consisted of 11 million cells. From the nostril openings out towards the surrounding air, the mesh was slowly grown so that the fine mesh resolving length scales in millimetres was gradually expanded out to length scales of centimetres to resolve the outer air. Figure 6. 2 shows the different sections and aspects of the meshing as well as some cross-sectional outlines of the internal respiratory airways. The final mesh size was 16 million cells which used up 912Mb in storage size. Earlier studies by the authors have found that a mesh in excess of 2million provided grid independence for the nasal cavity region (Inthavong et al. 2011a), Due to the large variation in length scales of the flow and geometry there is a greater demand on the computational mesh to minimise false diffusion caused by rapid changes in the mesh size. To ensure quality of results, and a high level of mesh integrity, a mesh independence test was performed by investigating the velocity profiles at a number of different locations until the profiles converged. Figure 6. 3 shows two such velocity profiles which were taken along lines at the cross-sections a-a' and b'b' inside the nasal cavity. The mesh became convergent at 8 million cells. As a conservative estimate, the final computational model used the model with 16 million cells. The visualisation and generation of the mesh was possible on a

PC computer with 32GB Ram, 2GB video card, and 8 processor cores. The simulations were computed by HPC cluster, which has 268 processor cores.

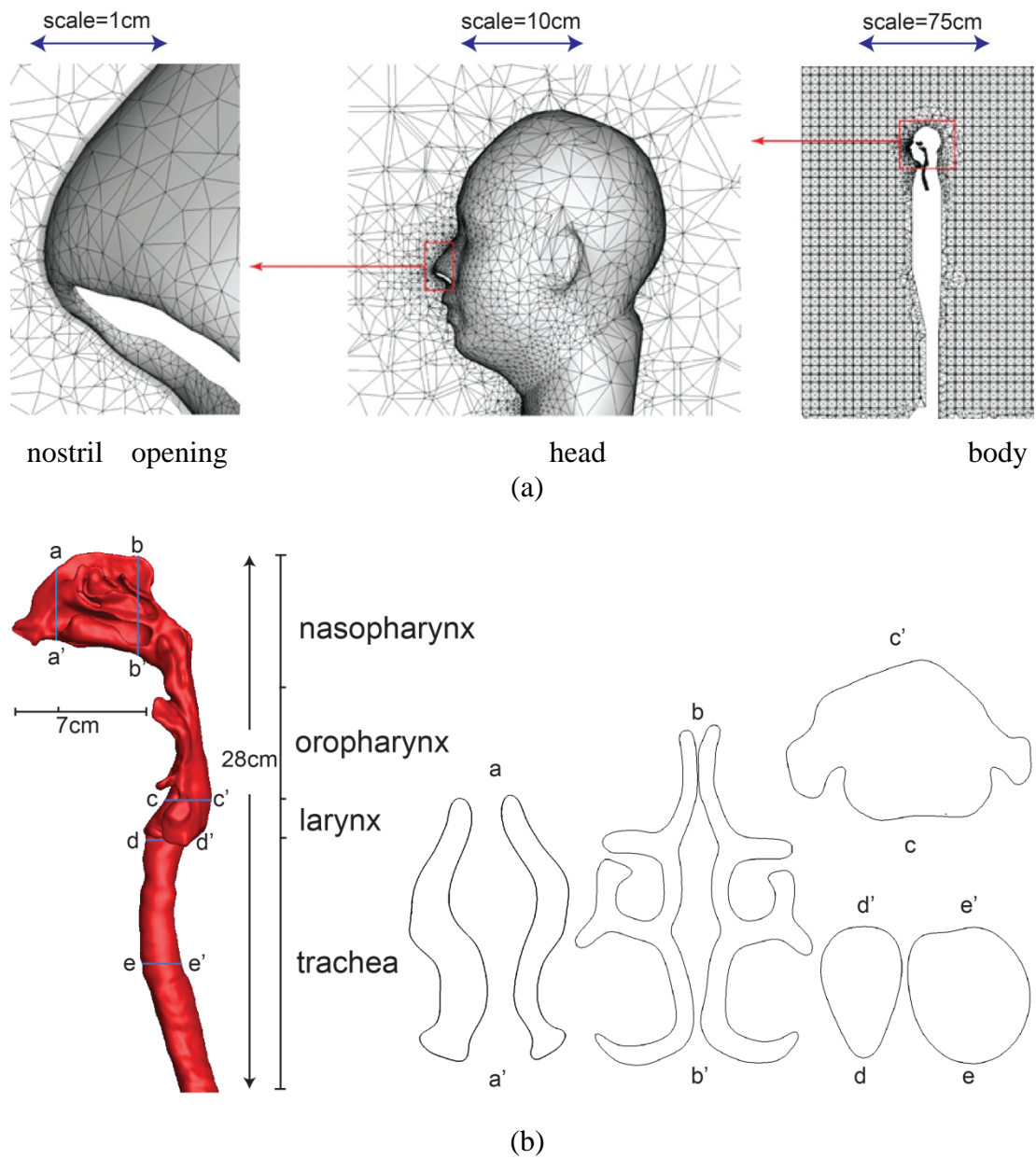


Figure 6. 2 (a) 3D CAD model incorporating the external surrounding room, human occupant, and the internal nasal-pharynx-larynx-trachea respiratory airway model. (b) Front view showing the detailed facial features. Geometry dimensions and details of the room and human occupant are given in Table 6. 1

---

## 6.2.2 Boundary Condition

A steady oncoming freestream of air towards the human occupant was applied in order to investigate the ‘*worst case scenario*’ for particle inhalability. This is confirmed by Kennedy et al (2002) which showed that the ‘facing-the-wind’ orientation produces an upper limit for inhalability compared with an averaged orientation which is produced by equally weighting particle inhalation over all angles from 0 to 360 orientation. The selection of the airflow speed was based on the comprehensive survey of airflow speeds in indoor workplaces by Baldwin et al (1998) which found a mean value of  $0.3 \text{ ms}^{-1}$  (ranging from  $0.04$  to  $2.02 \text{ ms}^{-1}$ ) over all work places, however this value is skewed by measurements made in a wood drying shed that had a value of  $1.79 \text{ ms}^{-1}$ , and that excluding this measurement produces a mean of  $0.2 \text{ ms}^{-1}$  (ranging from  $0.04$  to  $0.72 \text{ ms}^{-1}$ ). More specifically for different workplace environments the mean values are: office  $0.011$  to  $0.164 \text{ ms}^{-1}$ ; wood turning  $0.064$  to  $0.119 \text{ ms}^{-1}$ ; heavy steel industry  $0.063$  to  $1.737 \text{ ms}^{-1}$ . In this study we aim to look at the influence of airflow speeds on the respiration and particle locations entering the nasal cavity via the nostrils.

Table 6. 2 Inhalation and Room Flow Details

Inhalation details			Room and ventilation details	
	<i>Present Study</i>		<i>Geometry</i>	<i>Dimension</i>
Nostril openings	Right	Left	Length	250 cm
	Area = 1.52cm <sup>2</sup>	Area = 1.31cm <sup>2</sup>	Width	200 cm
	Perim = 4.72	Perim = 4.62cm	Height	350cm
	D <sub>h</sub> = 1.288 cm	D <sub>h</sub> = 1.134 cm		
Mouth openings	Area = 2.25 cm <sup>2</sup>		Room air velocity	0.2 m/s
	Perim =			
	D <sub>h</sub> = 1.288 cm			
<b>Dynamic similarity</b>	<b><i>Present study</i></b>	<b><i>Anthony et al.</i></b>		
Re <sub>freestream</sub> (room inlet)	48000	50250		
Re <sub>head</sub>	1850	1909		
Head hydraulic diameter	14cm	9.6cm		
V <sub>freestream</sub> (ms <sup>-1</sup> )	0.2m/s	0.3		

Reynolds number matching over the head of the humanoid was applied in order to obtain dynamic similarity between the CFD simulation with existing experimental data in the literature by Anthony (2005). For indoor airflows, reported results have shown much better flow separation and reattachment based on the  $k-\epsilon$  Renormalization Group model (RNG) (Edwards et al. 1997; Hofmann et al. 2003) which is an expected flow feature of the flow passing over the head. But in the human respiratory system, many researchers have used  $k-\omega$  turbulent model with Shear Stress Transport (SST) developed by Menter (1994) to analyse airflow in the nasal cavity model (V. N. Riazuddin 2011; Wen et al. 2008a; Zhang and Chen 2007) which combines the advantages of both the  $k-\omega$  turbulence and  $k-\epsilon$  turbulence. Similarly, the inhalation conditions through the mouth were also matched by the Reynolds number (see Table 2).

---

Two inhalation rates of 15 and 40 litres per minute (LPM) were studied for the aspiration efficiency through nasal and oral inhalation which represent light and heavy activity.

The particles were released from a diameter of 0.1m vertical plane which is 0.2 m distance away from the manikin face at eye level. The particles were tracked through the air using the Lagrangian approach and the modelling process of the one way coupling particle dispersed from the external space, through the human respiratory system from the nostril and out of the trachea. The flow field analysis was performed first to establish the surrounding environment. The number of particles tracked was checked for statistical independence since the turbulent dispersion is modelled based on a stochastic process. Independence was achieved for 50,000 particles since an increase of particles to 80,000 particles yielded a difference of 0.1% in the inhalation efficiency.

## **6.3 Results and Discussion**

### **6.3.1 Validation and Grid Independence**

In the airflow region of large gradients, as the external flow region compares with the internal flow region, the mesh should be fine enough to reduce the errors in the flow variables from cell to cell. The mesh has been optimised and hence is independent for the flow field where a compromise between computational resources and accuracy has been made. The early coarse model with around 4 million unstructured tetrahedral cells was initially used to solve the air flow field at a flow rate of 15L/min and wind velocity of 0.05m/s. Subsequently three models were produced with 8 million, 12 million and 16 million cells. A grid independence test is shown in Figure 6. 3. Results for Y-velocity were found at lines A and B, which form cross sections in the right nasal cavity. These

results became consistent as the mesh resolution approached 8million cells. Thus. in order to make a compromise between the result’s accuracy and computational cost, a model with 8 million elements was used in this chapter.

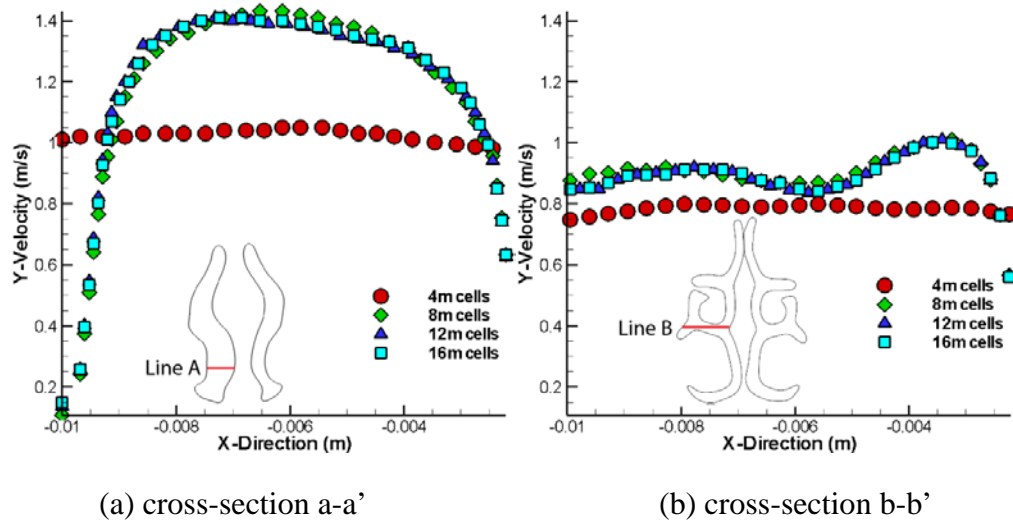
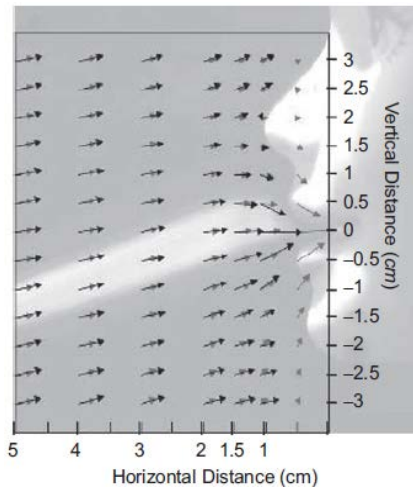
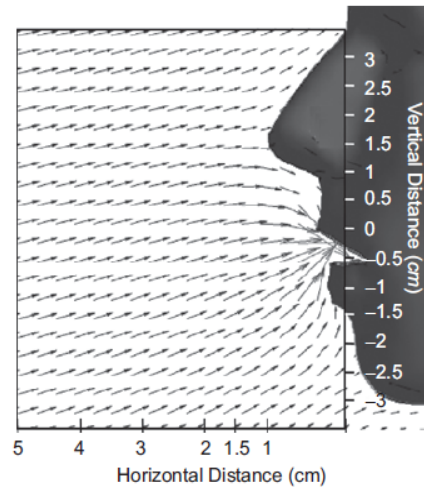


Figure 6. 3 Mesh independence for two velocity profiles from lines taken at the cross-sections a-a’ and b’b’.

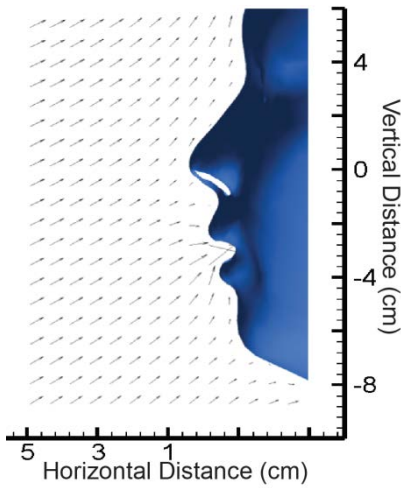
Velocity vectors in the y-z plane at the centreline of the humanoid ( $x = 0$  cm) are compared with the experimental data reported by Anthony et al. (2005) and computational data from (King Se et al. 2010) shown in Figure 6. 4. The flow field reported by the Particle Image Velocimetry (PIV) data in the near breathing region shows slight vertical direction caused by the presence of the torso where the airstream diverges as it flows past the body. As the inhaled air approaches the face, the vectors converge towards the mouth or pass over the nose and the upper regions of the face. The CFD simulation shows good qualitative comparisons with reported data in the literature. The normalized velocity profiles taken just upstream of the face at 1cm and 1.5cm are shown in Figure 6. 4b and Figure 6. 4c respectively.



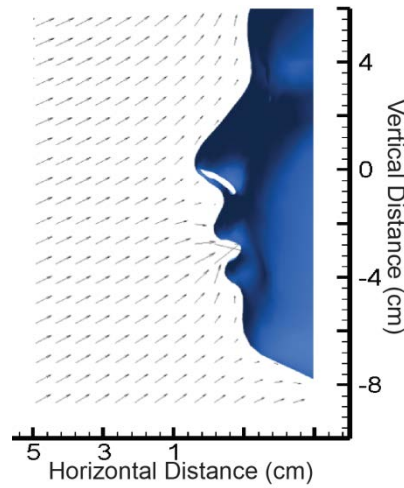
Experimental-mouth (PIV)



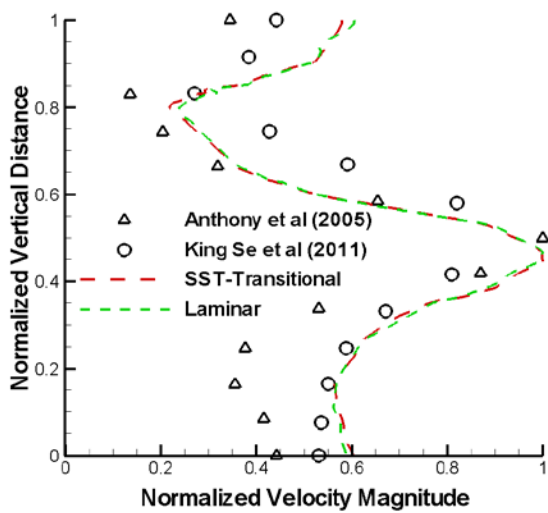
Simulation-mouth (RNG)



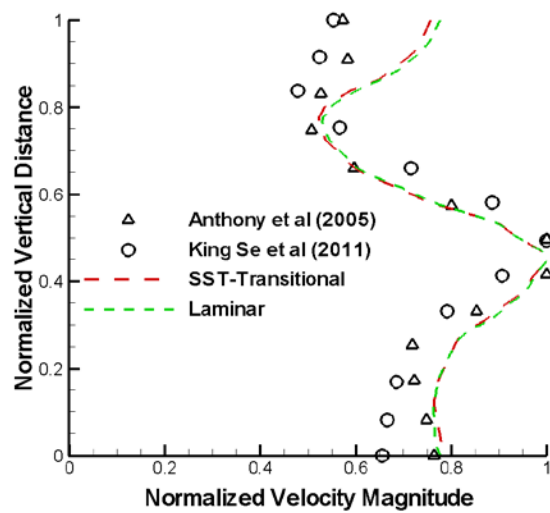
Simulation-mouth (laminar)



Simulation-mouth (SST)



1cm-mouth



1.5cm-mouth

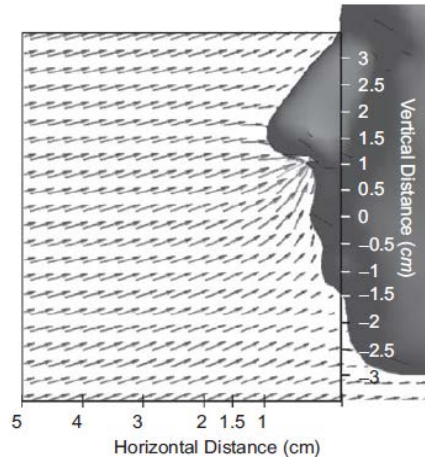
Figure 6. 4 Velocity vector plots for (a) CFD oral inhalation and (b) PIV experimental measurements from Anthony et al. (2005). (c) CFD mouth inhalation.



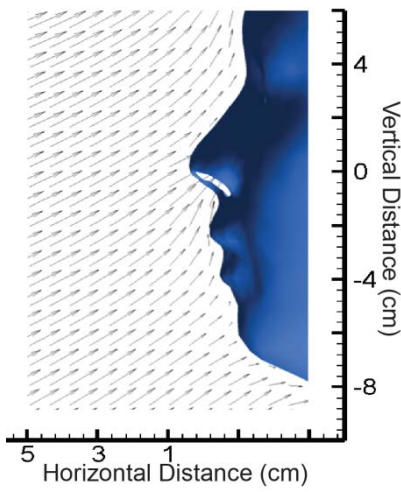
---

Inhalation vectors that are directed downwards towards the mouth occur earlier ( $y = 1.0$  cm) in the horizontal plane for the CFD model and the realistic facial feature model in comparison with the cylindrical human form ( $y = 0.5$  cm). Locally, the oncoming airflow bifurcates at the nose tip as well as at the chin. Downwards flow is found in the philtrum (space between the nose and the upper lip). In contrast, the same flow for nose inhalation is directed upwards towards the nostril openings. The effect of the vertical flow across the closed mouth region can enhance the inhalability of the particles if breathing through the mouth was to occur midway through a breath taken through the nose. Such case studies involving both the nose and mouth inhalations under different breathing situations were not investigated in this paper but would be interesting for future studies.

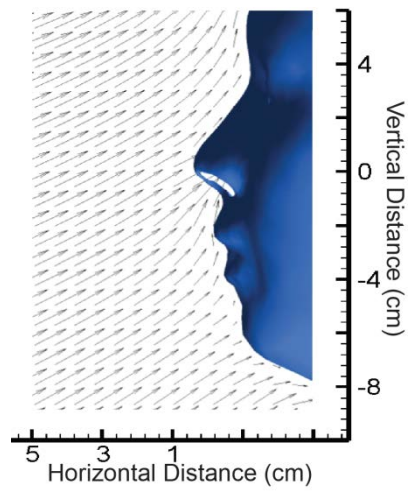
The other flow difference found between mouth inhalation and nose inhalation is the higher stagnation point (flow bifurcation) near the chin for the nose inhalation. Comparisons of the velocity profiles from the vector plots in Figure 4a and b in the near breathing regions at  $y = 1.0$  cm (the nose tip) and  $y = 1.5$  cm are shown in Figure 6. 5. There is good agreement between the profiles, especially at  $y = 1.5$  cm. Minimum velocities near the stagnation point at the nose tip height are found at the vertical distance of  $z = 2.0$  cm for both cases. Maximum velocities occur at the mouth at  $z = 0$  cm and just below the mouth region where the flow accelerates from the chin region. Slight differences are found in the chin region below the lower lip and also in the philtrum, which may be attributed to some differences in the exact facial features.



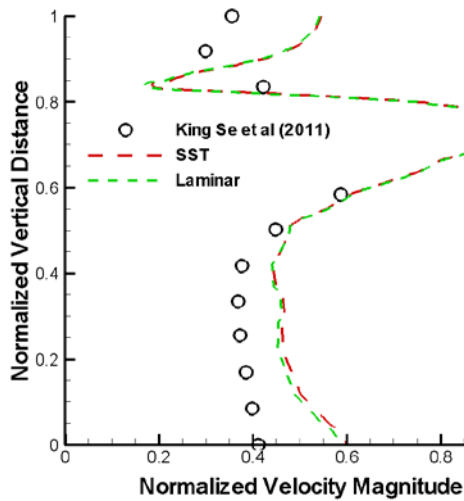
King Se-nose (RNG)



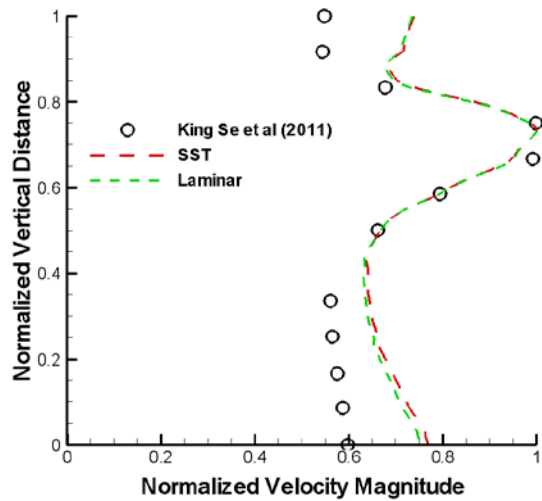
Simulation-nose (Laminar)



Simulation-nose (SST)



1cm-nose



1.5cm-nose

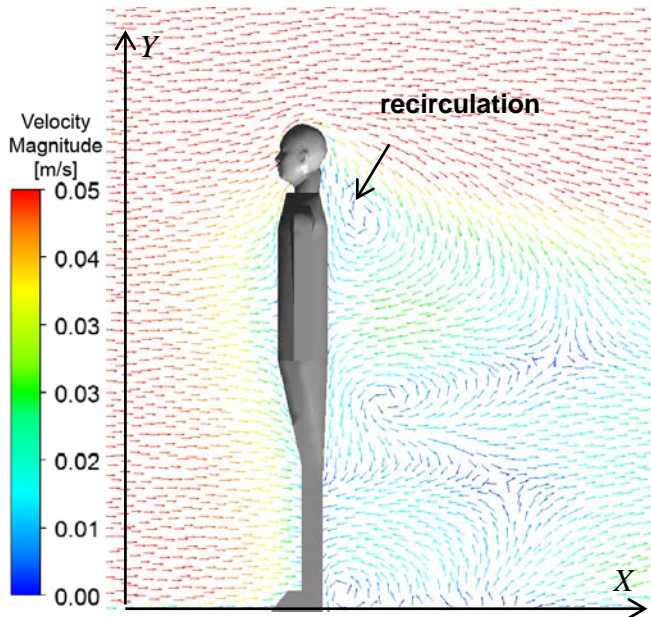
Figure 6. 5 Velocity vector plots for (a) CFD oral inhalation and (b) PIV experimental measurements from Anthony et al. (2005). (c) CFD mouth inhalation.

---

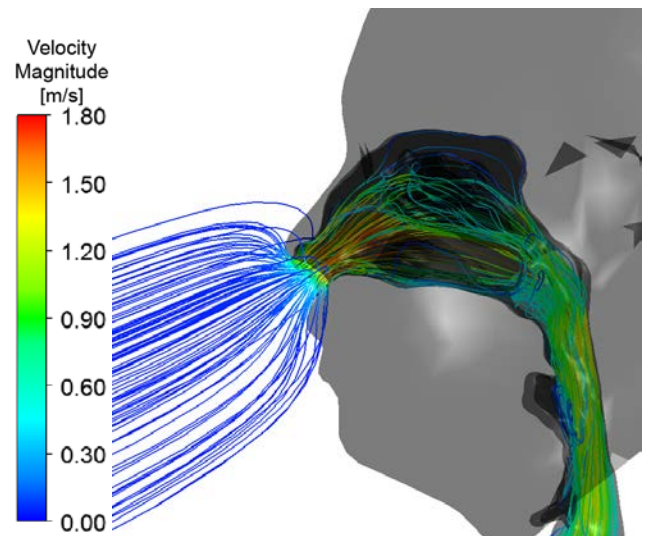
### 6.3.2 Influence of Ambient Flow Rate

Particle aspiration efficiency has been defined as the fraction of particles that are inhaled through the nose or mouth during breathing (Vincent et al. 1990), which is also referred to as ‘inhalability’. Factors that influence particle aspiration efficiency include the particle size and the external ambient air flow around the human body. In the cases presented in this study, the human body is facing the oncoming air, which transports the particles from upstream towards the breathing region. Figure 6. 6 shows the oncoming air diverging at the torso as it approaches the body and thus the air that is inhaled comes from underneath the face, rather than above. This implies that airborne particles that are present below the breathing region are more likely to be inhaled. Furthermore, the inhalation streamlines show that at a lower ambient air flow rate, a larger region of air is inhaled, in comparison to a higher ambient air flow rate. Under both conditions the inhaled air is being pulled from below the breathing region.

The air flow accelerates around the head of the body and the boundary layer separates at the rear, producing a wake, with a recirculation region forming just behind the head. An increase in the ambient air flow rate produces a recirculation region that is further from the body. The presence of the wake can influence a person’s exposure to toxic airborne contaminants, particularly if the contaminant source is in the vicinity of the breathing region. The scope of this study is the inhalability of particles from a source upstream from an oncoming flow, however the results of the wake flow shown in Figure 6. 6 indicate that if the ambient air flow was coming from behind the body, particles from a contaminant source in front of the body that may be disturbed and induced into the breathing region, thus enhancing the inhalability of the particles. The wake region can induce a well-mixed scenario through the presence of vortices that can entrain air.

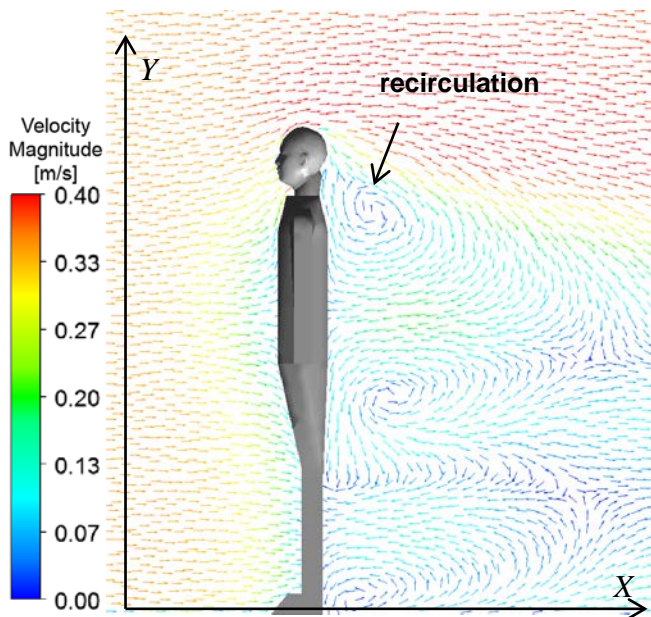


wake flow caused by human body

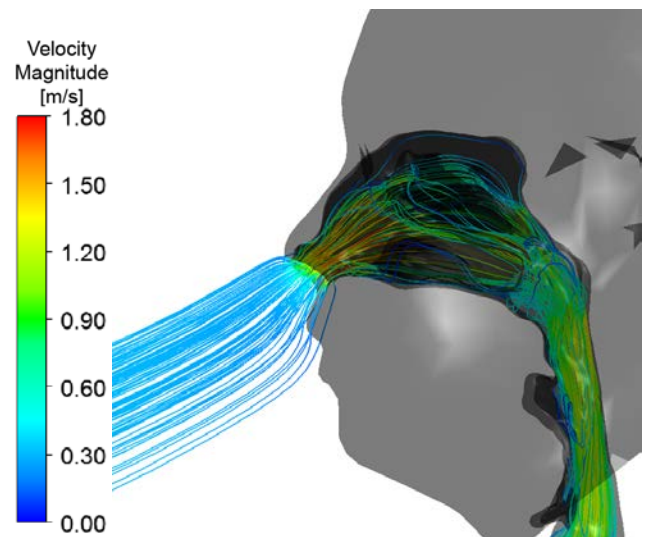


inhalation streamlines

a) ambient flow rate 0.05m/s



wake flow caused by human body



inhalation streamlines

b) ambient flow rate 0.35m/s

Figure 6. 6 Inhalation through nostrils at 15LPM

Contours of velocity magnitude at both nostrils are shown in Figure 6. 6. The velocity magnitude contour is at 15L/min breathing rate with different wind speeds. When wind velocity is at 0.05m/s, the 2D contours confirm flow acceleration occurring in both nostrils with peak velocities of 1.7m/s and 1.5m/s; the average velocities at the right

side and the left side are 1.2m/s and 1.12m/s, respectively. The right side has a slightly higher velocity than the left side. The difference of the average mass flow rate is only 0.31E-4kg/s. The main flow is at the bottom of the cross section and pockets of low velocity are found at the top and bottom of the slice. The low flows at 1m/s are found in Figure 6. 7. When wind velocity increases and the breathing rate is fixed, there is little change in the contours, the 2D streamlines and the average velocity are not invisibly changed. These indicate that the effect of the outside wind velocity is not significant to change the inlet flow field.

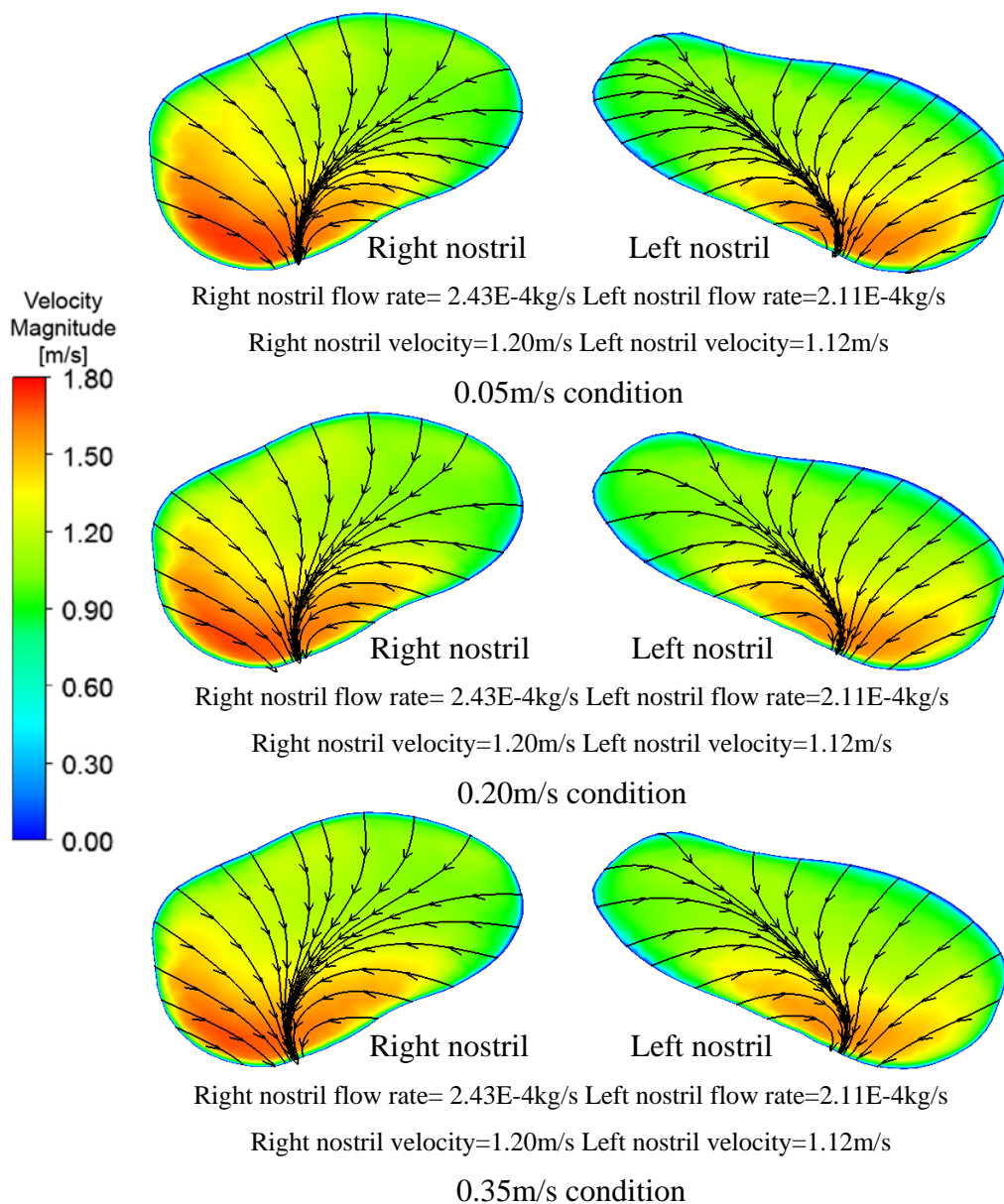
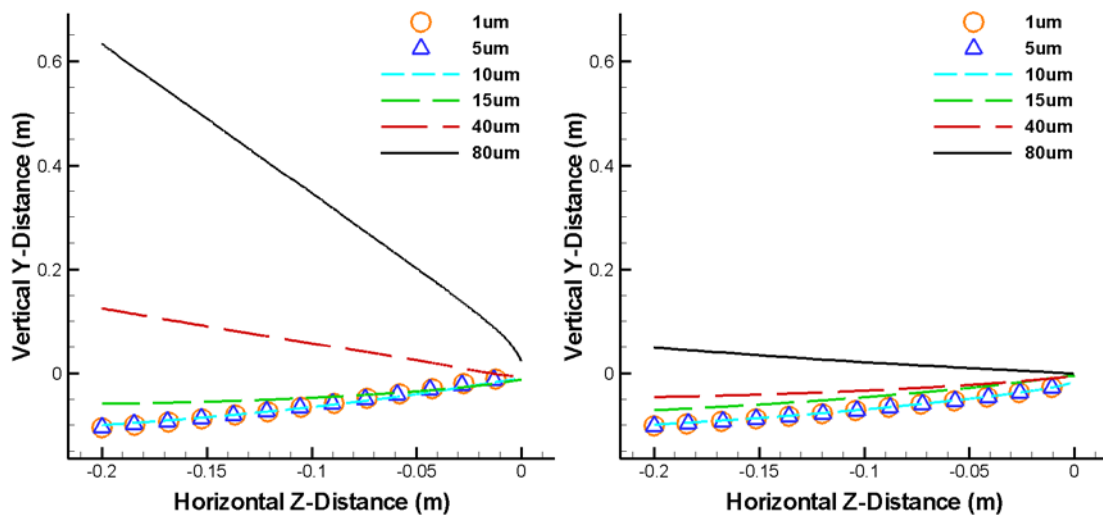


Figure 6. 7 Comparison of airflow pattern on the nostrils with different wind velocity at 15L/min.

## 6.3.3 Particle Profile and Deposition Pattern

### 6.3.3.1 Particle Inhalation Trajectory

Trajectories of particles originating from a plane located at a distance of 0.2m upstream from the nose tip are shown in Figure 6. 8 for ambient air flow rates of 0.05m/s and 0.35m/s. The vertical distance coordinate is set to  $y = 0$ m at the nostril levels, so that the trajectories of nasal inhaled particles converge to this point. The trajectories show that for 40 $\mu$ m and 80 $\mu$ m sized particles, gravitational settling dominates, where the particle source originates from a much higher vertical position in relation to the nostril openings.



(a)  $U_{\infty} = 0.05$  m/s, Inhalation = 15 LPM

(b)  $U_{\infty} = 0.35$  m/s, Inhalation = 15 LPM

Figure 6. 8 Trajectory of inhaled particles released at 20 cm upstream for different particle sizes and ambient air flow rates of 0.05m/s and 0.035m/s. The inhalation rate is 15LPM through both nostrils.

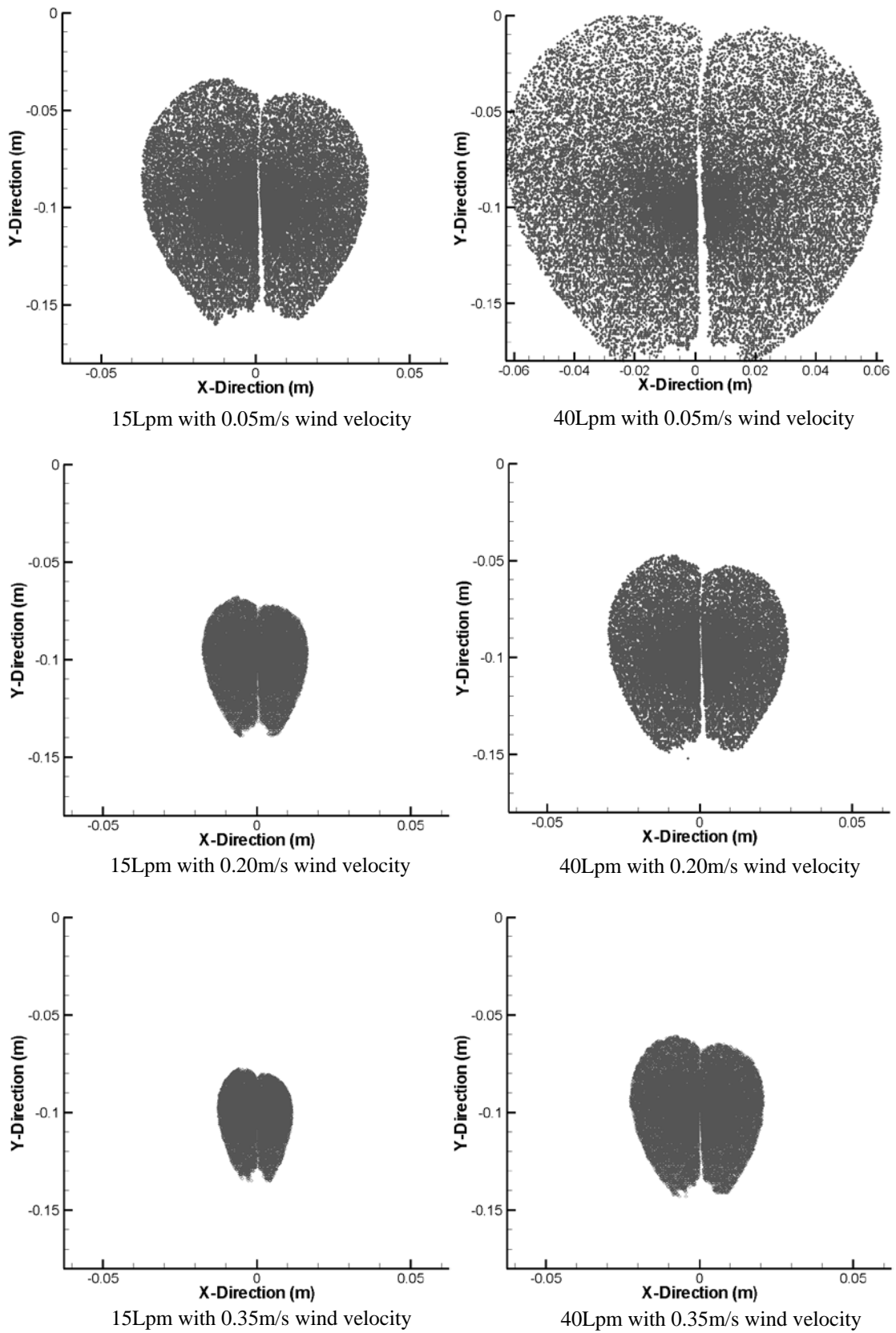
The trajectory of these particles is linear until they reach the nose, where acceleration towards the nostril occurs due to nasal inhalation. This linearity means that the location of the particle source for large particles can be easily identified for a given upstream distance through extrapolation. The further upstream the distance, the higher the

---

vertical distance should be for the particles to descend towards the nose. At higher ambient air flow rates the vertical distance needed for 40 $\mu$ m and 80 $\mu$ m particles to overcome gravitational settling is reduced significantly from 0.65m down to 0.05m. Smaller particles such as 1 $\mu$ m-20 $\mu$ m all possess much lighter masses and its inertia is more influenced by the surrounding flow field. These particles tend to follow the flow streamlines more and the upstream location of the particle source is at a vertical distance of approximately 0.05-0.1m below the nostrils, since it was shown earlier that the flow streamlines diverge at the torso region as the flow approaches the human body. At the higher ambient air flow rate the trajectories of the smaller particles do not change significantly.

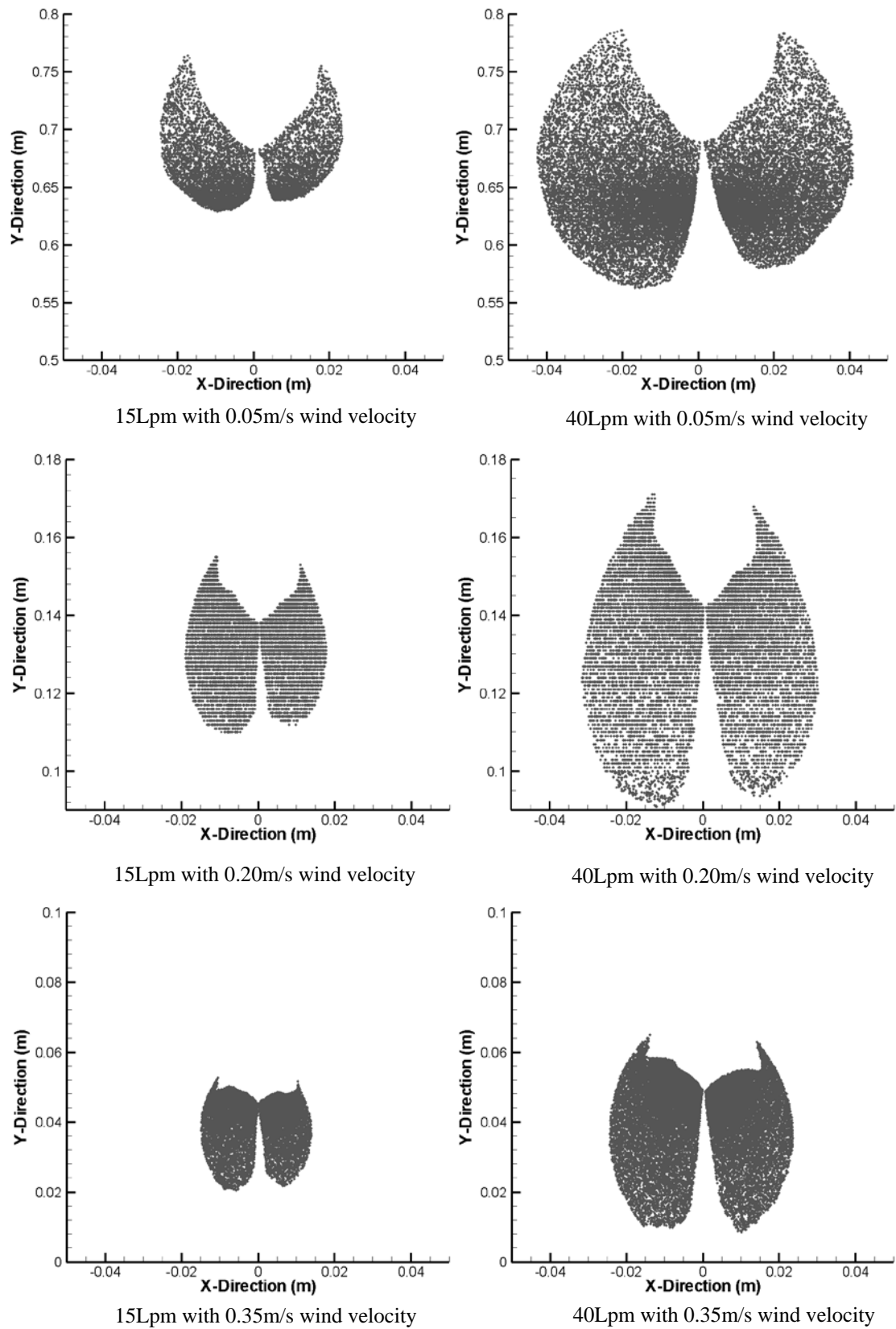
### **6.3.3.2 Comparison of Critical Area**

The critical shape area and size are compared with the different wind velocity at two kinds of breathing rate conditions and these are shown in Figure 6. 9. The area size decreases as the wind velocity increases with each breathing rate. Comparing the critical area size in the same wind velocity with a different breathing rate, we find that when the breathing rate is higher, the area is larger. In addition, despite the different wind velocity and breathing rate, the shape of the critical areas is very similar when the particle size is less than 15 $\mu$ m; except for the 80 $\mu$ m case results. In the 80 $\mu$ m cases, the shape of areas is comparable at the same breathing rate with different wind velocity. When the wind velocity is much lower such as at 0.05m/s and the shape is slightly different. These results indicate that smaller particles have less gravity force; the effect of wind velocity does not significantly change the shape of the area, only the area size. If the gravity force is large, the effect of wind velocity can significantly change the shape of the area.



(a) 1 micron size condition





(b) 80 micron size condition

Figure 6. 9 Comparison of critical area in integrated model at different wind speed

---

From each critical area, it is interesting to find that area of right side is larger than the area of left side. The nostril opening area of the left side is smaller and thus got a higher velocity flow (see the Table 6. 2 and Figure 6. 6). These results demonstrate that the critical area is not related to the nostril opening size, or, more accurately, dependent upon the main velocity inside the nostril

### **6.3.3.3 Particle Deposition Patterns**

Figure 10 shows the comparisons of particle deposition pattern in a whole model with different wind speeds at light breathing (15Lpm). The particle deposition pattern in the critical area is relative to the internal airway region, which defines where particles are inhaled and where they are deposited. (Blue: nasal region. Green: pharynx, Red: trachea and Gray: within the lung). At  $1\mu\text{m}$  and light breathing condition with three kinds of wind velocity, the proportion of particles going through the respiratory airway into the lung is around 93%. When the particle size is increased to  $15\mu\text{m}$ , the escape to the lung of particles is significantly decreased to 40% - 65%. For  $80\mu\text{m}$  particles, which exhibit the highest inertial properties of the three particles presented, maximum deposition occurs in the anterior regions of the nasal cavity and no particles reach the lung region. Overall for the light breathing condition,  $1\mu\text{m}$  particles exhibited the most inferior deposition in the respiratory region, while for the different wind velocity condition, all the wind velocities resulted in the same deposition efficacy in the airway regions. For  $15\mu\text{m}$  particles, if the wind velocity is lower, there is increased particle transport into the lung region. When the particle size becomes  $80\mu\text{m}$ , the number of escaped particles is very small. These findings show that as wind velocity, breathing rate and the particle size increase, the gravity force and particle inertia also increase to

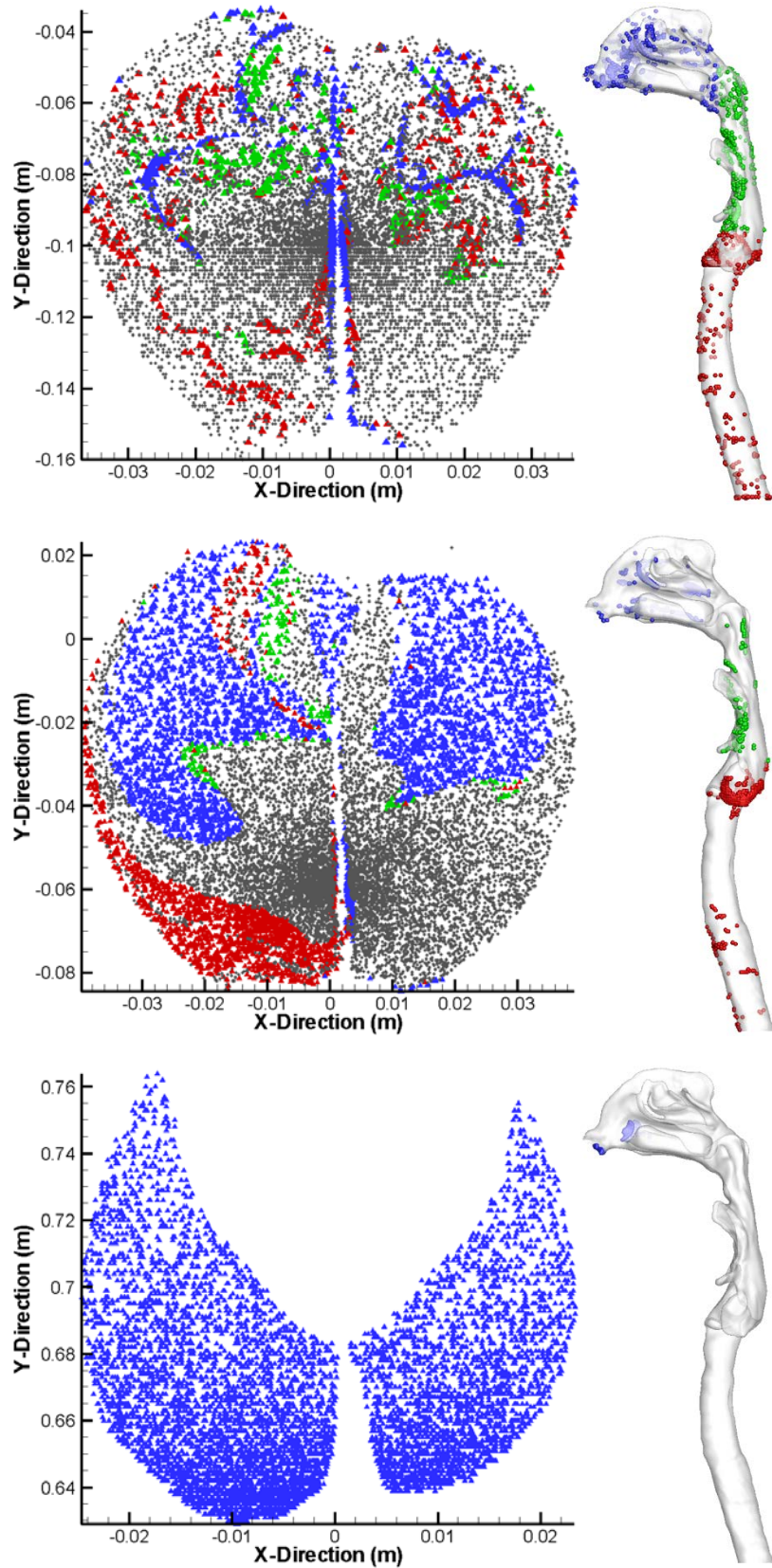
---

yield greater deposition efficacy. The gravity face is an especially important factor as it significantly increases the particle deposition efficiency.

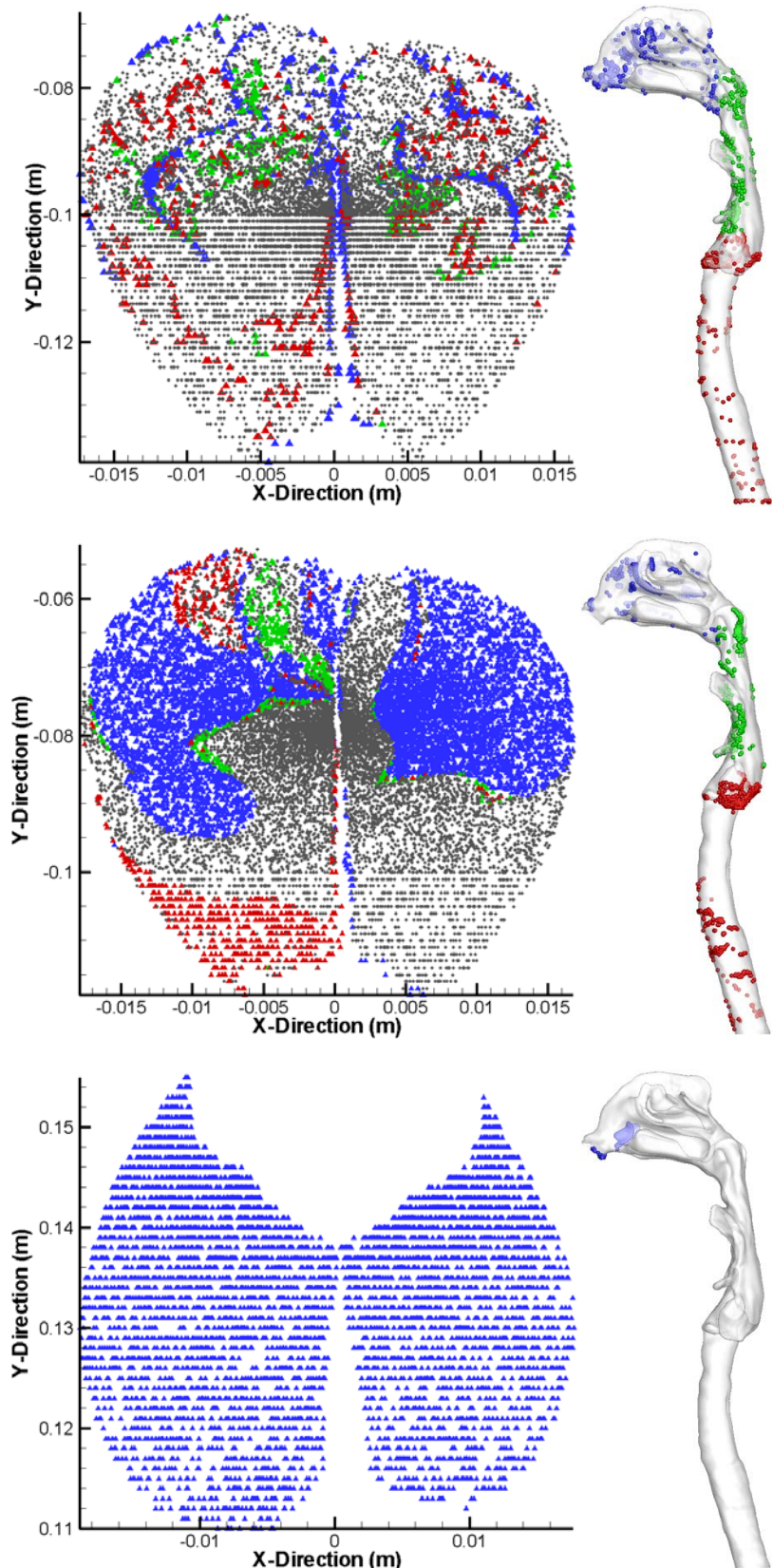
Comparison of the particle deposition pattern results in different wind conditions, which are monochromatically distributed in the critical area. For  $1\mu\text{m}$  particles, there is no real discerning pattern that can allow confident predictions of where a particle may deposit within the respiratory airway. For  $15\mu\text{m}$  particles nearly all the particles that deposit in the trachea region originate from the left side of the critical area, which may suggest that these particles that enter one side of the nasal chamber, travel through that airway geometry with a different air flow pattern that may be experienced if the particles had entered the other side of the nasal chamber. During normal nasal physiology, the nasal cavity is normally asymmetrical where one nasal passage is usually more patent than the other. This asymmetry is referred to as the nasal cycle, which is a result of congestion (swelling) of the erectile tissue (cavernous tissues of the mucosa) in one nasal cavity while at the same time decongestion (shrinking) occurs to the erectile tissue in the other cavity. The airflow through each nasal cavity is then governed by the resistance caused by the cross-sectional area of each airway. This asymmetry may explain the bias for those particles that exist in the lower left region of the critical area to deposit in the trachea region. Each second pattern that emerges from the  $15\mu\text{m}$  critical area is that the blue coloured particles (depositing in the nasal cavity region) exist in the upper half of the critical area, compared with the red coloured particles (depositing in the trachea) which exist in the lower half of the critical area. It has been established that for  $15\mu\text{m}$  sized particles early deposition in the nasal cavity is attributed to inertial deposition (Chung and Kim 2008; Worth Longest and Hindle), whereby particles that exhibit high momentum will not be able to stay entrained with the air flow streamlines. In Figure 6. 10 it was shown that as the particles approached

---

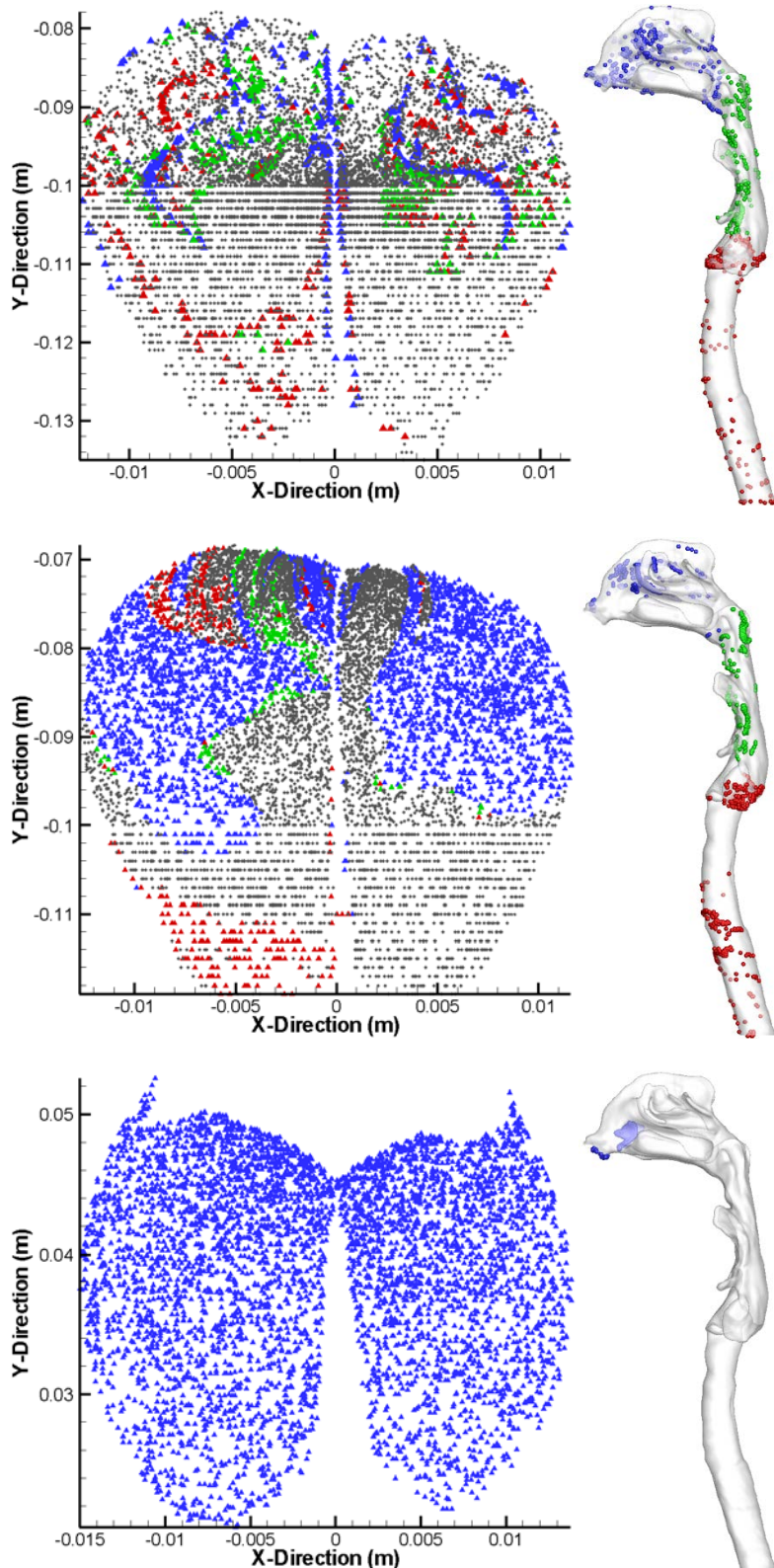
the nostrils, they were accelerated due to the inhaled air that complements the oncoming airflow. In addition, particles originating from above the nostrils are further accelerated by the gravitational pull which becomes more influential as the particles become larger in size. These two contributing factors cause the particles to exhibit higher inertia as they enter the respiratory domain, when compared to those particles that originate from below the nostrils. A further investigation found that a large number of those particles that deposited in the nasal region (total = 23.2%, 39.5%, 48.1%, respectively) are concentrated at or near the nostril inlet. For 80 $\mu$ m particles, the larger mass of the particle means that it is highly influenced by gravitational settling, and therefore the critical areas at the upstream location are located at a much higher vertical distance from the nostril inlets. Similar to the 15 $\mu$ m particles, the 80 $\mu$ m particles are further accelerated due to the inhaled air that complements the oncoming airflow, thereby increasing its inertial properties even further. This creates regions of high concentration of particles depositing at or near the nostril inlets. The shape of the critical area is that of two narrow teardrops where a larger concentration of particles is found near the bottom of the critical area.



(a) Light breath with different particle size at 0.05m/s wind velocity



(b) Light breath with different particle size at 0.20m/s wind velocity



(c) Light breath with different particle size at 0.35m/s wind velocity

Figure 6. 10 Comparison of particle deposition pattern in intergrade model in different wind speed at light breathing (15Lpm) (a) the wind velocity is 0.05m/s, (b) the wind velocity is 0.20m/s, (c) the wind velocity is 0.35m/s

---

#### 6.3.3.4 Particle Deposition Efficiency

Figure 6. 11 shows comparison of deposition efficiencies with previous using the inertia parameter. Under an inhalation flow rate of 15L/min and 40L/min, 100000 microparticles for each particle size of 1, 5, 15, 40, and 80 $\mu$ m were tracked in the respiratory model. The inertial deposition of micron particles in the nasal cavity was normalized by using the inertial parameter,  $I=Qd^2$ , where Q is the air flow rate ( $\text{cm}^3/\text{s}$ ) and d is the equivalent aerodynamic diameter ( $\mu\text{m}$ ). It is a convenient parameter that compares deposition against different flow rates and particle sizes at aerodynamic diameters. It is widely used for presenting particle deposition efficiencies, especially for in vivo data, where it is difficult to determine an adequate characteristic length for realistic human airways. The total deposition efficiency for the region spanning from the anterior nostril opening conducting airway to the trachea was determined and compared with boundary condition data. The comparative data comes from different forms of nasal cavity deposition studies which includes in-vivo human volunteers by Pattle (1961) and Cheng et al (2001), replicate cast models by Kelly et al. (2004a), and computational models by Inthavong et al (2008b). The deposition efficiency profile exhibits the ubiquitous increasing trend as particle size increases for the diffusion deposition of ultrafine particles. For IP between 250 and 5000 and  $IP>150000$ , the deposition efficiency dates are much the comparative data in Figure 6. 11. For  $5000<IP<150000$ , the simulation results significantly underestimate particle deposition. For the 40L/min case, the efficiency difference results for three different wind condition the are 20% to 25% and these data are lower than the previous data, and there is a 10% deposition efficiency of difference among the three cases. Comparisons between heavy breathing (40L/min) and light breathing (15L/min) and at the highest wind condition gives closer matching to existing literature data. With a decreased in wind velocity, the



difference between 26% and 58% is an increase of up to 35%. These indicate that the external environment significantly affects the efficiency when the particle is neither too big nor too small a size.

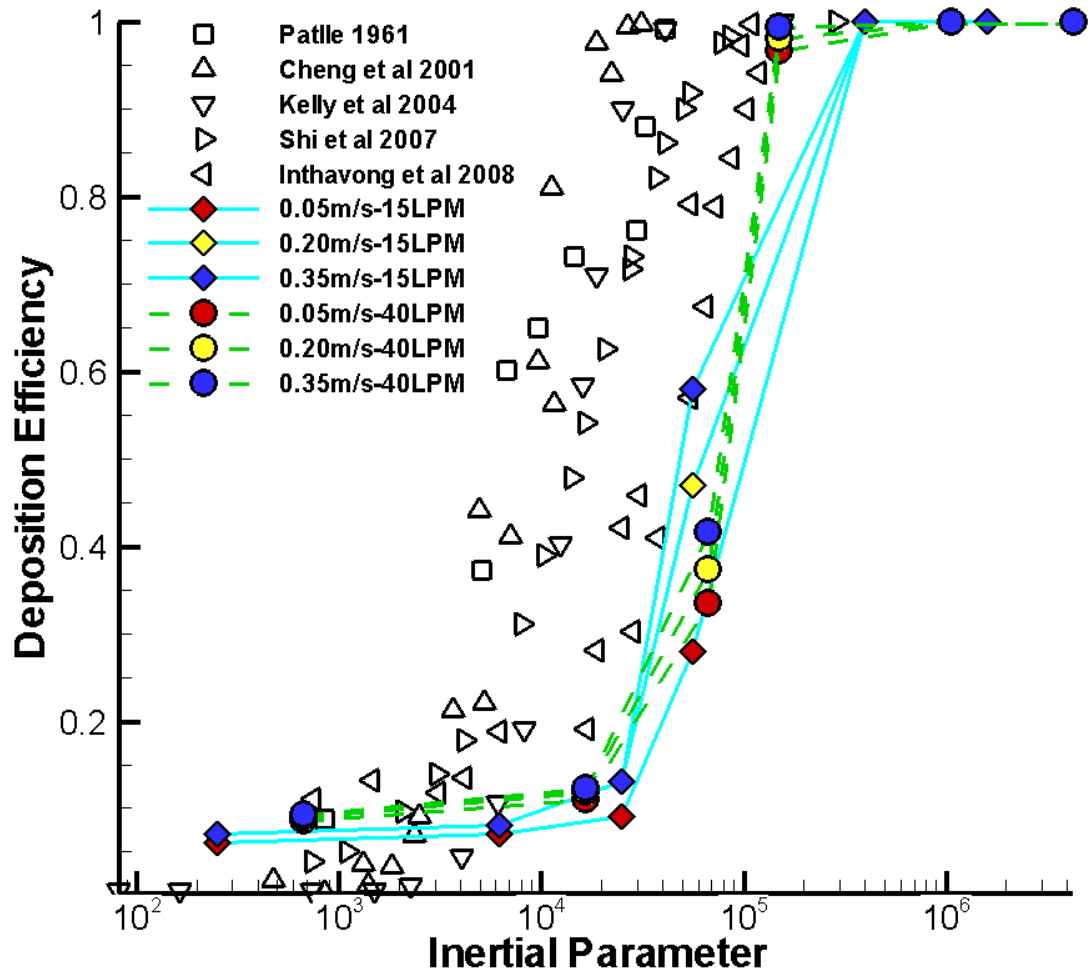


Figure 6. 11 Comparison of deposition efficiencies with previous using the inertia parameter

---

# Chapter 7

## Particle Deposition in a Human Nasal-Sinus Cavity

### 7.1 Introduction

Studies into ultrafine particle deposition caused by inhalation through the nasal cavity have been performed using i) CFD methods (Schroeter et al. 2006) ii) replicate casts of a nasal cavity (Cheng et al. 2001; Lin et al. 2011; Schroeter et al. 2011) or iii) in-vivo human subjects (Cheng et al. 1995; Cheng et al. 1996). The resulting data obtained from these first two methods are often used to compare and validate the particle deposition obtained in the nasal cavity of in-vivo experiments. However, deposition data on a human subject is inclusive of the paranasal sinuses and it is unknown to what extent this influences the total and local deposition fractions in the nasal cavity.

According to Cheng et al. (1996) aerosol deposition in the human respiratory airways is strongly influenced by three major factors: physical (particle diameter, shape, and density), physiological (respiratory ventilation and pattern), and morphological (airway size and shape). Deposition of micron particles is largely due to the particle inertia, and is significant for particles with aerodynamic diameters greater than  $5\mu\text{m}$ . Studies have shown that the sharp curvatures in the nasal cavity airway that change the airflow direction are responsible for inertial deposition of micron particles (Inthavong et al.

---

2011a; Worth Longest and Hindle 2010). This is particularly significant at the entrance to the main nasal passage and at the nasopharynx where the flow exhibits 90° curvatures. Inertial deposition mechanisms rely on flow convection, which transports the particles before a sharp curvature is present. With regards to micron particle deposition in the maxillary sinus, Xiong et al (2008b) indicated that little flow exchange occurred between the inner and outer aspects of the paranasal sinuses. This suggests that it is unlikely that micron particles will be lost to the sinus regions and omitting the sinus regions in CFD and replicate cast studies is acceptable.

On the other hand, ultrafine particles are dominated by diffusion and its deposition onto surfaces is reliant on a low convection to diffusion ratio (i.e Peclet number). If the flow rate through the nasal cavity is sufficiently low, it is hypothesised that the diffusion transport of ultrafine particles may be significant enough for the particles to pass into the paranasal sinuses. This suggests that ultrafine particles may be lost to the sinus regions and that CFD and replicate cast studies omitting the sinus regions may be invalid for describing the remaining deposition fraction entering airway regions downstream, such as the trachea and bronchial region.

The paranasal sinuses (maxillary, sphenoid, and frontal) are air-filled spaces connected to the nasal cavity by narrow passageways called the ostium. The exact biologic function of the sinuses is uncertain but is thought to contribute to the following: reduction of the weight of the front of the skull; act as a resonating chamber for voice production; humidifying, heating, and filtering of inhaled air through mucus secretions; and absorption of any force impacting on the face or skull (Keir 2009). To date, nearly all CFD studies of particle deposition through the nasal cavity have neglected the paranasal sinuses, although there have been two studies of air flow distribution through

---

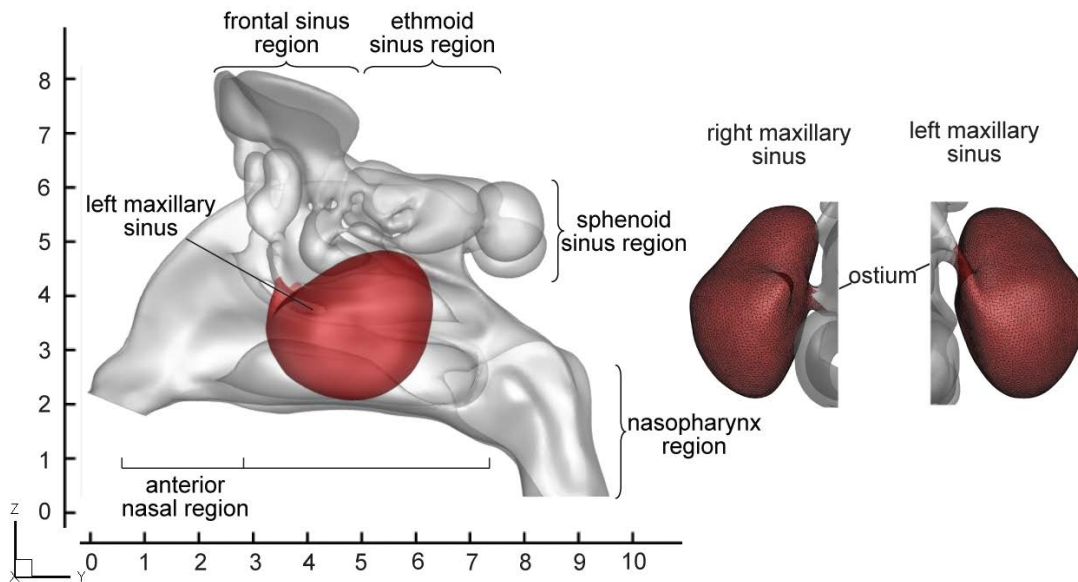
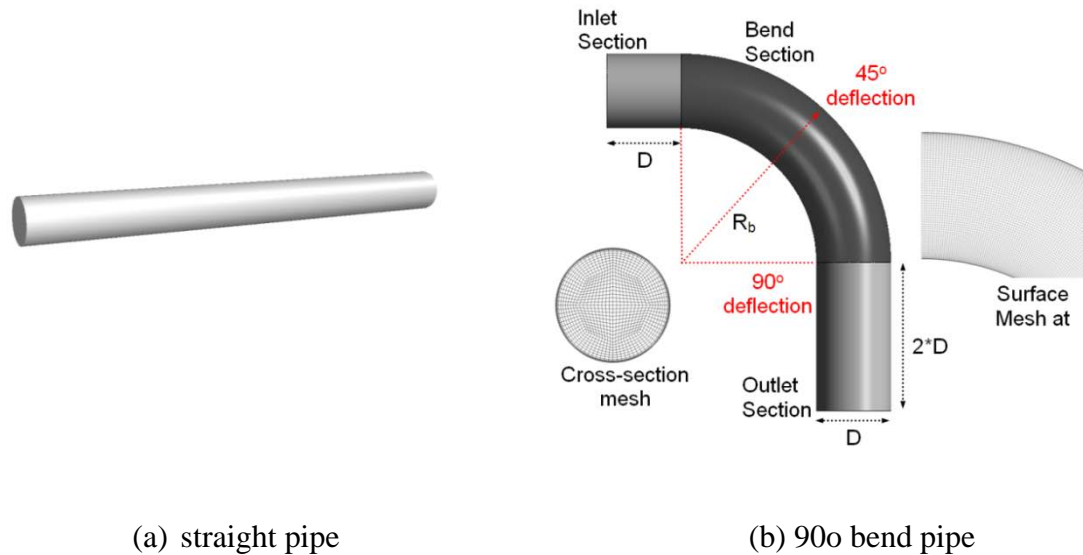
the nasal cavity that include the paranasal sinuses (Lindemann et al. 2005; Xiong et al. 2008b).

This chapter investigates the flow patterns in the nasal cavity, in the paranasal ostium and its corresponding sinus, to determine the uptake of ultrafine particles with a focus on the ostium region that may occlude due to deposition. The uptake of ultrafine particles within the nasal-sinus model and in a nasal cavity model for different particle sizes is given. In addition, special attention is made to the modelling of the Brownian diffusion process to ensure that the predictions of the ultrafine particles are reliable. Therefore, a secondary aim of this chapter is to study the applicability of the Gaussian white noise Brownian diffusion model commonly used in the commercial CFD software Ansys-FLUENT v12.1, since it has been shown that the same model in Fluent v6.3 failed to predict nanoparticle deposition (Inthavong et al. 2011b; Longest and Xi 2007).

## **7.2 Numerical Procedure**

### **7.2.1 Computational Models**

Four geometries were created for this study – a straight pipe, a 90° bend pipe, a human nasal cavity with paranasal sinuses included, and the same nasal cavity model without sinuses (Figure 7. 1) which it already present in the previous period at chapter III.



(c) nasal cavity model highlighting the maxillary sinus

Figure 7. 1 CFD geometries used in this study for (a) straight pipe (b) 90° bend pipe and (c) nasal cavity with sinus model.

Two nasal cavity models were reconstructed from the same CT scans, and are NC02 and NC02-S, The geometry of the NC02-S model is shown in Figure 7. 1c. Table 7. 1 summarizes the geometries detailing significant dimensions and the computational boundary conditions that are applied. The pipe models are used to validate the Brownian model and to ensure it is reliable before applying it to the more complex nasal cavity.

Table 7. 1 Dimensions and details of the geometries considered in this study

	Inlet Hydraulic Diameter ( $D_h$ )	Radius of curvature, $R_b$	Inlet Flow Rate (L/min)	Inlet Re number	Mesh size
Straight pipe	0.45 cm	-	1	322	750,000
			10	4840	
90° bend pipe	0.46 cm	1.43 cm	1.052	305	550,000
Nasal cavity without sinus (NC02)	1.0 cm	-	4	255	3.0million
			10	642	
Nasal cavity with sinus (NC02-S)	1.0 cm	-	4	278	4.0million
			10	705	

The length from the anterior most regions to the posterior nasopharynx region is approximately 9cm, while the height from the main nasal passage floor to the superior tip of the frontal sinus is approximately 7cm. This is summarised along with some dimensions and details of the model in Table 7. 2.

Table 7. 2 Summary of geometric characteristics of the nasal cavity.

	Without sinus cavity model			Sinus cavity model		
	Present study	Doorly et al. (2008)			Present study	Xiong et al. (2008)
		Model 1	Model2	Model3		
Overall cavity length (cm)	9.7	10.5	10.6	11	9.7	9.1
Overall cavity width (cm)	3.9	-	-	-	7.3	6.6
Surface area (cm <sup>2</sup> )	199	106*	107*	109*	290	NA
Volume (cm <sup>3</sup> )	NA	13.8	14.2	22.4	NA	NA

\*right nasal chamber only

---

## 7.2.2 Boundary Conditions

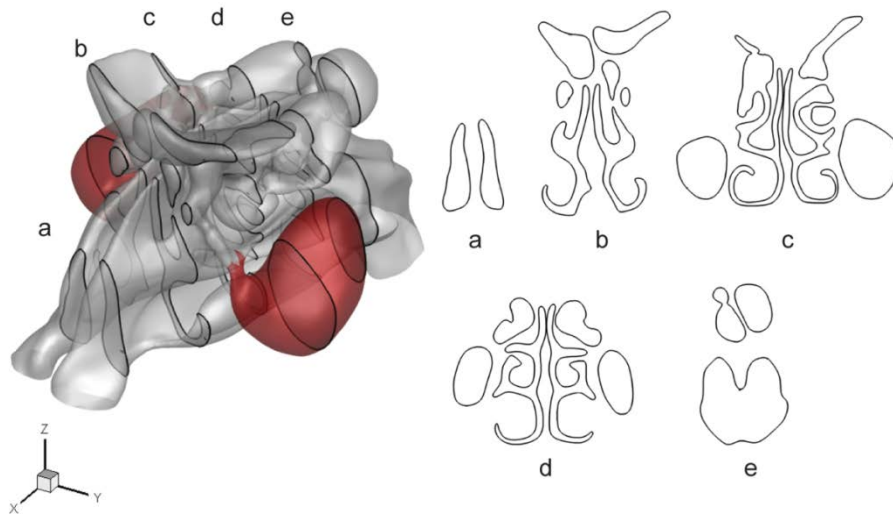
In order to achieve a fully developed flow for the straight and 90° bend pipes, an additional separate pipe 5-Diameters in length with the same cross-section and mesh were simulated with periodic boundaries applied. When the flow reached a fully developed state, the velocity profile from the periodic straight pipe model was extracted and used as the inflow condition at the inlet of the 90° bend pipe and the straight pipe. Two flow rates were considered for the straight pipe, 1 L/min, and 10 L/min. For the nasal cavity, inhalation is induced through a pressure difference between the nostril inlets ( $P_{in} = 0\text{Pa}$ ) and the nasopharynx outlet ( $P_{out}$ ), which is set to a negative pressure relative to atmospheric pressure, caused by the movement of the diaphragm. This method presents a more realistic approach to earlier modelling approaches, which used a uniform or developed velocity inlet at the nostrils (Inthavong et al. 2006; Keyhani et al. 1995).

Particles in the pipe simulation were released from an evenly dispersed circular region 0.01m from the inlet to prevent any spurious data occurring due to random particles exiting the inlet upon immediate release. Furthermore, a particle was located at no less than 0.1mm away from the wall to eliminate artificial immediate deposition on the walls due to the stochastic nature of the Brownian motion model. Turbulent dispersion is not considered in this study to isolate the effects of the Brownian motion at the higher flow rate and instead the so-called mean flow particle tracking approach (i.e. laminar tracking) is used. In the Lagrangian tracking scheme,  $u_i^s$  found in the slip velocity  $(u_i^s - u_i^p)$  in the chapter IV (Equation 4.46) is defined from the cell centre and a particle within any part of that cell takes  $u_i^s$  from the cell centre. For cells adjacent to the wall boundaries, the velocity profile should approach zero at the wall rather than be

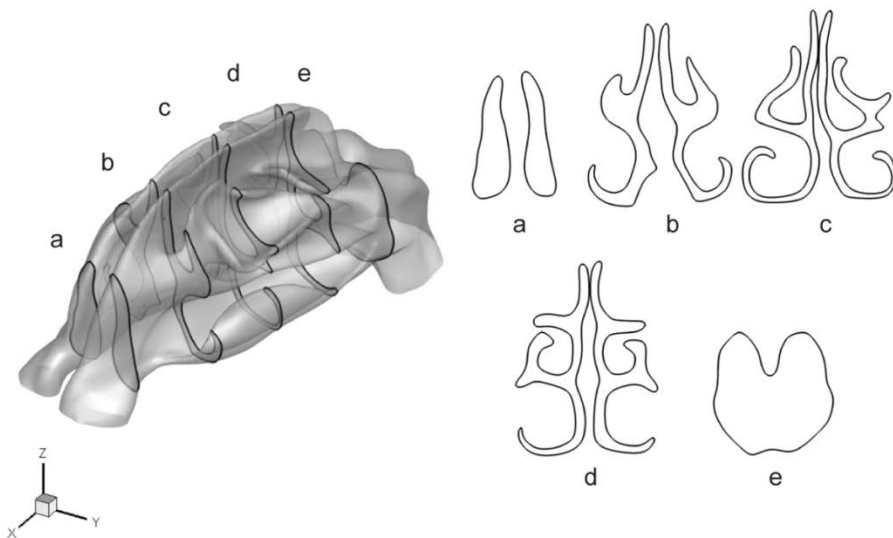




cross-sectional areas created by the inclusion of the sinuses. There are four pairs of sinuses; the maxillary sinuses, located in the cheekbones under the eyes; the frontal sinuses, located in the forehead above the main nasal passages and eyes; the ethmoid sinuses, located between the eyes and the nose and the sphenoid sinuses, located in the centre of the skull, behind the nose and the eyes.



(a) nasal-sinus cavity model (NC02-S). Shaded region is the maxillary sinus.



(b) nasal cavity model (NC02)

Figure 7. 3 Coronal slices of the airway comparing a (a) nasal cavity with sinus model highlighted by the maxillary sinus and (b) a nasal cavity model with the sinuses omitted.

The cross-sectional area versus distance from the anterior tip of the nose to the posterior nasal passage is compared with other nasal cavities published in the literature (Figure 7. 4). The NC02 model (without sinus) has a slightly greater cross-sectional area than other models in the anterior ( $x < 4$  cm) and posterior ( $x > 6$  cm) region. It is noted that the data from Cheng et al (1996) comes from four adult non-smoking male volunteers (ages 36-57 yr), Subramaniam et al (1998) from a 53-yr-old, non-smoking Caucasian male, and Wen et al (2008b) from a 25-year old Asian male. The NC02-S model (with sinus) shows a significant increase (up to 300%) in the cross-sectional area, mainly contributed to by the maxillary and frontal sinus. This begins at  $x = 0.0187$ cm with the frontal sinuses that protrude superiorly over the nasal passages. Further downstream the presence of maxillary and ethmoid sinuses also contributes to the cross-sectional area.

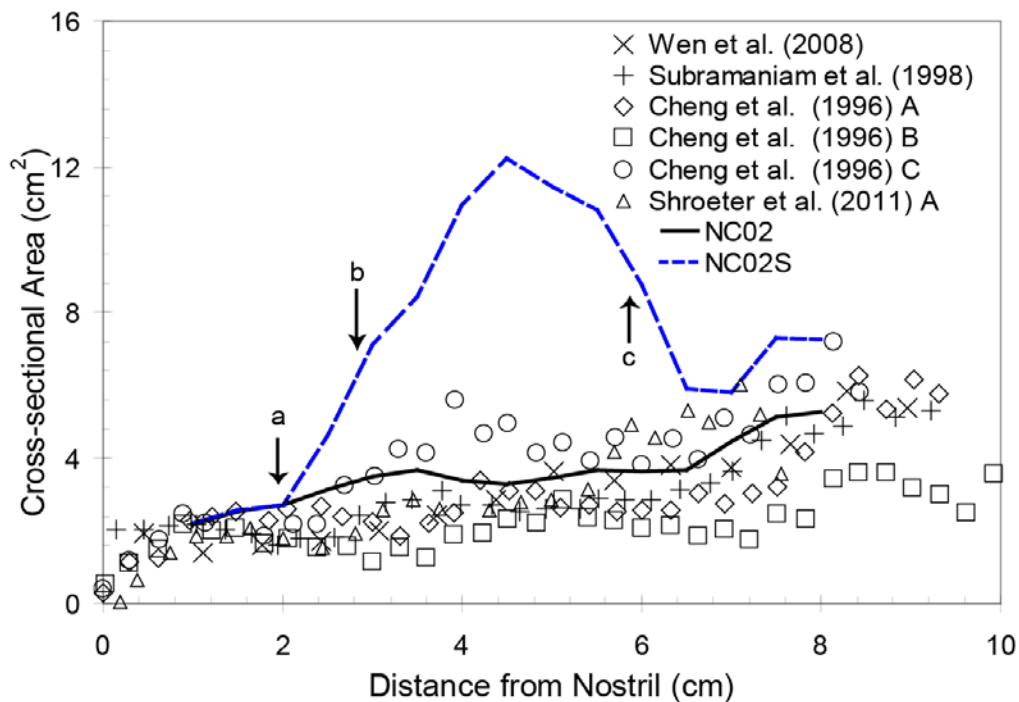


Figure 7. 4 Coronal cross-sectional areas from the nostrils to the posterior nasopharynx in a linear axial vector. The distance from the nostrils at  $x=0$ cm is taken as the anterior most tip of the nostril opening. Arrow (a) is at  $x = 0.0187$  cm and signifies the beginning of the frontal sinus (b) is at  $x = 0.0288$  cm signifying the anterior beginning of the maxillary sinus, and (c) is at  $x = 0.0566$  cm signifying the posterior end of the maxillary sinus

---

The pressure drop between the nostril inlets and the posterior nasal wall at the nasopharynx for different inhalation rates is shown in Figure 7. 5. Comparisons are made with other published data for nasal cavity (no sinuses) geometries. Currently there are inconsistencies in the representation of the inhalation using CFD in regards to the boundary condition settings for the inlet and outlets. One method is to use pressure inlet and outlet boundary conditions where the nostril inlets are set to gauge pressure, i.e.  $P = 0$  Pa and the nasopharynx outlet set at a relative negative pressure value corresponding to the inhalation effort created by the contraction of the diaphragm and expansion of the lungs. This setting is referred to as ‘pressure’ conditions. This differs to a forced flow applied at the nostril inlets to drive the inhalation. In terms of the numerical boundary conditions, this is produced by setting the nostril inlets with equal mass flow distribution (i.e. 5L/min per nostril for an inhalation rate of 10L/min) using the mass flow rate or velocity boundary condition, and the nasopharynx outlet as an outflow or opening boundary condition. This setting is labelled as ‘forced’ conditions and its results are compared with the pressure conditions method and also published data in Figure 7. 5. The forced method produces less resistance than the pressure method given that an even distribution of flow passes through both the left and right nasal chambers while the pressure method produces an asymmetric distribution of flow based on the resistance caused by the left and right nasal chamber geometries. A comparison with other nasal cavity geometries shows that the forced method produces less resistance per flow rate. This implies that smaller respiratory effort is required to produce an equivalent inhalation flow rate.

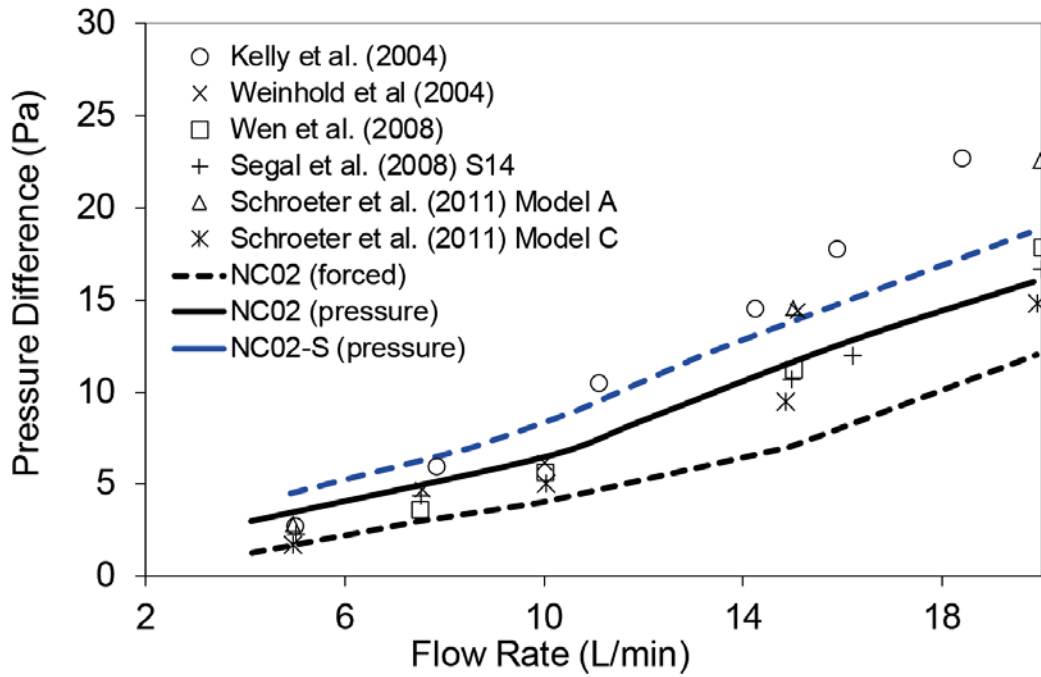


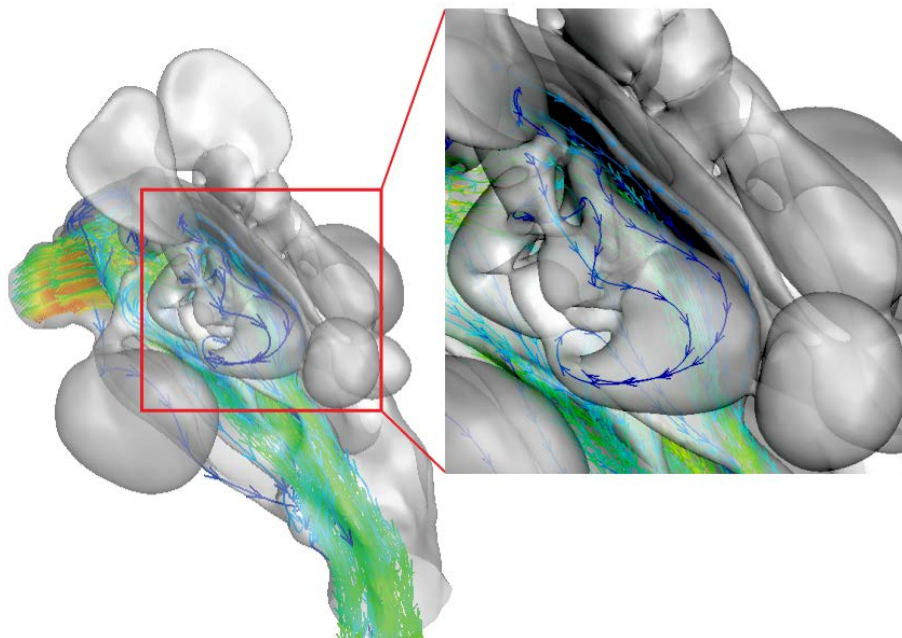
Figure 7.5 Comparison of the pressure drop for nasal cavity model NCO2 without sinus inclusion.

Comparisons of the pressure drop per inhalation flow rate with other models shows that the NC02 model has a flatter profile, meaning that it has a lower flow resistance. This is expected given that the cross-sectional area profile of NC02 shown in Figure 7.4 is larger than the comparative models. The addition of the paranasal sinuses to the nasal cavity produces additional holes or slits in the geometry in the form of the nasal ostium that connects the sinus to the main nasal cavity chambers. Pressure losses in any pipe system are found at openings, especially if part of the opening is aligned with the flow streamlines. As a consequence, additional effort is needed to overcome any pressure that may be lost through the nasal ostia. The pressure difference profile for the NC02-S model shows a steeper curve, which implies a larger pressure difference, and hence greater inhalation effort, is required to produce an equivalent inhalation flow rate.

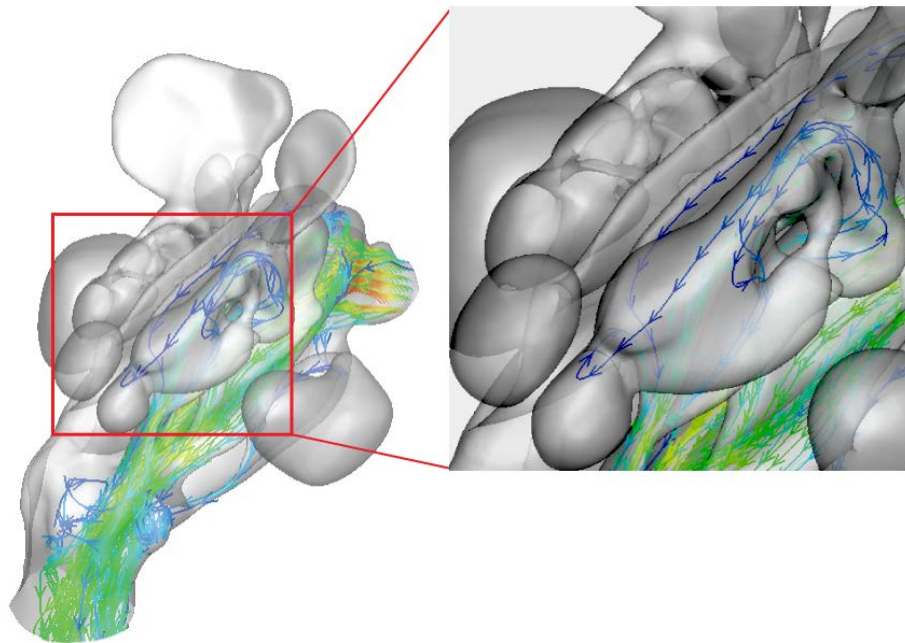
---

### 7.3.1 Flow Patterns and Streamlines

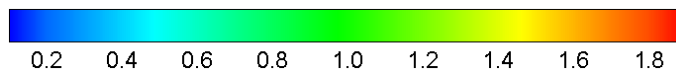
Flow streamlines were released from the left and right nostrils in order to trace the flow patterns. In both instances the streamlines initially accelerate near the nostril opening before passing mainly through the main nasal passage at mid-height. Some streamlines travel along the floor of the nasal cavity, while some reach the olfactory regions, and up towards the sphenoid and ethmoid sinuses, but these exhibit low velocity  $\approx 0.1\text{m/s}$ , as highlighted in Figure 7. 6. These streamlines, based on 100 release points uniformly released across the nostril inlets, do not show any paths leading into the maxillary nor the frontal sinus as the release points were uniformly released across the nostril inlets. To determine if any flow will actually pass into the maxillary sinus, we track some path streamlines in reverse from points inside the maxillary sinus.



(a) left nasal chamber



(b) right nasal chamber

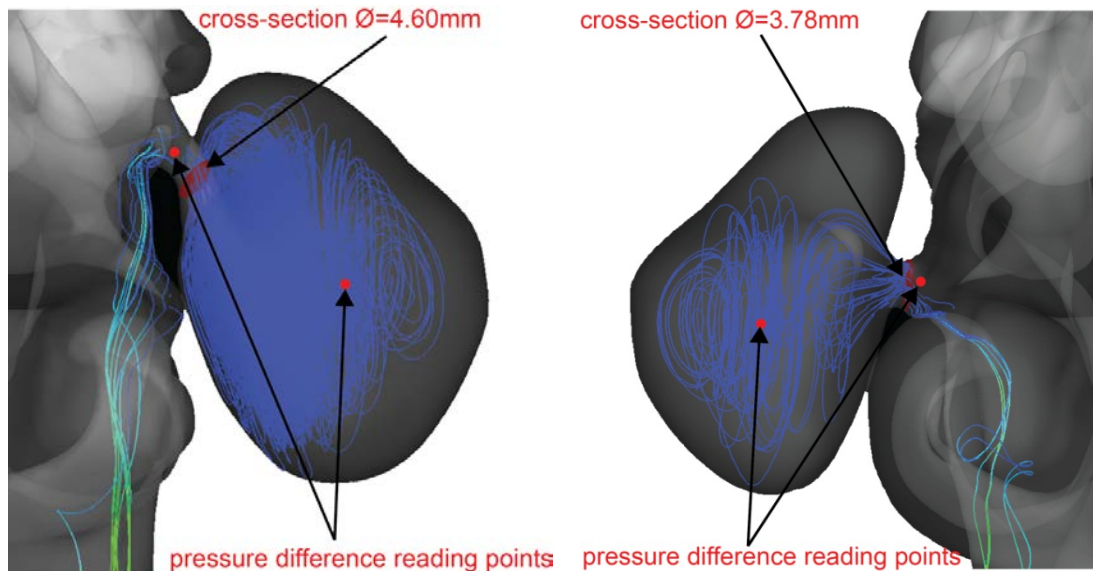


velocity magnitude [m/s]

Figure 7. 6 Streamlines passing through the nasal cavity that originate from the (a) left and (b) right nostrils at 10L/min. Magnified inset highlights the flow streamlines that reach the sphenoid and ethmoid sinus regions.

Figure 7. 7 shows that the flow inside the maxillary sinus occurs at a very low velocity and exhibits typical recirculation of near stagnant flows. Analysis of the geometry and airflow showed that the minimum ostium diameter is 4.6mm and 3.78mm, and the pressure difference between the ostium entrance and inside the maxillary sinus are 0.056Pa and 0.0026Pa for the left and right sides respectively. The mass flow rate through the left and right ostium is  $11.4 \times 10^{-9}$  kg/s and  $6.77 \times 10^{-9}$  kg/s, which are  $< 0.006\%$  of the total inhalation flow rate. This small percentage of flow is not conducive for convective transport of particles into the maxillary sinus and that if any deposition was to occur in this region, and then it would be caused by Brownian diffusion. On the other hand, the flow streamlines in the sphenoid and ethmoid sinuses are not recirculating but instead convect through with a discernible direction. This suggests that some

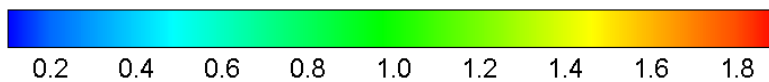
submicron particles may be transported to this region by convection, enhancing the likelihood of deposition onto the surfaces by diffusion.



(a) left maxillary sinus

(b) right maxillary sinus

velocity magnitude [m/s]



*Figure 7. 7 Streamlines passing through the nasal cavity that originates from the (a) left and (b) right nostrils at 10L/min*

Contours of velocity magnitude at slices A, B, D, and E (defined in Figure 7. 3) are shown in Figure 7. 8. Slice C is not shown as it produced a similar profile to that of slice D. The 2D contours confirm flow acceleration occurring in the anterior nasal cavity where a peak velocity of 1.8m/s is found at slice-A. The main flow is centred on the cross section and pockets of low velocity are found at the top and bottom of the slice. As the flow travels downstream the peak velocity decreases to a value of 1.3m/s found in slice-D. This is due to the airway passage expanding in cross-sectional area, resulting in lower velocities. The contours show that the bulk flow regions occur mainly through the mid-height region and close to the nasal septum, which separates the two cavities.

The contour at slice-E shows a well-mixed pattern, which is caused by the airflow from the left and right sides of the nasal cavity merging together. Very low flows of  $< 0.1\text{m/s}$  are found in the sinus regions.

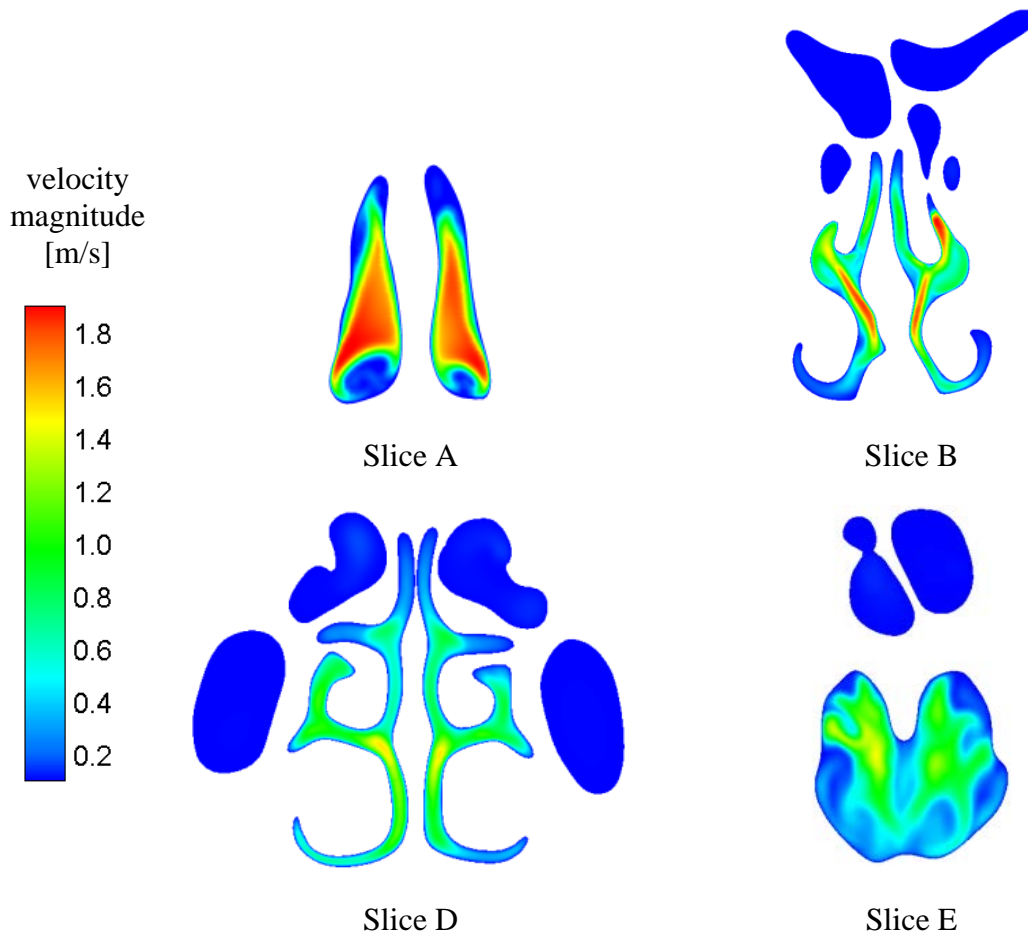


Figure 7. 8 Velocity magnitude contours at 10L/min

## 7.3.2 Particle Deposition

### 7.3.2.1 Preliminary Analysis

To test the accuracy of the particle tracking procedure, the flow and particle transport in the entrance region of a pipe and a  $90^\circ$  bend pipe are simulated and the results compared with experimental and analytical solutions. The number of particles tracked through the pipe and nasal cavity geometries was 80,000 (up to 300,000 particles were checked), which was statistically independent from the stochastic nature of the Brownian motion



---

model. The deposition efficiency of ultrafine particles in the range of 1-100nm was simulated in a straight pipe for flow rates of 1L/min and 10L/min, and 5-12nm particles for a 90° bend pipe. As discussed earlier, the Brownian motion model from Fluent v6.3 fails to predict the diffusion transport of ultrafine particles and this is evident in Figure 7. 9, where a discrepancy of up to two orders of magnitude are found in comparison with the experimental results from Wang et al (2002) and the analytical correlation from Ingham (1975).

$$DE = 1 - 0.819 \exp(-14.63\Delta) + 0.0976 \exp(-89.22\Delta) + 0.0325 \exp(-288.0\Delta) + 0.0509 \exp(-15.9\Delta^{2/3}) \quad 7.2$$

On the other hand, the Brownian model with a NWI using FLUENT v12.1 is able to handle the diffusion transport in a straight and 90° bend pipe. The Eulerian species model which accounts for pure diffusion (i.e. particle inertia effects are excluded), also shows satisfactory results. The Eulerian species simulation is valid for small nanoparticles, but with increased flow rate and particle size, the particle inertia becomes important (Xi and Longest 2008b). The deposition efficiency results for a straight pipe with a flow rate of 1L/min gives a similar trend to that of the 10L/min flow rate and therefore is not shown for brevity. It must be noted that the model for Brownian motion that are available in FLUENT v6.3 and v12.1 is the same model based on a Gaussian white noise process. Therefore it appears that the error occurring with Brownian model in FLUENT v6.3 is due to a computational bug, which has been rectified in the newer release.

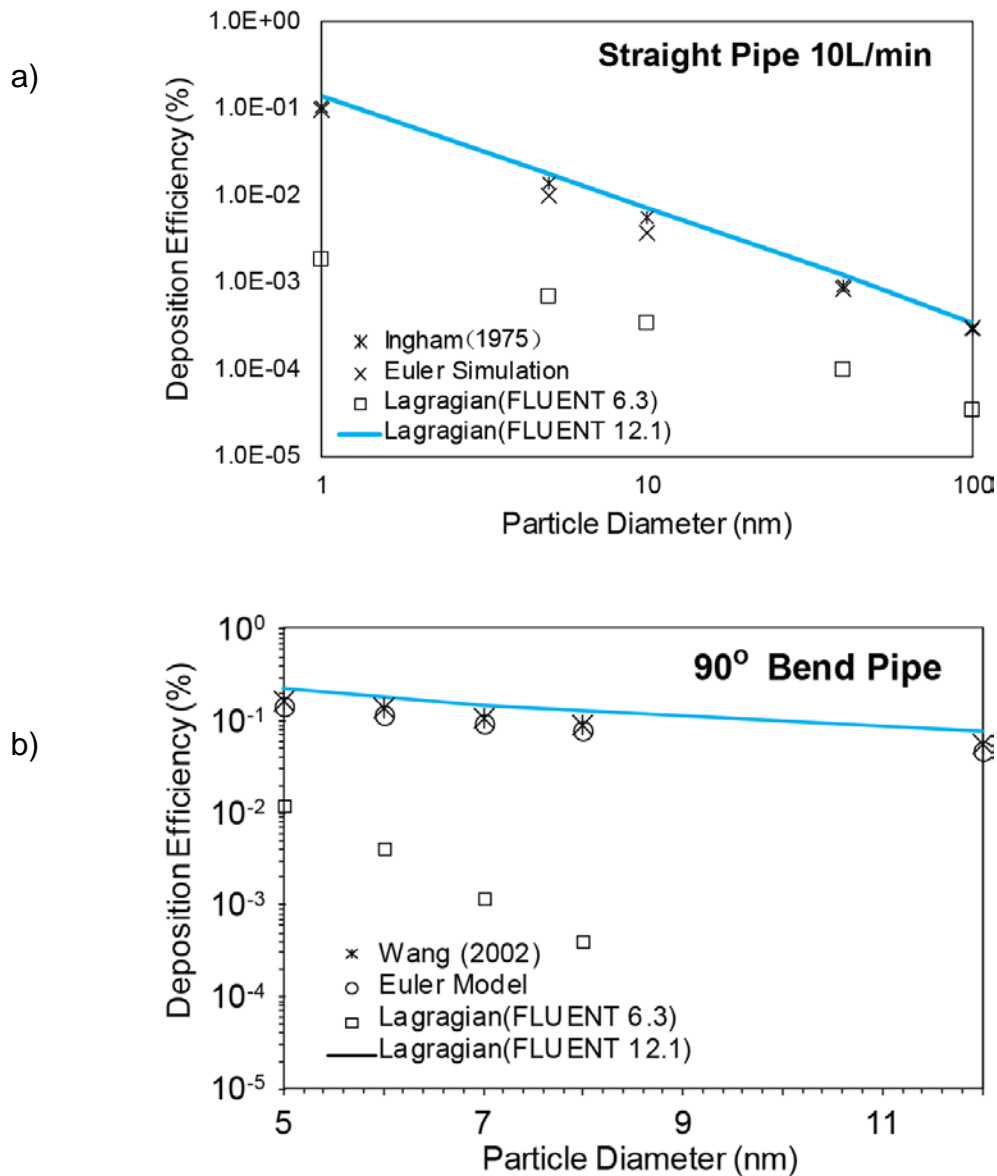


Figure 7. 9 Comparison of deposition efficiency results using the Eulerian species model, Brownian model- FLUENT 6.3, and Brownian model- FLUENT 12.1 in (a) straight pipe 10L/min, and a (b) 90° bend pipe.

### 7.3.2.2 Diffusion Deposition in the Nasal Cavity and Sinus

Under an inhalation flow rate of 10L/min, 70000 nanoparticles for each particle size of 1, 5, 10, 40, and 100nm were tracked within the two nasal cavity models. The total deposition efficiency for the region spanning from the anterior nostril opening conducting airway to the oropharynx was determined and compared with existing data (Figure 7. 10). The comparative data comes from different forms of nasal cavity

deposition studies which includes in-vivo human volunteers by Cheng et al. (1996), replicate cast models by Kelly et al. (2004a), and computational models by Wang et al. (2009) and Zamankhan et al. (2006). The deposition efficiency profile exhibits the ubiquitous decreasing trend as particle size increases for the diffusion deposition of ultrafine particles. For 1nm particles, there was 99.9% deposition within the nasal cavity. For 10nm particles the deposition decreases to 24% (NC02) and 30% (NC02-S). At 40nm the deposition decreases to 6% (NC02) and 9% (NC02-S) and remains at that level as the particle size increases to 100nm. The decreasing deposition efficiency trend is due to the decreased Brownian excitation of the nanoparticle. A smaller Brownian excitation produces a smaller dispersion, and hence reduces the potential for the particles to diffuse into the ostia and sinus regions. The hypothesis proposed suggests that the deposition efficiency for a nasal-sinus cavity model should have a higher value, due to diffusion transport of particles out to the nasal ostia and its sinuses.

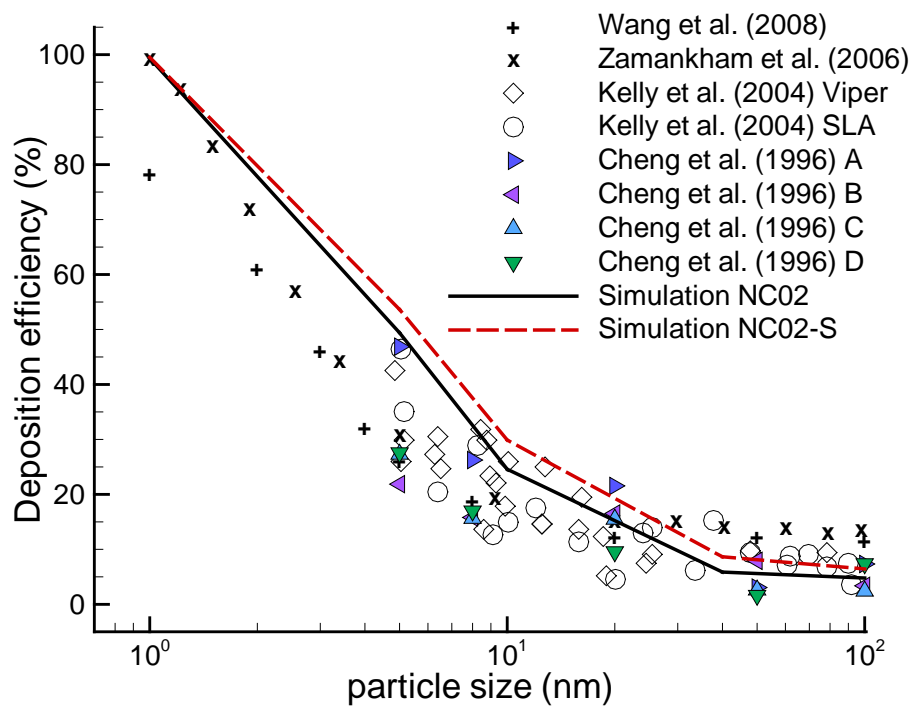


Figure 7. 10 Comparison simulation data for nasal without sinus deposition efficiency for 10L/min breathing rates

---

The results show that there is no difference between a nasal-sinus and nasal only model for a 1nm particle as both models predict near 100% deposition, while for 10nm the difference is 6%; 40nm the difference is 3% and; 100nm the difference is 2%. Therefore the maximum deposition difference occurs at 10nm and this difference reduces as the particles size increase to 100nm. Larger particles will experience a heightened state of inertia, which convect the particles though the computational domain. The critical value above which inertia significantly influences deposition and transport has been found to be  $St > 1.0 \times 10^{-5}$  (Xi and Longest 2008b). While the deposition for 1nm is the same for both models, the deposition may in actuality be different. Further analysis by visualisation is provided later to elucidate this.

The maximum difference in deposition efficiency between the two nasal cavity models that occurs is relatively low, when considering the variations between other deposition data, and therefore it may appear that omitting the sinuses for evaluating ultrafine particles may be acceptable. To ensure this, it is necessary to present the deposition efficiency between the two models under a lower flow rate of 4L/min. From the Pe number, which describes the rate of convection to the rate of diffusion by

$$Pe = U_0 L_h / \bar{D} \tag{7.3}$$

where  $U_0$  is the characteristic velocity,  $L_h$  the characteristic hydraulic length, and  $\bar{D}$  the diffusion coefficient based on the Stokes-Einstein equation, that a reduction in flow rate by 2.5x increases the influence of diffusion by the same amount for a given particle size. Figure 7. 11 shows the deposition efficiency for both nasal models where the red colour and open symbols represent the sinus NC02-S model. The lines represent the additional 15L/min case. The black colour represents the no sinus NC02 model. The difference in deposition efficiency between the two models at a flow rate of 4L/min is

most significant for 5nm and 10nm particles (17% and 16% difference respectively). As the particle size increases the difference between the two models diminishes. For 1nm particles, the difference is not discernable since the deposition efficiency is nearly at 100%. While the quantifiable difference is not noticeable it is expected that the 1nm particle diffusion will be much stronger at the lower flow rate of 4L/min, and that the deposition pattern locally will be different to that at a flow rate of 10L/min. For completeness, the particle deposition efficiency was also evaluated at a flow rate of 15L/min, which shows that the deposition values remain close to a flow rate of 10L/min for both models. Thus the differences caused by the sinus geometry remain similar as the flow rate increases from 10L/min to 15L/min.

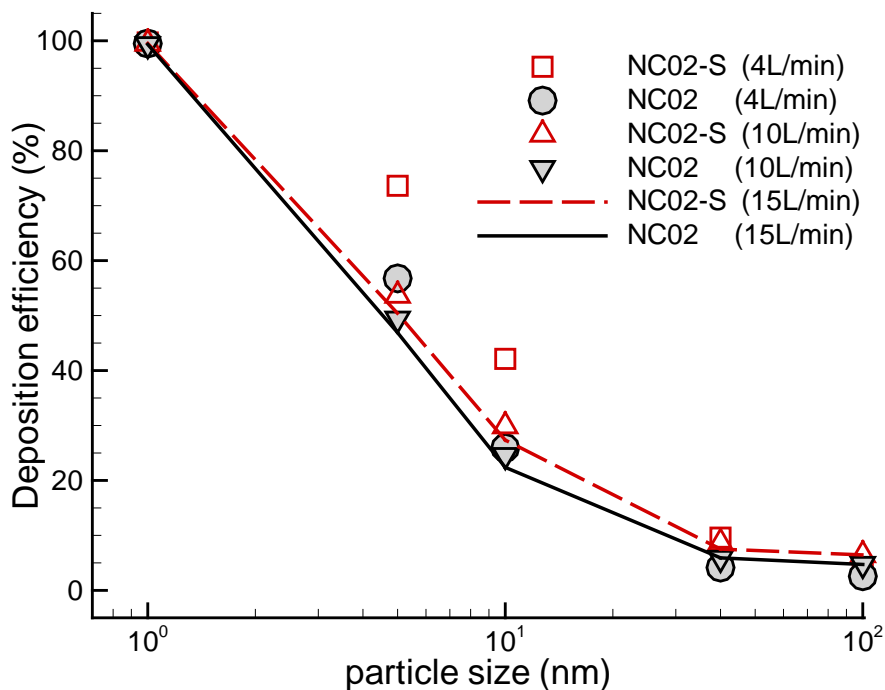


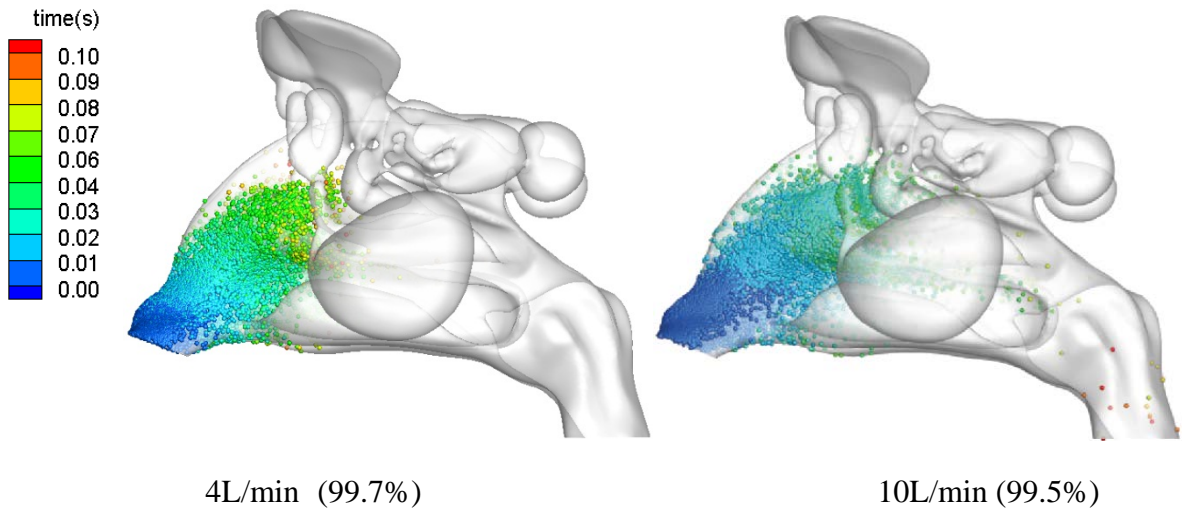
Figure 7. 11 Comparison simulation data for nasal without sinus deposition efficiency for 4L/min and 10L/min breathing rates

---

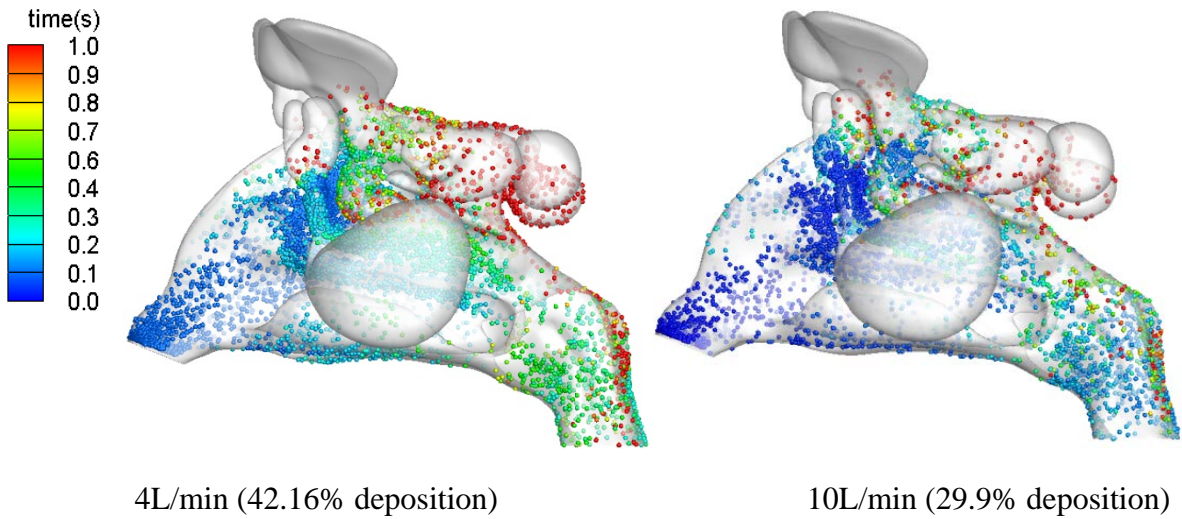
### 7.3.2.3 Visualization

To confirm that the 1nm excitation due to diffusion is much stronger at a lower flow rate, it is necessary to track each individual particle and record its spatial coordinates after impaction onto the surrounding surfaces. The coordinates are plotted and coloured by residence time as shown in Figure 7. 11. The distribution of 1nm shows that earlier deposition occurs where a large proportion of the particles persist for less than 0.022secs in the nasal-sinus cavity. The strength or influence of the Brownian diffusion increases as the flow rate decreases, and at a flow rate of 4L/min, deposition is found within the anterior half of the nasal-sinus cavity while at a flow rate 10L/min deposition is a little more dispersed with deposition sites found in the posterior half.

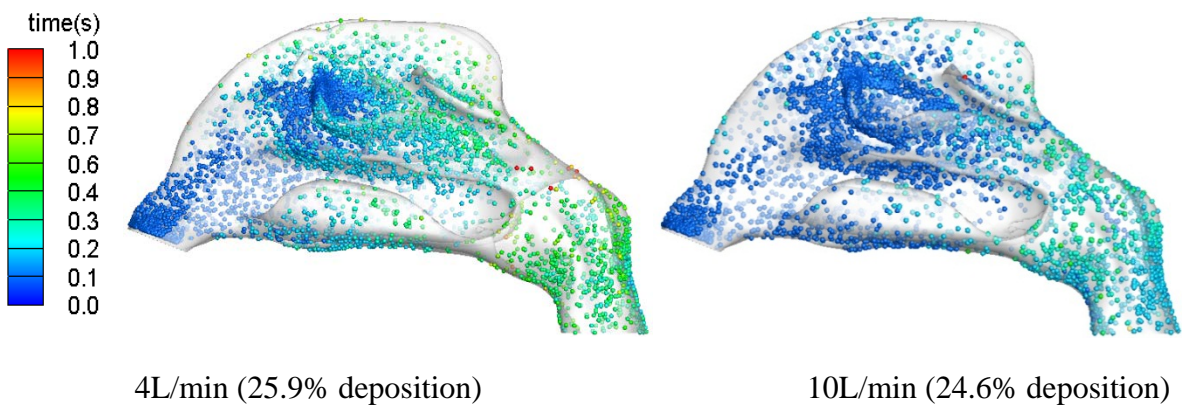
The deposition pattern for 10nm particles shows a more random and even distribution pattern. The residence time is ten times as great as that for 1nm, which suggests that the particles are transported with the inhaled flow field for longer and hence has the ability to travel deeper into the nasal cavity and perhaps down towards the lung region. The particle residence time is important for nanoparticle (NP) deposition studies as it gives an indication of the likelihood of deposition in different regions of the nasal cavity. For example, the shorter residence time of 1nm means that deposition occurs nearly immediately and the deposition zone is restricted to the nasal cavity and further deposition downstream is unlikely. This protects the sensitive lung airways from those NPs that exhibit dangerous properties for respiratory health. Conversely the ability to deposit particles in the middle regions of the nasal cavity or even deeper into the lung airways with high deposition, can be important for therapeutic drug delivery.



(a) 1nm particle, NC02-S



10nm particle, NC02-S



10nm particle, NC02

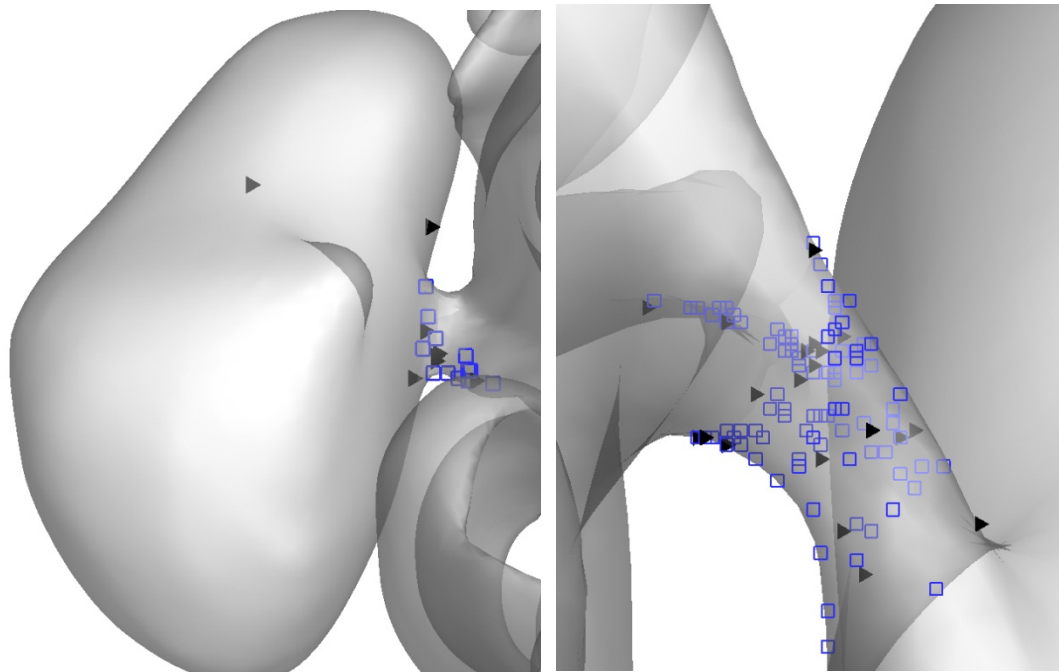
Figure 7. 12 NP deposition pattern in the nasal-sinus cavity for (a) 1nm - resulting in 98% deposition and (b) 10nm - resulting in 29.8% deposition. Particles are coloured by trajectory time within the nasal cavity before impacting onto the surfaces at 10L/min.

---

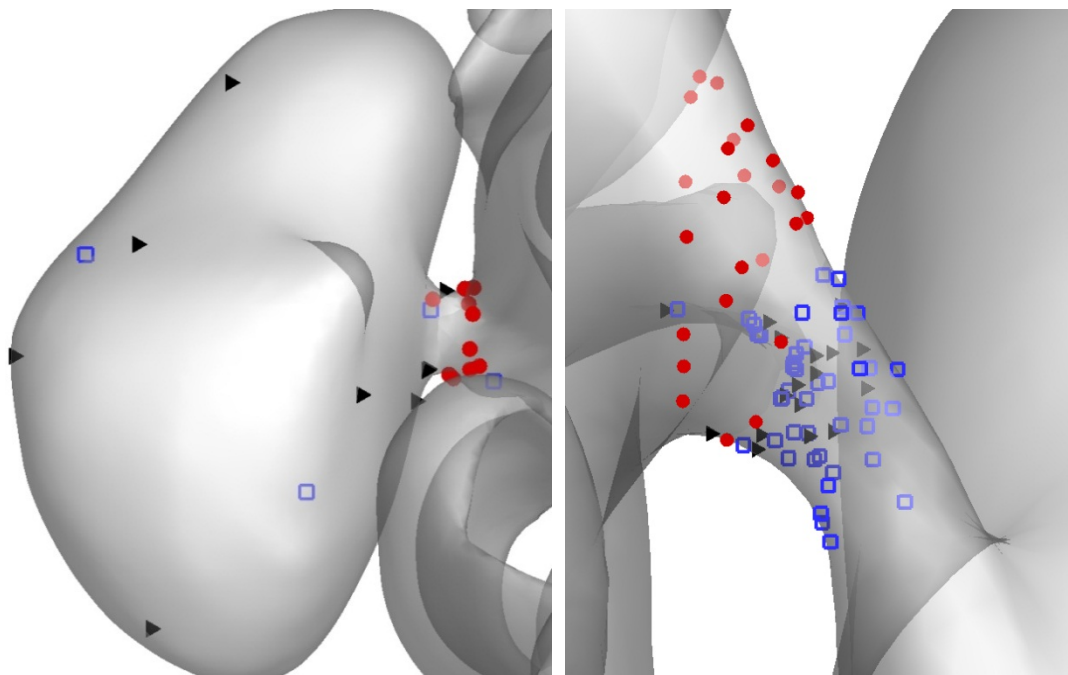
Figure 7. 12 is the visual representation of Figure 7. 11. Here we see that the slower flow rate allows increased potential for particle deposition. The comparisons between the two nasal cavity models, NCO2 and NC02-S show that the additional deposition caused by the difference in geometry (i.e. additional paranasal sinuses) occurs in the ethmoid and sphenoid sinus region, and negligible amounts deposit in the maxillary sinus. A possible reason for this particle transport phenomena can be referred back to the convective flow streamlines presented in Figure 7. 6, which showed clear directional stream paths reaching the ethmoid and sphenoid sinuses, albeit at low velocities. This would transport the particles to the superior regions of the nasal cavity and then allow for the diffusion process to occur – a phenomenon that allows for the physiological function of olfaction.

Deposition in the maxillary sinus is so low that the hypothesis that the diffusion process is dominant enough for particles to pass into the paranasal sinuses appears to only be supported if there is some convection involved (e.g. deposition sites in the sphenoid and ethmoid sinuses). In the maxillary sinuses the ostium protrudes at nearly right angles to the main flow field. To further investigate this we examine the maxillary ostium and locate the deposition of individual 1nm, 10nm and 40nm particles within the region as shown in Figure 7. 13. In the right maxillary sinus, inclusive of the ostium, a small percentage of particles <0.04% are deposited. At a flow rate of 4L/min there are no 1nm particles deposited due to its early deposition in the main nasal passage. For both models, 10nm and 40nm particles are found concentrated within the ostium. Thus it appears that despite a lower flow rate, there is a lack of particle deposition within the maxillary sinus.





(a) Right maxillary sinus 4L/min (b) Left maxillary sinus 4L/min



(c) Right maxillary sinus 10L/min (d) Left maxillary sinus 10L/min

Figure 7. 13 Frontal view showing the NP deposition in the maxillary ostium and sinus for the (a) right nasal cavity, and (b) the left nasal cavity at 10L/min. Different sized particles are coloured as follows: 1nm red circle; 10nm blue square; 40nm black triangle.

For a flow rate of 10L/min it can be seen that 1nm particles are captured within the narrow ostium and in fact don't make it through to the maxillary sinus. For the left

---

maxillary sinus, no particles were able to pass through the ostium, but a larger percentage of particles <0.5% deposited within the ostium alone. This is mainly due to the curved geometry and longer ostium length providing a narrow tube passageway for the particles to diffuse onto. These results support the report by Hood et al (2009), that ostium sinus ventilation is limited (unless the ostium is very large) and that the gas exchange of nitric oxide (NO) between the air in the maxillary sinus and the nasal air does not contribute greatly to the overall NO concentration.

---

# Chapter 8

## Nasal Drug Delivery with a Nasal Spray Device

### 8.1 Introduction

Nasal drug delivery has long been used for local treatment of the common cold and allergic rhinitis. The nasal route also provides a great opportunity when considering systemic treatment through the delivery of new drug formulations or molecules, such as nicotine to assist in smoking cessation, calcium for osteoporosis, or insulin for diabetes. Therefore, studies into local droplet deposition becomes of great significance in the delivery of drugs via the nasal airway. Various studies adopting human subjects or nasal cavity replicas have found relationships for droplet deposition efficiencies with nasal spray parameters, such as spray cone angle and the droplet size distribution (Cheng et al. 2001; Suman et al. 2002). However in-vivo and nasal cavity replica methods are limited in providing detailed results due to the intrusive, time consuming and expensive nature associated with experimental implementation. In recent studies the authors (Inthavong et al. 2006; Tian et al. 2008a) sprayed droplet deposition in the nasal cavity was performed based on the characteristics of the atomised drug particles released from a nasal spray. It was found that for a flow rate of 20 L/min, 10-20 $\mu$ m the deposition of particles was sensitive to initial injection velocity, insertion angle, and

---

spray cone angle as its size increased. Larger particles exhibiting high Stokes numbers caused it to be insensitive to these spray parameters. In the previous studies the nasal spray device within the nasal cavity was absent from the computational model, while the experimental data did not provide a range of particle sizes.

In this chapter, which is a step towards establishing more realistic drug delivery simulations, two computational models of a human nasal cavity model were reconstructed from CT-scans, where the difference between the two models was the presence of the nasal spray device to account for the airway blockage at one of the nostrils. Past studies of spray particle deposition have ignored the device within the nasal cavity. The airflow field was also induced from a negative pressure flow condition applied at the pharynx instead of constant flow rates between the left and right nasal cavities. The subsequent airflow patterns and its effects on particle deposition, with and without a spray device are firstly compared for two typical types of nasal spray nozzles (hollow spray cone and full spray cone). Following the flow field analysis, the atomisation of the liquid from a nasal spray device is visually presented to elucidate the external spray characteristics. Additional analysis using a PDIA was performed in order to get the Sauter mean particle size near the spray nozzle region. This data is important as it will provide confidence for setting up the initial particle conditions of the computational model.

## **8.2 Numerical Procedure**

### **8.2.1 Experimental Setup**

The experimental setup employed for this study is shown in Figure 8. 1 which includes a test chamber, a pressurised water supply system, a liquid collection system and a

---

visualization system. Water was stored in a pressure tank and was fitted with a pressure line at one end and a pressure regulator was used to monitor a constant pressure in the system. The maximum pressure was applied upstream and a pressure regulator was used to monitor a constant pressure in the system. A PDIA digital image analysis technique by Oxford Lasers® was used, which was capable of determining the properties of individual droplets such as its velocity, size, shape and concentration over a finite region of interest in the flow. For capturing of the spray, a double-pulsed Nd:YAG laser was used as the illumination source with pulse duration of 5 ns. Droplet images were acquired with a non-intensified 12-bit digital camera (PCO Sensicam) and a long distance microscope lens with a magnification of 2.46. This provided a 1280 × 1024 pixel array to capture a physical region of 3.85mm x 3.08mm. A long distance microscope lens provided a magnification of 2.46 offering a resolution of approximately 3.01 μm/pixel. The camera was mounted on a traversing unit which allowed precise movements in all three coordinates (+/- 17μm precision) to reposition the camera in order to capture the spray in full. A constant upstream pressure of 600kPa was applied and the water was released through a pressure regulator-valve and allowed to reach steady conditions before the images were taken. A single run was limited to approximately three minutes in order to avoid pressure variations associated with a decreasing liquid volume within the pressure tank. The spray nozzle used in the present study was a nasal spray device kindly provided by Saint-Gobain®/Calmar®, Product Number 43110-016.

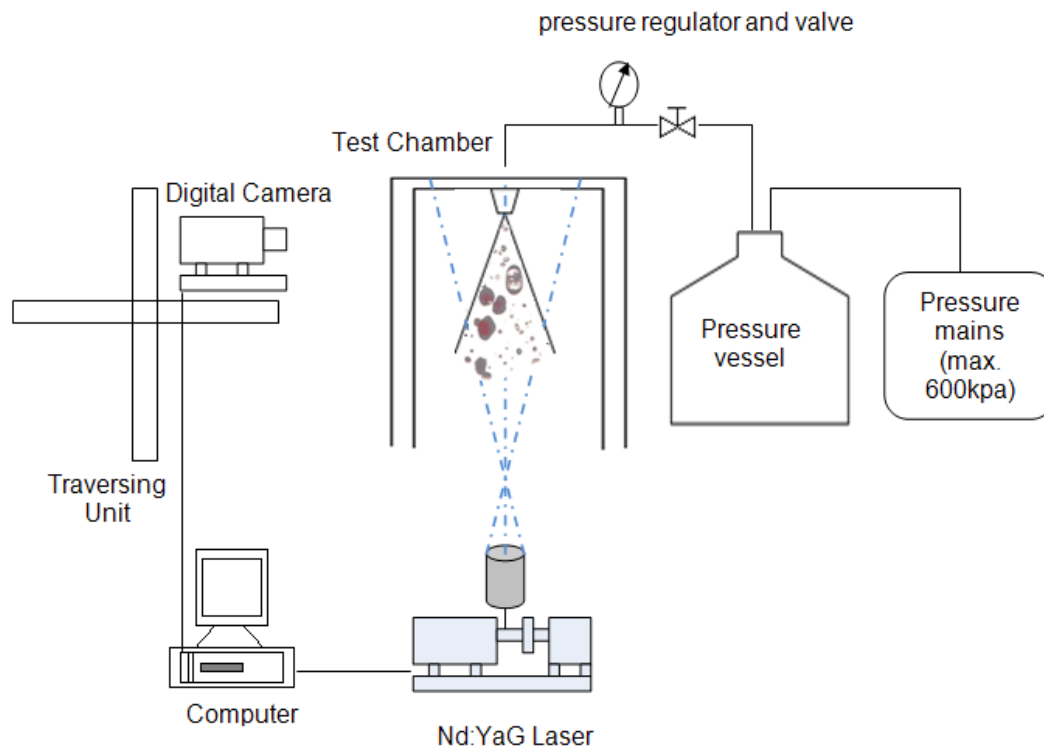


Figure 8. 1 Schematic of the experimental setup for spray particle measurements

## 8.2.2 PDIA and Particle Diameters

The principle of PDIA is to use an automated segmentation threshold algorithm for the quantitative analysis of droplet images (Lide 1994). This method is based on the original approach adopted by (Kiely and McNicholas 2000), using the degree of image focus determined from the edge intensity gradient of a droplet or droplet image to determine the distance of the droplet from the focal plane. The diameter and sphericity of a droplet is determined from an estimate of the pixel area of the droplet image with a correction for out-of-focus effects. Out-of-focus droplets typically appear up to 30% larger than they actually are. The PDIA technique uses two thresholds, one to measure the grey out-of-focus border area, and the other to measure the dark core area. From the ratio of these two areas, the true droplet size and its distance from the plane of best focus can be deduced. Additionally, the PDIA algorithm also corrects the bias introduced by droplets that touch the edges.

---

In the experiment, diameter measurements in PDIA are based on an area estimate of the shadow image of an individual droplet (straightforward for a perfect sphere). Four commonly used statistical mean diameters are: the number mean diameter,  $D_{10}$ ; the volume mean diameter,  $D_{30}$ ; the Sauter (or surface weighted) mean diameter,  $D_{32}$ , and the volume weighted mean diameter,  $D_{43}$ . The various diameters are defined using the equation:

$$D_{mn} = \left[ \frac{\sum d_i^{m-3} V_i}{\sum d_i^{n-3} V_i} \right]^{1/(m-n)} \quad 8.1$$

where  $V_i$  is the relative volume of droplets with diameter,  $d_i$ , and  $m$  and  $n$  are integer values that describe the mean being used. Thus the Sauter mean diameter,  $D_{32}$ , is defined by the equation:

$$D_{32} = \left[ \frac{\sum d_i^3}{\sum d_i^2} \right] \quad 8.2$$

The Sauter mean diameter was selected to represent the mean diameter of droplets within the flotation cell and is particularly relevant to hydrodynamics and mass transfer, since both drag and reaction rates are proportional to the droplet area.

### 8.2.3 Computational Boundary conditions

For this study, the computational model is displayed in the chapter III Figure 3. 12, which is the nasal cavity with the spray drive. Inhalation through the nasal cavity is induced through the pressure difference caused by the movement of the diaphragm compressing and decompressing the lung. Therefore the outlet of the nasal cavity (pharynx) was set as a negative pressure equivalent to 20 L/min relative to the

---

atmospheric pressure at the nostril inlets. This method presents a more realistic approach to nasal cavity modelling when compared with a prescribed inlet velocity set at the nostrils. Inducing the flow from the pharynx considers the geometrical factor of the nostrils, as well as the inner structure of the nasal cavity. The wall boundary condition for the particles was set to ‘trap’, so that all particle trajectories ceased once they touch a wall and the effects of accretion and erosion of particles at the walls are not considered. The sprayed particles adopted the properties of spherical water particles, as most drug formulations are diluted with water. Other assumptions include no particle rebounding off the walls/surfaces, no particle break-up or coagulation, and no particle deformation.

## **8.3 Results and Discussion**

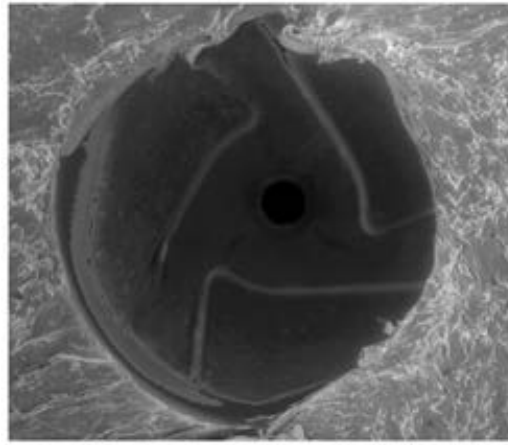
### **8.3.1 Sprayed Particle Characteristics**

Figure 8. 2a shows the internal spray nozzle, which was scanned from a microscope after cutting away the exterior. It reveals three tangential slots for the liquid to pass through with a small orifice at the vertex which is common in pressure-swirl type atomisers. Theory of pressure-swirl type atomisers suggests that the swirling liquid spreads out of the orifice under the action of both axial and radial forces, forming a tulip-shaped or conical sheet beneath the orifice (Lefebvre 1989; Liu 2000). From the images, it is uncertain whether the liquid exiting from the nozzle is a hollow/annular or full solid cone or is partially solid since the designs of pressure-swirl atomizers can be typically hollow coned or a solid cone (Yule et al. 2000). However, the use of tangential slots presumes that it is a hollow cone type. For a hollow-cone spray, the spray pattern varies depending on the injection pressure. At very low pressures, liquid dribbles from the nozzle orifice. With sufficient pressure a conical liquid sheet forms with radial and

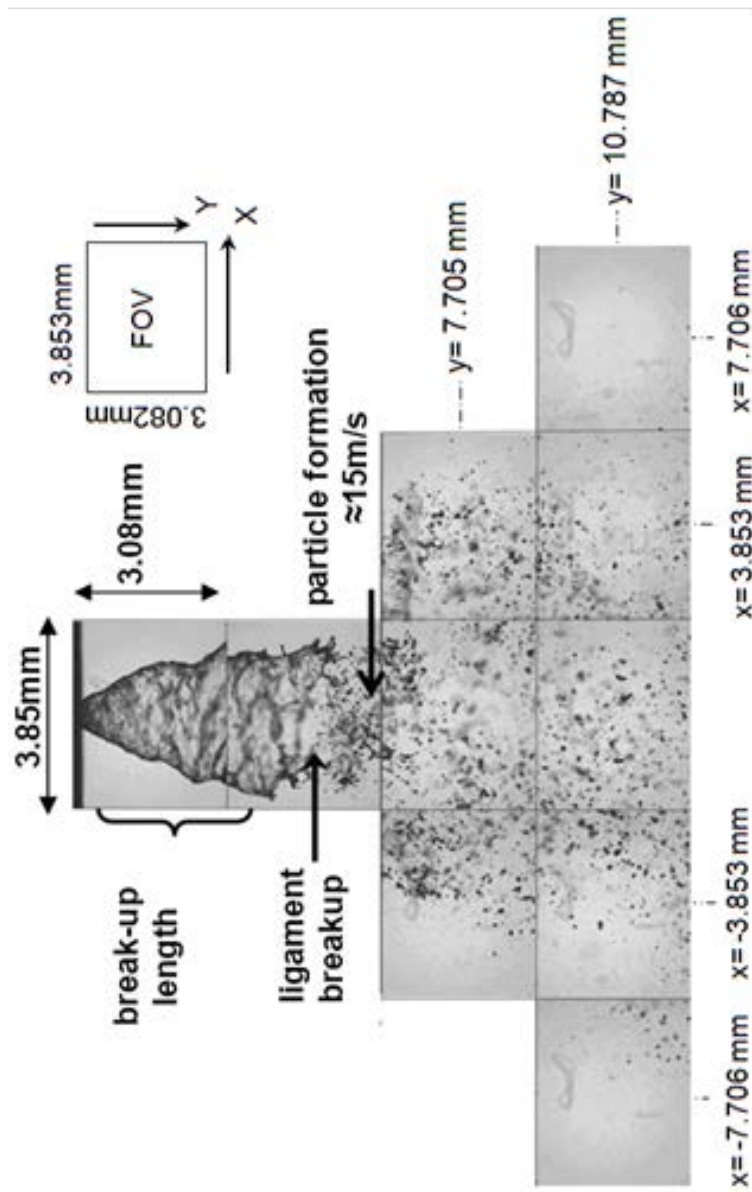


---

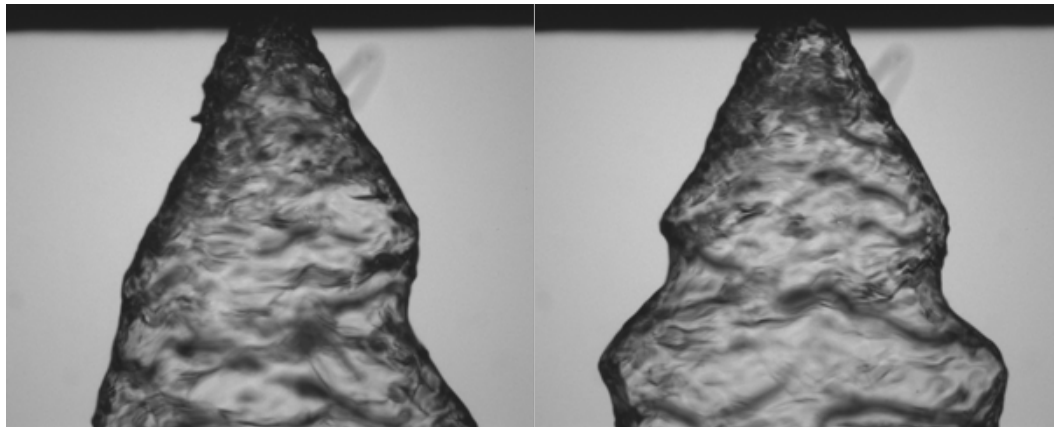
axial velocity. As the radial distance from the centerline to the sheet increases, the rotation decreases, as indicated by conservation of angular momentum. As the sheet extends, its thickness diminishes, due to instabilities on the liquid sheet, until it becomes unstable and breaks into ligaments and then droplets. The interaction between the air and the liquid is not well understood but it is generally accepted that an aerodynamic instability such as the Kelvin-Helmholtz instabilities on the liquid, causes the sheet to break up (Schmidt et al. 1999). Using a traversing system, the camera with a field of view of 3.082mm x 3.853mm is moved into ten different positions in order to capture the full range of the spray field (Figure 8. 2b) In the near nozzle region the nasal spray produces a continuous stream of liquid. Figure 8. 2b shows images of the near-nozzle region. In Figure 8. 2c the liquid appears to oscillate and roll downstream in waves. Further downstream, the liquid becomes critically unstable and breaks up into ligaments before further breakup into droplets. The two separate images show the destructive change on the liquid sheet as a consequence of the instability growth on the liquid surface. This initial stage of breakup is called the primary breakup of atomisation. The distance at which clearly formed particles are observed is called the breakup length, which occurs just after the ligament breakup region, (between the second and the third row (Figure 8. 2b). At this location, the particles are not necessarily located at a single point (i.e. at the nozzle/orifice point) but rather the particles are dispersed over a diameter. This is an important feature for the numerical setup since the particle initialisation in the computational model needs to be defined at the break-up length rather than as a point source at the nozzle exit. Additional parameters measured for this particular nasal spray, include nozzle diameter (~0.5mm), spray cone angle (~30°), initial particle velocity (~15m/s) and break-up length (~5mm).



(a)



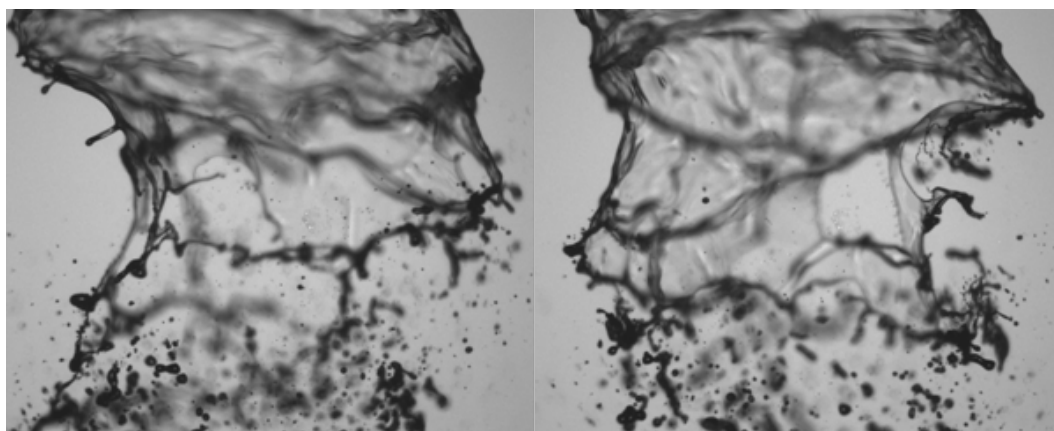
(b)



Near nozzle region, T1

T1 + 0.2s

Separate snapshots of the liquid spray in the near nozzle region



Ligament breakup region, T2

T2 + 0.2s

Separate snapshots of the liquid spray atomization in the ligament break region

(c)

Figure 8. 2 (a) Microscope scan of the internal spray atomiser nozzle.(b) Instantaneous images with field of view (FOV) of 3.853-mm x 3.082-mm of the external spray characteristics taken at ten locations and collated together (c) Two sets of images separated by in time showing the spray particle formation at the near-nozzle region and at the ligament breakup region

The Sauter mean diameter was also measured for the bottom two rows of images (Figure 8. 2b) that were captured by the camera (obviously the first two rows were not able to be analysed because the liquid had not yet been atomised). Eight mean diameters, three along the fourth row and five across the fifth row are shown in Figure 8. 3. Larger Sauter mean diameters are located centrally near the bulk spray flow region. In the centre panel at  $y=7.705\text{mm}$  the largest diameters measured in range of  $10\mu\text{m}$ ,

which was statistically significant (having at least 0.1% number count) at 291-301 $\mu\text{m}$ , while the smallest diameter was 11-21 $\mu\text{m}$ , having a number count of 49%. Further downstream the diameters continue to breakup into smaller particles. This stage of breakup is called the secondary atomisation breakup. In the outer periphery, smaller Sauter mean diameters are found. In the far left and right panels ( $x = \pm 7.706\text{mm}$ ,  $y = 10.787\text{mm}$ ) the largest diameter range having at least 0.1% number count was 131-141 $\mu\text{m}$  while the smallest diameter range of 11-21 $\mu\text{m}$  had a number count of 77.86 $\mu\text{m}$ .

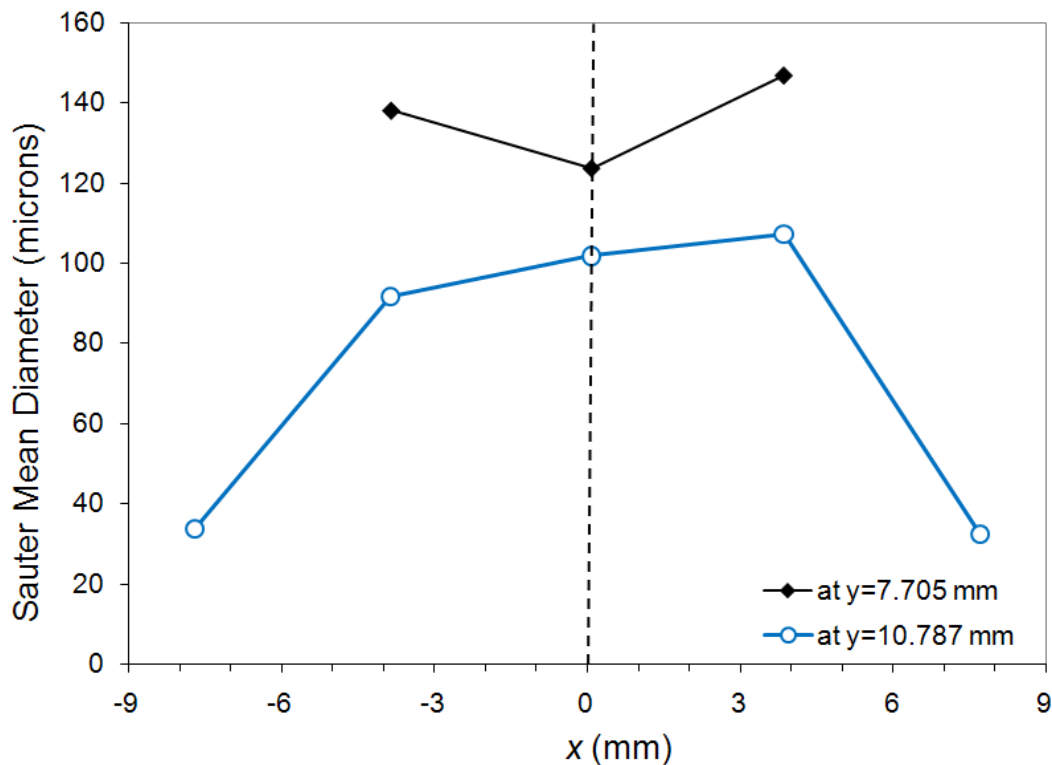


Figure 8. 3 Sauter mean diameter  $D_{32}$ , taken for each FOV section or the fourth ( $y = 7.705\text{mm}$ ) and fifth rows ( $y = 10.787\text{mm}$ ) as depicted in Figure 8. 7b.

These measurements provide confidence in setting a realistic range of values initialising the particle boundary condition in the computational modelling. In addition, a more effective parametrical study can be performed in order to provide better guidance in the design and development stages of nasal sprays for improving nasal drug

---

delivery. The spray device was included in the model by placing it into the left nasal chamber at an insertion angle of  $10^\circ$  to the vertical axis. The dispersion of the particles is represented by the spray cone angle, which was set at an angle of  $30^\circ$ , and the swirl fraction was 0.5, which is only applicable for a hollow spray cone type. Initial tests of particles with the nominal mean diameters suggested by the experimental data (e.g.  $> 80\mu\text{m}$ ) found that all the particles deposited immediately in the anterior nasal cavity region. Sprayed particles were introduced into the nasal cavity from a breakup length,  $L_{bu}$  of 4mm. The spray cone diameter at the breakup length,  $d_{bul}$  was 3mm, while the initial particle velocity was 15m/s, which were both determined from the PDIA measurements (Figure 8. 2).

### **8.3.2 Computational Model Validation**

Validation of the computational model may be checked through comparisons of the reported pressure drop across the nasal cavity under different flow rates. In this study the flow field is induced by the negative pressure boundary condition set at the nasopharynx, caused by the dilation of the lungs during inhalation. Therefore the pressure drop becomes the dependent variable and a series of pressure values at the nasopharynx exit were simulated. Figure 8. 4 shows the mass flow rates obtained from the average pressure drop between the nostril and nasopharynx ranging from 5Pa to 60 Pa (Figure 8. 4). At these pressure drops, the corresponding range of Reynolds numbers at the inlets is 981 to 3951. The numerical results show good agreement with reported experimental data, especially at flow rates of 20L/min or less where the flow is laminar.

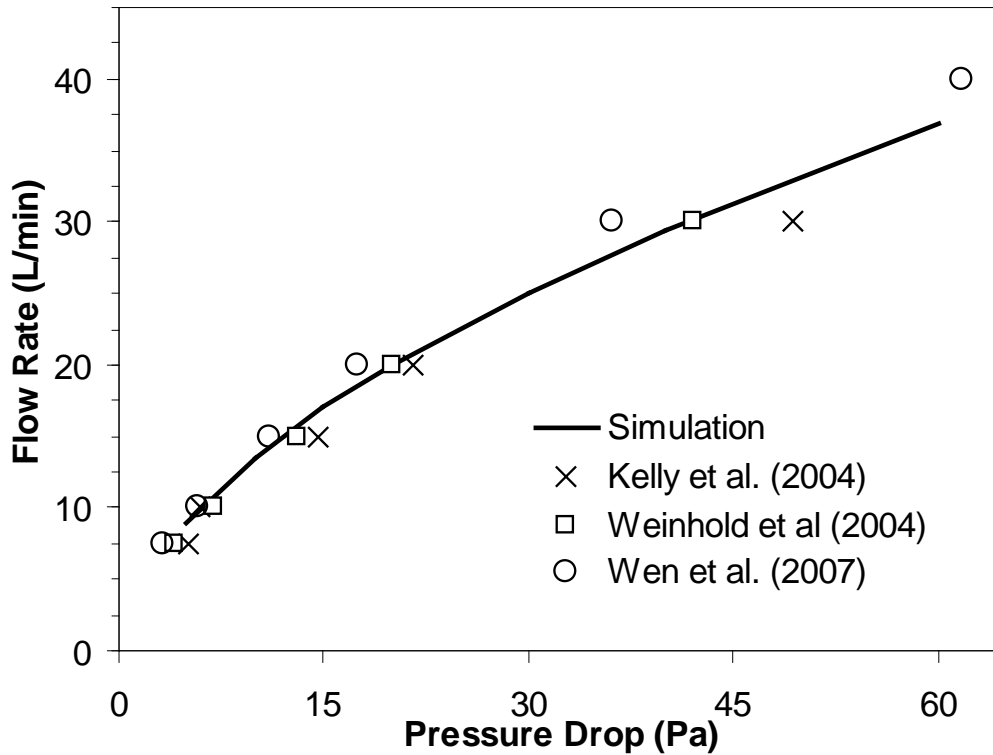


Figure 8. 4 Flow rate through the nasal cavity as a function of a pressure drop between the nostril and the nasopharynx

Particle deposition efficiencies have been reported in the literature for particles released into the nasal cavity (Cheng et al. 2001; Kelly et al. 2004b; Shi et al. 2006). The deposition of particles as a function of the inertial parameter ( $d_a^2 Q$ ) is shown in Figure 8. 5, which displays the characteristic curve associated with inertial deposition. Differences in deposition may be attributed to the inter- subject variability between the nasal cavity models obtained by (Kelly et al. 2004b) (53 year-old Caucasian male) with the model used in the present study (25 year-old Asian male) while (Häußermann et al. 2001) also states that nasal cavity replicate casts with wider airways can cause less deposition due to secondary flow. The DRW model significantly overestimates particle deposition for an inertial parameter (IP) < 10,000. The modification to the model by dampening the turbulent kinetic energy allows the normal fluctuating velocity to be

reduced, bringing it closer to the correct value. The effect on particle deposition is a better agreement to the reported data for  $IP < 10,000$ .

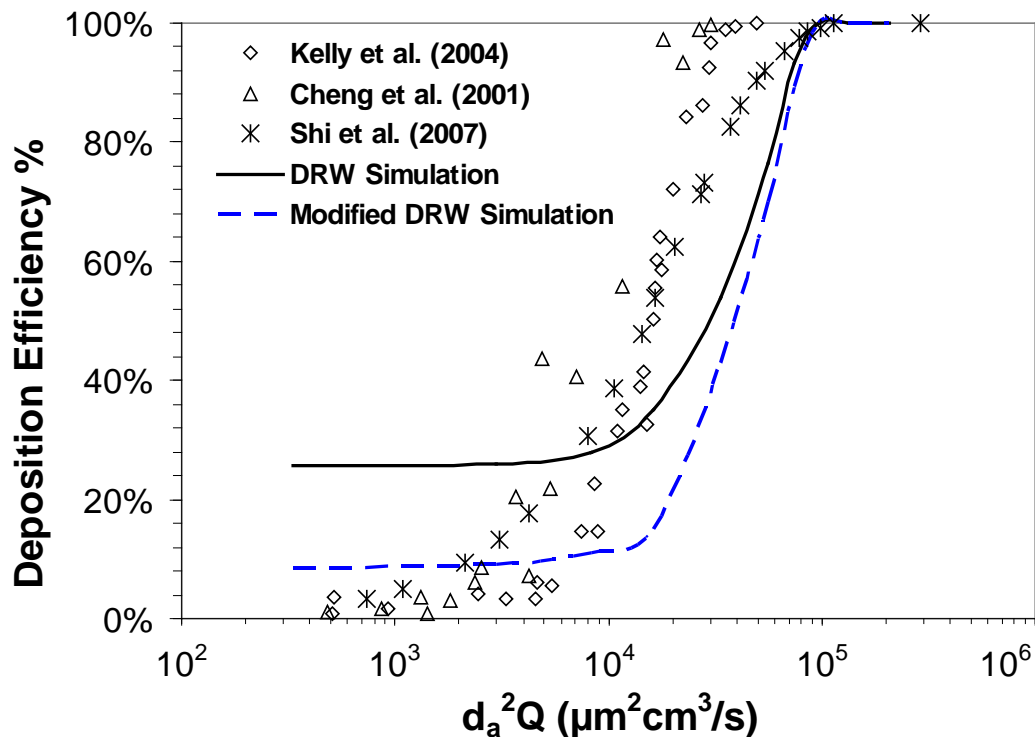


Figure 8. 5 Inertial deposition efficiency for micron particles in the left cavity side of a human nasal cavity compared with reported data.

### 8.3.3 Airflow Field

The total flow and its distribution between the left and right nasal chamber as a result of the airway geometry resistance with and without the nasal spray device are plotted in Figure 8. 6. In both cases the right nasal chamber shows a greater proportion of flow distribution. Further calculations show that the volume of the left cavity is smaller by about 13% than the right cavity, which explains the biased distribution between the left and right airway, which is 44%–56% without the nasal spray and 32–68% with the presence of the nasal spray.

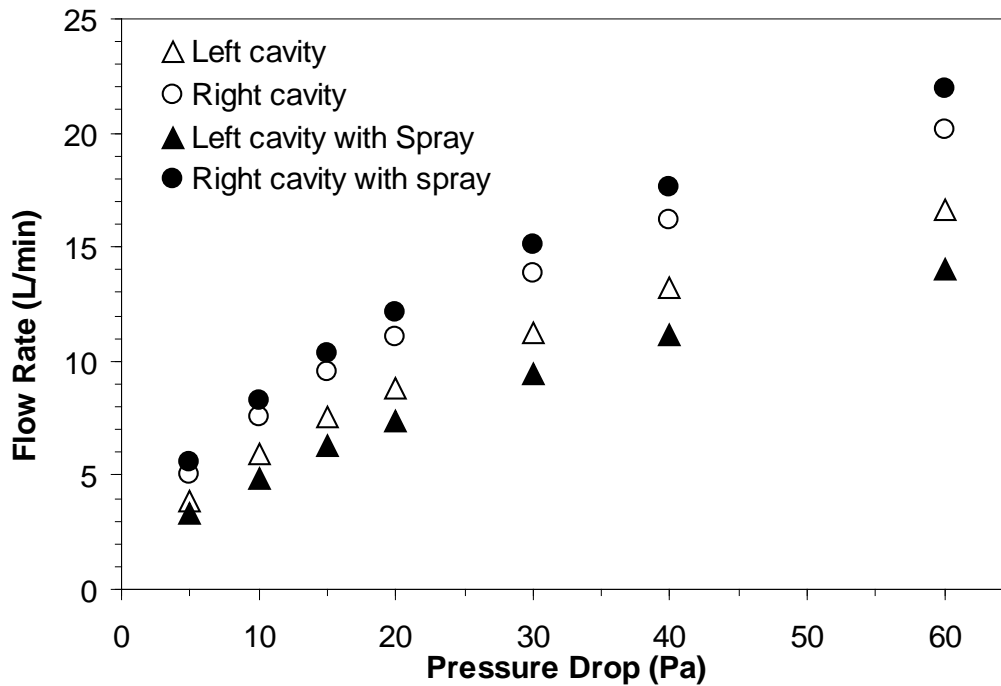


Figure 8. 6 Flow rate distribution between the left and right nasal chamber. Comparison is also made with the presence of the nasal spray device. White symbols –model without the spray device; Black symbols –model inclusive of the spray device; Triangles – left cavity; Circle – right cavity.

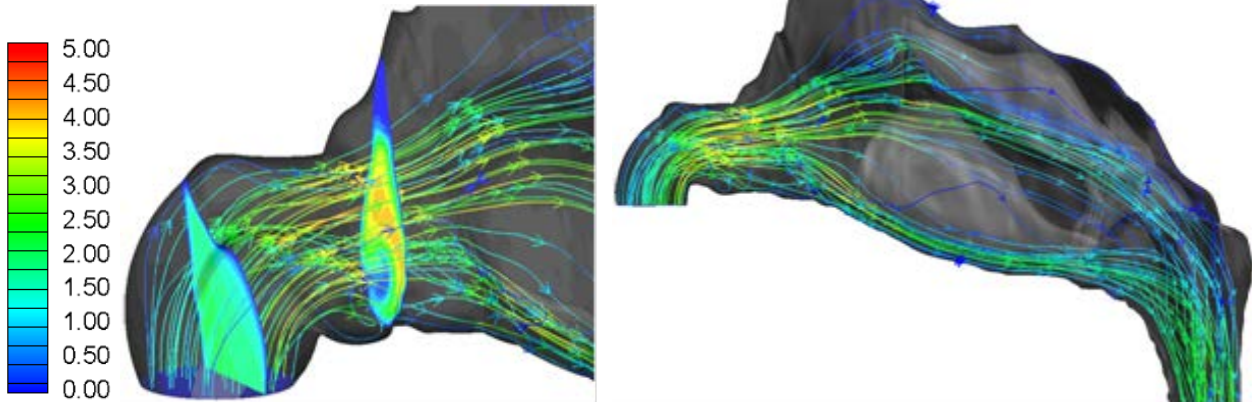
Path streamlines that track the fluid motion from the nostril inlet are shown in Figure 8. 7 (a) for a plain nasal cavity model and (b) a nasal cavity including the spray device. For the plain nasal model, the flow streamlines are generally undisturbed as it flows from the nostril inlet into the nasal valve. The main feature of the flow appears in the nasal valve region where the flow accelerates through the narrowest cross-section of the airway. This region of flow also exhibits some vortical flow proximal to the airway floor as the flow changes direction from a vertical flow to a horizontal flow due to the 90°-like bend at the nostril. This flow feature is similar to the flow characteristics found in a forward-facing step configuration. The bulk flow passes mainly through the middle of the cross-section and then partitions into the upper, middle, and lower flow. The presence of the spray device taking up space in the nasal vestibule shows an increase in disturbance within the flow. The effective area of the nostril to the open air is reduced



and within the narrow air spaces, the flow is accelerated through. At the top of the spray, the streamlines separate and begin to swirl through the nasal valve region.

velocity

[m/s]



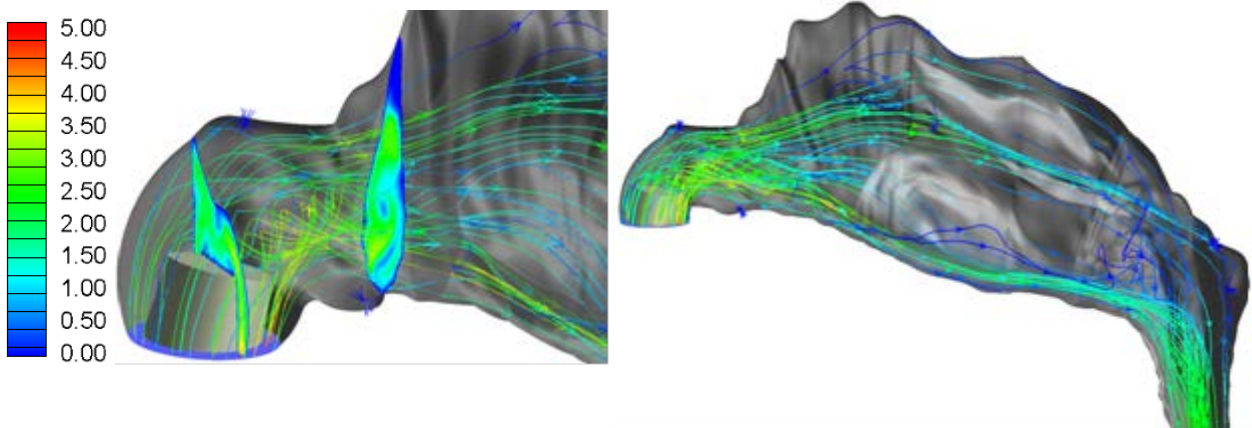
Magnified view of internal nostril region

Path streamlines throughout the left nasal chamber

**(a) Plain nasal cavity model**

velocity

[m/s]



Magnified view of internal nostril region

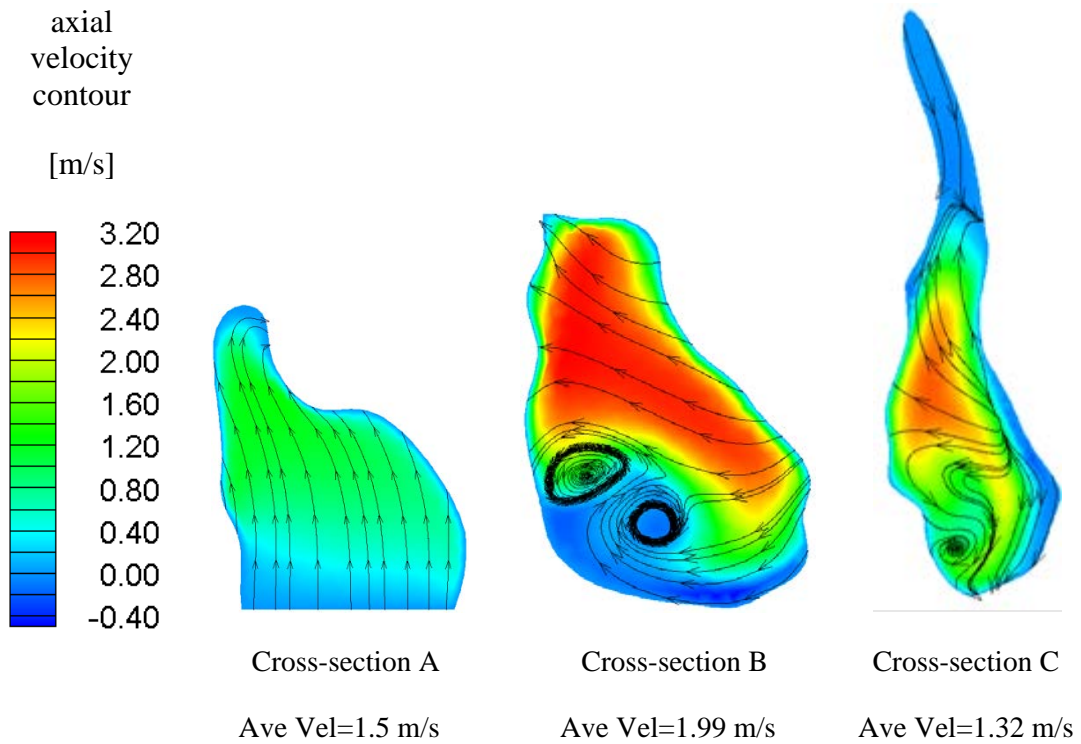
Path streamlines throughout the left nasal chamber

**(b) Nasal cavity model with spray device**

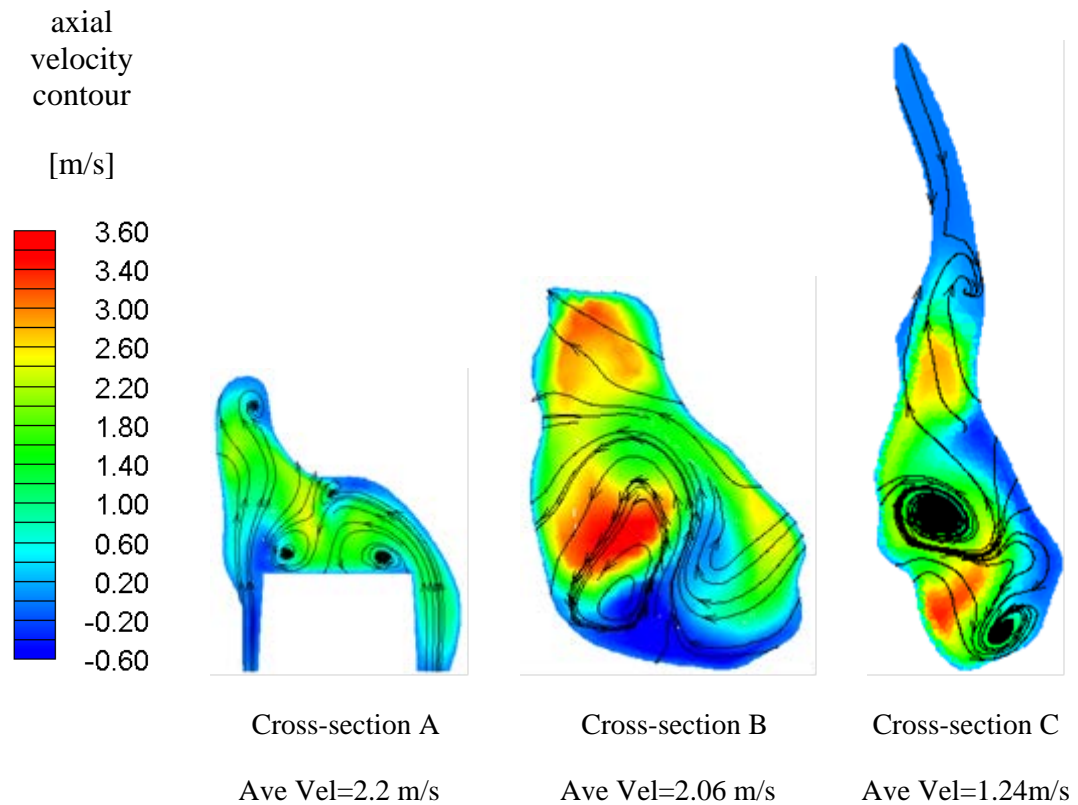
*Figure 8. 7 Path streamlines in the anterior region of the nasal cavity affected by the presence of the nasal spray device.*

---

Contours of velocity magnitude with streamwise and crossflow velocities superimposed were applied to cross-sectional slices (Figure 8. 8) taken at the three locations ( $x=0.6\text{cm}$ ,  $1.6\text{cm}$  and  $2.5\text{cm}$  from the nose tip) as depicted in Figure 3. 12. The presence of the spray device causes high velocities in the confined space of the nostril periphery as shown in the path streamlines. The vertical streamlines reflect the inhalation being induced through the nostrils and travelling vertically. At the spray head, the flow field experiences flow separation and two recirculating vortices are found at the edge of the spray device. Particles are produced at a breakup distance from the nozzle head and therefore would experience the downstream effects of the disturbed flow. At the cross-section B,  $x=1.6\text{cm}$ , vortices are present in the lower corners due to the elevation of the geometry. The streamlines show the flow still rising vertically. At cross-section C,  $x=2.5\text{cm}$ , the flow patterns are quite different for the two models which suggests that the influence of the spray nozzle inside the nasal cavity is prevalent up to  $x=2.5\text{cm}$ .



**(a) Plain nasal cavity model**



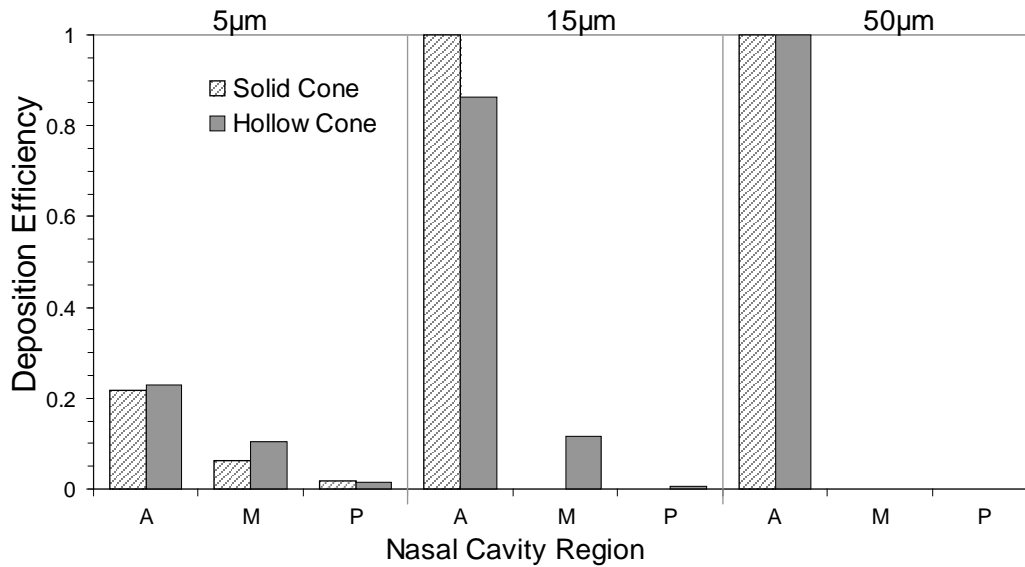
**(b) Nasal cavity model with spray device**

*Figure 8. 8 Crossflow streamlines superimposed onto contours of velocity magnitudes at different coronal cross-sections as defined in Figure 3. 12.*

---

### 8.3.4 Particle Deposition

Sprayed particle depositions in each region (A – Anterior region; M – Middle region; and P – Posterior region) from the two spray types (solid and hollow cones) are shown in Figure 8.9. In general there are small differences between the hollow and solid spray cones. For 5 $\mu$ m particles, hollow spray cones provide greater deposition, which may be due to the radial distribution of the particles caused by the swirling component. As the particle size increases so does the particle inertia. For 15 $\mu$ m particles, the atomised hollow spray achieves 12% deposition in the middle region of the nasal cavity, whereas a solid sprayed cone achieves 100% deposition in the anterior region, and therefore 0% in the middle region. The radial velocity component of the hollow spray cone allows a horizontal component in directing the initial particle trajectory. This helps direct the particles towards the nasal valve region, leading to increased particle flow through to the middle nasal cavity. For 50 $\mu$ m particles, which exhibit the highest inertial properties of the three particles presented, maximum deposition occurs in the anterior regions and no particles reach the middle region. Overall for the solid cone spray, 5 $\mu$ m particles exhibited greatest deposition in the middle region, while for the hollow cone, both the 5 $\mu$ m and 15 $\mu$ m particles deposited in the middle regions. It should also be noted that a large number of 5 $\mu$ m particles escaped through the nasopharynx. This will lead to deposition later downstream in the respiratory tract, and may even deposit deep in the lungs, which may have an adverse health response.



(a)

(b)

(c)

Figure 8.9 Sprayed particle deposition from a hollow and a solid spray cone. The x-axis labels, A, M, P represent Anterior, Middle, and Posterior regions respectively.

The deposition pattern along with the initial particle trajectories for 5µm and 15 µm particles is shown in Figure 8.10 and Figure 8.11 respectively. In addition, the particle velocity as it impacts onto the surface walls was recorded and an average value was taken. Note that this average particle impaction velocity, ( $V_{pi}$ ), is not the same as the deposition velocity,  $V^+ = \frac{U_{ave}A}{u^* P \Delta x} \log(N_{in} / N_{out})$  (Kallio and Reeks 1989) used to characterize the rate of deposition, but rather a way to determine the influence of the initial particle conditions imparted as the particles are introduced into the airflow stream during atomisation.

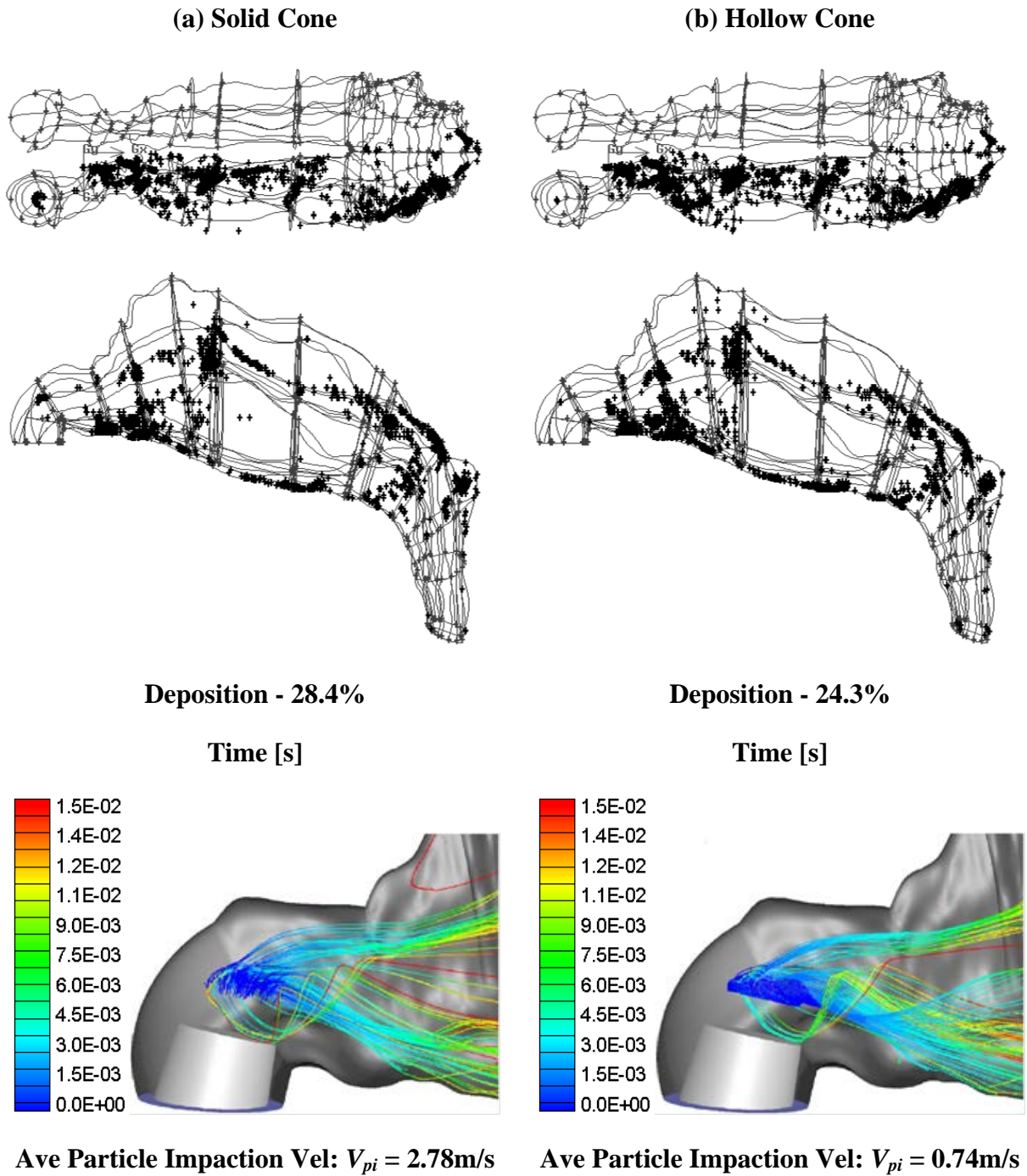
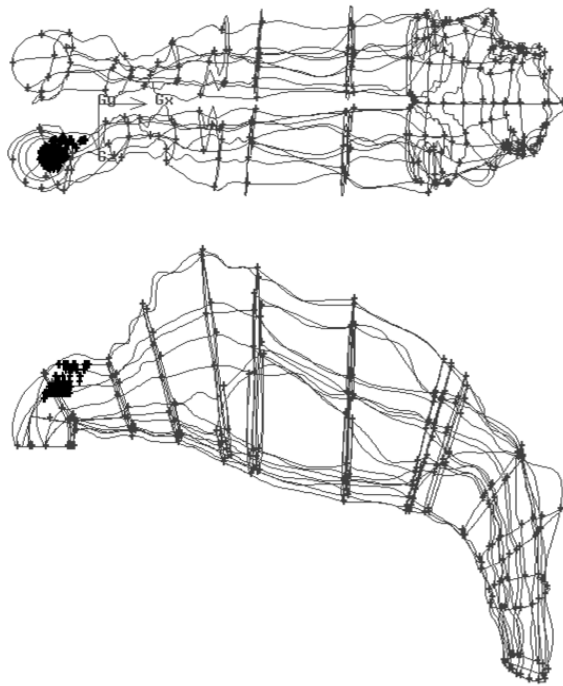


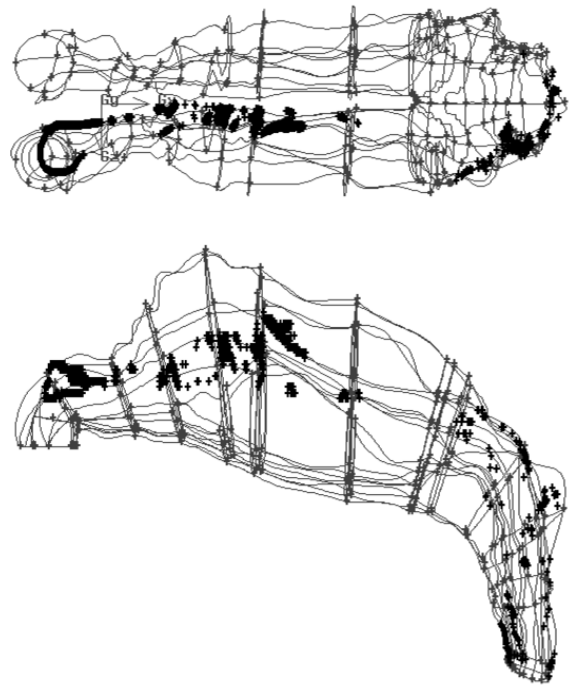
Figure 8. 10 Deposition patter of  $5\mu\text{m}$  in the nasal cavity for a solid and hollow spray cone. The particle trajectories are coloured by residence time.

(a) Solid Cone



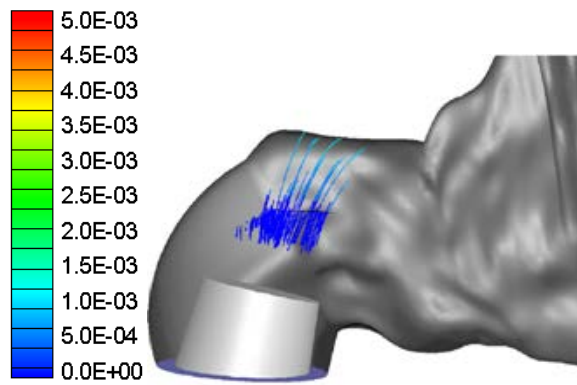
Deposition - 96.1%

(b) Hollow Cone

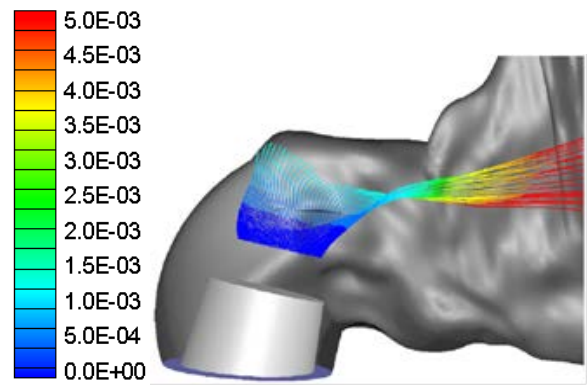


Deposition - 85.5%

Time [s]



Time [s]



Ave Particle Impaction Vel:  $V_{pi} = 9.61$  m/s

Ave Particle Impaction Vel:  $V_{pi} = 6.80$  m/s

Figure 8. 11 Deposition of  $15\mu\text{m}$  in the nasal cavity. The particle trajectories are coloured by residence time.

---

The deposition patterns for the 5 $\mu$ m particle for the two spray types are similar and this is evident in the particle trajectories which show similar flow paths. The small differences between the two sprays include a greater number of particles immediately above the spray nozzle, and the higher  $V_{pi}$  for the solid spray cone. This  $V_{pi}$  value suggests that the solid spray cone has a larger proportion of particles impacting immediately above the spray nozzle, since the initial particle velocity of an atomized spray is 15 m/s. The lower  $V_{pi}$  suggests that more particles have become entrained in the airflow. The particle trajectories are coloured by particle residence time, which helps explain the looping motion of the particle near the spray nozzle. Some particles which are directed away from the main nasal passage lose enough of their initial velocity to re-orient their direction and get close to the spray nozzle.

15 $\mu$ m particles exhibit an increase in inertial properties from a 5 $\mu$ m particle, and this highlights the effect of the initial particle conditions further. The deposition patterns for the two spray types above the spray nozzle show the formation of the spray type. While this simulation does not account for particle splattering onto the surface and eventual and smearing along the nasal walls, it demonstrates the influence of the initial particle conditions (such as the swirl component and the insertion angle) on higher inertial particles. The hollow spray cone allows a small proportion of particles to squeeze through the nasal valve region. It is then inferred that these particles are entrained in the flow before depositing downstream when the particle can no longer follow the flow streamline. The  $V_{pi}$  for the solid cone shows that on average the initial particle velocity has decreased from 15m/s to 9.61m/s over the small distance from particle injection to the upper walls. Improvements to the spray atomizer during its design stage may involve atomizing the particles at a slower velocity, and to achieve a much finer particle size distribution. For the user, it may be instructed that aligning the spray device more

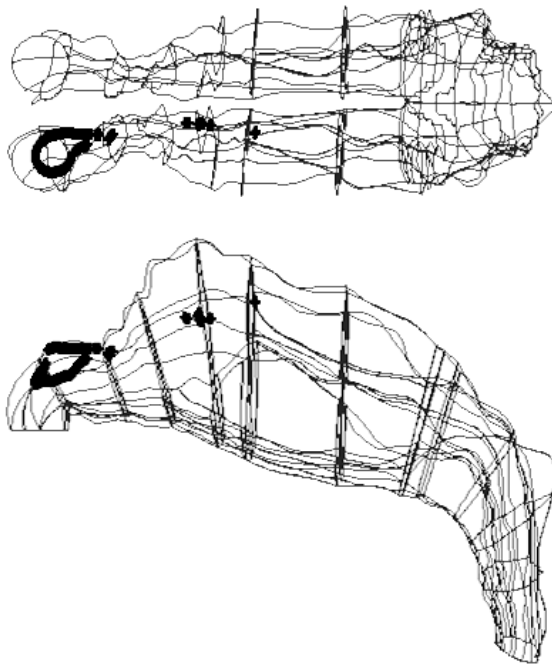


---

horizontally to the main nasal passage could enhance deposition downstream from the anterior region. This may involve tilting of the head backwards to allow better alignment.

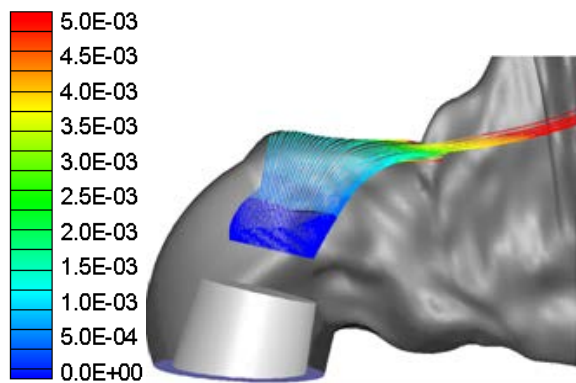
Further parametrical studies were investigated by determining the effects of the swirl fraction (Figure 8. 12) and the spray cone angle (Figure 8. 13). The swirl fraction controls the amount of radial velocity component, and therefore mimics the design of the slots within the swirl atomiser. A higher swirl fraction will lead to a greater radial component and increasing the time taken to travel in the axial distance. This helps to reduce the particle inertia and can provide much longer residence times for the particle. This is evident in the particle trajectories which show very high levels of radial motion, leading to a reduction in the deposition efficiency, mainly within the anterior nasal cavity. More particles are then distributed further downstream, with an increase in deposition in the middle and posterior regions. The average  $V_{pi}$  is also reduced, indicating that more particles have become entrained with the flow field. Similarly, the spray cone angle can provide a wider dispersion, but this time the radial velocity component is fixed. The wider spray angle allows more particles to be closer aligned to the horizontal axis, in which the main nasal passage lies. This effect is important since the insertion of the spray device into the nasal cavity is naturally vertical or close to it. The effect on the deposition efficiency for 15 $\mu$ m particles is not very significant. For larger particles the influence of the spray cone angle to re-alignment of the particles in the airway will be more significant since the higher particle momentum will force the particle through without any external influences from the flow field. Conversely, for smaller particles the spray cone angle is less significant.

(a) Swirl fraction 0.1



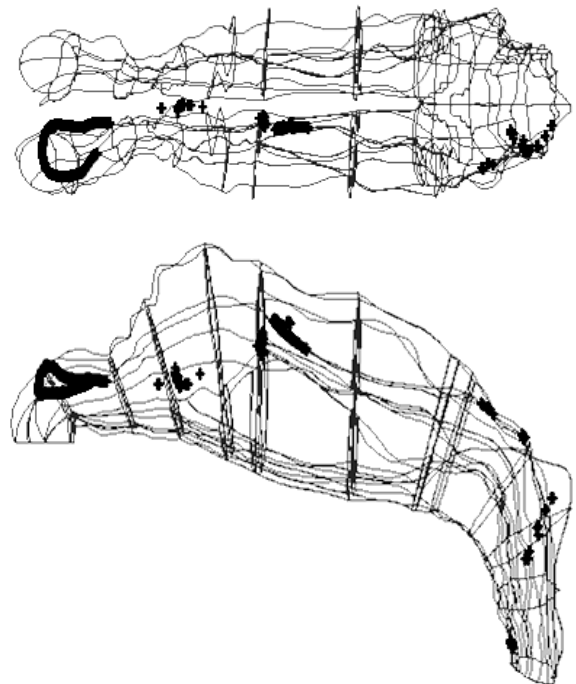
Deposition - 91.0%

Time [s]



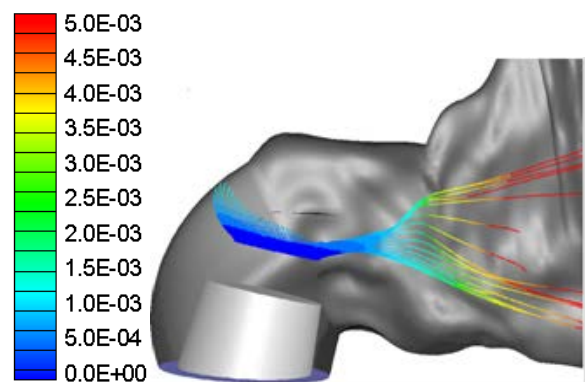
Ave Particle Impaction Vel:  $V_{pi} = 8.05\text{m/s}$

(b) Swirl Fraction 0.8



Deposition - 80.3%

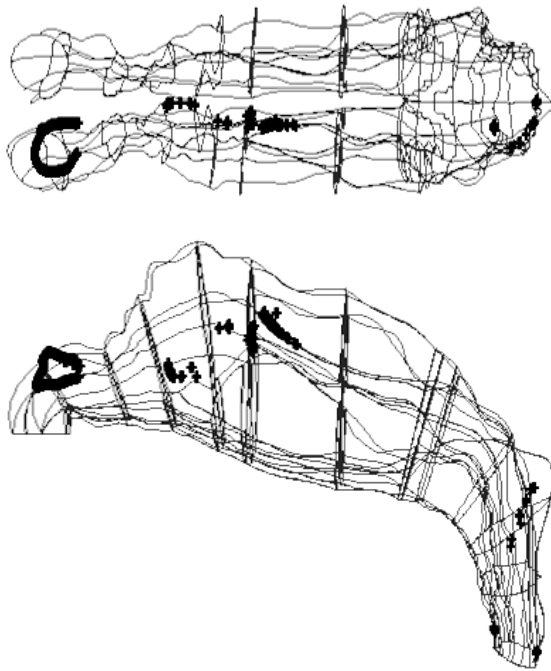
Time [s]



Ave Particle Impaction Vel:  $V_{pi} = 5.73\text{ m/s}$

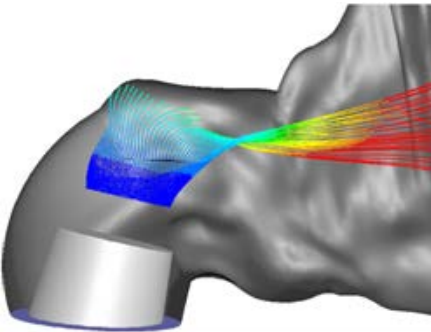
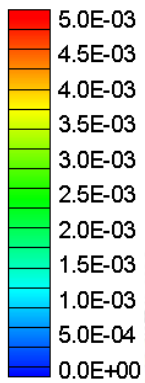
Figure 8. 12 Effect of the swirl fraction on the deposition of  $15\mu\text{m}$  in the nasal cavity with a hollow cone spray with a cone angle of  $30^\circ$ . The particle trajectories are coloured by residence time

(a) Spray Cone Angle 15°



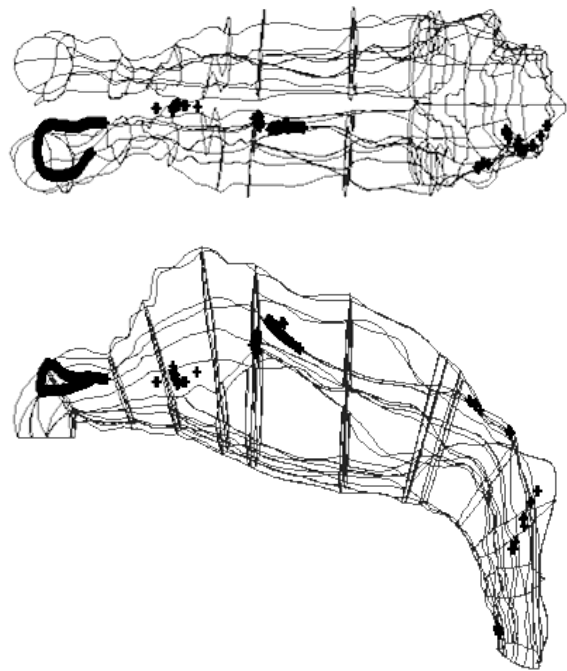
Deposition - 84.8%

Time [s]



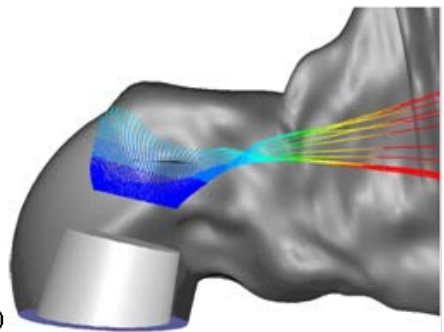
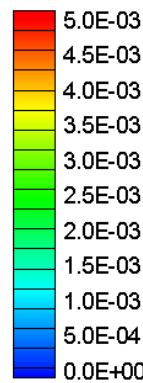
Ave Particle Impaction Vel:  $V_{pi} = 7.12$  m/s

(b) Spray Cone Angle 50°



Deposition - 74.1%

Time [s]



Ave Particle Impaction Vel:  $V_{pi} = 6.79$  m/s

Figure 8. 13 Effect of the swirl fraction on the deposition of 15 $\mu$ m in the nasal cavity with a hollow cone spray with a swirl fraction of 0.5. The particle trajectories are coloured by residence time

---

## 8.4 Discussion

Two computational models of nasal cavity were created and analysed, where the difference between the two models was the presence of a nasal spray device inserted into the left nasal chamber. Firstly, the airflow distribution and patterns between the two models was compared. It was found that the presence of the nasal spray device creates additional resistance, obstructing the inhaled air, and reducing the flow rate. While the percentage breakdown is similar throughout the pressure drop range, the flow rate distribution is most similar when the pressure drop is low but the difference (due to the geometry) is magnified as the pressure drop increases. During the respiration cycle, the airflow through the nasal passage is normally asymmetrical, where one nasal passage achieves greater airflow. This asymmetry is referred to as the nasal cycle, which is a result of congestion (swelling) of the erectile tissue (cavernous tissues of the mucosa) in one nasal cavity while at the same time decongestion (shrinking) occurs to the erectile tissue in the other cavity. The airflow through each nasal cavity is then governed by the resistance caused by the cross-sectional area of each airway. Streamlines of secondary flows found that vortices are present in regions of low velocity magnitudes (blue contours), and in regions where the geometry expands, such as the nasal valve and the spray head regions.

Experimental images were then obtained to establish a better understanding of the nasal spray device characteristics. It was deduced that the internal spray atomiser was that of a pressure-swirl type, which is distinguished by the ability to produce greater spray cone angles. This can range from  $30^\circ$  to  $180^\circ$ , depending on the relative magnitude of the radial and axial velocity components at the nozzle exit, which can be controlled by adjusting these variables (Liu 2000). The droplet size produced was considerably high

---

having  $D_{32}$  in the order of  $100\mu\text{m}$  in the centre plane of the spray while at the periphery  $D_{32}$  was approximately  $30\mu\text{m}$ . The particle size produced is a function of liquid pressure and swirl chamber dimensions where the smaller the swirl chamber is, the finer the resultant droplets can become, but a greater back pressure is needed to force the liquid through the atomiser. The decisions undertaken during the design of the spray atomiser are therefore critical to achieve high efficacy for targeted drug delivery, since the initial conditions of the atomised particles play an important role as boundary conditions for the particle trajectory.

It is well recognized that one of the functions of the nose is to filter out foreign particulates during inhalation, which is mainly thought to be attributed to cilia (nasal hairs) movement within the nose. The filtering curvature in the frontal sections along with the constricting nasal valve region is most significant for therapeutic drug delivery as it prohibits larger particles to penetrate into the middle cavity region for deposition onto the highly vascularised mucosal walls. The initial particle conditions from the experimental data showed that the atomised particles are large in size, leading to early deposition in the anterior nasal cavity. The particles that are introduced into the airway therefore need to have their inertia stripped away. The swirling fraction, which represents the radial component from the swirl atomizer, presents the most effective method to reduce the axial velocity. In addition to this spray parameter are other parameters that have an effect on the deposition. This includes, the spray cone angle, insertion angle, particle size distribution, initial particle velocity and the location of injection, where these variables need to be integrated together to obtain a better prediction of deposition efficiency.

---

Finally, some limitations and improvements of this study need to be noted. In this study one-way coupling is used, which assumes that the flow of particles does not affect the fluid flow. This assumption is valid where the volume fraction of the particles is relatively low (<10%). This occurs downstream as the particles disperse through the nasal cavity. However, near the spray nozzle region (i.e. dense spray region), where the particles are atomising, the volume fraction is much higher. The flow field in this region is therefore expected to be under predicted in the direction that the spray is aligned ( $10^\circ$  from the vertical). From the spray images, the two-way coupling influence for momentum exchange is limited to approximately 6 mm from the spray nozzle. Turbulence modulation is therefore also not included, which requires an additional loop in the numerical iteration within the current methodology. This is left for a future study which will incorporate an unsteady breathing profile. Other assumptions include no particle break-up or coagulation, no particle deformation, and evaporation.

---

# Chapter 9

## Conclusion & Recommendation

This thesis has presented isolated nasal cavity models; a nasal cavity model with paranasal sinuses included; a human body model with detailed facial features and an integrated model, which includes a human body, facial features and internal airways. These were obtained through CT scans of the human respiratory airway of two healthy and non-smoking Asian male volunteers. They became the basis of fluid dynamics analysis in order to investigate the inhalation of micron and submicron particles for toxicological and therapeutic cases. In this chapter, major findings, problems solved and research methods that were developed will be summarised.

### **9.1 Toxic Particles around the Human Body**

#### **9.1.1 Transportation of Toxic Particles**

The computational model used in this study combined detailed facial features with a simplified human body to better understand the effects of ambient human body heat on particle transport and inhalation by a human manikin in an indoor environment. . Computations were conducted under both facing-the-wind and back-to-the-wind

---

conditions, as well as isothermal and thermal conditions, respectively. Satisfactory agreement was obtained between the numerical results and the experimental data available in the literature. First of all, body heat causes a significant rising airflow velocity in the downstream side of the manikin. This rising velocity plays an important role in transporting particles from the lower level into the breathing zone. Secondly, the occupant-wind orientation plays another important role in particle inhalation. When the occupant is facing the wind, the critical area is located at the nose level, while it is located at a lower level when the occupant has his back to the wind. Finally, the importance of body heat on particle transport and inhalation decreases with increasing free stream speed. Therefore, the effect of body heat has to be taken into account when the indoor wind speed is low.

### **9.1.2 Inhalation of Toxic Particles**

The integrated CFD model simulation was performed to better understand the air and particle flow patterns in human exposure to indoor air pollutants. A realistic upper respiratory airway model based on CT-scans was created and integrated into a human body. During inhalation, the flow patterns near the face show vertically aligned flow streams which transport the particles towards either the nose during nasal inhalation or mouth during oral inhalation. The influence of the ambient air flow rate on the flow patterns is the increased acceleration of flow that begins as the air flow diverges at the torso. Flow separation occurs at the rear of the human head and there is a shift in the recirculation region, and different wake effects are found. This indicates that if the ambient air flow was coming from behind the body, particles forming a contaminant source in front of the body may be disturbed and induced into the breathing region. Trajectories of the inhaled particles found that the source of large inhaled particles



---

(e.g. 40 $\mu\text{m}$  and 80 $\mu\text{m}$ ) that are originating from upstream must be above the nose as gravitational settling is significant for these particles. For the smaller particles, (1 $\mu\text{m}$ -20 $\mu\text{m}$ ) particles tend to follow the flow streamlines and their original upstream location must be below the nostrils. The critical area shapes were determined by reverse tracking the particles to their origins and colour coding their positions in order to determine if a pattern could be deduced for predictions of local respiratory region deposition. It was found that only the 15 $\mu\text{m}$  particle size produced a discernible pattern. This studied improved the understanding of particle inhalability and enhanced state of the art CFD modeling towards a holistic simulation for exposure of airborne particles.

## **9.2 Inhalation of Toxic and Sprayed Particles in the Isolated Nasal Model**

### **9.2.1 Nasal Cavity with Paranasal Sinus**

A nasal model with paranasal sinus was created in order to determine if any nanoparticles would deposit within the paranasal sinuses given that these particles are transported through the nasal cavity mainly by diffusion. Under a flow rate of 10L/min it was shown that 1nm particles deposited early and in the anterior half of the nasal cavity with a deposition efficiency of 99%. As the particle increased in size to 10nm the diffusive nature of the nanoparticle decreased and the deposition efficiency reduced to 30%. However a more evenly distributed deposition pattern was found for 10nm particles. The effect of including the sinus compartments with the nasal geometry on the deposition efficiency was most significant for 10nm particles. This difference is further amplified when the flow rate is decreased, which allows the

---

diffusion to be more influential. These results aimed to identify the possible differences that may occur when evaluating particle inhalation for toxicology or drug delivery using cast or computational models that exclude the sinus regions. This is particularly important for the case where flow rates are low and particle sizes are around 5-10nm and comparative studies between human subjects and nasal cavity casts or CFD models that neglect the sinus airways should consider the diffusion effects of nanoparticles.

### **9.2.2 Nasal Cavity with Spray Device**

Two computational models of the human nasal cavity without paranasal sinus were created in this study, where the difference between the two models was the presence of a nasal spray device. This was coupled with experimental data, which was used to provide realistic initial particle boundary conditions. The experimental data was obtained from PDIA measurements, which provided visualisation of the spray development as well as the Sauter mean diameter at different sections of the spray. Important features of the spray characteristics include the spray cone angle, particle size, diameter of the spray cone and break-up length from the nozzle. The measured values provided a basis for setting appropriate initial particle conditions for the computational model. The two nasal cavity models were first simulated to investigate the differences in the air flow field caused by the presence of the nasal spray head. Increased levels of disturbed flow were found where the spray device was placed in the nasal vestibule. The increase in vortices can have two effects: i) the swirling vortices, which have radial and tangential velocities, may in fact slow down the linear velocity of the sprayed particles thereby reducing the particle inertia, and ii) the dispersion of the particles is increased due to the vortices.

---

Droplet deposition was found to be high in the anterior regions of the nasal cavity caused by the particle inertia, which is a major stumbling block for particles to get through the narrow nasal valve region to the middle regions where the drugs are absorbed. Evaluation of the two spray cone types found that hollow spray cones produced more deposition in the middle regions of the nasal cavity for  $5\mu\text{m}$  and  $15\mu\text{m}$  particles. For increased efficacy in nasal drug delivery design, issues such as atomisation for finer particle size distribution and slower initial particle velocity is suggested. In addition, instructing the user to align the spray with the main nasal passage may also help. These results demonstrate the use of CFD to provide insight into design issues related to the spray atomiser performance for nasal drug delivery. In addition this work is a step forward towards a more integrated drug delivery simulation, which currently still lacks additional physics such as unsteady inhalation, and further complex physics such as multiphase turbulence and fluid structure interactions.

### **9.3 Recommendations for Further Study**

There are several further studies that can be performed to continue this research in the aspects of simulation.

Firstly, in the numerical model technique, there are several turbulence models that need to be tested for comparison in future work, such as the Direct Numerical Simulation (DNS) model and the Large Eddy Simulation (LES) model. Turbulence state is the typical motion of fluids when at larger Reynolds number conditions. The governing equations used for both laminar and turbulent flows are the same in the Navier-Stokes equations, the difference is use different variable such as the kinetic energy ( $k$ ) and dissipation ( $\epsilon$ ). Turbulence state is the typical motion of fluids when at

---

larger Reynolds number conditions. Huge computational resources are needed to proceed to their direct solution without any model. This approach is Direct Numerical Simulation (DNS). DNS is important to provide data for the development and validation of turbulence models (both Large Eddy Simulation (LES) and Reynolds Averaged Navier-Stokes (RANS) models) and also to be directly applied to certain types of flows.

Secondly, in the integrated model of a human manikin within the space of a room, this current study investigates the influence of different wind velocities on only one particle size. In the further work, it will be necessary to analyse results with different conditions by changing specific parameters (e.g. inlet velocity and particle size). Another possible simulation to test and validate would involve a number of manikins in a room with different orientations such as face to face, face to back and back to back, which would be very helpful to understand exposure risk as well as determine ideal ventilation designs in public and occupational health.

Additionally, for the internal respiratory model, these studies in total used two subjects' patent airways; one nasal cavity with paranasal sinuses is among the models. The individual model including the paranasal sinus has limitations due to the inter-subject variability in anatomy between different people. Further studies may examine the differences in a wide range of subjects (age, sex, ethnicity etc.) and with a larger sample size. However in general, gross flow features and overall particle deposition can provide sufficient insight into the trends that are consistent among different geometries. On the assumption that the subject within this study is without pathology and representative of an 'average' patient, the preliminary results from this study will aid in gaining an appropriate understanding of the effect of paranasal

---

sinuses on nano-particle deposition. Chronic sinusitis is a common problem in our population with a prevalence in the United States of 14.6% and results in significant morbidity, costing the US health care system approx. \$3.4–5 billion annually (Pleis and Lucas 2009). There is potential in future work to speculate the implications of sinusitis and obstruction of paranasal sinuses on particle flow and deposition in the nasal airways. These results may be applicable to improving novel delivery of therapies to treat conditions like chronic sinusitis.

The final recommendation involves running the simulations under transient flow. Since data has been established for steady simulations, an unsteady simulation will provide important comparisons into airflow structures and particle dynamics. The unsteady simulations may provide insight into different types of inhalation such as at high levels (sniffing) and the holding of breaths, which influence particle flow dynamics. Different breathing patterns may also be investigated by using unsteady simulations. The type of inhalation affecting the deposition patterns of particles will then determine whether one form of inhalation is more effective than another for drug delivery. Studies of abnormalities to the nasal cavity can also be performed to investigate possible surgical interventions. The simulations can provide cause-and-effect results from ‘virtual surgery’ where walls and sections of the nasal cavity can be modified in the computational model to explore the effects on airflow and heat transfer. This concept is also highly applicable to sleep apnoea where the influence of airway geometries plays a critical role in the breathing ability of patients.

---

# References

- Aitken, R. J., Baldwin, P. E. J., Beaumont, G. C., Kenny, L. C. and Maynard, A. D. (1999). Aerosol Inhalability in Low Air Movement Environments. *Journal of Aerosol Science* 30:613-626.
- Ansys (2007). Fluent User Manual. *Ansys Inc. USA*.
- Anthony, T. R. and Flynn, M. R. (2006). Computational Fluid Dynamics Investigation of Particle Inhalability. *Aerosol Science* 37:750-765.
- Anthony, T. R., Flynn, M. R. and Eisner, A. (2005). Evaluation of Facial Features on Particle Inhalation. *Annals of Occupational Hygiene* 49:179-193.
- Aykac, D., Hoffman, E. A., McLennan, G. and Reinhardt, J. M. (2003). Segmentation and Analysis of the Human Airway Tree from Three-Dimensional X-Ray CT Images. *IEEE Transactions on Medical Imaging* 22:940-950.
- B. Shome, L.-P. Wang, M. H. Santare, A. K. Prasad, Szeri, A. Z. and Roberts, D. (1998). Modeling of Airflow in the Pharynx With Application to Sleep Apnea. *Journal of Biomechanical Engineering* Volume 120:7 pages.
- Baldwin, P. E. J. and Maynard, A. D. (1998). A Survey of Wind Speeds in Indoor Workplaces. *Ann. Occup. Hyg.* 42:303-313.
- Beare, R. (2006). A Locally Constrained Watershed Transform. *IEEE transactions on pattern analysis and machine intelligence* 28:1063-1074.
- Bird, A. J. (2005). Use of Numerical Calculations to Simulate the Sampling Efficiency Performance of a Personal Aerosol Sampler. *Aerosol Science and Technology* 39:14.
- Bogdanffy, M. S. and Sarangapani, R. (2003). Physiologically-based kinetic modeling of vapours toxic to the respiratory tract. *Toxicology Letters* 138:103-117.
- Cai, F. S. and Yu, C. P. (1988). Inertial and Interceptional Deposition of Spherical Particles and Fibres in a Bifurcating Airway. *J. Aerosol Science* 19:679-688.
- Calay, R. K., Kurujareon, J. and Holdø, A. E. (2002). Numerical Simulation of Respiratory Flow Patterns within Human Lung. *Respiratory Physiology & Neurobiology* 130:201-221.
- Cash, J. R. and Karp, A. H. (1990). A variable order Runge-Kutta Method for Initial Value Problems with Rapidly Varying Right-Hand Sides. *ACM Transactions on Mathematical Software* 16:201-222.
- Chang, H. K. and El Masry, O. A. (1982). A Model Study of Flow Dynamics in Human Central Airways. Part I: Axial Velocity Profiles. *Respiration Physiology* 49:75-95.
- Chen, Q., Lee, K., Mazumdar, S., Poussou, S., Wang, L., Wang, M. and Zhang, Z. (2010). Ventilation Performance Prediction for Buildings: Model Assessment. *Building and Environment* 45:295-303.

- 
- Cheng, K.-H., Cheng, Y.-S., Yeh, H.-C. and Swift, D. L. (1995). Deposition of Ultrafine Aerosols in the Head Airways During Natural Breathing and During Simulated Breath Holding Using Replicate Human Upper Airway Casts. *Aerosol Science and Technology* 23:465-474.
- Cheng, Y. S., Holmes, T. D., Gao, J., Guilmette, R. A., Li, S., Surakitbanharn, Y. and Rowlings, C. (2001). Characterization of Nasal Spray Pumps and Deposition Pattern in a Replica of the Human Nasal Airway. *J. Aerosol Medicine* 14:267-280.
- Cheng, Y. S., Yeh, H. C., Guilmette, R. A., Simpson, S. Q., Cheng, K. H. and Swift, D. L. (1996). Nasal Deposition of Ultrafine Particles in Human Volunteers and Its Relationship to Airway Geometry. *Aerosol Science and Technology* 25:274-291.
- Cheng, Y. S., Zhou, Y. and Chen, B. T. (1999). Particle Deposition in a Cast of Human Oral Airways. *Aerosol Science Technol.* 31:286-300.
- Chung, I. P., Trinh, T. and Dunn-Rankin, D. (1994). Experimental Investigation of a Two-Dimensional Cylindrical Sampler. *Journal of Aerosol Science* 25:935-955.
- Chung, S.-K. and Kim, S. K. (2008). Digital particle image velocimetry studies of nasal airflow. *Respiratory Physiology & Neurobiology* 163:111-120.
- Comte, P., Daude, F. and Mary, I. (2008). Simulation of the Reduction of Unsteadiness in a Passively Controlled Transonic Cavity Flow. *Journal of Fluids and Structures* 24:1252-1261.
- Craven, B. A. and Settles, G. S. (2006). A Computational and Experimental Investigation of the Human Thermal Plume. *Journal of Fluids Engineering* 128:1251-1258.
- Croce, C., Fodil, R., Durand, M., Sbirlea-Apiou, G., Caillibotte, G., Papon, J. F., Blondeau, J. R., Coste, A., Isabey, D. and Louis, B. (2006). In Vitro Experiments and Numerical Simulations of Airflow in Realistic Nasal Airway Geometry. *Annals of Biomedical Engineering* 34:997-1007.
- David K. Heist<sup>a</sup>, A. D. E., William Mitchell<sup>b</sup> & Russell Wiener<sup>b</sup> (2003). Airflow Around a Child-Size Manikin in a Low-Speed Wind Environment. *Aerosol Science and Technology* 37:11.
- de Rochefort, L., Vial, L., Fodil, R., Maitre, X., Louis, B., Isabey, D., Caillibotte, G., Thiriet, M., Bittoun, J., Durand, E. and Sbirlea-Apiou, G. (2007). In Vitro Validation of Computational Fluid Dynamic Simulation in Human Proximal Airways with Hyperpolarized <sup>3</sup>He Magnetic Resonance Phase-Contrast Velocimetry. *J Appl Physiol* 102:2012-2023.
- Doorly, D. J., Taylor, D. J. and Schroter, R. C. (2008). Mechanics of Airflow in the Human Nasal Airways. *Respiratory Physiology & Neurobiology* 163:100-110.
- Edwards, D. A., Hanes, J., Caponetti, G., Hrkach, J., Ben-Jebria, A., Eskew, M. L., Mintzes, J., Deaver, D., Lotan, N. and Langer, R. (1997). Large porous particles for pulmonary drug delivery. *Science* 276:1868-1872.
- Elad, D., Liebenthal, R., Wenig, B. L. and Einav, S. (1993). Analysis of Air Flow Patterns in the Human Nose. *Medical & Biological Engineering & Computing* 31:585-592.
- Fabio, R. (2003). From Point Cloud to Surface: The Modelling and Visualisation Problem, in *International Workshop on Visualisation and Animation of Reality-based 3D Models*, Tarasp-Vulpera, Switzerland.
- Ferron, G. A., Hillebrecht, A., Peter, J., Priesack, E., Thoma, M., Künzer, I., Mederer, R. and Klump, U. G. (1991). Airflow Simulation in Two-Dimensional Bifurcations. *Journal of Aerosol Science* 22:S809-S812.

- 
- Gao, N. and Niu, J. (2004). CFD Study on Micro-Environment around Human Body and Personalized Ventilation. *Building and Environment* 39:795-805.
- Gao, N. and Niu, J. (2006). Transient CFD simulation of the respiration process and inter-person exposure assessment. *Building and Environment* 41:1214-1222.
- Garcia, G. J. M., Bailie, N., Martins, D. A. and Kimbell, J. S. (2007). Atrophic Rhinitis: A CFD Study of Air Conditioning in the Nasal Cavity. *J Appl Physiol* 103:1082-1092.
- Gemci, T., Ponyavin, V., Chen, Y., Chen, H. and Collins, R. (2008). Computational Model of Airflow in Upper 17 Generations of Human Respiratory Tract. *Journal of Biomechanics* 41:2047-2054.
- GeoMagic (2005). Geomagic Documentation. *Geomagic Inc. NC, USA*.
- Gosman, A. D. and Ioannides, E. (1981). Aspects of Computer Simulation of Liquid-Fuelled Combustors., in *AIAA 19th Aerospace Sciences Meeting*, St Louis, MO., Paper AIAA-81-0323.
- Gowadia, H. A. and Settles, G. S. (2001). Natural sampling of airborne trace signals from explosives concealed upon the human body. *Journal of Forensic Sciences* 46:1324-1331.
- Gradon, L. and Orlicki, D. (1990). Deposition of Inhaled Aerosol Particles in a Generation of the Tracheobronchial Tree. *Journal of Aerosol Science* 21:3-19.
- Graham, D. I. and James, P. W. (1996). Turbulent Dispersion of Particles using Eddy Interaction Models. *International Journal of Multiphase Flow* 22:157-175.
- Green, A. S. (2004). Modelling of Peak-Flow Wall Shear Stress in Major Airways of the Lung. *Journal of Biomechanics* 37:661-667.
- Guilmette, R. A., Cheng, Y. S., Yeh, H. C. and Swift, D. L. (1994). Deposition of 0.005-12µm Monodisperse Particles in a Computer-Milled, MRI-Based Nasal Airway Replica. *Inhal. Toxicol.* 6:395-399.
- Häußermann, S., Bailey, A. G., Bailey, M. R., Etherington, G. and Youngman, M. J. (2001). The influence of breathing patterns on particle deposition in a nasal replicate cast. *J. Aerosol Science* 33:923-933.
- Heyder, J. and Rudolf, G. (1977). Deposition of aerosol particles in the human nose, in *Inhaled particles*, W. H. Walton, ed., Pergamon Press, Oxford UK, 107-125.
- Hinds, W. C., Kennedy, N. J. and Talyan, K. (1998). Inhalability of large particles for mouth and nose breathing. *Journal of Aerosol Science* 29, Supplement 1:S277-S278.
- Hofmann, W., Golser, R. and Balashazy, I. (2003). Inspiratory Deposition Efficiency of Ultrafine Particles in a Human Airway Bifurcation Model. *Aerosol Science Technol.* 37:988-994.
- Holmberg, S. and Li, Y. (1998). Modelling of the indoor environment - particle dispersion and deposition. *Indoor Air* 8:113-122.
- Homma, H. and Yakiyama, M. (1988). Examination of free convection around occupant's body caused by its metabolic heat. *ASHRAE Transactions* 94:104-124.
- Hood, C. M., Schroter, R. C., Doorly, D. J., Blenke, E. J. S. M. and Tolley, N. S. (2009). Computational Modeling of Flow and Gas Exchange in Models of the Human Maxillary Sinus. *J Appl Physiol* 107:1195-1203.
- Horschler, I., Schroder, W. and Meinke, M. (2010). On the assumption of steadiness of nasal cavity flow. *Journal of Biomechanics* 43:1081-1085.



- 
- Horsfield, K., Gladys, D., Olson, D. E., Finlay, G. F. and Cumming, G. (1971). Models of the Human Bronchial Tree. *J. Appl. Physiol.* 31:207-217.
- Hounam, R. F., Black, A. and Walsh, M. (1971). Deposition of Aerosol Particles in the Nasopharyngeal Region of the Human Respiratory Tract. *J. Aerosol Sci* 2:341-352.
- Howarth, J., Wilson, J., Bousquet, S., Rak, R. and Pauwels, R., eds. (2001). *Airway Remodeling*. Marcel Dekker, New York.
- Hsu, D.-J. and Swift, D. L. (1999). The Measurements of Human Inhalability of Ultralarge Aerosols in Calm Air using Mannikins. *Journal of Aerosol Science* 30:1331-1343.
- Huston, R. L. (2008). Principles of Biomechanics, in *Principles of Biomechanics*, L. L. Faulkner, ed., CRC Press.
- Ingham, D. B. (1975). Diffusion of Aerosols from a Stream Flowing Through a Cylindrical Tube. *J. Aerosol Sci* 6:125-132.
- Inthavong, K. (2006). A Numerical Study into Local Deposition Sites in the Nasal Cavity for Therapeutic and Pollutant Inhalation, in *Ansys Australasian Users Conference Proceedings 2006*, Melbourne, Australia.
- Inthavong, K., Choi, L.-T., Tu, J., Ding, S. and Thien, F. (2010). Micron Particle Deposition in a Tracheobronchial Airway Model under Different Breathing Conditions. *Medical Engineering & Physics* 32:1198-1212.
- Inthavong, K., Ge, Q., Se, C. M. K., Yang, W. and Tu, J. Y. (2011a). Simulation of Sprayed Particle Deposition in a Human Nasal Cavity Including a Nasal Spray Device. *Journal of Aerosol Science* 42:100-113.
- Inthavong, K., Tian, Z. F., Li, H. F., Tu, J. Y., Yang, W., Xue, C. L. and Li, C. G. (2006). A Numerical Study of Spray Particle Deposition in a Human Nasal Cavity. *Aerosol Science Technology* 40.
- Inthavong, K., Tian, Z. F. and Tu, J. Y. (2009a). Effect of Ventilation Design on Removal of Particles in Woodturning Workstations. *Building and Environment* 44:125-136.
- Inthavong, K., Tian, Z. F., Tu, J. Y., Yang, W. and Xue, C. (2008a). Optimising Nasal Spray Parameters for Efficient Drug Delivery using Computational Fluid Dynamics. *Computers in Biology and Medicine* 38:713-726.
- Inthavong, K., Wang, S., Wen, J., Tu, J. Y. and Xue, C. (2008b). Comparison of Micron and Nano Particle Deposition Patterns in a Realistic Human Nasal Cavity, in *13th International Conference on Biomedical Engineering (ICBME2008)*, Singapore, Singapore.
- Inthavong, K., Wen, J., Tian, Z. F. and Tu, J. Y. (2008c). Numerical Study of Fibre Deposition in a Human Nasal Cavity. *Journal of Aerosol Science* 39:253-265.
- Inthavong, K., Wen, J., Tu, J. Y. and Tian, Z. F. (2009b). From CT Scans to CFD Modelling – Fluid and Heat Transfer in a Realistic Human Nasal Cavity. *Engineering Applications of Computational Fluid Mechanics* 3:321-335.
- Inthavong, K., Zhang, K. and Tu, J. (2011b). Numerical modelling of nanoparticle deposition in the nasal cavity and the tracheobronchial airway. *Computer Methods in Biomechanics and Biomedical Engineering* 14:633-643.
- Isabey, D. and Chang, H. K. (1981). Steady and Unsteady Pressure-flow Relationships in Central Airways. *J. Appl. Physiol.* 51:1338-1348.

---

Isabey, D. and Chang, H. K. (1982). A Model Study of Flow Dynamics in Human Central Airways. Part II: Secondary Flow Velocities. *Respiration Physiology* 49:97-113.

Ishikawa, S., Nakayama, T., Watanabe, M. and Matsuzawa, T. (2009). Flow Mechanisms in the Human Olfactory Groove: Numerical Simulation of Nasal Physiological Respiration During Inspiration, Expiration, and Sniffing. *Arch Otolaryngol Head Neck Surg* 135:156-162.

Jayarajua, S. T., Brounsa, M., Lacora, C., Belkassemb, B. and Verbanckc, S. (2008). Large Eddy and Detached Eddy Simulations of Fluid Flow and Particle Deposition in a Human Mouth–Throat. *Journal of Aerosol Science* 39:862-875.

Jiang, J. and Zhao, K. (2010). Airflow and Nanoparticle Deposition in Rat Nose under Various Breathing and Sniffing Conditions--A Computational Evaluation of the Unsteady and Turbulent Effect. *Journal of Aerosol Science* 41:1030-1043.

Johnson, A. E., Fletcher, B. and Saunders, C. J. (1996). Air Movement around a Worker in a Low-Speed Flow Field. *The Annals of Occupational Hygiene* 40:57-64.

Kallio, G. A. and Reeks, M. W. (1989). A Numerical Simulation of Particle Deposition in Turbulent Boundary Layers. *International Journal of Multiphase Flow* 15:433-446.

Kato, S. and Yang, J.-H. (2008). Study on Inhaled Air Quality in a Personal Air-Conditioning Environment using New Scales of Ventilation Efficiency. *Building and Environment* 43:494-507.

Keir, J. W. d. w. h. p. s. T. J. o. L. O.-. (2009). Why do We have Paranasal Sinuses? *The Journal of Laryngology & Otology* 123:4.

Kelly, J., Asgharian, B., Kimbell, J. and Wong, B. (2004a). Particle Deposition in Human Nasal Airway Replicas Manufactured by Different Methods. Part II: Ultrafine Particles. *Aerosol Science and Technology* 38:1072 - 1079.

Kelly, J. T., Asgharian, B., Kimbell, J. S. and B.A., W. (2004b). Particle Deposition in Human Nasal Airway Replicas Manufactured by Different Methods. Part 1: Inertial Regime Particles. *Aerosol ScienceTech.* 38.

Kelly, J. T., Prasad, A. K. and Wexler, A. S. (2000). Detailed Flow Patterns in the Nasal Cavity. *J Appl. Physiol.* 89:323-337.

Kennedy, N. J. and Hinds, W. C. (2002). Inhalability of Large Solid Particles. *Journal of Aerosol Science* 33:237-255.

Keyhani, K., Scherer, P. W. and Mozell, M. M. (1995). Numerical Simulation of Airflow in the Human Nasal Cavity. *J. Biomechanical Engineering* 117:429-441.

Keyhani, K., Scherer, P. W. and Mozell, M. M. (1997). A Numerical Model of Nasal Odorant Transport for the Analysis of Human Olfaction. *J.Theor. Biol* 186:279-301.

Khoo, M. C. K., Shin, J. J. W., Asyali, M. H., Kim, T.-S. and Berry, R. B. (1998). Ventilatory dynamics of transient arousal in patients with obstructive sleep apnea. *Respiration Physiology* 112:291-303.

Kiely, J. and McNicholas, W. (2000). Cardiovascular Risk Factors in Patients with Obstructive Sleep Apnoea Syndrome. *Eur Respir J* 16:128-133.

Kim, C. S. and Fisher, D. M. (1999). Deposition Characteristics of Aerosol Particles inVSequentially Bifurcating Airway Models. *Aerosol Science Technol.* 31:198-220.

---

Kim, C. S., Fisher, D. M., Lutz, D. J. and Gerrity, T. R. (1994). Particle Deposition in Bifurcating Airway Models with Varying Airway Geometry. *Journal of Aerosol Science* 25:567-581.

Kimbell, J., Shroeter, J. D., Asgharian, B., Wong, B. A., Segal, R. A., Dickens, C. J., Southall, J. P. and Miller, F. J. (2004). Optimisation of Nasal Delivery Devices using Computational Models. *Res. Drug Del.* 9.

Kimbell, J. S., Segal, R. A., Asgharian, B., Wong, B. A., Schroeter, J. D., Southall, J. P., Dickens, C. J., Brace, G. and Miller, F. J. (2007). Characterization of Deposition from Nasal Spray Devices using a Computational Fluid Dynamics Model of the Human Nasal Passages. *J. Aeros. Med.* 20:59-74.

King Se, C. M., Inthavong, K. and Tu, J. (2010). Inhalability of Micron Particles through the Nose and Mouth. *Inhalation Toxicology* 22:287-300.

Kleinstreuer, C. and Zhang, Z. (2003). Targeted Drug Aerosol Deposition Analysis for a Four-Generation Lung Airway Model with Hemispherical Tumours. *Journal of Biomechanical Engineering* 125:197-206.

Kleinstreuer, C. and Zhang, Z. (2010). Airflow and Particle Transport in the Human Respiratory System. *Annual Review of Fluid Mechanics* 42:301-334.

Langtry, R. B., Menter, F. R., Likki, S. R., Suzen, Y. B., Huang, P. G. and Volker, S. (2006). A Correlation-Based Transition Model Using Local Variables---Part II: Test Cases and Industrial Applications. *Journal of Turbomachinery* 128:11.

Lefebvre, A. H. (1989). *Atomization and Sprays*. Hemisphere Publishing Corporation.

Li, A. and Ahmadi, G. (1992). Dispersion and deposition of spherical particles from point sources in a turbulent channel flow. *Aerosol Sci. Technol.* 16:209-226.

Li, X., Inthavong, K. and Tu, J. (2012). Particle inhalation and deposition in a human nasal cavity from the external surrounding environment. *Building and Environment* In Press, Corrected Proof.

Li, Z., Kleinstreuer, C. and Zhang, Z. (2007a). Simulation of Airflow Fields and Microparticle deposition in Realistic Human Lung Airway Models. Part I: Airflow Patterns. *European Journal of Mechanics B/Fluids* 26:632-649.

Li, Z., Kleinstreuer, C. and Zhang, Z. (2007b). Simulation of Airflow Fields and Microparticle Deposition in Realistic Human Lung Airway Models. Part II: Particle Transport and Deposition. *European Journal of Mechanics - B/Fluids* 26:650-668.

Lide, D. R. (1994). *Characteristics of Particles and Particle Dispersoids. Handbook of Chemistry and Physics*. CRC Press, 1994, Florida.

Lin, C.-L., Tawhai, M. H., McLennan, G. and Hoffman, E. A. (2007). Characteristics of the Turbulent Laryngeal Jet and its Effect on Airflow in the Human Intra-Thoracic Airways. *Respiratory Physiology & Neurobiology* 157:295-309.

Lin, Z., Yao, T., Chow, T. T., Fong, K. F. and Chan, L. S. (2011). Performance Evaluation and Design Guidelines for Stratum Ventilation. *Building and Environment* 46:2267-2279.

Lindemann, J., Brambs, H.-J., Keck, T., Wiesmiller, K. M., Rettinger, G. and Pless, D. (2005). Numerical Simulation of Intranasal Airflow after Radical Sinus Surgery. *American Journal of Otolaryngology* 26:175-180.

- 
- Lindemann, J., Keck, T., Wiesmiller, K., Sander, B., Brambs, H. J., Rettinger, G. and Pless, P. (2004). A numerical Simulation of Intranasal Air Temperature during Inspiration. *The Laryngoscope* 114:1037-1041.
- Liu, D.-m., Liu, S.-h., Wu, Y.-l. and Xu, H.-y. (2009a). LES Numerical Simulation of Cavitation Bubble Shedding on ALE 25 and ALE 15 Hydrofoils. *Journal of Hydrodynamics, Ser. B* 21:807-813.
- Liu, H. (2000). Science and Engineering of Droplets - Fundamentals and Applications, William Andrew Publishing/Noyes.
- Liu, Y., Johnson, M. R., Matida, E. A., Kherani, S. and Marsan, J. (2009b). Creation of a Standardized Geometry of the Human Nasal Cavity. *J Appl Physiol* 106:784-795.
- Liu, Y., Matida, E. A., Junjie, G. U. and Johnson, M. R. (2007). Numerical simulation of aerosol deposition in a 3-D human nasal cavity using RANS, RANS/EIM, and LES. *Journal of Aerosol Science* 38:683-700.
- Liu, Y., So, R. M. C. and Zhang, C. H. (2002). Modeling the Bifurcating Flow in a Human Lung Airway. *Journal of Biomechanics* 35:465-473.
- Liu, Y., So, R. M. C. and Zhang, C. H. (2003). Modeling the Bifurcating Flow in an Asymmetric Human Lung Airway. *Journal of Biomechanics* 36:951-959.
- Longest, P. W., Hindle, M., Das Choudhuri, S. and Xi, J. (2008). Comparison of ambient and spray aerosol deposition in a standard induction port and more realistic mouth-throat geometry. *Journal of Aerosol Science* 39:572-591.
- Longest, P. W. and Kleinstreuer, C. (2004). Interacting Effects of Uniform Flow, Plane Shear, and Near-Wall Proximity on the Heat and Mass Transfer of Respiratory Aerosols. *International Journal of Heat and Mass Transfer* 47:4745-4759.
- Longest, P. W. and Oldham, M. J. (2006). Mutual Enhancements of CFD Modeling and Experimental Data: A Case Study of 1- $\mu$ m Particle Deposition in a Branching Airway Model. *Inhalation Toxicology: International Forum for Respiratory Research* 18:761 - 771.
- Longest, P. W. and Xi, J. (2007). Computational Investigation of Particle Inertia Effects on Submicron Aerosol Deposition in the Respiratory Tract. *Journal of Aerosol Science* 38:111-130.
- Luo, H. Y. and Liu, Y. (2008). Modeling the Bifurcating Flow in a CT-Scanned Human Lung Airway. *Journal of Biomechanics* 41:2681-2688.
- Mandal, S. C. and Mandal, M. (2010). Current Status and Future Prospects of New Drug Delivery System. *Pharma Times* 42:4.
- Martonen, T. B., Zhang, Z. and Lessmann, R. C. (1993). Fluid Dynamics of the Human Larynx and Upper Tracheobronchial Airways. *Aerosol science and technology* 19:23.
- Materialise (2008). Mimics Documentation. *Materialise NV*.
- Matida, E. A., Finlay, W. H., Lange, C. F. and Grgic, B. (2004). Improved Numerical Simulation for Aerosol Deposition in an Idealized Mouth-Throat. *J Aerosol Science* 35:1-19.
- Menter, F. R. (1994). Two-equation eddy-viscosity turbulence models for engineering applications. *American Institute of Aeronautics and Astronautics Journal* 32:7.
- Menter, F. R., Kuntz, M. and Langtry, R. B. (2003). Ten Years of Industrial Experience with the SST Turbulence Model. *Turbulence, Heat and Mass Transfer* 4:7.

- 
- Mihaescu, M., Murugappan, S., Kalra, M., Khosla, S. and Gutmark, E. (2008). Large Eddy Simulation and Reynolds-Averaged Navier-Stokes modeling of flow in a realistic pharyngeal airway model: An investigation of obstructive sleep apnea. *Journal of Biomechanics* 41:2279-2288.
- Mumford, D. and Shah, J. (1989). Optimal Approximations by Piecewise Smooth Functions and Associated Variational Problems. *Communications Pure and Applied Mathematics* XLII:577-685.
- Nagels, M. A. and Cater, J. E. (2009). Large Eddy Simulation of High Frequency Oscillating Flow in an Asymmetric Branching Airway Model. *Medical Engineering & Physics* 31:1148-1153.
- Nanduri, J. R., Pino-Romainville, F. A. and Celik, I. (2009). CFD Mesh Generation for Biological Flows: Geometry Reconstruction using Diagnostic Images. *Computers & Fluids* 38:1026-1032.
- Oberdörster, G. (2000). Pulmonary effects of inhaled ultrafine particles. *International Archives of Occupational and Environmental Health* 74:1-8.
- Oberdörster, G., Sharp, Z., Atudorei, V., Elder, A., Gelein, R., Kreyling, W. and Cox, C. (2004). Translocation of Inhaled Ultrafine Particles to the Brain. *Inhalation Toxicology: International Forum for Respiratory Research* 16:437 - 445.
- Ounis, H., Ahmadi, G. and J.B., M. (1991). Brownian Diffusion of Submicrometer Particles in the Viscous Sublayer. *J. Colloid and Interface Science* 143:266-277.
- Pal, N. R. and Pal, S. K. (1993). A Review on Image Segmentation Techniques. *Pattern Recognition* 26:1277-1294.
- Patankar, S. V. (1980). Numerical Heat Transfer and Fluid Flow. *Taylor & Francis*.
- Pattle, R. E. (1961). The Retention of Gases and Particles in the Human Nose, in *Inhaled particles and vapors*  
C. N. Davies, ed., Pergamon Press, Oxford, UK, 302-309.
- Perzl, M. A., Schultz, H., Parezke, H. G., Englmeier, K. H. and Heyder, J. (1996). Reconstruction of the Lung Geometry for the Simulation of Aerosol Transport. *J. Aerosol Medicine* 9:409-418.
- Piegl, L. A. and Tiller, W. (1995). *The NURBS book*. Springer-Verlag, New York, NY.
- Pleis, J. R. and Lucas, J. W. (2009). Summary health statistics for U.S. adults, in *Vital Health Stat 10*, National Health Interview Survey.
- Popiolek, T. L., Awruch, A. M. and Teixeira, P. R. F. (2006). Finite element analysis of laminar and turbulent flows using LES and subgrid-scale models. *Applied Mathematical Modelling* 30:177-199.
- Proetz, A. W. (1951). Air Currents in the Upper Respiratory Tract and their Clinical Importance. *Ann Otol Rhinol Laryngol* 60:439-467.
- Richmond, C. (2004). Sir Godfrey Hounsfield. *British Medical Journal* 329:687.
- Riederer, S. J. (2004). MR Imaging: Its Development and the Recent Nobel Prize. *Radiology* 231:4.
- Rim, D. and Novoselac, A. (2009a). Transport of particulate and gaseous pollutants in the vicinity of a human body. *Building and Environment* 44:1840-1849.
- Rim, D. and Novoselac, A. (2009b). Transport of Particulate and Gaseous Pollutants in the Vicinity of a Human Body. *Building and Environment* 44:1840-1849.

- 
- Robinson, R., Oldham, M., Clinkenbeard, R. and Raj, P. (2006). Experimental and Numerical Smoke Carcinogen Deposition in a Multi-Generation Human Replica Tracheobronchial Model. *Annals of Biomedical Engineering* 34:373-383.
- Saffman, P. G. (1965). The Lift on a Small Sphere in a Slow Shear Flow. *J. Fluid Mechanics* 22:385-400.
- Sandeau, J., Katz, I., Fodil, R., Louis, B., Apiou-Sbirlea, G., Caillibotte, G. and Isabey, D. (2010). CFD Simulation of Particle Deposition in a Reconstructed Human Oral Extrathoracic Airway for Air and Helium-Oxygen Mixtures. *Journal of Aerosol Science* 41:281-294.
- Schmees, D. K., Wu, Y. H. and Vincent, J. H. (2008). Visualization of the airflow around a life-sized, heated, breathing mannequin at ultralow windspeeds. *The Annual of Occupational Hygiene* 52:351-360.
- Schmehl, R., Roskamp, H., Willmann, M. and Wittig, S. (1999). CFD Analysis of Spray Propagation and Evaporation including Wall Film Formation and Spray/Film Interactions. *International Journal of Heat and Fluid Flow* 20:520-529.
- Schmidt, D. P., Nouar, I., Senecal, P. K., Rutland, C. J., Martin, J. K., Reitz, R. D. and Hoffman, J. A. (1999). Pressure-Swirl Atomization in the Near Field. *Transactions of SAE* 1:1999-1901-0496.
- Schroeter, J. D., Garcia, G. J. M. and Kimbell, J. S. (2011). Effects of Surface Smoothness on Inertial Particle Deposition in Human Nasal Models. *Journal of Aerosol Science* 42:52-63.
- Schroeter, J. D., Kimbell, J. S. and Asgharian, B. (2006). Analysis of Particle Deposition in the Turbinate and Olfactory Regions using a Human Nasal Computational Fluid Dynamics Model. *J. Aerosol Med.* 19:301-313.
- Schroter, R. C. and Sudlow, M. F. (1969). Flow Patterns in Models of the Human Bronchial Airways. *Respiration Physiology* 7.
- Shapiro, L. G. S., G.C. (2001). Computer Vision. *Prentice-Hall, New Jersey*:146.
- Shi, H., Kleinstreuer, C. and Zhang, Z. (2006). Laminar Airflow and Nanoparticle or Vapor Deposition in a Human Nasal Cavity Model. *J. Biomech. Eng.* 128:697-706.
- Shome, B., Wang, L. P., Santare, M. H., Prasad, A. K., Szeri, A. Z. and Roberts, D. (1998). Modeling of Airflow in the Pharynx With Application to Sleep Apnea. *Journal of Biomechanical Engineering* Volume 120:7 pages.
- Smith, W. S., Reisner, J. M. and Kao, C. Y. J. (2001). Simulations of Flow Around a Cubical Building: Comparison with Towing-Tank Data and Assessment of Radiatively Induced Thermal Effects. *Atmospheric Environment* 35:3811-3821.
- Snyer, W. S., Cook, M.J., Nasset, E.S., Karhausen, L.R., Parry Howells, G. and Tipton, I.H. (1975). *Report of the Task Group on Reference Man*. Pergamon Press.
- Straatsma, J., Van Houwelingen, G., Steenbergen, A. E. and De Jong, P. (1999). Spray Drying of Food Products:1.Simulation Model. *J. Food Eng.* 42:67-72.
- Subramaniam, R. P., Richardson, R. B., Morgan, K. T., Kimbell, J. S. and Guilmette, R. A. (1998). Computational Fluid Dynamics Simulations of Inspiratory Airflow in the Human Nose and Nasopharynx. *Inhalation Toxicology* 10.
- Suman, J. D., Laube, B. L., Lin, T. C., Brouet, G. and Dalby, R. (2002). Validity of in Vitro Tests on Aqueous Spray Pumps as Surrogates for Nasal Deposition. *Pharma. Res.* 19:1-6.

- 
- Swift, D. L. (1991). Inspiratory Inertial Deposition of Aerosols in Human Nasal Airway Replicate Casts: Implication for the Proposed NCRP Lung Model. *Radiat. Prot. Dosim.* 38:29-34
- Talbot, L., Cheng, R. K., Schefer, R. W. and Willis, D. R. (1980). Thermophoresis of Particles in a Heated Boundary Layer. *J. Fluid Mech* 101:737-758.
- Tarabichi, M. and Fanous, N. (1993). Finite Element Analysis of Airflow in the Nasal Valve. *Arch Otolaryngol Head Neck Surg* 119:169-172.
- Tian, Z. F., Inthavong, K., Tu, J. Y. and Yeoh, G. H. (2008a). Numerical Investigation into the Effects of Wall Roughness on a Gas-Particle Flow in a 90-Degree Bend. *International Journal of Heat and Mass Transfer* 51:1238-1250.
- Tian, Z. F., Inthavong, K., Tu, J. Y. and Yeoh, G. H. (2008b). Numerical investigation into the effects of wall roughness on a gas-particle flow in a 90° bend. *International Journal of Heat and Mass Transfer* 51:1238-1250.
- Tilley, A. (1993). The Measure of Man and Woman. *New York: The Whitney Library of Design.*
- Tippe, A., Perzl, M., Li, W. and Schulz, H. (1999). Experimental Analysis of Flow Calculations Based on HRCT Imaging of Individual Bifurcations. *Respiration Physiology* 117:181-191.
- Tschirren, J., Hoffman, E. A., McLennan, G. and Sonka, M. (2005). Segmentation and Quantitative Analysis of Intrathoracic Airway Trees from Computed Tomography Images. *Proc Am Thorac Soc* 2:484-487.
- Tu, J., Yeoh, G. H. and Liu, C. (2008). Some Applications of CFD with Examples, in *Computational Fluid Dynamics*, Butterworth-Heinemann, Burlington, 277-363.
- V. N. Riazuddin, M. Z., M. Z. Abdullah, R. Ismail, I. L. Shuaib, A. H. Suzina and K. A. Ahmad, (2011). Comparison of Inspiratory and expiratory flow inside the nasal cavity using numerical methods. *J. Med. Biol. Eng* 31:6.
- van Ertbruggen, C., Hirsch, C. and Paiva, M. (2005). Anatomically Based Three-Dimensional Model of Airways to Simulate Flow and Particle Transport using Computational Fluid Dynamics. *J. Appl. Physiol.* 98:970-980.
- van Reimersdahl, T., Hörschler, I., Gerndt, A., Kuhlen, T., Meinke, M., Schlöndorff, G., Schröder, W. and Bischof, C. H. (2001). Airflow Simulation inside a Model of the Human Nasal Cavity in a Virtual Reality based Rhinological Operation Planning System. *International Congress Series* 1230:87-92.
- Vial, L., Perchet, D., Fodil, R., Caillibotte, G., Fetita, C., Preteux, F., Beigelman-Aubry, C., Grenier, P., Thiriet, M., Isabey, D. and Sbirlea-Apiou, S. (2005). Airflow Modeling of Steady Inspiration in Two Realistic Proximal Airway Trees Reconstructed from Human Thoracic Tomodensitometric Images. *Comput. Method Biomech. Biomed Eng.* 8:267-277.
- Vincent, J. H., Mark, D., Miller, B. G., Armbruster, L. and Ogden, T. L. (1990). Aerosol inhalability at higher windspeeds. *J. Aerosol Science* 21:577-586.
- Vincent, J. H., Schmees, D. K. and Wu, Y. H. (2008). Visualization of the airflow around a life-sized, heated, breathing mannequin at ultralow windspeeds. *Ann Occup Hyg* 52:351-360.
- Wang, J., Flagan, R. C. and Seinfeld, J. H. (2002). Diffusional Losses in Particle Sampling Systems Containing Bends and Elbows. *Journal of Aerosol Science* 33:843-857.

---

Wang, S. M., Inthavong, K., Wen, J., Tu, J. Y. and Xue, C. L. (2009). Comparison of micron- and nanoparticle deposition patterns in a realistic human nasal cavity. *Respiratory Physiology & Neurobiology* 166:142-151.

Wang, Y. and James, P. W. (1999). On the Effect of Anisotropy on the Turbulent Dispersion and Deposition of Small Particles. *Int. J. of Multiphase Flows* 25:551-558.

Weibel, E. R. (1963). *Morphometry of the Human Lung*. Academic Press., New York, US.

Wen, J., Inthavong, K., Tu, J. and Wang, S. (2008a). Numerical Simulations for Detailed Airflow Dynamics in a Human Nasal Cavity. *Respiratory Physiology & Neurobiology* 161:125-135.

Wen, J., Inthavong, K., Tu, J. Y. and Wang, S. (2008b). Numerical simulations for detailed airflow dynamics in a human nasal cavity. *Respiratory Physiology & Neurobiology* 161:125-135.

Wiesmiller, K., Keck, T., Leiacker, R., Sikora, T., Rettinger, G. and Lindemann, J. (2003). The Impact of Expiration on Particle Deposition within the Nasal Cavity. *Clinical Otolaryngology & Allied Sciences* 28:304-307.

Womersley, J. R. (1955). Method for the calculation of velocity, rate of flow and viscous drag in arteries when the pressure gradient is known. *J. Physiol.* 127:553-563.

Worth Longest, P. and Hindle, M. CFD simulations of enhanced condensational growth (ECG) applied to respiratory drug delivery with comparisons to in vitro data. *Journal of Aerosol Science* In Press, Corrected Proof.

Worth Longest, P. and Hindle, M. (2010). CFD Simulations of Enhanced Condensational Growth (ECG) Applied to Respiratory Drug Delivery with Comparisons to in Vitro Data. *Journal of Aerosol Science* 41:805-820.

Xi, J. and Longest, P. W. (2008a). Effects of Oral Airway Geometry Characteristics on the Diffusional Deposition of Inhaled Nanoparticles. *Journal of Biomechanical Engineering* 130:011008-011001-011008-011016.

Xi, J. and Longest, P. W. (2008b). Numerical Predictions of Submicrometer Aerosol Deposition in the Nasal Cavity using a Novel Drift Flux Approach. *International Journal of Heat and Mass Transfer* 51:5562-5577.

Xiong, G., Zhan, J., Zuo, K., Li, J., Rong, L. and Xu, G. (2008a). Numerical Flow Simulation in the Post-Endoscopic Sinus Surgery Nasal Cavity. *Medical and Biological Engineering and Computing* 46:1161-1167.

Xiong, G. X., Zhan, J. M., Jiang, H. Y., Li, J. F., Rong, L. W. and Xu, G. (2008b). Computational Fluid Dynamics Simulation of Airflow in the Normal Nasal Cavity and Paranasal Sinuses. *American Journal of Rhinology* 22:477-482.

Xu, C., Sin, S., McDonough, J. M., Udupa, J. K., Guez, A., Arens, R. and Wootton, D. M. (2006). Computational Fluid Dynamics Modeling of the Upper Airway of Children with Obstructive Sleep Apnea Syndrome in Steady Flow. *Journal of Biomechanics* 39:2043-2054.

Yakhot, V. and Orszag, S. A. (1986). Renormalization Group Analysis of Turbulence. I. Basic Theory. *Journal of Scientific Computing* 1:3-51.

Yu, G., Zhang, Z. and Lessman, R. (1998). Fluid Flow and Particle Deposition in the Human Upper Respiratory System. *Aerosol Science Technol.* 28:146-158.



---

Yule, A. J., Sharief, R. A., Jeong, J. R., Nasr, G. G. and James, D. D. (2000). The Performance Characteristics of Solid-Cone-Spray Pressure-Swirl Atomizers. *Atomization and Sprays* 10.

Zamankhan, P., Ahmadi, G., Wang, Z., Hopke, P. H., Cheng, Y. S., Su, W. C. and Leonard, D. (2006). Airflow and Deposition of Nanoparticles in a Human Nasal Cavity. *Aerosol Science Technol.* 40:463-476.

Zhang, T. and Chen, Q. (2007). Identification of contaminant sources in enclosed spaces by a single sensor. *Indoor Air* 17:439-449.

Zhang, Y. and Finlay, W. H. (2005). Measurement of the Effect of Cartilaginous Rings on Particle Deposition in a Proximal Lung Bifurcation Model. *Aerosol Science Tech.* 39:394-399.

Zhang, Y., Mcaury, B. S. and Shirazi, S. A. (2009a). Improvements of Particle Near-Wall Velocity and Erosion Predictions Using a Commercial CFD Code. *Journal of Fluids Engineering* 131:9.

Zhang, Z., Kleinstreuer, C. and Kim, C. S. (2002). Micro-Particle Transport and Deposition in a Human Oral Airway Model. *Aerosol Science* 33:1635-1652.

Zhang, Z., Kleinstreuer, C. and Kim, C. S. (2009b). Comparison of Analytical and CFD Models with Regard to Micron Particle Deposition in a Human 16-Generation Tracheobronchial Airway Model. *Journal of Aerosol Science* 40:16-28.

Zhao, B., Li, X. and Yan, Q. (2003). A Simplified System for Indoor Airflow Simulation. *Building and Environment* 38:543-552.

Zhao, K., Dalton, P., Yang, G. C. and Scherer, P. W. (2006). Numerical Modeling of Turbulent and Laminar Airflow and Odorant Transport during Sniffing in the Human and Rat Nose. *Chem. Senses* 31:107-118.

Zhao, K., Scherer, P. W., Hajiloo, S. A. and Dalton, P. (2004). Effect of Anatomy on Human Nasal Air Flow and Odorant Transport Patterns: Implications for Olfaction. *Chem. Senses* 29:365-379.

Zhu, J. H., Lee, H. P., Lim, K. M., Lee, S. J. and Wang, D. Y. (2011). Evaluation and Comparison of Nasal Airway Flow Patterns among Three Subjects from Caucasian, Chinese and Indian Ethnic Groups using Computational Fluid Dynamics Simulation. *Respiratory Physiology & Neurobiology* 175:62-69.

Zhu, S., Kato, S., Murakami, S. and Hayashi, T. (2005). Study on Inhalation Region by Means of CFD Analysis and Experiment. *Building and Environment* 40:1329-1336.

Zhuang, Z., Landsittel, D., Benson, S., Roberge, R. and Shaffer, R. (2010). Facial Anthropometric Differences among Gender, Ethnicity, and Age Groups. *Annals of Occupational Hygiene* 54:11.

---

# Appendix A

## Fluid Equations

The equations forms are given as:

**mass conservation**

$$\frac{\partial u}{\partial x} + \frac{\partial v}{\partial y} + \frac{\partial w}{\partial z} = 0 \quad 4.1$$

**u-momentum**

$$\frac{\partial u}{\partial t} + \frac{\partial(uu)}{\partial x} + \frac{\partial(vu)}{\partial y} + \frac{\partial(wu)}{\partial z} = -\frac{1}{\rho} \frac{\partial p}{\partial x} + \frac{\partial}{\partial x} \left[ (v + v_T) \frac{\partial u}{\partial x} \right] + \frac{\partial}{\partial y} \left[ (v + v_T) \frac{\partial u}{\partial y} \right] + \frac{\partial}{\partial z} \left[ (v + v_T) \frac{\partial u}{\partial z} \right] + S_u \quad 4.2$$

**v-momentum**

$$\frac{\partial v}{\partial t} + \frac{\partial(vv)}{\partial x} + \frac{\partial(vv)}{\partial y} + \frac{\partial(wv)}{\partial z} = -\frac{1}{\rho} \frac{\partial p}{\partial y} + \frac{\partial}{\partial x} \left[ (v + v_T) \frac{\partial v}{\partial x} \right] + \frac{\partial}{\partial y} \left[ (v + v_T) \frac{\partial v}{\partial y} \right] + \frac{\partial}{\partial z} \left[ (v + v_T) \frac{\partial v}{\partial z} \right] + S_v \quad 4.3$$

**w-momentum**

$$\frac{\partial w}{\partial t} + \frac{\partial(uw)}{\partial x} + \frac{\partial(vw)}{\partial y} + \frac{\partial(ww)}{\partial z} = -\frac{1}{\rho} \frac{\partial p}{\partial z} + \frac{\partial}{\partial x} \left[ (v + v_T) \frac{\partial w}{\partial x} \right] + \frac{\partial}{\partial y} \left[ (v + v_T) \frac{\partial w}{\partial y} \right] + \frac{\partial}{\partial z} \left[ (v + v_T) \frac{\partial w}{\partial z} \right] + S_w \quad 4.4$$

**energy equation**

$$\frac{\partial T}{\partial t} + \frac{\partial(uT)}{\partial x} + \frac{\partial(vT)}{\partial y} + \frac{\partial(wT)}{\partial z} = \frac{\partial}{\partial x} \left[ \left( \frac{v}{\text{Pr}} + \frac{v_T}{\text{Pr}_T} \right) \frac{\partial T}{\partial x} \right] + \frac{\partial}{\partial y} \left[ \left( \frac{v}{\text{Pr}} + \frac{v_T}{\text{Pr}_T} \right) \frac{\partial T}{\partial y} \right] + \frac{\partial}{\partial z} \left[ \left( \frac{v}{\text{Pr}} + \frac{v_T}{\text{Pr}_T} \right) \frac{\partial T}{\partial z} \right] + S_T \quad 4.5$$

---

The governing equations have the same generic form, and for a fluid property  $\phi$ , the equation can be written as

$$\frac{\partial \phi}{\partial t} + \frac{\partial(u\phi)}{\partial x} + \frac{\partial(v\phi)}{\partial y} + \frac{\partial(w\phi)}{\partial z} = \frac{\partial}{\partial x} \left[ \Gamma \frac{\partial \phi}{\partial x} \right] + \frac{\partial}{\partial y} \left[ \Gamma \frac{\partial \phi}{\partial y} \right] + \frac{\partial}{\partial z} \left[ \Gamma \frac{\partial \phi}{\partial z} \right] + S\phi \quad 4.6$$

This is otherwise referred to as, the scalar transport of  $\phi$ . By setting the transport property  $\phi$  equal to 1,  $u$ ,  $v$ ,  $w$ ,  $T$ , and selecting appropriate values for the diffusion coefficient  $\Gamma$  and source terms  $S_\phi$ , the continuity ( $\phi=1$ ), momentum ( $\phi=u, v, w$ ) or energy ( $\phi=T$ ) equations can be produced. The transport equation includes the local acceleration and convection terms on the left hand side which is respectively equivalent to the diffusion term ( $\Gamma =$  diffusion coefficient) and the source term ( $S\phi$ ) on the right hand side sources. Source terms can represent gravity that influences the fluid motion, or in the case of  $S_T$  in the energy equation may contain heat sources or sinks within the flow domain.

---

# **Appendix B**

## **Published Papers**



## Numerical study of the effects of human body heat on particle transport and inhalation in indoor environment

Qinjiang Ge<sup>a</sup>, Xiangdong Li<sup>a</sup>, Kiao Inthavong<sup>a</sup>, Jiyuan Tu<sup>a,b,\*</sup>

<sup>a</sup>School of Aerospace, Mechanical and Manufacturing Engineering, RMIT University, PO Box 71, Plenty Road, Bundoora, VIC 3083, Australia

<sup>b</sup>Institute of Nuclear and New Energy Technology, Tsinghua University, PO Box 1021, Beijing 100084, China

### ARTICLE INFO

#### Article history:

Received 2 May 2012

Received in revised form

18 July 2012

Accepted 2 August 2012

#### Keywords:

Body heat

Airflow field

Particle inhalation

Wind speed

CFD

### ABSTRACT

The inhalation of micron particles by a manikin standing in a ventilated indoor environment was numerically investigated using Computational Fluid Dynamics (CFD). Computations were conducted with various combinations of the free stream velocity (0.05–0.25 m/s representing typical indoor wind speeds.), occupant orientation relative to the free stream (back-to-the-wind or facing-the-wind) and heat transfer (isothermal or thermal flow). It was found that the body heat has a significant impact on the airflow field in the vicinity of the manikin by causing an upwards airflow on the downstream side of the manikin. It was also found that the effect of body heat on particle inhalation depends on the manikin orientation relative to the free stream. When the manikin is facing-the-wind, body heat has a little effect on particle inhalation and can be neglected. However for a back-to-the-wind orientation, the situation is much more complicated as the source height of inhaled particles depends on the speed of free stream. When the wind speed is low (0.05 m/s), the critical area is located near the floor level. The central height of the critical area then increases with increasing free stream speed until it reaches the nose height when the wind speed rises up to 0.25 m/s. This indicates that the body heat is an important consideration when investigating contaminant inhalation by human occupants in low-speed (typically less than 0.2 m/s) indoor environment.

© 2012 Elsevier Ltd. All rights reserved.

### 1. Introduction

The transport characteristics of aerosol particles and their inhalation characteristics by human occupants in indoor environments have been attached a great importance as people spend approximately 90% of their time indoors and a number of health problems have been found to be associated with particle inhalation [1]. During the past decades, numerous experimental and numerical investigations [2–7] have been conducted under various conditions. It is generally accepted nowadays that the particle inhalability by a human occupant is subjected to many factors such as the particle size, ambient wind speed, occupant movement, airflow pattern, inhalation rate, inhalation pattern (mouth or nasal inhalation), and even the human facial features.

However, most of the previous investigations on particle inhalation failed to take into account the effects of the metabolic heat released from a human body. In fact, a human body is continually

exchanging energy with its environment. The average thermal energy generated by a human body with an ordinary activity level and at a moderate room temperature was found to be up to 100 W [8]. Due to this heat, a temperature gradient is formed and drives a buoyant convection in the vicinity of the human body, which is known as the *human thermal plume*. Homma and Yakiyama [9] measured the human thermal plume around a person standing in quiescent air using smoke wire photography and hot-wire anemometry. It was found that the thermal boundary layer was approximately 50 mm thick at the face level and its velocity was up to 0.25 m/s. Using a laser Doppler anemometer, Johnson et al. [10] measured the airflow around a human body standing with its back towards the free stream (0.2 m/s). A significant upward airflow was observed in the downstream side of the human body and the upward velocity was found to be approximately 0.19 m/s at the nose level. A synthetic literature survey demonstrated that the human thermal plume can produce vertical air velocities of 0.1–0.25 m/s in the breathing zone [9–12]. This vertical velocity induced by body heat is roughly equal to the average wind speed in most indoor environments (0.05–0.25 m/s according to Baldwin et al. [13] and Schmees et al. [14]), it is therefore reasonable to expect that the buoyancy-driven convection may change

\* Corresponding author. School of Aerospace, Mechanical and Manufacturing Engineering, RMIT University, PO Box 71, Plenty Road, Bundoora, VIC 3083, Australia. Tel.: +61 3 9925 6191; fax: +61 3 9925 6108.

E-mail address: [jiyuan.tu@rmit.edu.au](mailto:jiyuan.tu@rmit.edu.au) (J. Tu).

significantly the airflow pattern and play an important role in transporting aerosol particles in the vicinity of a human body. This is especially true for fine and ultrafine particles as their movement is mostly controlled by the indoor flow field [15].

During the past years, the effects of human thermal plume on aerosol particle transport and inhalation in quiescent air have been investigated by few researchers. For example, using a sedentary thermal manikin, Rim and Novoselac [12] experimentally investigated the effects of human thermal plume on the inhalability of fine/ultrafine particles in stratified indoor air. It was found that when the particle source was at floor level and in near proximity to an occupant, the inhaled particle concentration by the manikin was up to 4 times higher than the ambient concentration. This proved that the thermal plume plays an important role in transporting pollutants and particles from the floor level to the breathing zone. However, the conclusions based on quiescent or quasi-quiescent indoor air conditions may not be quantitatively applicable to realistic situations where ventilation is operating and the orientation of an occupant relative to the free stream may be random. Therefore, for the purpose of accurate description of the effects of human metabolic heat on particle transport and inhalation, some important factors including the wind speed and the occupant orientation relative to the wind have to be taken into account.

Therefore in this study, in order that the role of human body heat in particle transport and inhalation could be better understood, a series of CFD computations were conducted using a standing thermal manikin. Various factors including the wind speed (0.05–0.25 m/s), manikin orientation relative to the free stream (back-to-the-wind or facing-the-wind) and their combinations were investigated. For the purpose of comparison, computations with isothermal conditions were also performed. The predicted airflow field was in good agreement with the experimental data available in the literature. The trajectories of inhaled particles under various conditions were also presented and discussed. The outcome yielded from this study can help to reduce contaminant exposure through appropriate orientation arrangement in indoor environments.

## 2. Numerical methods

### 2.1. Geometric model and boundary conditions

The computational domain of this study was a rectangular wind tunnel containing a 1.6 m tall standing human manikin facing

the +X direction and with its nose tip in the plane of  $X = 0$  m, as illustrated in Fig. 1. The dimensions of the computational wind tunnel (4 m-width  $\times$  7 m-depth  $\times$  3 m-height) were created large enough so that the flow field near the manikin was free from the effects of the no-slip condition of the stationary surrounding walls. In order that the detailed airflow pattern and particle transport characteristics in the breathing zone could be captured, the manikin head was carefully built to represent 50 percentage of a human male aged between 20 and 65 years [16]. For the purpose of saving computational cost, the manikin body was simplified. Unstructured tetrahedral and prism meshes were adopted to discretize the computational domain, with fine meshes around the manikin to capture the geometric features of the manikin and the effects of human thermal plume, as illustrated in Fig. 2. The grid sensitivity test proved that the mesh independence was achieved at 4.0 million cells, with the skewness of the cells and  $y^+$  value on the walls dropped below 0.8 and 0.78 respectively.

In total 21 cases were computed with various combinations of free stream speed, manikin orientation relative to the free stream and the status of heat transfer, as summarized in Table 1. For each computational case, evenly distributed airflow velocity profile was applied at the tunnel inlet and a zero pressure boundary condition was applied at the tunnel outlet. For the facing-the-wind cases, the inlet was on the +X side and the outlet was on the -X side of the tunnel, which makes the free stream flows in the -X direction (Fig. 1). On the contrary, the inlet was on the -X side and the outlet was on the +X side of the tunnel for the back-to-the-wind cases, which makes the free stream flows in the +X direction (Fig. 1). The free stream velocity was chosen to be in the range of 0.05–0.25 m/s, which represents the typical wind speeds in most indoor occupational environments [14]. The periodic respiration activities of the human body were neglected and the inhalation was assumed to be steady according to Horschler et al. [17]. A constant inhalation rate of 15 litres per minute (LPM) representing a human light breath at light activity conditions [7,18] was applied equally at the manikin nostrils, namely 7.5 LPM for each nostril.

For heat transfer modelling, the heat transfer between the air phase and the particle phase is neglected due to the dilute particle concentration. A constant free stream temperature of 26 °C, which is a typical air-conditioning ventilation temperature in summer seasons, was applied at the inlet and a constant temperature of 31 °C was applied at the manikin surface, as recommended by Gao and Niu [19]. The tunnel walls were assumed to be adiabatic.

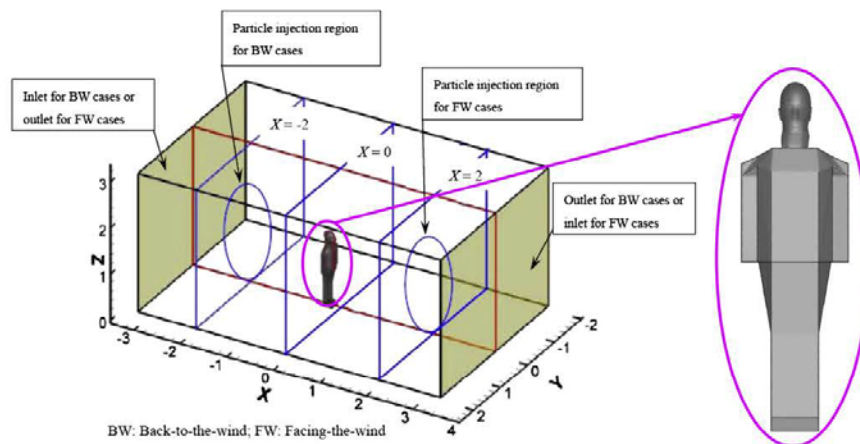


Fig. 1. The computational domain and human manikin.



Fig. 2. Refined meshes around the manikin model.

In order that the particle trajectories are fully developed before being affected by the thermal plume, particles with density of  $1000 \text{ kg/m}^3$  are released from a circular region with 1.6 m diameter and located far away enough (2.0 m) from the nose tip plane. Namely, the particle release region is located in the  $X = 2.0 \text{ m}$  plane for the facing-the-wind cases and in the  $X = -2.0 \text{ m}$  plane for the back-to-the-wind cases (See Fig. 1). The particle size was chosen to be small enough ( $1.0 \mu\text{m}$ ) so that the effect of gravitational settling could be neglected and the transport of particles is mostly controlled by the airflow field [20]. To achieve a uniform particle concentration assumption and to satisfy the “negligible bluff-off effects” criteria proposed by Chung et al. [21], the particles were released at the same velocity as that of the free stream.

Table 1  
Computational cases.

Case no.	Wind speed (m/s)	Orientation	Type of flow	$T_{\text{inlet}}$ (°C)	$T_{\text{manikin}}$ (°C)
1	0.05	Facing the wind	Isothermal	–	–
2	0.1				
3	0.15				
4	0.2				
5	0.25				
6	0.05	Facing the wind	Thermal	26	31
7	0.1				
8	0.15				
9	0.2				
10	0.25				
11	0.05	Back to the wind	Isothermal	–	–
12	0.1				
13	0.15				
14	0.2				
15	0.25				
16	0.05	Back to the wind	Thermal	26	31
17	0.1				
18	0.15				
19	0.2				
20	0.23				
21	0.25				

## 2.2. Flow and heat transfer models

The steady, incompressible Navier–Stokes equations are solved for the airflow field, where the continuity, momentum and energy equations are given in Equations (1)–(3), respectively.

$$\nabla \cdot (\rho \bar{U}) = 0 \quad (1)$$

$$\nabla \cdot (\rho \bar{U} \otimes \bar{U}) = \nabla \cdot (\mu + \mu_t) \left( \nabla \bar{U} + (\nabla \bar{U})^T - \frac{2}{3} \delta_{ij} \nabla \cdot \bar{U} \right) - \nabla p + S_{\text{buoy}} \quad (2)$$

$$\nabla \cdot (\rho \bar{U} h) = \nabla \cdot (\lambda \nabla T) + \tau : \nabla \bar{U} \quad (3)$$

where,  $\rho$ ,  $\bar{U}$ ,  $p$ ,  $h$  and  $T$  are density, velocity, pressure, enthalpy and temperature of the air, respectively.  $\delta_{ij}$  is the Kronecher delta,  $\mu$  and  $\mu_t$  are molecular and turbulent viscosity, respectively.  $\tau : \nabla \bar{U}$  is the viscous dissipation.  $S_{\text{buoy}}$ , which represents the momentum source term due to the buoyancy force induced by the air temperature gradient, is defined by

$$S_{\text{buoy}} = -\rho_{\text{ref}} \beta (T - T_{\text{ref}}) \quad (4)$$

where,  $\beta$  is the thermal expansivity of air.  $\rho_{\text{ref}}$  and  $T_{\text{ref}}$  are the buoyancy reference density and temperature, which take values of the air density and temperature at the inlet, respectively.

The Re-Normalisation Group (RNG)  $k-\varepsilon$  model was chosen for the airflow turbulence because of its successful utilization in the simulations of indoor pollutant transport [22]. To resolve the boundary layer in the near wall regions, the Scalable Wall Function [23] was used. The pressure-velocity coupling was resolved using the SIMPLEC algorithm. The convective terms of the transport equations were discretized using second-order-upwind scheme in order to obtain sufficiently accurate solutions.

The particles are tracked through the air separately using the Lagrangian approach. There are many forces acting on a particle submerged in a continuous fluid, however, for micron particles with high density, the forces that depend on the density ratio are negligibly small [16]. Therefore, only the drag force  $F_D$  and the buoyancy force  $F_B$  are considered in this study and the equation of particle motion is given by

$$m_p \frac{d\bar{U}_p}{dt} = \bar{F}_D + \bar{F}_B \quad (5)$$

The drag force and buoyancy force are defined by

$$\bar{F}_D = \frac{1}{2} C_D \rho A_p |\bar{U} - \bar{U}_p| (\bar{U} - \bar{U}_p) \quad (6)$$

$$\bar{F}_B = (m_p - m) \bar{g} = \frac{\pi}{6} d_p^3 (\rho_p - \rho) \bar{g} \quad (7)$$

where,  $m_p$ ,  $\bar{U}_p$  and  $d_p$  are the particle mass, velocity and diameter, respectively,  $A_p$  is the projected particle area in the flow direction. The drag coefficient  $C_D$  is modelled by

$$C_D = \max \left( \frac{24}{\text{Re}} \left( 1 + 0.15 \text{Re}_p^{0.687} \right), 0.44 \right) \quad (8)$$

The above equations were solved in ANSYS CFX 12.1 using a segregated solver with an implicit formulation. The residual

values of the transport equations were set to converge at  $10^{-5}$  or below for all simulation cases.

### 3. Results and discussion

#### 3.1. Airflow field

The predicted airflow field was compared against Heist et al.'s [24] experimental data. In their experiments, Heist et al. [24] investigated the airflow pattern around a child-size manikin (80 cm in height, without breathing) standing with its back towards the coming free stream in a wind tunnel using laser Doppler anemometry. Particle transport was not included in the experiments. Heist et al.'s [24] experiments were conducted under isothermal and thermal conditions, respectively. In the isothermal condition, both the free stream and the manikin had the same temperature (21 °C) while in thermal condition, the temperatures of the free stream and the manikin surface were maintained at 21 °C and 33 °C, respectively. In order to achieve hydrodynamic and thermodynamic similarities with the experimental setup, boundary conditions of the CFD model were carefully chosen to produce an equal Reynolds number for the isothermal case and an equal Richardson number (Ri) for the thermal case, respectively, as listed in Table 2. The Richardson number is defined by

$$Ri = \frac{Gr}{Re^2} = \frac{g\beta(T_s - T_{ref})H}{u^2} \quad (9)$$

where, Gr and Re are the Grashof number and Reynolds number, respectively.  $T_s$  is the manikin surface temperature,  $H$  is the manikin height and  $u$  is the velocity of the free stream.

The predicted airflow fields around the manikin under isothermal and thermal conditions are compared against the experimental results in Figs. 3 and 4, respectively. For the convenience of comparison, the coordinates in the figures are normalized with the manikin height ( $H$ ).

Fig. 3 (a) and (b) illustrates the airflow velocity vectors in the symmetry plane of the manikin ( $Y = 0$  m). It was found that under the isothermal conditions, a wake region containing two counter-rotating vortices is formed on the downstream side of the manikin. One of the vortices is larger and is located in the breathing zone while the other one is smaller and is located at a lower height (near the legs). The former vortex entrains air flowing around the head into the breathing zone. This suggests that aerosol contaminants that may be inhaled by an occupant are released from a source located at a height of the breathing zone. Similarly, due to the obstacle of the solid manikin, vortices are also observed in the horizontal planes. Fig. 3 (c) and (d) illustrates the airflow vectors in the horizontal plane of  $Z/H = 0.6$ , where two counter-rotating elliptical vortices are distributed symmetrically on the downstream side of the manikin.

However, both the experiments and the numerical simulations under the thermal conditions presented a totally different figure of the airflow pattern. As illustrated in Fig. 4 (a) and (b), when heat transfer between the manikin and the air is included, the vortex

region on the downstream side of the manikin (Fig. 3 (a) and (b)) is replaced by an upward rising airflow. Because of this rising airflow, the air in the breathing zone was observed to come from a lower height, especially from near the floor level, which indicates that the air and contaminants that may be inhaled are released from a source located near the floor. This difference makes the body heat an important consideration when locating the contaminant sources in actual situations. Meanwhile, the counter-rotating vortices in the horizontal plane of  $Z/H = 0.6$  (Fig. 3 (c) and (d)) are significantly suppressed in the thermal condition, as illustrated in Fig. 4 (c) and (d).

Comparisons illustrated in Figs. 3 and 4 suggest that the simulated airflow fields generally agree well with the experimental results. The difference in the local vector distributions (Fig. 3 (a) and (b)) may be due to the different geometric shape of the manikins. More importantly, it is proved that due to the heat transfer between a human body and its surrounding air, there actually exists a distinct upward rising airflow on the downstream side of the body. Because of this rising airflow, air and particulate contaminants in the breathing zone that may be inhaled by a human occupant actually come from a lower level than that of the breathing zone. Therefore, for the purpose of effective assessment of particle transport and inhalation, the effect of human body heat has to be taken into account, which will be discussed in the following sections.

The airflow field was also validated using the CFD result of our previous study [7] which employed the same manikin model but different mesh arrangement, as shown in Fig. 5. An isothermal and thermal case under the facing-the-wind condition (Case 4 and Case 9 respectively) were chosen for the validation since they had the same wind speed and manikin orientation with those in our previous study [7]. The airflow velocity distribution along a vertical line which was 1 mm in front of the nose tip and had a length of 10 cm (the red vertical dot line starting at the chin height, see Fig. 5) was plotted and compared against King Se's [7] CFD results. For the convenience of comparison, the airflow velocity and the  $Z$  coordinate were normalized with the maximum velocity in this line and the length of the line, respectively. It was found that the predicted air velocity distribution was in a good agreement with our previously validated data. It also seemed that under facing-to-the-wind condition, the body heat has no obvious effects on air velocity distribution in the breathing zone. (For interpretation of the references to colour in this figure legend, the reader is referred to the web version of this article.)

#### 3.2. Particle trajectories

As aforementioned, the affected region of body heat in a ventilated space is located at the downstream side of a human body. This indicates that when the manikin is facing the wind, the effect of body heat on particle inhalation is not significant since the airflow field in the breathing zone does not change significantly. Computations demonstrated that for the facing-the-wind cases, despite the totally different airflow field on the downstream side of the manikin, the tracks of inhaled particles are slightly different for the isothermal and thermal cases (Fig. 6). However, when the wind speed is low (typically lower than 0.1 m/s), the particle tracks on the upstream side of the manikin were observed to ascend in an isothermal case while slightly descending for a thermal case. Similar phenomena were also observed by Schmees et al. [14] in their visualization experiments of the airflow field around a thermal manikin standing in a wind tunnel (Fig. 6(b)), which had a similar thermo-hydrodynamic condition with that in this study. It was revealed that the ascending particle tracks in an isothermal case are due to the

**Table 2**  
Experimental setup and boundary conditions of validation computations.

	$u$ (m/s)	$T_{ref}$ (°C)	$T_s$ (°C)	$H$ (m)	Re	Ri
Experiment-isothermal [19]	0.1	21	21	0.8	5481	–
Simulation-isothermal	0.051	21	21	1.6	5481	–
Experiment-thermal [19]	0.1	21	33	0.8	–	1.27
Simulation-thermal	0.051	21	22.6	1.6	–	1.27



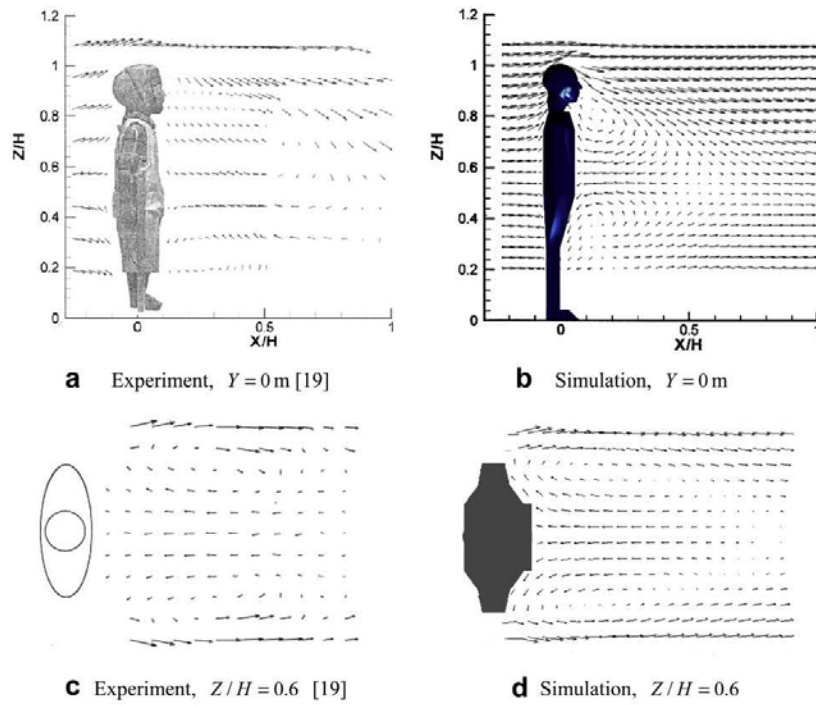


Fig. 3. Airflow velocity vectors under the isothermal condition.

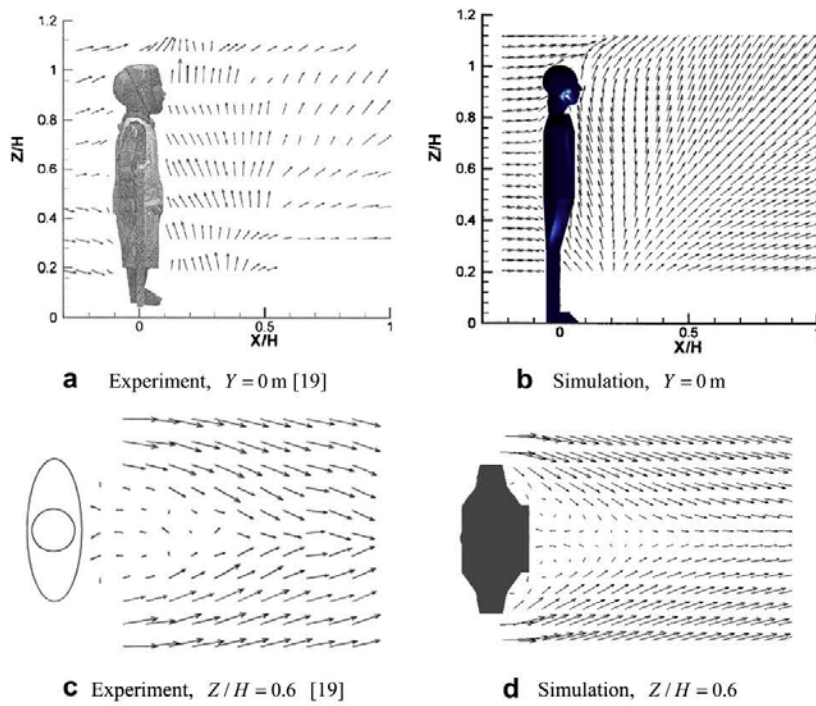


Fig. 4. Airflow velocity vectors under the thermal condition.

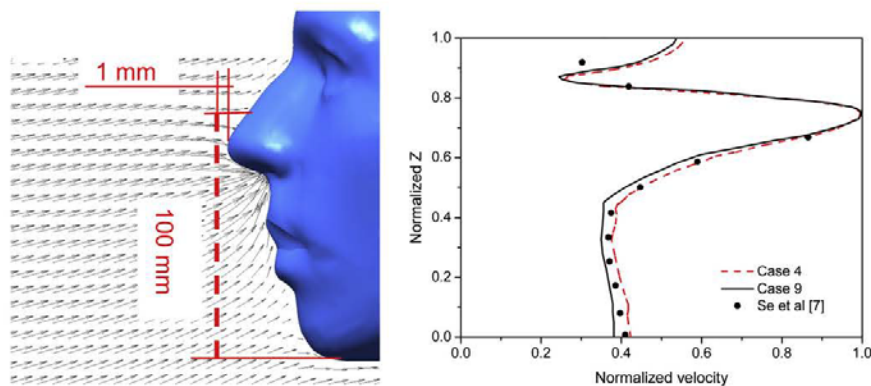


Fig. 5. Air velocity distribution in front of the nose tip.

rising airflow which bypasses the manikin while the descending particle tracks in a thermal case are associated with the body heat and the limited flow domain in the tunnel. As illustrated in Fig. 6(b), for a thermal manikin standing in a low-speed wind tunnel, the uprising airflow caused by the body heat forms a vortex flow when it reaches the top of the wind tunnel and is then mixed with the cold free stream. This vortex suppresses the oncoming airflow and causes a downward velocity. As a result of this, the airflow stream lines and the particle tracks upstream of the vortex are observed to descend. This vortex region is gradually eliminated with the increasing free stream speed. It was found that when the wind speed is larger than 0.2 m/s, no visible difference could be detected between the particle tracks predicted using the isothermal and thermal conditions, respectively.

On the other hand, when the manikin is back-to-the-wind oriented, computations presented totally different pictures of the tracks of inhaled particles for the isothermal and thermal cases, respectively. Fig. 7 illustrates typical airflow velocity vectors and tracks of inhaled particles under the isothermal and back-to-the-wind condition. It was found that when heat transfer is excluded from the CFD model, the predicted airflow field is similar to that shown in Fig. 3(b) and the inhaled particles are released from a source located at the breathing zone height and then passes the manikin head before being inhaled. It was also found that for the isothermal case, an increase in wind speed has no significant effect on the particle tracks and the airflow field profile.

Situations under the thermal and back-to-the-wind condition are much more complicated. Fig. 8 (a) illustrates that under the low wind-speed condition (0.05 m/s) and when heat transfer is included in the CFD model, a significant uprising airflow which is similar to that shown in Fig. 4 (b) is predicted and the particles being inhaled are actually released from a source located much lower than the breathing zone (near the floor level). As shown in Fig. 8 (a), particles approaching the manikin with the airflow bend their way upwards due to the buoyancy induced by the body heat. This is obviously different to what is shown in Fig. 7 but in good agreement with Rim's [12] experimental observations. In addition, it is also noticed that the uprising airflow on the downstream side of the manikin gradually develops into a vortex flow with increasing wind speed. With further increasing wind speed, the size of the vortex region increases in the horizontal direction while decreases in the vertical direction, as shown in Fig. 8 (b)–(d). Accordingly, particles go through a longer curved path before

being inhaled due to the increased inertia. At the same time, it is noticed that another vortex with reverse rotation begins to appear and then expand its size and intensity at the manikin face height. The second vortex is formed due to the increased intensity of the free stream relative to the uprising airflow induced by the body heat. Computations proved that when the wind speed increases up to 0.23 m/s, particles released at the manikin face height, whose movement trajectories are not affected by the body heat, are also inhaled together with those released at a lower height whose tracks are controlled by the rising airflow (Fig. 8(c)). This indicates that the effect of body heat is suppressed by the increased wind speed. Finally, as the wind speed reaches 0.25 m/s (Fig. 8(d)), the thermal convection is not able to entrain particles into the breathing zone from the lower level so that only particles released at the face height are inhaled. A comparison of the airflow velocity vectors in Fig. 8(d) with those in Fig. 7 suggests that under such a high wind speed, body heat has only a negligibly weak effect on the airflow field.

### 3.3. The critical area

The particle tracks were further analysed using the so-called "critical area" concept, which is defined by Anthony et al. [2] as a finite area upstream of the breathing person where particles are inhaled. For the issue of this study, the critical area is located in the plane of particle injection (2.0 m upstream of the manikin). It was found that for the back-to-the-wind cases and when heat transfer was not included in the CFD model, the predicted critical areas (illustrated by solid marks in Fig. 9) were roughly located at the nose height and their dimensions were quite small. On the other hand when the body heat was taken into account, the predicted critical areas (illustrated by hollow marks in Fig. 9) were much larger but located at a lower height (around at the knee height). In addition, it was also noticed that the critical areas were roughly symmetrically distributed around the  $Y = 0$  plane. This is physically reasonable since particles had to pass around the manikin (Fig. 8) before being inhaled. Under the thermal condition, the critical area shrank and moved upwards with increasing wind speed so that the body heat seemed to have no effect on particle inhalation when the wind speed reached 0.25 m/s as the critical area moved up to the nose height and overlapped the critical areas predicted using the isothermal conditions. This phenomenon makes it very crucial to take into account the body heat when investigating particle transport and inhalation in low-speed indoor environment.

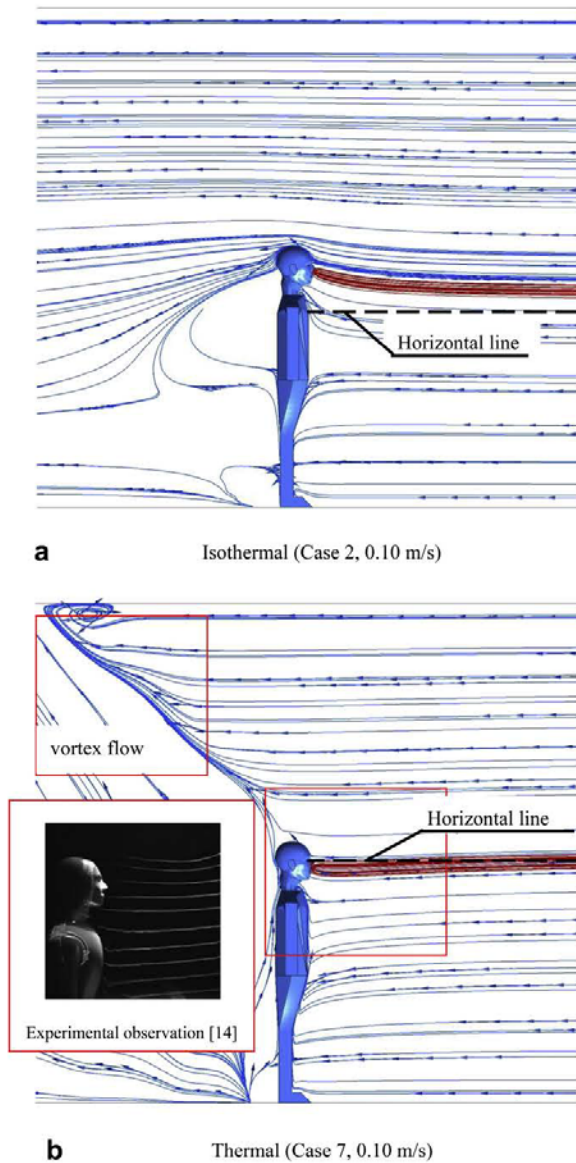


Fig. 6. Particle tracks and stream lines in the facing-the-wind cases.

For the purpose of further comparison, the central height of the critical areas under various conditions, including thermal and isothermal, as well as facing-the-wind and back-to-the-wind cases, are illustrated in Fig. 10. It is found that when the manikin is facing-the-wind and heat transfer is not included in the model, the wind speed has no effect on the central height of critical areas. When heat transfer is included in the facing-the-wind computations, the central height of critical area decreases gradually with increasing wind speed and finally approaches that of the isothermal cases. This phenomenon can be reasonably explained using Fig. 6 (b). In addition, when the manikin is back-to-the-wind and heat transfer is not considered, the predicted central height of critical area is still around the nose level, but slightly rises with increasing wind speed

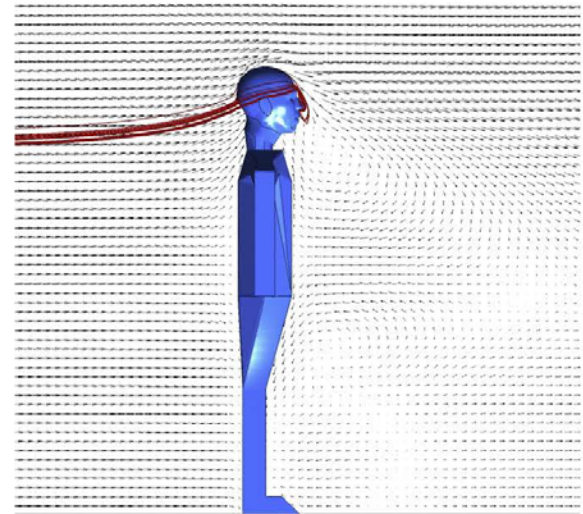


Fig. 7. Typical airflow field and particle tracks under the back-to-the-wind and isothermal condition (Case 15, 0.25 m/s).

until approaching the horizontal lines representing the facing-the-wind and isothermal cases. However, the curve for the back-to-the-wind and thermal cases is totally different from the others. Fig. 10 illustrates that the central height of the critical area is quite low (typically near the floor) at low wind speed, then rises slightly with increasing wind speed. When the wind speed is larger than 0.2 m/s, the central height of critical area increases sharply because particles released at the nose height start to be inhaled. The portion of inhaled higher-level particles increases sharply so that when the wind speed approaches 0.25 m/s, no particles from the lower level could be inhaled and the effect of body heat on particle inhalation is totally suppressed.

Fig. 10 actually suggests that although the human metabolic heat has a significant effect on the airflow field in the vicinity of an occupant, its effect on particle inhalation is associated with the wind speed and the occupant-wind orientation. When an occupant is facing-the-wind, the particle tracks are slightly affected by the body heat and this effect is eliminated when the wind speed is over 0.2 m/s. However, when the occupant is back-to-the-wind, the inclusion of heat transfer in the CFD model leads to a totally different track distribution of inhaled particles. Similarly, it seems that the effect of body heat is largely suppressed as the wind speed is over 0.2 m/s. Despite this, for the purpose of effective modelling, human body heat remains an important consideration when investigating particle inhalation in indoor environment since the wind speed in most indoor spaces is lower than 0.25 m/s and the occupant-wind orientation may be random.

In summary, the effects of human body heat on particle inhalation can be summarized as follows: (1) When an occupant is facing the wind, the effects of body heat can be safely ignored since the affected region is located on the downstream side of the body. (2) When an occupant is oriented to be back-to-the-wind and the wind speed is lower than 0.2 m/s, the thermal plume caused by body heat plays an important role in transporting particle into the breathing zone from lower levels. However, even under the back-to-the-wind condition the effect of body heat on particle inhalation is gradually suppressed with increasing wind speed. As the wind speed rises up to 0.25 m/s, the effects of body heat on airflow

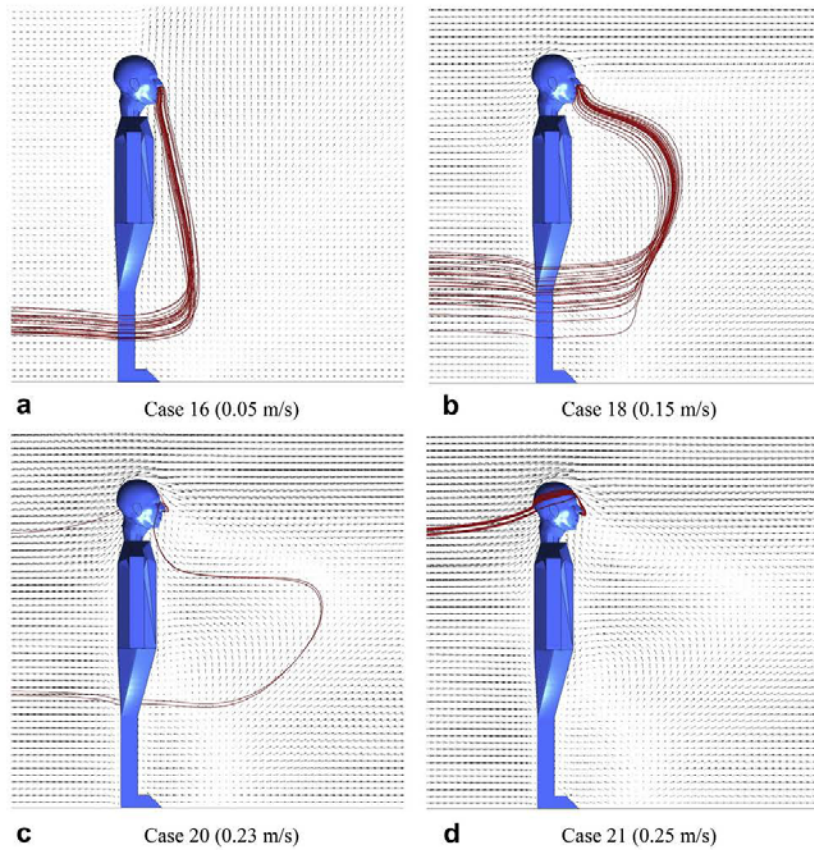


Fig. 8. Particle tracks under the thermal and back-to-the-wind condition.

field as well as particle transport and inhalation could not be detected and therefore could be ignored.

It should also be noted that since the average wind speed in most indoor environments is lower than 0.2 m/s according to the

survey conducted by Baldwin and Maynard [13], the human body heat still remains an important consideration when investigating particle inhalation in indoor environment and assessing the health risks associated with particle inhalation.

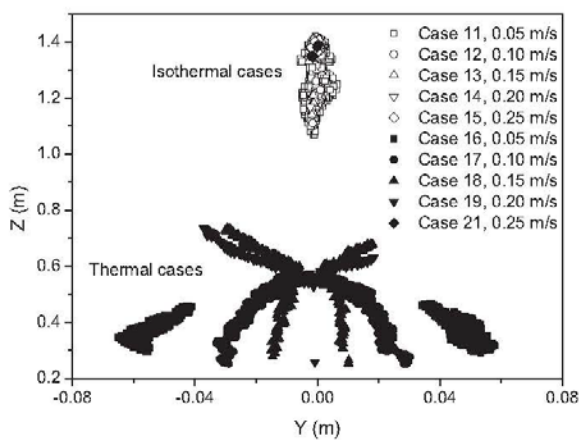


Fig. 9. Critical areas under the back-to-the-wind condition.

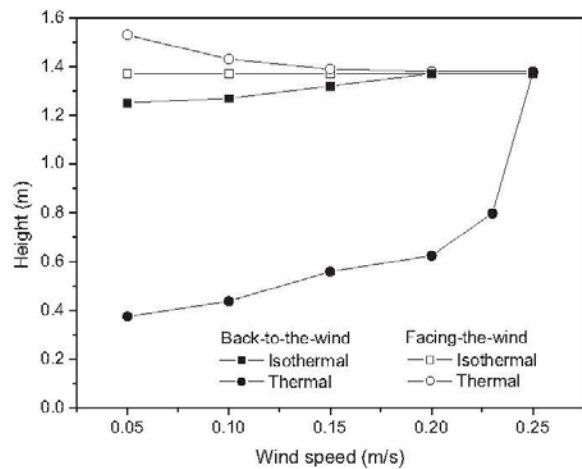


Fig. 10. Central height of the critical area vs. wind speed.

#### 4. Conclusion

The effect of body heat on particle inhalation by a human manikin in a ventilated indoor environment was numerically investigated using CFD. Computations were conducted under both the facing-the-wind and back-to-the-wind conditions, as well as the isothermal and thermal conditions, respectively. Satisfactory agreement was obtained between the predicted airflow fields and the experimental observations available in the literature. The main conclusions arising from this study are as follows:

- (1) For most indoor environments where the wind speed is lower than 0.2 m/s, the body heat causes a significant uprising airflow on the downstream side of the human body, which makes the occupant orientation relative to the free stream a crucial factor determining the importance of body heat on particle inhalation. When the occupant is facing-the-wind, the effect of body heat on particle inhalation could be safely neglected. However, when the manikin is back-to-the-wind, body heat plays an important role in transporting particles from near the floor level into the breathing zone.
- (2) Although the effect of body heat is gradually suppressed by the increasing wind speed and this effect can be safely ignored when the wind speed is over 0.25 m/s, it still remains an important consideration when investigating particle transport and inhalation in most indoor environments where the wind speed is lower than 0.25 m/s.

#### Acknowledgements

The financial supports provided by the National Basic Research Program (973) of China (Grant No. 2012CB720100) and by the Australian Research Council (project ID LP110100140) are gratefully acknowledged.

#### References

- [1] Inthavong K, Tian ZF, Tu JY. Effects of ventilation design on removal of particles in woodturning workstations. *Build Environ* 2009;44:125–36.
- [2] Anthony TR, Flynn MR. Computational fluid dynamics investigation of particle inhalability. *J Aerosol Sci* 2006;37:750–65.
- [3] Anthony TR, Flynn MR, Eisner A. Evaluation of facial features on particle inhalation. *Ann Occup Hyg* 2005;49:179–93.
- [4] Aitken RJ, Baldwin PEJ, Beaumont GC, Kenny LC, Maynard AD. Aerosol inhalability in low air movement environments. *J Aerosol Sci* 1999;30:613–26.
- [5] Hsu D-J, Swift DL. The measurements of human inhalability of ultralarge aerosols in calm air using mannikins. *J Aerosol Sci* 1999;30:1331–43.
- [6] Hinds WC, Kennedy NJ, Tatyana K. Inhalability of large particles for mouth and nose breathing. *J Aerosol Sci* 1998;29(Suppl. 1):S277–8.
- [7] King Se CM, Inthavong K, Tu J. Inhalability of micron particles through the nose and mouth. *Inhal Toxicol* 2010;22:287–300.
- [8] Gowadia HA, Settles GS. Natural sampling of airborne trace signals from explosives concealed upon the human body. *J Forensic Sci* 2001;46:1324–31.
- [9] Homma H, Yakiyama M. Examination of free convection around occupant's body caused by its metabolic heat. *ASHRAE Trans* 1988;94:104–24.
- [10] Johnson AE, Fletcher B, Saunders CJ. Air movement around a worker in a low-speed flow field. *Annu Occup Hyg* 1996;40:57–64.
- [11] Craven BA, Settles GS. A computational and experimental investigation of the human thermal plume. *J Fluid Eng-T Asme* 2006;128:1251–8.
- [12] Rim D, Novoselac A. Transport of particulate and gaseous pollutants in the vicinity of a human body. *Build Environ* 2009;44:1840–9.
- [13] Baldwin PEJ, Maynard AD. A survey of wind speeds in indoor workplaces. *Ann Occup Hyg* 1998;42:303–13.
- [14] Schmees DK, Wu YH, Vincent JH. Visualization of the airflow around a life-sized, heated, breathing mannequin at ultralow windspeeds. *Annu Occup Hyg* 2008;52:351–60.
- [15] Longest PW, Kleinstreuer C, Buchanan JR. Efficient computation of micro-particle dynamics including wall effects. *Comput Fluids* 2004;33:577–601.
- [16] Li X, Inthavong K, Tu J. Particle inhalation and deposition in a human nasal cavity from the external surrounding environment. *Build Environ* 2011;47:32–49.
- [17] Horschler I, Schroder W, Meinke M. On the assumption of steadiness of nasal cavity flow. *J Biomech* 2010;43:1081–5.
- [18] Snyder WS, Cook MJ, Nasset ES, Karhausen LR, Parry Howells G, Tipton JH. Report of the task group on reference man. Pergamon Press; 1975.
- [19] Gao N, Niu J. CFD study on micro-environment around human body and personalized ventilation. *Build Environ* 2004;39:795–805.
- [20] Jiang J, Zhao K. Airflow and nanoparticle deposition in rat nose under various breathing and sniffing conditions—A computational evaluation of the unsteady and turbulent effect. *J Aerosol Sci* 2010;41:1030–43.
- [21] Liu H, Zou C, Shi B, Tian Z, Zhang L, Zheng C. Thermal lattice-BGK model based on large-eddy simulation of turbulent natural convection due to internal heat generation. *Int J of Heat and Mass Transfer* 2006;49:4672–80.
- [22] van Treeck C, Rank E, Krafczyk M, Tölke J, Nachtwey B. Extension of a hybrid thermal LBE scheme for large-eddy simulations of turbulent convective flows. *Comput Fluids* 2006;35:863–71.
- [23] Mortensen M, Reif BAP, Wasberg CE. Assessment of the finite volume method applied to the V2F model. *Int J Numer Methods Fluids* 2010;63:495–516.
- [24] Heist DK, Eisner AD, Mitchell W, Wiener R. Airflow around a child-size manikin in a low-speed wind environment. *Aerosol Sci Technol* 2003;37:303–14.

RESEARCH ARTICLE

# Local deposition fractions of ultrafine particles in a human nasal-sinus cavity CFD model

Qin Jiang Ge<sup>1</sup>, Kiao Inthavong<sup>1</sup>, and Ji Yuan Tu<sup>1,2</sup>

<sup>1</sup>School of Aerospace, Mechanical and Manufacturing Engineering, RMIT University, Australia and <sup>2</sup>Department of Building Science, Tsinghua University, Beijing, China

## Abstract

Ultrafine particle deposition studies in the human nasal cavity regions often omit the paranasal sinus regions. Because of the highly diffusive nature of nanoparticles, it is conjectured that deposition by diffusion may occur in the paranasal sinuses, which may affect the residual deposition fraction that leaves the nasal cavity. Two identical CFD models of a human nasal cavity, one with sinuses and one without, were reconstructed from CT-scans to determine the uptake of ultrafine particles. In general, there was little flow passing through the paranasal sinuses. However, flow patterns revealed that some streamlines reached the upper nasal cavity near the olfactory regions. These flow paths promote particle deposition in the sphenoid and ethmoid sinuses. It was found that there were some differences in the deposition fractions and patterns for 5 and 10 nm particles between the nasal-sinus and the nasal cavity models. This difference is amplified when the flow rate is decreased and at a flow rate of 4 L/min the maximum difference was 17%. It is suggested that evaluations of nanoparticle deposition should consider some deposition occurring in the paranasal sinuses especially if flow rates are of concern.

**Keywords:** Nasal cavity, sinus, nanoparticle, CFD

## Introduction

Particle deposition studies caused by inhalation through the nasal cavity have been performed using (i) computational fluid dynamics (CFD) methods (Schroeter et al., 2006a), (ii) replicate cast models of a nasal cavity (Cheng et al., 2001; Kelly et al., 2004) or by using and (iii) *in-vivo* human subjects (Cheng et al., 1995; Cheng et al., 1996b). The particle deposition data obtained from these methods are used interchangeably to compare and verify results. In CFD and replicate cast methods the nasal cavity is extracted from MRI or CT-scans of the respiratory system, and often the end product omits the paranasal sinuses. However, deposition data on a human subject is inclusive of the paranasal sinuses and it is unknown to what extent this influences the total and local deposition fractions in the nasal cavity.

According to Cheng et al. (1996a) aerosol deposition in the human respiratory airways is strongly influenced

by three major factors: physical (particle diameter, shape, and density), physiological (respiratory ventilation and pattern), and morphological (airway size and shape). Deposition of micron sized particles in the nasal cavity and the lung conductive airways is largely due to the particle inertia, and in general, significant for particles with aerodynamic diameters approximately greater than  $\sim 2 \mu\text{m}$ .

Studies have shown that the sharp curvatures in the nasal cavity airway that change the airflow direction are responsible for inertial deposition of micron particles (Inthavong et al., 2006, 2011a). This is particularly significant at the entrance to the main nasal passage and at the nasopharynx where the flow exhibits 90° curvatures. Inertial deposition mechanisms rely on flow convection which transports the particles before a sharp curvature is present. With regards to micron particle deposition in the maxillary sinus, (Xiong et al., 2008) indicated that little flow exchange occurred between the inner and outer

*Address for Correspondence:* Prof Jiyuan Tu, School of Aerospace, Mechanical and Manufacturing Engineering, RMIT University, PO Box 71, Bundoora Vic 3083, Australia. Tel: +61-3-9925 6191. Fax: +61-3-9925 6108. E-mail: jiyuan.tu@rmit.edu.au

(Received 28 February 2012; revised 09 May 2012; accepted 14 May 2012)

aspects of the paranasal sinuses. This suggests that it is unlikely that micron particles will be lost to the sinus regions and CFD and replicate cast studies omitting the sinus regions is applicable.

On the other hand, ultrafine particles are dominated by diffusion and their deposition onto its surrounding surfaces is reliant on a low convection to diffusion ratio (i.e. Peclet number). It should be noted that ultrafine particles are defined as particles between 1-100 nm in size which coincidentally is the same size range definition that is often used for nanoparticles (Auffan et al., 2009), and hence these two terms are often used interchangeably in the literature (Longest & Xi, 2007b). In this study the term ultrafine particles will be used to encompass particles 1-100 nm. If the flow rate through the nasal cavity is sufficiently low, the diffusion transport of ultrafine particles may be significant enough for the particles to pass into the paranasal sinuses. This suggests that ultrafine particles may be lost to the sinus regions (to what extent is unknown) and that the residual deposition fraction that leaves the nasal cavity and enters the downstream airway regions such as the trachea and bronchial region may need to be reconsidered.

The paranasal sinuses (maxillary, sphenoid, ethmoid and frontal) are air-filled spaces connected to the nasal cavity by narrow passageways called ostia. The exact biologic function of the sinuses is uncertain but are thought to contribute to the following: reduction of the weight of the front of the skull; act as a resonating chamber for voice production; humidifying, heating, and filtering of inhaled air through mucus secretions; and absorption of any force impacting on the face or skull (Keir, 2009).

Deposition of ultrafine particles within these sinuses or around the ostia is important due to their potential clinical ramifications. Ultrafine particles that cause irritation or an allergic reaction can result in swelling of the ostium, impaired sinus mucus drainage and subsequent sinusitis, a condition that exacerbates existing respiratory ailments (Slavin, 1988). Furthermore, the paranasal sinuses (in particular the maxillary sinus) are a potential site for malignancy. For example, it is well established that there are links between tobacco smoke, formaldehyde (Halperin et al., 1983), and nasal cancer, but studies have shown that inhalation of airborne toxic ultrafine particles such as wood dust (Elwood, 1981), air pollution and fumes (Calderón-Garciduenas et al., 2000) may be a significant risk factor in the development of paranasal sinus cancer. As nanotechnology plays a bigger part in society and day to day exposure to ultrafine particles increases, diffusion of these potentially carcinogenic ultrafine particles into the sinuses could be a significant contributor to malignant tumors of the sinuses. Paranasal sinus tumors are often diagnosed late and thus have a very poor prognosis. To date, nearly all CFD studies of particle deposition through the nasal cavity have neglected the paranasal sinuses, although there have been two studies of air flow

distribution through the nasal cavity that include the paranasal sinuses (Lindemann et al., 2005; Xiong et al., 2008).

Therefore, the aim of this study is to investigate the flow patterns in the nasal cavity, in the paranasal ostium and its corresponding sinus, and to determine the uptake of ultrafine particles with a focus on the ostium region that may occlude due to deposition. The uptake of the ultrafine particles within the nasal-sinus model and in a nasal cavity model for different particle sizes is given. In addition, special attention is made to the modeling of the Brownian diffusion process to ensure that the predictions of the ultrafine particles are reliable. Micron sized particles which can be defined as anything greater than 1  $\mu\text{m}$  (although PM2.5 or fine particles - aerodynamic diameters <2.5  $\mu\text{m}$  and PM10 or coarse particles - aerodynamic diameters between 2.5  $\mu\text{m}$  and 10  $\mu\text{m}$ , are the standard classifications in toxicology), are not reported here as our preliminary testing found that micron particles from 1-100  $\mu\text{m}$  showed negligible differences between the nasal-sinus model, and nasal cavity model.

## Method

### Computational models

Four geometries were created for this study - a straight pipe, a 90° bend pipe, a human nasal cavity with paranasal sinuses included, and the same nasal cavity model without sinuses (Figure 1). Table 1 the geometries detailing significant dimensions and the computational boundary conditions that are applied. The pipe models are used to validate the Brownian model and to ensure it is reliable before applying it to the more complex nasal cavity. For the nasal cavity model, CT-scans of a healthy nose from a 51-year-old Asian male, was obtained. The scans were performed using a whole body scanner by Phillips® at No.3 Hospital, Shanghai with the subject's approval and consent for participation in this study. The scan protocol included slice thickness is 0.625 mm, and the single pixel space is 0.976 × 0.976 mm, a 300 × 500 mm field of view, 30 kV peak, and 200 mA.

The outline of the model was segmented from the CT-scans and a computational mesh for CFD analysis was applied. Two nasal cavity models were reconstructed from the same CT-scans, and are labeled as NC02 (nasal cavity without paranasal sinuses) and NC02-S (nasal cavity with paranasal sinuses), noting that the difference in the labels is the character S to denote the addition of the sinuses. The geometry of the NC02-S model is shown in Figure 1c. The length from the anterior most region to the posterior nasopharynx region is approximately 9 cm, while the height from the main nasal passage floor to the superior tip of the frontal sinus is approximately 7 cm. It should be noted that the surface walls of the computational model are smooth and rigid, and lacks nose hair and mucous. For ultrafine particles, where the deposition is diffusion dominant, the presence of nose hair can have some impact on the deposition. This phenomenon is yet to be researched.

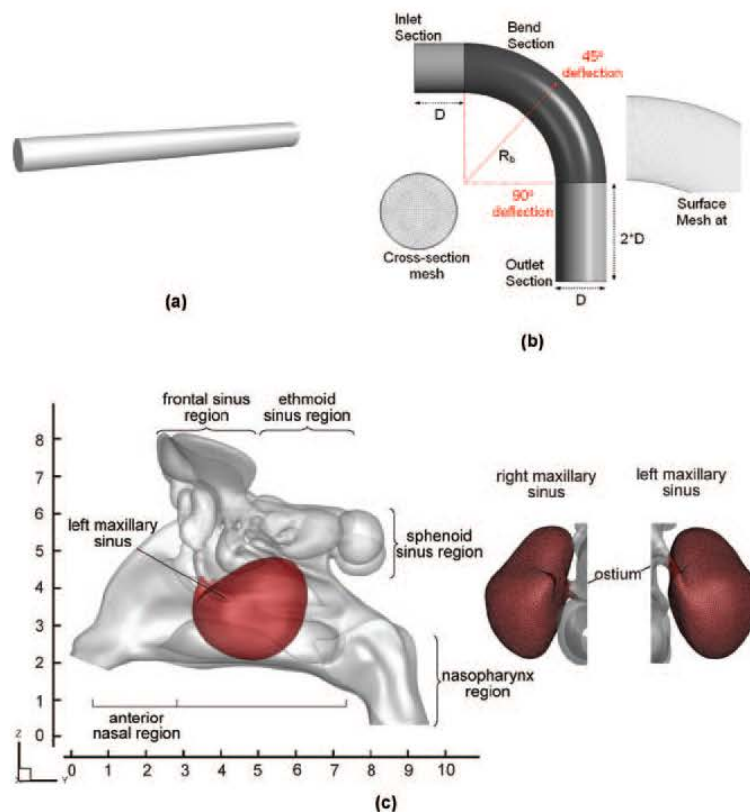


Figure 1. CFD geometries used in this study for (a) straight pipe, (b) 90° bend pipe, and (c) nasal cavity with sinus model.

Table 1. Dimensions and details of the geometries considered in this study.

	Inlet hydraulic diameter ( $D_h$ )	Radius of curvature, $R_b$	Inlet flow rate (L/min)	Inlet Renumber	Mesh size
Straight pipe	0.45 cm	-	1	322	750,000
90° bend pipe	0.46 cm	1.43 cm	1.052	4840	550,000
Nasal cavity without sinus (NC02)	1.0 cm	-	4	255	3.0 million
Nasal cavity with sinus (NC02-S)	1.0 cm	-	4	278	4.0 million
			10	705	

The meshing scheme used a hybrid mesh that included six-prismatic layers with an inner tetrahedral core. Grid independence based on velocity profiles at the outlet was performed (up to 10 million cells) where the optimum number of cells (3 million for NC02 and 4 million for NC02-S) for each geometry is given in Table 1, along with dimensions and details of the flow rate. This implies that the geometries showed less than 1% change in velocity profiles when the mesh was further refined.

The influence of computational smoothing on airflow resistance and particle deposition has been discussed in Schroeter et al. (2011). The models used in this study

underwent 5% level of smoothing to ensure that any artificial residual artefacts persisting from the scanned images were omitted from the final computational model. Given that images obtained from CT-scans are more prone to artefacts than other conventional radiographs, the level of smoothing applied allowed a compromise between retention of real geometry artefacts (e.g. overlying mucus) to artificially created artefacts caused by CT-scans and its segmentation (e.g. streaking, distortion and shading due inconsistency and inaccuracy of scanner, or patient movement or the presence of metallic materials in or on the patient) and CAD file interpretations.



### Fluid modeling

The geometries were inputted into a commercial CFD code, Ansys-FLUENT v12.1, where the governing equations for fluid flow under steady-state conditions were modeled. Flow rates of 1, and 10 L/min were used for the straight pipe and 90° bend pipe while low steady flow rates of 4, and 10 L/min were used for the nasal cavity to allow similar comparisons with *in-vivo* data at 10 L/min (Cheng et al., 1996a), *in-vitro* replicate cast deposition data at 4, 10 L/min (Cheng et al., 1995; Kelly et al., 2004), and numerical studies (Zamankhan et al., 2006; Shi et al., 2008). The inspiratory flow rates for adults can range between 5–12 L/min for light breathing and 12–40 L/min for non-normal conditions such as during exertion and physical exercise. Usually breathing switches from pure nasal flow to oral-nasal flow at this higher range. Interestingly Robert (2001) tested 68 patients to obtain forced inspiratory nasal flow-volume curves, which showed that some inspiratory peak flows reached up to 150 L/min, although this is highly unsustainable over any breathing cycle.

Up to a flow rate of 15 L/min the flow regime in the respiratory airways has been determined as dominantly laminar (Hahn et al., 1993; Swift & Proctor, 1977b; Kelly et al., 2000; Zamankhan et al., 2006), although traces of turbulent flow structures may exist. There is some debate to the correct treatment of the flow field as laminar or transitional turbulence. Like many unstable flows within complex geometries, the critical flow rate and hence the critical Reynolds number ( $Re_{cr}$ ) at which the flow transitions from a laminar regime cannot be succinctly defined, nor can it be applied generally to all nasal cavities which inherently possess geometry differences. The varying critical  $Re$  is mainly due to sharp and sudden changes in the nasal cavity geometries that create diverging flows and flow separation, all contributing to flow instability. Experimental studies by Swift and Proctor (1977a) and Kelly et al. (2000) have suggested that a laminar flow regime dominates for low flow rates around 10 L/min. Hahn et al. (1993) results also concur where a flow rate for a single nasal chamber subjected to a flow rate of 10.8 L/min (-21.6 L/min for both nasal chamber sides) resulted in flow patterns that appeared laminar-like suggesting that for normal resting breathing, laminar-like flow dominates much of the nasal cavity. At higher flow rates of 33.6 and 66 L/min (-67.2 and 132 L/min for both nasal chamber sides), the flow was described as turbulent. Further experimental results by Churchill et al. (2004) showed that for ten nasal replicate cast models, the average rate at which flow switched from transitional to turbulent was 11 L/min. Despite this, a survey of more recent numerical simulations of realistic nasal airways show a consensus among researchers in using a laminar flow for flow rates less than 20 L/min (Schroeter et al., 2006b; Garcia et al., 2007). In this study a laminar flow model is used to focus on the diffusion process of the ultrafine particles and because of the low flow rates ( $\leq 10$  L/min).

The steady-state continuity and momentum equations for the gas phase (air) in Cartesian tensor notation can be cast as:

$$\frac{\partial}{\partial x_i}(\rho_g u_i^g) = 0 \quad (1)$$

$$u_j^g \frac{\partial u_i^g}{\partial x_j} = -\frac{1}{\rho} \frac{\partial p_g}{\partial x_i} + \frac{\partial}{\partial x_j} \left( \nu_g \frac{\partial u_i^g}{\partial x_j} \right) \quad (2)$$

where  $u_i^g$  is the  $i$ -th component of the time averaged velocity vector and  $\rho_g$  is the air density. The equations were discretized with the QUICK scheme while the pressure-velocity coupling was resolved through the SIMPLE method.

### Particle flow modeling

For a low volume fraction of dispersed phase (particles), the Lagrangian approach with one-way coupling is used, i.e. the airflow transports the particles, but the effect of particle movements on the flow is neglected. In this approach, the airflow field is first simulated, and then the trajectories of individual particles are tracked by integrating a force balance equation on the particle, which can be written as:

$$\frac{du_i^p}{dt} = F_D + F_g + F_E \quad (3)$$

$F_D$  is the drag force per unit particle mass taking the form of Stokes' drag law (Ounis et al., 1991) defined as,

$$F_D = \frac{(u_i^g - u_i^p)}{\tau_p} \quad (4)$$

where  $\tau_p$  is the particle response time defined as

$$\tau_p = \frac{18\mu}{d_p^2 \rho_p C_c}$$

$F_g$  is the gravity term, which is defined as

$$F_g = \frac{g(\rho_p - \rho_g)}{\rho_p} \quad (5)$$

and  $\rho_p$  and  $\rho_g$  denotes the density of particle material and air, respectively.  $C_c$  is the Cunningham correction factor to Stokes' drag law, which can be calculated from,

$$C_c = 1 + \frac{2\lambda}{d_p} \left( 1.257 + 0.4e^{-(1.1d_p/2\lambda)} \right) \quad (6)$$

where  $\lambda$  is the mean free path of air, assumed to be 65 nm. Amplitudes of the Brownian force components are of the form,

$$F_{\bar{b}} = \zeta \sqrt{\frac{\pi S_0}{\Delta t}} \quad (7)$$

where  $\zeta$  is a zero mean, unit variance independent Gaussian random numbers.  $\Delta t$  is the time-step for particle integration, and  $S_0$  is a spectral intensity function,

$$S_0 = \frac{216 \nu k_b T}{\pi^2 \rho d_p^5 \left(\frac{\rho_p}{\rho}\right)^2 C_c} \quad (8)$$

where  $T$  is the absolute temperature of air (an isothermal flow of 298 K is assumed), and  $k_b$  is the Boltzmann constant. It is noted that the Saffman lift force, for the range of ultrafine particles used in this study, is negligible and is not included in Equation (3). Particle rebounding from the surfaces is ignored and particle deposition is determined when the distance between the particle centre and a surface is less than or equal to the particle radius. The particle tracking is then terminated.

The Eulerian species/components approach to modeling the nanoparticle diffusion involves a single mixture fluid with the nanoparticles treated as a chemical species. A scalar  $c$ , representing the concentration of the nanoparticles is applied to the transport equation as:

$$\frac{\partial(u_j c)}{\partial x_j} = \frac{\partial}{\partial x_j} \left[ \left( \tilde{D} + \frac{\nu T}{S} \right) \frac{\partial c}{\partial x_j} \right] \quad (9)$$

which neglects the effects of particle inertia. Longest and Xi (2007a) showed that the effects of particle inertia plays a minor role in ultrafine aerosol deposition and that inertia effects could be neglected for particle Stokes numbers below  $5 \times 10^{-6}$ .

### Boundary conditions and numerical solution

In order to achieve a fully developed flow for the straight and 90° bend pipes, an additional separate pipe 5D in length with the same cross-section and mesh were simulated with periodic boundaries applied. When the flow reached a fully developed state the velocity profile from the periodic straight pipe model was extracted and used as the inflow condition at the inlet of the 90° bend pipe and the straight pipe. Two flow rates were considered for the straight pipe, 1 L/min, and 10 L/min. For the nasal cavity, inhalation is induced through a pressure difference between the nostril inlets ( $P_{in} = 0$  Pa) and the nasopharynx outlet ( $P_{out}$ ) that is set to a negative pressure relative to atmospheric pressure that is caused by the movement of the diaphragm. This is a more realistic representation of the inhalation cycle that considers the effects of nasal patency that is captured by the CT-scans of the airway.

Past experimental and numerical studies of airflow patterns in the nasal cavity have defined at the flow field at the nostril inlet by enforcing a fixed velocity or mass flow rate boundary condition (Xiong, Zaman). Where both cavities of the nose were used an equivalent flow rate at each nostril gives the presumption of an equivalent flow distribution through each cavity, before the flow merges at the nasopharynx, which may not occur given that the flow is induced by a pressure difference from the extension and contraction of the diaphragm. In addition the use of a single cavity with a nasopharynx extension does not capture the airflow mixing patterns caused by the merging of the two cavities in the nose. During normal nasal physiology, one the nasal cavity is normally asymmetrical where one nasal passage is usually more patent than the other. This asymmetry is referred to as the nasal cycle which is a result of congestion (swelling) of the erectile tissue (cavernous tissues of the mucosa) in one nasal cavity while at the same time decongestion (shrinking) occurs to the erectile tissue in the other cavity. The airflow through each nasal cavity is then governed by the resistance caused by the cross-sectional area of each airway which can be captured by using the pressure difference boundary condition approach.

Particles in the pipe simulation were released from an evenly dispersed circular region 0.01 m from the inlet to prevent any spurious data occurring due to random particles exiting the inlet upon immediate release. Furthermore, a particle was located at no less than 0.1 mm away from the wall to eliminate artificial immediate deposition on the walls due to the stochastic nature of the Brownian motion model. In the Lagrangian tracking scheme,  $u_i^c$  found in the slip velocity ( $u_i^c - u_i^p$ ) in Equation 4 is defined from the cell centre and a particle within any part of that cell takes  $u_i^c$  from the cell centre. For cells adjacent to the wall boundaries, the velocity profile should approach zero at the wall rather than be uniform throughout the cell. Therefore, a near wall interpolation (NWI) is applied to account for the diminishing velocity that approaches zero at the wall. Details of the scheme are given in Inthavong et al. (2011b).

The small diameter size of ultrafine particles results in very small particle response times which produce the so-called stiff ordinary differential equation problem. This makes the Runge-Kutta algorithm prohibitive in solving the particle trajectory equation (Equation 3). Instead the implicit Euler method is used in conjunction with a sufficiently small time-step size varying from  $1 \times 10^{-6}$  to  $1 \times 10^{-5}$  s for particles from 1 to 100 nm.

## Results and discussion

### Geometry and pressure drop in the nasal-sinus cavity

Thirteen evenly spaced coronal cross-sectional slices were created to allow analysis of geometry and flow characteristics. Figure 2 shows a sample of the cross-sections for the nasal and nasal-sinus computational models. The obvious difference is the larger cross-sectional areas created by the inclusion of the sinuses. There are four pairs of sinuses;

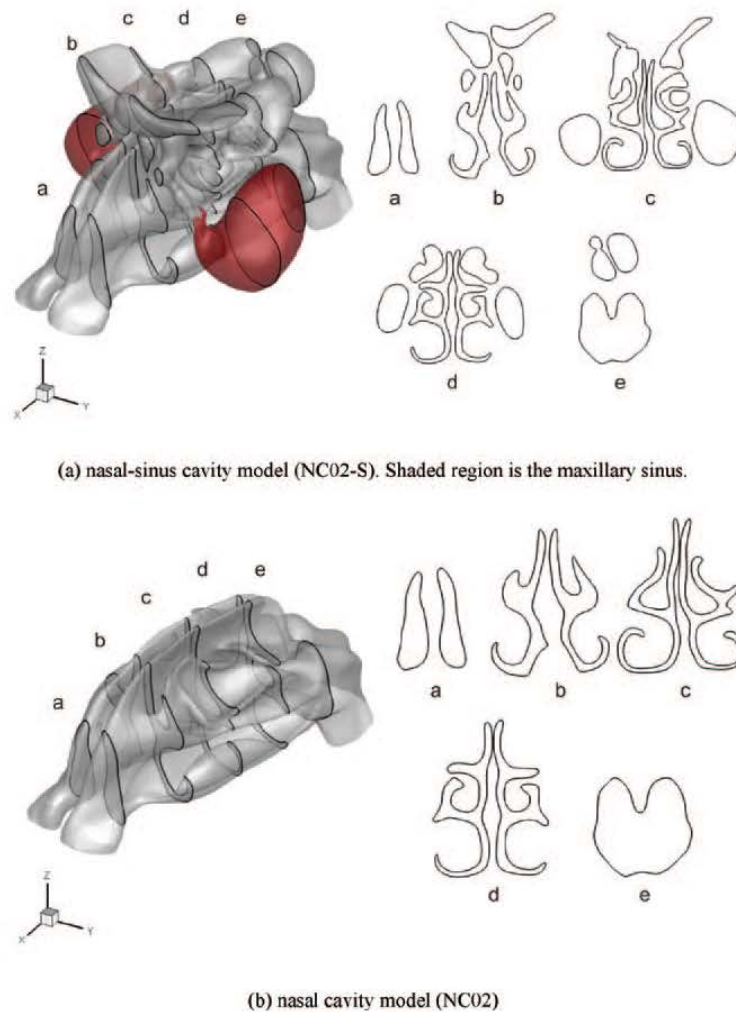


Figure 2. Coronal slices of the airway comparing a (a) nasal cavity with sinus model highlighted by the maxillary sinus and (b) a nasal cavity model with the sinuses omitted.

the maxillary sinuses, located in the cheekbones under the eyes; the frontal sinuses, located in the forehead above the main nasal passages and eyes; the ethmoid sinuses, located between the eyes and the nose and; the sphenoid sinuses, located in the centre of the skull, behind the nose and the eyes. The cross-sectional area versus distance from the anterior tip of the nose to the posterior nasal passage is compared with other nasal cavities published in the literature (Figure 3). The NC02 model (without sinus) has a slightly greater cross-sectional area than other models in the anterior ( $x < 4$  cm) and posterior ( $x > 6$  cm) region. It is noted that the data from Cheng et al. (1996b) comes from four adult nonsmoking male volunteers (ages 36–57 year), Subramaniam et al. (1998) from a 53-year-old, nonsmoking Caucasian male, and Wen et al. (2008) from a 25 years old, Asian male. The NC02-S model (with sinus) shows a significant increase (up to 300%) in the cross-sectional area, mainly contributed to by the maxillary and frontal

sinus. This begins at  $x = 0.0187$  cm with the frontal sinuses that protrude superiorly over the nasal passages. Further downstream the presence of maxillary and ethmoid sinuses contributes to the cross-sectional area.

The pressure drop between the nostril inlets and the posterior nasal wall at the nasopharynx for different inhalation rates is shown in Figure 4. Comparisons are made with other published data for nasal cavity (no sinuses) geometries. Currently there are inconsistencies in the representation of the inhalation using CFD in regards to the boundary condition settings for the inlet and outlets. One method is to use pressure inlet and outlet boundary conditions where the nostril inlets are set to gauge pressure, i.e.  $P = 0$  Pa and the nasopharynx outlet, a relative negative pressure value corresponding to the inhalation effort created by the diaphragm contraction and expansion of the lungs. This setting is referred to as “pressure” conditions. This differs to a forced flow applied

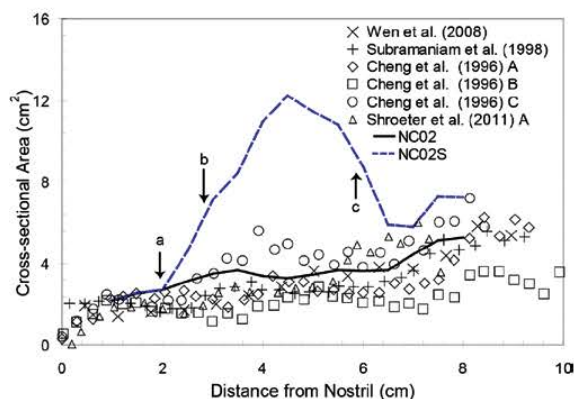


Figure 3. Coronal cross-sectional areas from the nostrils to the posterior nasopharynx in a linear axial vector. The distance from the nostrils at  $x = 0$  cm is taken as the anterior most tip of the nostril opening. Arrow (a) is at  $x = 0.0187$  cm and signifies the beginning of the frontal sinus (b) is at  $x = 0.0288$  cm signifying the anterior beginning of the maxillary sinus, and (c) is at  $x = 0.0566$  cm signifying the posterior end of the maxillary sinus.

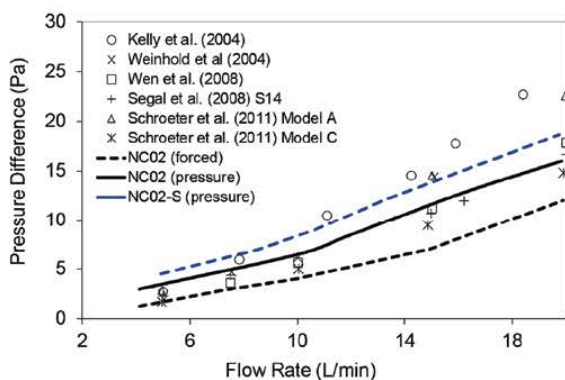


Figure 4. Comparison of the pressure drop for nasal cavity model NC02 without sinus inclusion.

at the nostril inlets to drive the inhalation. In terms of the numerical boundary conditions this is produced by setting the nostril inlets with equal mass flow distribution (i.e. 5 L/min per nostril for an inhalation rate of 10 L/min) using the mass flow rate or velocity boundary condition, and the nasopharynx outlet as an outflow or opening boundary condition. This setting is labeled as “forced” conditions and its results are compared with the pressure conditions method and also published data in Figure 4. The forced method produces less resistance than the pressure method given that an even distribution of flow passes through both the left and right nasal chambers while the pressure method produces an asymmetric distribution of flow based on the resistance caused by the left and right nasal chamber geometries. A comparison with other nasal cavity geometries shows that the forced method produces less resistance per flow rate. This

implies that smaller respiratory effort is required to produce an equivalent inhalation flow rate.

Comparisons of the pressure drop per inhalation flow rate with other models shows that the NC02 model has a flatter profile meaning that it has a lower flow resistance. This is expected given that the cross-sectional area profile of NC02 shown in Figure 3 is larger than the comparative models. The addition of the paranasal sinuses to the nasal cavity produces additional holes or slits in the geometry in the form of the nasal ostium that connects the sinus to the main nasal cavity chambers. Pressure losses in any pipe system are found at openings, especially if part of the opening is aligned with the flow streamlines. As a consequence, additional effort is needed to overcome any pressure that may be lost through the nasal ostia. The pressure difference profile for the NC02-S model shows a steeper curve which implies a larger pressure difference, and hence greater inhalation effort, is required to produce an equivalent inhalation flow rate.

### Flow patterns and streamlines

Flow streamlines were released from the left and right nostrils in order to trace the flow patterns. In both instances, the streamlines initially accelerate near the nostril opening before passing mainly through the main nasal passage at mid-height. Some streamlines travel along the floor of the nasal cavity, while some reach the olfactory regions, and up towards the sphenoid and ethmoid sinuses, but these exhibit low velocity  $\approx 0.1$  m/s as highlighted in Figure 5. These streamlines, based on 100 release points uniformly released across the nostril inlets, do not show any paths leading into the maxillary sinus, nor the frontal sinus as the release points were uniformly released across the nostril inlets. To determine if any flow will actually pass into the maxillary sinus, we track some path streamlines in reverse from points inside the maxillary sinus.

Figure 6 shows that the flow inside the maxillary sinus occurs at a very low velocity and exhibits typical recirculation of near stagnant flows. Analysis of the geometry and airflow showed that the minimum ostium diameter is 4.6 mm and 3.78 mm, and the pressure difference between the ostium entrance and inside the maxillary sinus are 0.056 Pa and 0.0026 Pa for the left and right sides respectively. The mass flow rate through the left and right ostium is  $11.4e-9$  kg/s and  $6.77e-9$  kg/s which are  $<0.006\%$  of the total inhalation flow rate. This small percentage of flow is not conducive for convective transport of particles into the maxillary sinus and that if any deposition was to occur in this region, then it would be caused by Brownian diffusion. On the other hand the flow streamlines in the sphenoid and ethmoid sinuses are not recirculating but instead convert through with a discernible direction. This suggests that some submicron particles may be transported to this region by convection, enhancing the likelihood of deposition onto the surfaces by diffusion.

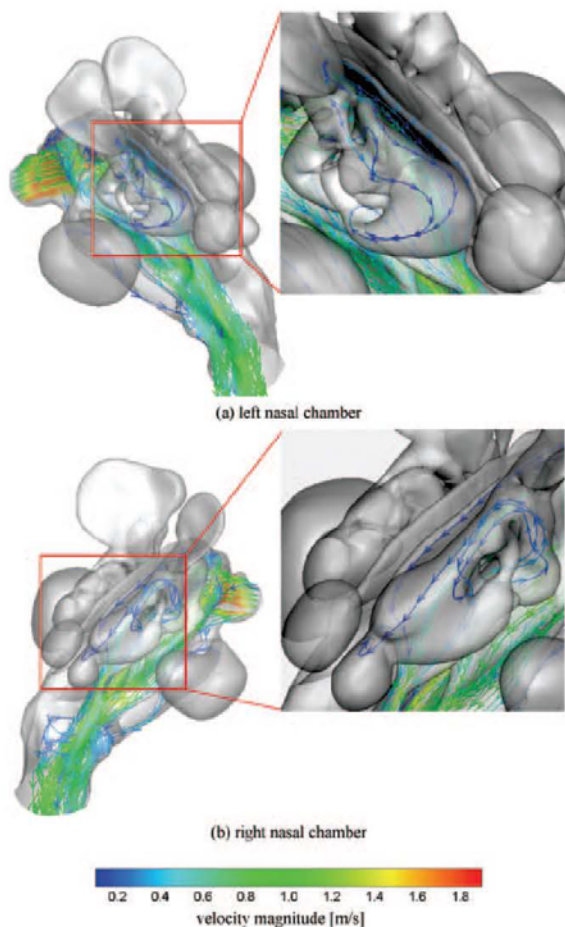


Figure 5. Streamlines passing through the nasal cavity that originates from the (a) left and (b) right nostrils at 10L/min. Magnified inset highlights the flow streamlines that reach the sphenoid and ethmoid sinus regions.

Contours of velocity magnitude at slices A, B, D, and E (defined in Figure 2) are shown in Figure 7. Slice C is not shown as it produced a similar profile to that of slice D. The 2D contours confirm flow acceleration occurring in the anterior nasal cavity where a peak velocity of 1.8 m/s is found at slice-A. The main flow is centered on the cross-section and pockets of low velocity are found at the top and bottom of the slice. As the flow travels downstream the peak velocity decreases to a value of 1.3 m/s found in slice D. This is due to the airway passage expanding in cross-sectional area resulting in lower velocities. The contours show that the bulk flow regions occur mainly through the mid-height region and close to the nasal septum which separates the two cavities. The contour at slice E shows a well-mixed pattern which is caused by the airflow from the left and right sides of the nasal cavity merging together. Very low flows at <0.1 m/s are found in the sinus regions.

## Particle deposition

### Preliminary analysis

To test the accuracy of the particle tracking procedure, the flow and particle transport in the entrance region of a pipe and a 90° bend pipe are simulated and the results compared with experimental and analytical solutions. The number of particles tracked through the pipe and nasal cavity geometries was 80,000 (up to 300,000 particles were checked) which was statistically independent from the stochastic nature of the Brownian motion model. The deposition efficiency of ultrafine particles in the range of 1–100 nm was simulated in a straight pipe for a flow rate of 10L/min, and 5–12 nm particles for a 90° bend pipe. Figure 8 shows the simulated results in comparison with the experimental results from Wang et al. (2002) and the analytical correlation

$$DE = 1 - 0.819 \exp(-14.63\Delta) + 0.0976 \exp(-89.22\Delta) + 0.0325 \exp(-288.0\Delta) + 0.0509 \exp(-15.9\Delta^{2/3}) \quad (10)$$

from Ingham (1975). The Lagrangian particle tracking model that includes the Brownian model with a NWI using Fluent v12.1 is able to handle the diffusion transport in a straight and 90° bend pipe.

The Eulerian model species model which accounts for pure diffusion (i.e. particle inertia effects are excluded), also shows satisfactory results. The Eulerian species simulation is valid for small nanoparticles but with increased flow rate and particle size, the particle inertia becomes important (Xi & Longest, 2008). The deposition efficiency results for a straight pipe with a flow rate of 1L/min gives a similar trend to that of the 10L/min flow rate and therefore is not shown for brevity.

### Diffusion deposition in the nasal cavity and sinus

Under an inhalation flow rate of 10L/min, 80000 nanoparticles for each particle size of 1, 5, 10, 40, and 100 nm were tracked within the two nasal cavity models. The total deposition efficiency for the region spanning from the anterior nostril opening conducting airway to the oropharynx is shown in Figure 9. The comparative data comes from different forms of nasal cavity deposition studies which includes *in-vivo* human volunteers by Cheng et al. (1996b), replicate cast models by Kelly et al. (2004), and computational models by Wang et al. (2009) and Zamankhan et al. (2006). The deposition efficiency profile exhibits the ubiquitous decreasing trend as particle size increases for the diffusion deposition of ultrafine particles. For 1 nm particles, there was 99.9% deposition within the nasal cavity. For 10 nm particles the deposition decreases to 24% (NC02) and 30% (NC02-S). At 40 nm the deposition decreases to 6% (NC02) and 9% (NC02-S) and remains at that level as the particle size increases to 100 nm. The decreasing deposition efficiency trend is due to the decreased Brownian excitation of the nanoparticle. A smaller Brownian excitation produces a

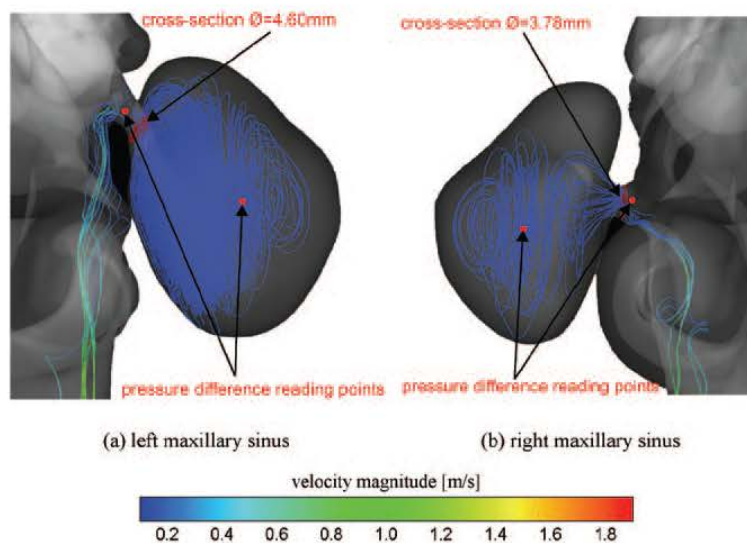


Figure 6. Streamlines passing through the nasal cavity that originates from the (a) left and (b) right nostrils at 10 L/min.

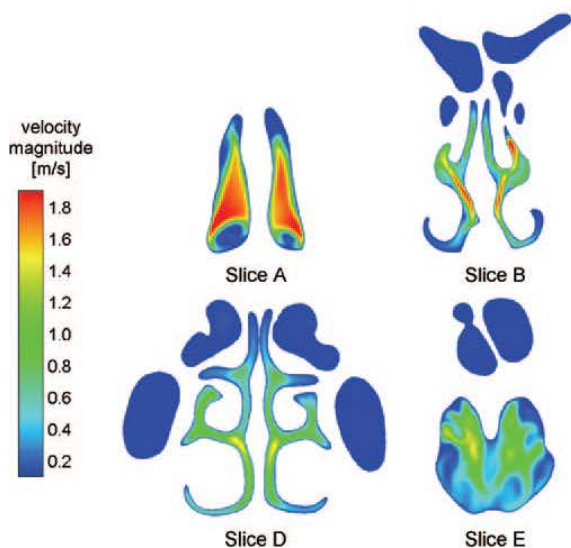


Figure 7. Velocity magnitude contours at 10 L/min.

smaller dispersion, and hence reduces the potential for the particles to diffuse into the ostia and sinus regions. The hypothesis proposed suggests that the deposition efficiency for nasal-sinus cavity model should have a higher value, due to diffusion transport of particles out to the nasal ostia and its sinuses. The results show that there is no difference found for 1 nm particle as both models predict near 100% deposition, while for 10 nm the difference is 6%; 40 nm the difference is 3% and; 100 nm the difference is 2% (Table 2). Therefore, the max deposition difference occurs at 10 nm and this difference reduces as the particles size increase to 100 nm. Larger particles

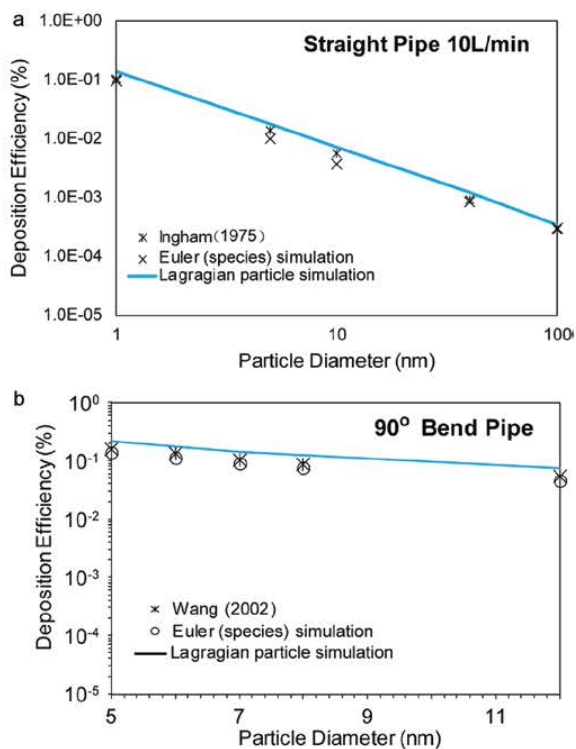


Figure 8. Comparison of deposition efficiency results using the Eulerian species model, Brownian model-Fluent 6.3, and Brownian model-Fluent 12.1 in (a) straight pipe 10 L/min (1 L/min was also performed which produced similar trends) and a (b) 90° bend pipe.

will experience a heightened state of inertia, which connect the particles through the computational domain. The critical value above which inertia significantly influences deposition and transport has been found to be  $St > 1.0 \times 10^{-5}$  (Xi & Longest, 2008). While the deposition for 1 nm is the same for both models, the deposition may be different. Further analysis, by visualization is provided later to elucidate this.

The maximum difference in deposition efficiency between the two nasal cavity models that occurs is relatively low, when considering the variations between other deposition data, and therefore it may appear that omitting the sinuses for evaluating ultrafine particles may be acceptable. To ensure this we present the deposition efficiency between the two models under a lower flow rate at 4 L/min. From the  $Pe$  number which describes the rate of convection to the rate of diffusion by

$$Pe = \frac{U_0 L_h}{\tilde{D}}$$

where  $U_0$  is the characteristic velocity,  $L_h$  the characteristic hydraulic length, and  $\tilde{D}$  the diffusion coefficient based on the Stokes-Einstein equation, we see that a reduction in flow rate by 2.5× increases the influence of diffusion by the same amount for a given particle size. Figure 10 shows the deposition efficiency

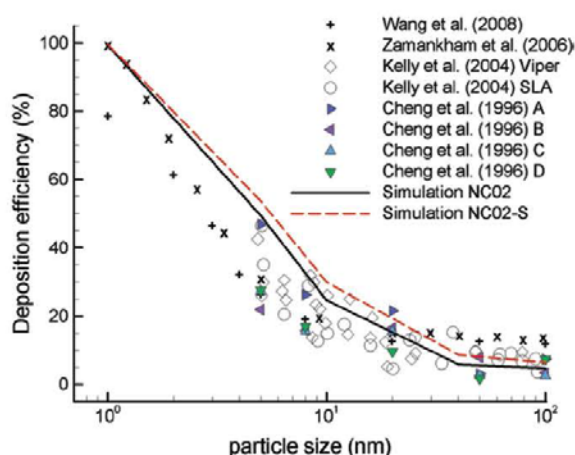


Figure 9. Comparison simulation data for nasal without sinus deposition efficiency for 10 L/min breathing rates.

for both nasal models where the red color and open symbols represent the sinus NC02-S model. The lines represent the additional 15 L/min case. The black color represents the no sinus NC02 model. The difference in deposition efficiency between the two models at a flow rate of 4 L/min is most significant for 5 nm and 10 nm particles (17% and 16% difference respectively). As the particle size increases the difference between the two models diminishes. For 1 nm particles, the difference is not discernable since the deposition efficiency is nearly at 100%. While the quantifiable difference is not noticeable it is expected that the 1 nm particle diffusion will be much stronger at the lower flow rate of 4 L/min, and that the deposition pattern locally will be different to that at a flow rate of 10 L/min. For completeness the particle deposition efficiency was also evaluated at a flow rate of 15 L/min which shows that the deposition values remain close to a flow rate of 10 L/min for both models. Thus, the differences caused by the sinus geometry remain similar as the flow rate increases from 10 L/min to 15 L/min.

### Visualization

To confirm that the 1 nm excitation due to diffusion is much stronger at a lower flow rate, we track each individual particle and record its spatial coordinates after

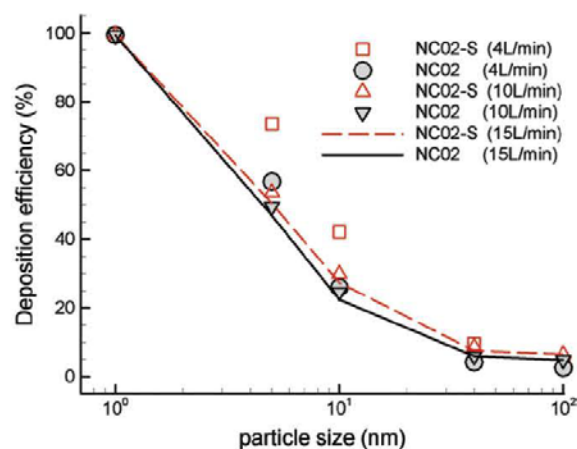


Figure 10. Comparison simulation data for nasal without sinus deposition efficiency for 4 L/min and 10 L/min breathing rates.

Table 2. Summary of geometric characteristics of the nasal cavity.

	Without sinus cavity model				Sinus cavity model	
	Present study	Doorly et al. (2008)			Present study	Xiong et al. (2008)
Model 1		Model 2	Model 3			
Overall cavity length (cm)	9.7	10.5	10.6	11	9.7	9.1
Overall cavity width (cm)	3.9	-	-	-	7.3	6.6
Surface area (cm <sup>2</sup> )	199	106 <sup>a</sup>	107 <sup>a</sup>	109 <sup>a</sup>	290	NA
Volume (cm <sup>3</sup> )	NA	13.8	14.2	22.4	NA	NA

<sup>a</sup>Right nasal chamber only.

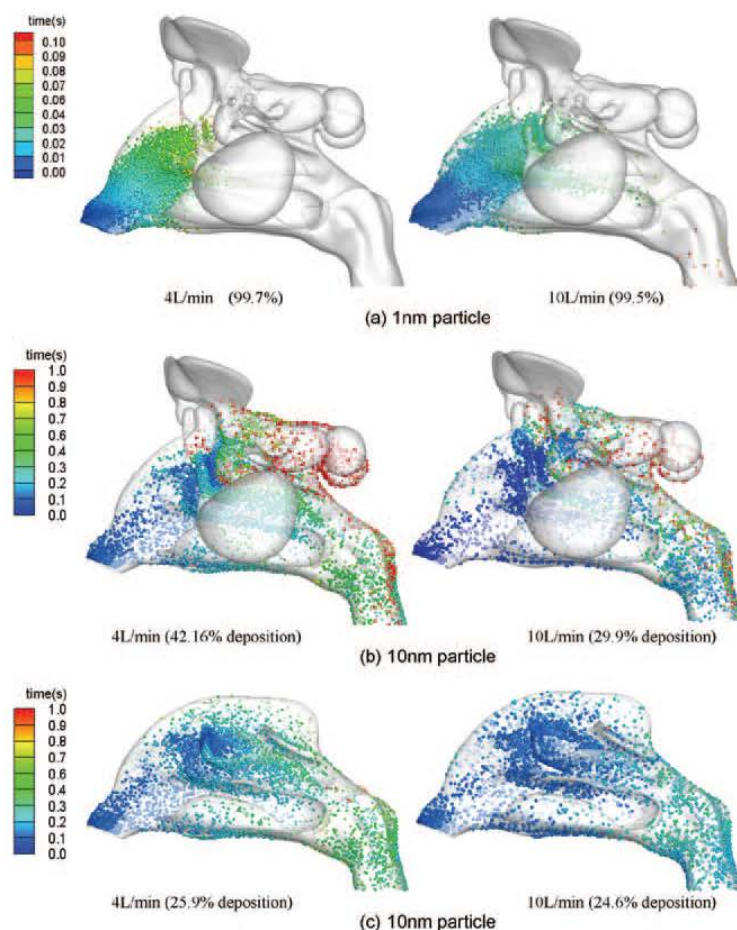


Figure 11. NP deposition pattern in the nasal-sinus cavity for (a) 1 nm, resulting in 98% deposition and (b) 10 nm, resulting in 29.8% deposition. Particles are colored by trajectory time within the nasal cavity before impacting onto the surfaces at 10 L/min.

impaction onto the surrounding surfaces. The coordinates are plotted and colored by residence time as shown in Figure 11. The distribution of 1 nm shows that earlier deposition occurs where a large proportion of the particles persist for less than 0.022 s in the nasal-sinus cavity. The strength or influence of the Brownian diffusion increases as the flow rate decreases, and at a flow rate of 4 L/min, deposition is found within the anterior half of the nasal-sinus cavity while at a flow rate 10 L/min deposition is a little more disperse with deposition sites found in the posterior half.

The deposition pattern for 10 nm particles shows a more random and even distribution pattern. The residence time is 10 $\times$  as great as that for 1 nm which suggests that the particles are transported with the inhaled flow field for longer and hence has the ability to travel deeper into the nasal cavity and perhaps down towards the lung region. The particle residence time is important for NP deposition studies as it gives an indication of the likelihood of deposition in different regions of the nasal cavity.

For example the shorter residence time of 1 nm means that deposition occurs nearly immediately and the deposition zone is restricted to the nasal cavity and further deposition downstream is unlikely. This protects the sensitive lung airways from those NPs that exhibit dangerous properties for respiratory health. Conversely the ability to deposit particles in the middle regions of the nasal cavity or even deeper into the lung airways with high deposition, can be important for therapeutic drug delivery.

Figure 11 is the visual representation of Figure 10. Here we see that the slower flow rate allows increased potential for particle deposition. The comparisons between the two nasal cavity models, NCO2 and NCO2-S show that the additional deposition caused by the difference in geometry (i.e. additional paranasal sinuses) occurs in the ethmoid and sphenoid sinus region, and negligible amounts deposit in the maxillary sinus. A possible reason for this particle transport phenomena can be referred back to the convective flow streamlines presented in Figure 5 which showed clear



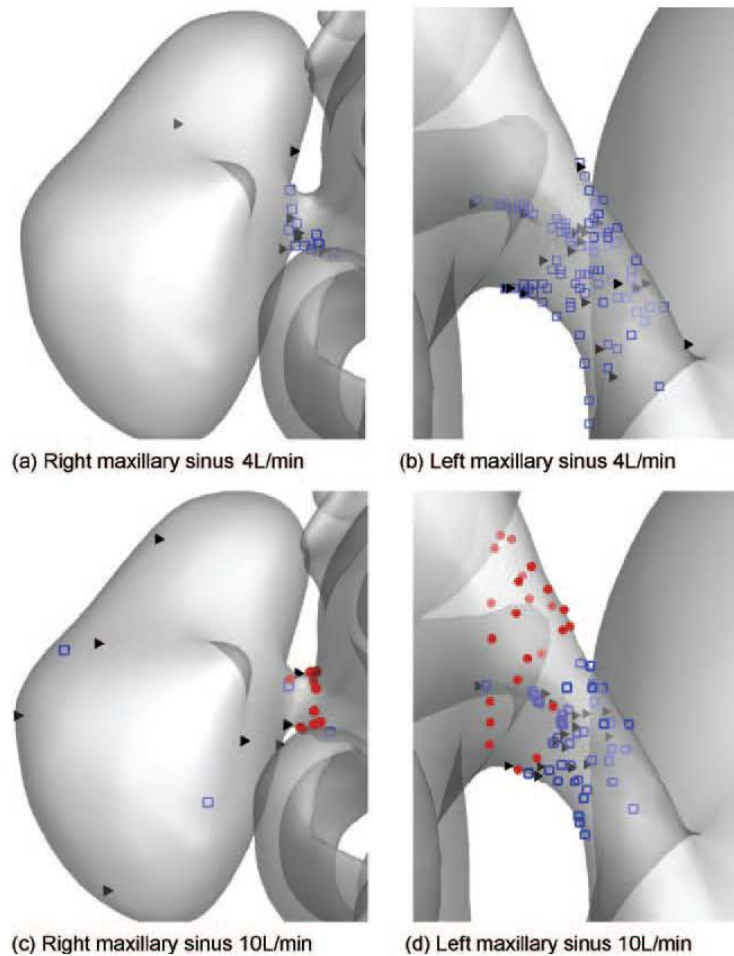


Figure 12. Frontal view showing the NP deposition in maxillary ostium and sinus for the (a) right nasal cavity, and (b) the left nasal cavity at 10L/min. Different sized particles are colored as follows: 1 nm red circle; 10 nm blue square; and 40 nm black triangle.

directional streampaths reaching the ethmoid and sphenoid sinuses, albeit at low velocities. This would transport the particles to the superior regions of the nasal cavity and then allow for the diffusion process to occur – a phenomena that allows for the physiological function of olfaction.

Deposition in the maxillary sinus is very low and our hypothesis that the diffusion process may be dominant enough for particles to pass into the paranasal sinuses appears to only be supported if there is some convection involved (e.g. deposition sites in the sphenoid and ethmoid sinuses). In the maxillary sinuses the ostium protrudes at nearly right angles to the main flow field. To further investigate this we examine the maxillary ostium and locate the deposition of individual 1 nm, 10 nm and 40 nm particles within the region as shown in Figure 12. In the right maxillary sinus, inclusive of the ostium, a small percentage of particles <0.04% are deposited. At a flow rate of 4L/min there are no 1 nm

particles depositing due to its early deposition in the main nasal passage. For both models, 10 nm and 40 nm particles are found concentrated within the ostium. Thus it appears that despite a lower flow rate, there is a lack of particle deposition within the maxillary sinus.

For a flow rate of 10L/min it can be seen that 1 nm particles are captured within the narrow ostium and in fact don't make it through to the maxillary sinus. For the left maxillary sinus, no particles were able to pass through the ostium, but a larger percentage of particles <0.5% deposited within the ostium alone. This is mainly due to the curved geometry and longer ostium length providing a narrow tube passageway for the particles to diffuse onto. These results support the report by Hood et al. (2009), that ostium sinus ventilation is limited (unless the ostium is very large) and that the gas exchange of nitric oxide (NO) between the air in the maxillary sinus and the nasal air does not contribute greatly to the overall NO concentration.

In this study, the passageway into the paranasal sinuses via the ostia were open, and obstruction was not included in the model. At this stage no data exists for the type and amount of blockage that is typical of sinusitis. However in such a case, any inflammation and hence obstruction within the main nasal passage will cause sharper accelerations and more erratic flow behavior to the air and particle flows, while obstructions in the ostia and paranasal sinuses may not influence the bulk flow but will influence the nitric oxide gas exchange within the sinuses (Hood et al., 2009).

### Study limitations and future study

This study used only a single subject's nasal airway and paranasal sinuses which has limitations due to the inter-subject variability in anatomy between different people. Further studies may examine the differences in a wide range of subjects and with a larger sample size (age, sex, ethnicity etc.). However in general, gross flow features and overall particle deposition can provide sufficient insight into the trends that are consistent among different geometries. On the assumption that the subject within this study is without pathology and representative of an "average" patient, the preliminary results from this study will aid in gaining an appropriate understanding of the effect of paranasal sinuses on nanoparticle deposition.

This current study focuses on the deposition of NPs in healthy subjects and the potential of these particles to cause pathology like sinusitis. Chronic sinusitis is a common problem in our population with a prevalence in the United States of 14.6% and results in significant morbidity, costing the US health care system approx. \$3.4–5 billion annually (Pleis et al., 2009). There is potential in future work to speculate the implications of sinusitis and obstruction of paranasal sinuses on particle flow and deposition in the nasal airways. These results may be applicable to improving novel delivery of therapies to treat conditions like chronic sinusitis.

### Conclusion

A nasal cavity model including the sinuses was created in order to determine if any NPs would deposit within the paranasal sinuses given that these particles are transported through the nasal cavity mainly by diffusion. Under a flow rate of 10L/min it was shown that 1nm particles deposited early and in the anterior half of nasal cavity with a deposition efficiency of 99%. As the particle increased in size to 10nm the diffusive nature of the NP decreased and the deposition efficiency reduced to 30%. However a more evenly distributed deposition pattern was found for 10nm particles. The effect of including the sinus compartments with the nasal geometry on the deposition efficiency was most significant for 10nm particles. This difference is further amplified when the flow rate is decreased which allows the diffusion to be more influential. These results aimed to identify the possible differences that may occur when evaluating

particle inhalation for toxicology or drug delivery using cast or computational models that exclude the sinus regions. This is particularly important for the case where flow rates are low and particle sizes are around 5–10 nm particle sizes and comparative studies between human subjects and nasal cavity cast or CFD models that neglect the sinus airways should consider the diffusion effects of nanoparticles. It was noted that this study only looked at one subject, so future work in this field will be required to look at the variable anatomy between different patients and its effect on simulation results. In addition, there is room for future research using models of patients with pathology, such as sinusitis, where there is partial loss of paranasal sinuses and ostia obstruction. Results from this work will have high clinical relevance for sufferers of these chronic conditions.

### Declaration of interest

The authors would like to gratefully acknowledge the financial support provided by the National Basic Research Program (973) of China, Grant No. 2012CB720100 and the Australian Research Council (project ID: DP120103958).

### References

- Auffan M, Rose J, Bottero JY, Lowry GV, Jolivet JP, Wiesner MR. 2009. Towards a definition of inorganic nanoparticles from an environmental, health and safety perspective. *Nat Nanotechnol* 4:634–641.
- Calderón-Garcidueñas L, Delgado R, Calderón-Garcidueñas A, Meneses A, Ruiz LM, De La Garza J, Acuna H, Villarreal-Calderón A, Raab-Traub N, Devlin R. 2000. Malignant neoplasms of the nasal cavity and paranasal sinuses: A series of 256 patients in Mexico City and Monterrey. Is air pollution the missing link? *Otolaryngol Head Neck Surg* 122:499–508.
- Cheng K H, Cheng Y S, Yeh H C, Swift DL. 1995. Deposition of ultrafine aerosols in the head airways during natural breathing and during simulated breath holding using replicate human upper airway casts. *Aerosol Sci Tech* 23:465–474.
- Cheng KH, Cheng YS, Yeh HC, Guilmette A, Simpson SQ, Yang YH, Swift DL. 1996a. *In-vivo* measurements of nasal airway dimensions and ultrafine aerosol deposition in the human nasal and oral airways. *J Aerosol Sci* 27:785–801.
- Cheng YS, Yeh HC, Guilmette RA, Simpson SQ, Cheng KH, Swift DL. 1996b. Nasal deposition of ultrafine particles in human volunteers and its relationship to airway geometry. *Aerosol Sci Tech* 25:274–291.
- Cheng YS, Holmes TD, Gao J, Guilmette RA, Li S, Surakitbanharn Y, Rowlings C. 2001. Characterization of nasal spray pumps and deposition pattern in a replica of the human nasal airway. *J Aerosol Med* 14:267–280.
- Churchill SE, Shackelford LL, Georgi JN, Black MT. 2004. Morphological variation and airflow dynamics in the human nose. *Am J Hum Biol* 16:625–638.
- Doorly DJ, Taylor DJ, Gambaruto AM, Schroter RC, Tolley N. 2008. Nasal architecture: form and flow. *Phil Trans Math Phys Eng Sci* 366:3225–3246.
- Elwood JM. 1981. Wood exposure and smoking: Association with cancer of the nasal cavity and paranasal sinuses in British Columbia. *Can Med Assoc J* 124:1573–1577.
- García GJ, Baillie N, Martins DA, Kimbell JS. 2007. Atrophic rhinitis: A CFD study of air conditioning in the nasal cavity. *J Appl Physiol* 103:1082–1092.

- Hahn J, Scherer PW, Mozell MM. 1993. Velocity profiles measured for airflow through a large-scale model of the human nasal cavity. *J Appl Physiol* 75:2273–2287.
- Halperin WE, Goodman M, Stayner L, Elliott LJ, Keenlyside RA, Landrigan PJ. 1983. Nasal cancer in a worker exposed to formaldehyde. *JAMA* 249:510–512.
- Hood CM, Schroter RC, Doorly DJ, Blenke EJ, Tolley NS. 2009. Computational modeling of flow and gas exchange in models of the human maxillary sinus. *J Appl Physiol* 107:1195–1203.
- Ingham DB. 1975. Diffusion of aerosols from a stream flowing through a cylindrical tube. *J Aerosol Sci* 6:125–132.
- Inthavong K, Tian ZF, Li HF, Tu JY, Yang W, Xue CL, Li CG. 2006. A numerical study of spray particle deposition in a human nasal cavity. *Aerosol Sci Technol* 40:1034–1045.
- Inthavong K, Ge Q, Se CMK, Yang W, Tu JY. 2011a. Simulation of sprayed particle deposition in a human nasal cavity including a nasal spray device. *J Aerosol Sci* 42:100–113.
- Inthavong K, Zhang K, Tu J. 2011b. Numerical modelling of nanoparticle deposition in the nasal cavity and the tracheobronchial airway. *Comput Methods Biomech Biomed Engin* 14:633–643.
- Keir J. 2009. Why do we have paranasal sinuses? *J Laryngol Otol* 123:4–8.
- Kelly JT, Prasad AK, Wexler AS. 2000. Detailed flow patterns in the nasal cavity. *J Appl Physiol* 89:323–337.
- Kelly J, Asgharian B, Kimbell J, Wong B. 2004. Particle deposition in human nasal airway replicas manufactured by different methods. Part II: Ultrafine particles. *Aerosol Sci Technol* 38:1072–1079.
- Lindemann J, Brambs HJ, Keck T, Wiesmiller KM, Rettinger G, Pless D. 2005. Numerical simulation of intranasal airflow after radical sinus surgery. *Am J Otolaryngol* 26:175–180.
- Longest PW, Xi J. 2007a. Computational investigation of particle inertia effects on submicron aerosol deposition in the respiratory tract. *J Aerosol Sci* 38:111–130.
- Longest PW, Xi J. 2007b. Effectiveness of direct Lagrangian tracking models for simulating nanoparticle deposition in the upper airways. *Aerosol Sci Technol* 41:380–397.
- Ounis H, Ahmadi G, McLaughlin JB. 1991. Brownian diffusion of submicrometer particles in the viscous sublayer. *J Colloid Interface Sci* 143:266–277.
- Pleis JR, Lucas JW, Ward BW. 2009. Summary health statistics for U.S. adults: National Health Interview Survey, 2008. *Vital Health Stat* 10:1–157.
- Robert GH. 2001. Forced inspiratory nasal flow–volume curves: A simple test of nasal airflow. *Mayo Clin Proc* 76:990–994.
- Schroeter JD, Kimbell JS, Asgharian B. 2006a. Analysis of particle deposition in the turbinate and olfactory regions using a human nasal computational fluid dynamics model. *J Aerosol Med* 19:301–313.
- Schroeter JD, Kimbell JS, Asgharian B. 2006b. Analysis of particle deposition in the turbinate and olfactory regions using a human nasal computational fluid dynamics model. *J Aerosol Med* 19:301–313.
- Schroeter JD, Garcia GJ, Kimbell JS. 2011. Effects of Surface Smoothness on Inertial Particle Deposition in Human Nasal Models. *J Aerosol Sci* 42:52–63.
- Shi H, Kleinstreuer C, Zhang Z. 2008. Dilute suspension flow with nanoparticle deposition in a representative nasal airway model. *Phys Fluid* 20:1–23.
- Slavin RG. 1988. Sinusitis in adults and its relation to allergic rhinitis, asthma, and nasal polyps. *J Allergy Clin Immunol* 82:950–956.
- Subramaniam RP, Richardson RB, Morgan KT, Kimbell JS, Guilmette RA. 1998. Computational fluid dynamics simulations of inspiratory airflow in the human nose and nasopharynx. *Inhal Toxicol* 10:91–120.
- Swift DL, Proctor DF. 1977. Access of air to the respiratory tract. In: Brain JD, Proctor DF, Reid LM, eds. *Respiratory Defense Mechanism*. New York: Marcel Dekker, 63–93.
- Wang J, Flagan RC, Seinfeld JH. 2002. Diffusional losses in particle sampling systems containing bends and elbows. *J Aerosol Sci* 33:843–857.
- Wang SM, Inthavong K, Wen J, Tu JY, Xue CL. 2009. Comparison of micron- and nanoparticle deposition patterns in a realistic human nasal cavity. *Respir Physiol Neurobiol* 166:142–151.
- Wen J, Inthavong K, Tu J, Wang S. 2008. Numerical simulations for detailed airflow dynamics in a human nasal cavity. *Respir Physiol Neurobiol* 161:125–135.
- Xi J, Longest PW. 2008. Numerical predictions of submicrometer aerosol deposition in the nasal cavity using a novel drift flux approach. *Int J Heat and Mass Tran* 51:5562–5577.
- Xiong GX, Zhan JM, Jiang HY, Li JF, Rong LW, Xu G, Xu G. 2008. Computational fluid dynamics simulation of airflow in the normal nasal cavity and paranasal sinuses. *Am J Rhinol* 22:477–482.
- Zamankhan P, Ahmadi G, Wang Z, Hopke PH, Cheng YS, Su WC, Leonard D. 2006. Airflow and deposition of nanoparticles in a human nasal cavity. *Aerosol Science Technol* 40:463–476.



Contents lists available at ScienceDirect

Journal of Aerosol Science

journal homepage: [www.elsevier.com/locate/jaerosci](http://www.elsevier.com/locate/jaerosci)



## Simulation of sprayed particle deposition in a human nasal cavity including a nasal spray device

K. Inthavong<sup>a</sup>, Qinjiang Ge<sup>a</sup>, Camby M.K. Se<sup>a</sup>, W. Yang<sup>b</sup>, J.Y. Tu<sup>a,\*</sup>

<sup>a</sup> School of Aerospace, Mechanical and Manufacturing Engineering, RMIT University, PO Box 71, Plenty Road, Bundoora, Victoria 3083, Australia

<sup>b</sup> Division of Minerals, Commonwealth Scientific and Industrial Research Organization, Blackburn Road, Clayton, Victoria, Australia

### ARTICLE INFO

#### Article history:

Received 27 July 2010

Received in revised form

17 November 2010

Accepted 30 November 2010

Available online 7 December 2010

#### Keywords:

Nasal cavity

Spray

Deposition

CFD

Modelling

Simulation

### ABSTRACT

Effective nasal drug delivery is highly dependent on the delivery of drug from the nasal spray device. Atomisation of liquid spray occurs through the internal atomizer that can produce many forms of spray patterns and two of these, hollow-cone and full-cone sprays, are evaluated in this study to determine which spray pattern produced greater deposition in the middle regions of the nasal cavity. Past studies of spray particle deposition have ignored the device within the nasal cavity. Using computational fluid dynamics (CFD), two computational models of human nasal cavity model were reconstructed from CT-scans, where the difference between the two models was the presence of the nasal spray device accounting for the airway blockage at one of the nostrils. Experimental measurements from Particle Droplet Image Analyser (PDIA) were taken in order to gain confidence in determining the initial particle conditions for the computational models. An airflow field is induced through a negative pressure flow condition applied at the pharynx instead of constant flow rates at the left and the right nasal cavities. Subsequent airflow patterns and its effects on particle deposition, with and without a spray device, are compared. Contours and streamlines of the flow field revealed that the presence of a spray device in the nasal vestibule produced higher levels of disturbed flow, which helped the dispersion of the sprayed particles. Particle deposition was found to be high in the anterior regions of the nasal cavity caused by its inertia. Evaluation of the two spray types found that hollow spray cones produced more deposition in the middle regions of the nasal cavity. This paper also demonstrates the CFD methodology used, which can help in better understanding the design of future atomizers for nasal spray use.

Crown Copyright © 2010 Published by Elsevier Ltd. All rights reserved.

### 1. Introduction

Nasal drug delivery has long been used for local treatment of the common cold and allergic rhinitis. The nasal route also provides a great opportunity when considering new drug formulations, such as nicotine to assist in smoking cessation, calcium for osteoporosis, or insulin for diabetes. Therefore studies into local droplet deposition are of great significance in the delivery of drugs via the nasal airway. Various studies adopting human subjects or nasal cavity replicas have found relationships for droplet deposition efficiencies with nasal spray parameters, such as the spray cone angle and the droplet size distribution (Cheng et al., 2001; Suman, Laube, Lin, Brouet, & Dalby, 2002). However in-vivo and nasal cavity replica methods are limited in providing detailed results due to the intrusive, time consuming, and expensive nature associated with experimental methods.

\* Corresponding author. Tel.: +61399256191; fax: +61399256108.

E-mail address: [jyuan.tu@rmit.edu.au](mailto:jyuan.tu@rmit.edu.au) (J.Y. Tu).

Recent developments in medical imaging, e.g. magnetic resonance imaging (MRI) and computed tomography (CT) scanning, coupled with computational science, have opened new possibilities for physically realistic numerical simulations of nasal airflow. Keyhani, Scherer, and Mozell (1995) examined airflow through one side of the human nose in a three-dimensional model that was truncated anterior to the nasopharynx. Subramaniam, Richardson, Morgan, Kimbell, and Guilmette (1998) simulated the airflow structures of the rest and light breathing conditions (15 and 26 L/min) using a laminar flow. Other airflow studies include the work by Zamankhan et al. (2006) and Wang, Denney, Morrison, and Vodyanoy (2005), which briefly discussed airflows through one nasal cavity. Numerical studies provide an alternate method that helps to complement the existing experimental data through a wider range of studies (e.g. repeatability and accuracy of a nasal spray injection released from the same location) that is based on advancements in computational models employing computational fluid dynamics (CFD) techniques.

In recent studies by the authors (Inthavong et al., 2006; Inthavong, Tian, Tu, Yang, & Xue, 2008) sprayed droplet deposition in the nasal cavity was performed based on the characteristics of the atomised drug particles released from a nasal spray. It was found that for a flow rate of 20 L/min 10–20  $\mu\text{m}$  particles are sensitive to initial injection velocity, insertion angle, and spray cone angle as its size is increased. Larger particles exhibiting high Stokes numbers caused it to be insensitive to these spray parameters. In the previous studies the nasal spray device within the nasal cavity was absent from the computational model, while the experimental data did not provide a range of particle sizes.

In this study, which is a step towards establishing more realistic drug delivery simulations, two computational models of human nasal cavity model were reconstructed from CT-scans, where the difference between the two models was the presence of a nasal spray device accounting for the airway blockage at one of the nostrils. Past studies of spray particle deposition have ignored the device within the nasal cavity. An airflow field is also induced from a negative pressure flow condition applied at the outlet boundary (pharynx) instead of equal flow rates between the left and the right nasal cavities. Subsequent airflow patterns and its effects on particle deposition, with and without a spray device, are firstly compared for two nasal spray nozzles (hollow spray cone and full spray cone). Following the flow field analysis, the atomisation of the liquid from a nasal spray device is visually presented to elucidate the external spray characteristics. This is aimed at obtaining a better understanding of the particles, leading to improved initial particle boundary conditions. Additional analysis using a particle droplet image analyser (PDIA) was performed in order to get Sauter mean particle diameters at the near spray nozzle region. This data is important as it provides confidence for setting up the initial particle conditions of the computational model.

## 2. Methods

### 2.1. Computational model

An existing computational model of the nasal cavity is used, and for brevity the details of its model construction and verification can be found in Inthavong, Wen, Tian, and Tu (2008) and Inthavong, Wen, Tu, and Tian (2009). In earlier studies by the authors (Inthavong, 2006) among others in the literature (Kleinstreuer & Zhang, 2003; Li, Kleinstreuer, & Zhang, 2007; Straatsma, Van Houwelingen, Steenbergen, & De Jong, 1999), the computational model of the nasal cavity was limited by the available computing power. In this study with increased computing power (HPxw6600 Workstation 16GB Ram, 16 Processors), a nasal cavity with 3.5 million cells (193 Mb in computational memory size) was developed using unstructured tetrahedral cells with mesh refinements at the near wall regions and high curvature geometric features. The finer mesh especially near the wall boundaries allows better modelling of the sharp gradients found in the boundary layer. In addition the maximum  $y^+$  value in any cell of the model is needed to be in the order of 1 ( $y_{max}^+ = 0.78$ ) to resolve the near wall region for the low Reynolds number  $k-\omega$  turbulence model. Grid independence was achieved for a mesh size of 1 million cells (Inthavong, 2006); however it was found that a small percentage of adjacent wall cells had a  $y^+$  value greater than 1, which was addressed in the final model. Based on this nasal cavity model, a second model was created to include the presence of a nasal spray device inside the left nostril. The spray device has a head diameter of 7 mm inserted at an angle from the vertical of 10°. The computational model with a nose spray is depicted in Fig. 1, which consists of 3 regions namely *anterior*, *middle*, and *posterior* regions.

### 2.2. Fluid flow modelling

Airflow through the nasal cavity was treated as a steady incompressible, isothermal fluid. The two computational models were simulated under a laminar flow for flow rates up to 15 L/min, while above this value the low-Reynolds number  $k-\omega$  turbulent model was used. For the sprayed particle comparisons a flow rate of 20 L/min was used. Details of the model such as the turbulent viscosity, and the production and dissipation terms can be found in Wilcox (1993) and the Ansys-Fluent documentation (Ansys, 2007). These equations are discretised using the finite volume CFD code, Fluent 6.3.26. The QUICK scheme is used to approximate the momentum equation, whilst the pressure-velocity coupling is handled through the SIMPLE method.

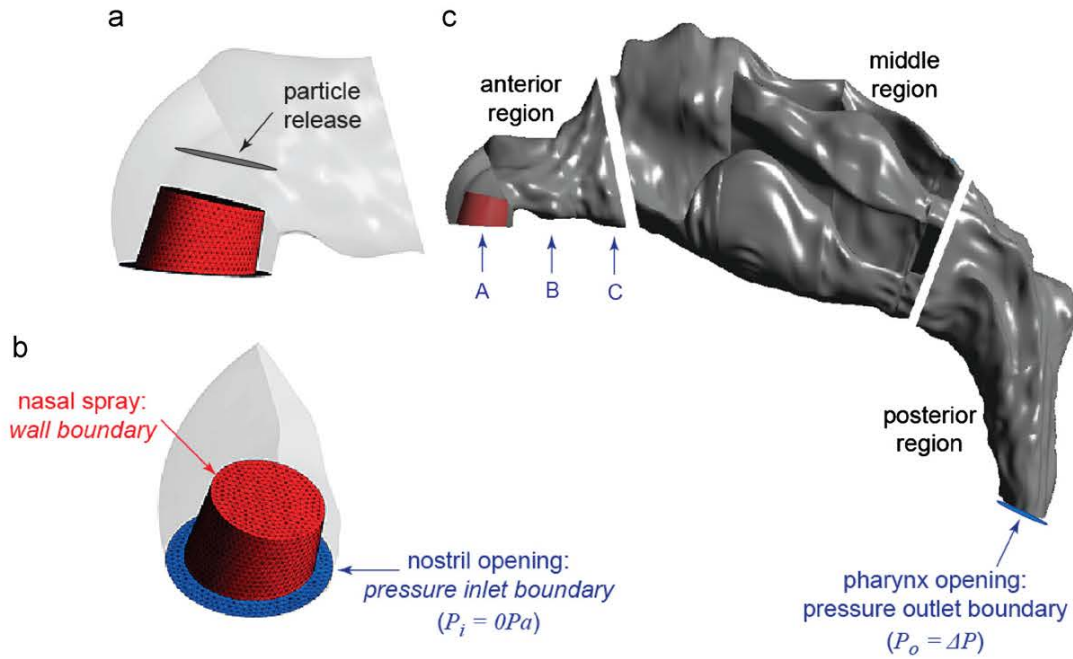


Fig. 1. Computational model inclusive of the nasal spray device, highlighted in red. (a) Particle release region at a distance away from the nasal spray. (b) Cut away of the nostril vestibule where the nasal spray device is inserted. The nasal spray is defined as a wall boundary. The blue annulus region represents the surface inlet opening space, left over from the spray device partially blocking the opening. (c) Computational model subdivided into three regions (anterior, middle, and posterior). Labels A, B, C represent three coronal slices in the left nasal chamber created for visualisation of airflow patterns that are located 0.6, 1.6, and 2.5 cm from the nostril tip. (For interpretation of the references to colour in this figure legend, the reader is referred to the web version of this article.)

### 2.3. Particle phase Modelling

Particles are individually tracked under the Lagrangian approach by integrating the force balance equations on the particle as follows:

$$\frac{du_p}{dt} = F_D(u_g - u_p) + \frac{g(\rho_p - \rho_g)}{\rho_p} + F_s \quad (1)$$

where

$$F_D = \frac{18\mu_g C_D \text{Re}_p}{\rho_p d_p^2} \quad (2)$$

$$\text{Re}_p = \frac{\rho_p d_p |u_p - u_g|}{\mu_g} \quad (3)$$

$$C_D = a_1 + \frac{a_2}{\text{Re}_p} + \frac{a_3}{\text{Re}_p^2} \quad (4)$$

where the  $a$ 's are empirical constants for smooth spherical particles over several ranges of particle Reynolds number (Morsi & Alexander, 1972). The second term in Eq. (1) is the gravity term, while the third term,  $F_s$ , represents other possible forces such as virtual mass force, Basset force, pressure gradient force, lift force, thermophoretic force and Brownian force, which are not applicable for micron particles with  $\rho_p \gg \rho_g$ .

The treatment of one-way turbulent particle dispersions can be performed through a stochastic methodology. The simplest approach and the one available in Ansys-Fluent is the eddy-interaction model (EIM), which is also called the discrete or discontinuous random walk model (DRW). The DRW model is widely used in turbulent particle flows for its conceptual simplicity and uncomplicated reconstruction of the local eddies whose scales are deduced from the local mean flow quantities. The fluid velocity in the particle motion equation (Eq. (1)) becomes  $u_g = \bar{u} + u'$ . The flow field is then assumed to consist of random discrete eddies, each of which is defined by a lifetime, length, and velocity scale. From the model of Gosman and Ioannides (1981) the eddy scales for homogeneous isotropic stationary turbulence are determined from the fluid

turbulence model as

$$L_e = (C_\mu)^{3/4} \frac{k^{3/2}}{\varepsilon}, \quad \tau_e = \frac{L_e}{(2k/3)^{0.5}} = \sqrt{3/2} (C_\mu)^{3/4} \frac{k}{\varepsilon} \quad \text{and} \quad u_e = (2k/3)^{0.5} \quad (5)$$

Graham and James (1996) suggests that these same representative scales should be doubled for non-homogeneous turbulence as the length and time scales are expected to under-estimate particle dispersion. The fluctuating velocity components  $u_i$  that prevail during the lifetime of the turbulent eddy are sampled assuming that they obey a Gaussian probability distribution. The fluctuating velocity is then

$$u_i = \zeta \sqrt{u_i^2} \quad (6)$$

where  $\zeta$  is a normally distributed random number. Assuming that the local root mean square (RMS) velocity fluctuation is isotropy, it can be obtained by

$$\sqrt{u_i^2} = \sqrt{\frac{2K_g}{3}} \quad (7)$$

The interaction time between the particles and the eddies is the smaller than the eddy lifetime  $\tau_e$  and the particle eddy crossing time  $\tau_{cross}$ . The characteristic lifetime of the eddy is defined as

$$\tau_e = -T_L \log(r) \quad \text{in which} \quad T_L \approx \frac{0.15}{\omega} \quad (8)$$

$$\tau_{cross} = -\tau \ln \left[ 1 - \left( \frac{L_e}{\tau |u_g - u_p|} \right) \right] \quad (9)$$

$$\tau_p = \frac{\rho_p d_p^2}{18 \mu_g} \quad (10)$$

The particle interacts with the fluid eddy over the interaction time. When the eddy lifetime is reached, a new value of the instantaneous velocity is obtained by applying a new value of  $\zeta$  in Eq. (6). For one-way coupling the fluid velocity is 'frozen' and the eddy lifetime diminishes to an infinitesimal value as it approaches the wall leading to a build up in particle concentration, an effect which increases as particle inertia reduces. This causes the particles to move very slowly and despite increases in the number of integration steps, they may still not touch the near walls. To alleviate this, different values for the numerical timestep ( $\Delta t = 10^{-6}$  s for  $\tau_p^+ < 3$  and  $\Delta t = 10^{-5}$  s for  $\tau_p^+ \geq 3$ ) were chosen based on preliminary testing in a pipe simulation and the results from Matida, Nishino, and Torii (2000) and Longest and Xi (2007), where  $\tau_p^+$  is the normalisation of  $\tau_p$  by the friction velocity  $u^*$  and kinematic viscosity  $\nu_g$ , given as

$$\tau_p^+ = \tau_p \frac{u^*}{\nu_g} = \frac{\rho_g d_p^2 u^* \rho_p}{18 \mu_g^2 \rho_g} \quad (11)$$

When using RANS turbulence models that are based on an isotropic assumption ( $u' = v' = w' = (2k/3)^{0.5}$ ), the deposition of the small particles ( $\tau_p^+ < 10$ ) is over-predicted. The over-prediction is primarily caused by  $v'$ , which is much smaller in comparison with the other fluctuating components  $u'$  and  $w'$ . This can be accounted for by correcting the near wall fluctuations (Matida, Finlay, Lange, & Grgic, 2004; Wang & James, 1999), using the following function:

$$k_{new} = [1 - \exp(-0.02y^+)]^2 k \quad \text{for } y^+ < 60 \quad (12)$$

Preliminary pipe flow tests were performed at a  $Re = 2300$  ( $Re_\tau = 56$ ), which is a similar flow regime to nasal cavity airflows. Fig. 2 shows the  $v'^+$  profile of the isotropic decomposition of  $k$  (turbulent kinetic energy), which overestimates the fluctuation in the near wall region. It is evident that the isotropic decomposition over-predicts the  $v'^+$ . The near wall correction improves this profile and it is expected to improve the particle deposition also.

#### 2.4. Boundary conditions

Inhalation through the nasal cavity is induced through the pressure difference caused by the movement of the diaphragm compressing and decompressing the lung. Therefore the outlet of the nasal cavity (pharynx) was set as a negative pressure equivalent to 20 L/min relative to the atmospheric pressure at the nostril inlets. The wall boundary condition for the particles was set to 'trap' that all particle trajectories ceased once they touch a wall and the effects of accretion and erosion of particles at the walls are not considered. The sprayed particles adopted the properties of spherical water particles, as most drug formulations are diluted with water. Other assumptions include no particle rebounding off the walls/surfaces, no particle breakup or coagulation, and no particle deformation. The number of particles tracked was checked for statistical independence since the turbulent dispersion is a stochastic process. Particle number independence was deemed for 30,000 particles since an increase to 50,000 particles yielded a difference of 0.1% in the inhalation efficiency.

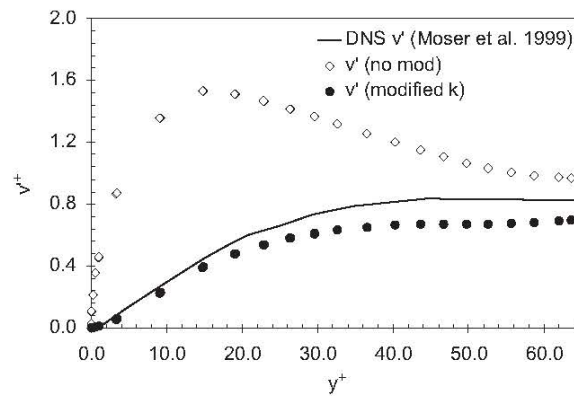


Fig. 2. RMS of normal-to-the-wall velocity fluctuations,  $v'$ . The CFD simulation for the  $k-\omega$  has a  $Re_\tau=56$  while the DNS data from Moser, Kim, and Mansour (1999) is shown for  $Re_\tau=180$ .  $v'$  is normalised by the friction velocity ( $u_\tau$ ).

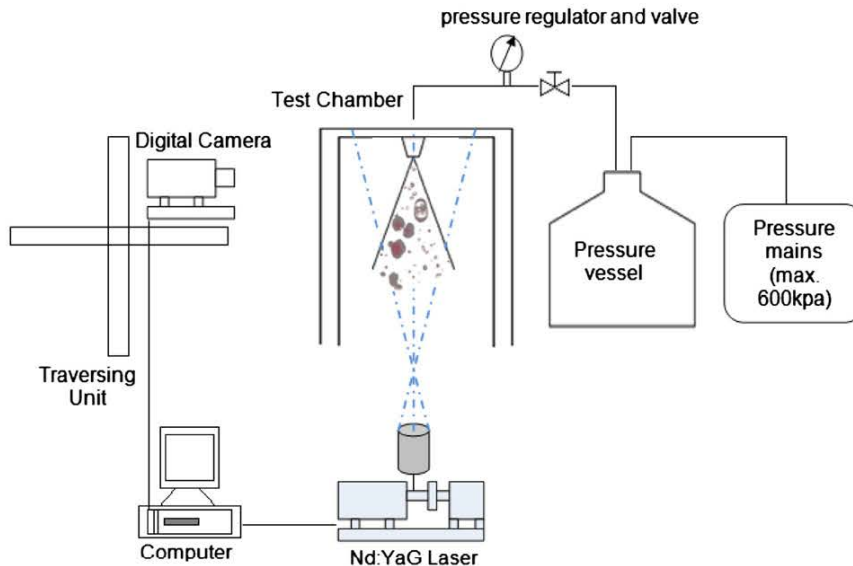


Fig. 3. Schematic of the experimental setup for spray particle measurements.

### 2.5. Experimental setup

The experimental setup for this study is shown in Fig. 3, which includes a test chamber, a pressurised water supply system, a liquid collection system, and a visualisation system. A particle/droplet image analysis (PDIA) digital image analysis technique by Oxford Lasers<sup>®</sup> was used, which was capable of determining the properties of individual particles such as its velocity, size, shape, and concentration over a finite region of interest in the flow. For capturing the spray, a double-pulsed Nd:YAG laser was used as the illumination source with a pulse duration of 5 ns. Droplet images were acquired with a non-intensified 12-bit digital camera (PCO Sencicam) and a long distance microscope lens with a magnification of 2.46. This provided a  $1280 \times 1024$  pixel array to capture a physical region of  $3.85 \text{ mm} \times 3.08 \text{ mm}$ . A long distance microscope lens provided a magnification of 2.46 offering a resolution of approximately  $3.01 \mu\text{m}/\text{pixel}$ . The camera was mounted on a traversing unit, which allowed precise movements in all three coordinates ( $\pm 17 \mu\text{m}$  precision) to reposition the camera in order to capture the spray in full. A constant upstream pressure of 5 Bar was applied and the water was released through a pressure regulator-valve and allowed to reach steady conditions before the images were taken. A single run was limited to approximately 3 min in order to avoid pressure variations associated with a decrease in liquid volume within the pressure tank. The spray nozzle used in the present study was a nasal spray device kindly provided by Saint-Gobain<sup>®</sup>/Calmar<sup>®</sup>, Product Number 43110-016.



Diameter measurements in PDIA are based on an area estimate of the shadow image of an individual droplet (straightforward for a perfect sphere). Four commonly used statistical mean diameters are: the number mean diameter,  $D_{10}$ ; the volume mean diameter,  $D_{30}$ ; the Sauter (or surface weighted) mean diameter,  $D_{32}$ , and the volume weighted mean diameter,  $D_{43}$ . The various diameters are defined using the equation:

$$D_{mn} = \left[ \frac{\sum d_i^{m-3} V_i}{\sum d_i^{n-3} V_i} \right]^{1/(m-n)} \quad (13)$$

where  $V_i$  is the relative volume of droplets with diameter,  $d_i$ , and  $m$  and  $n$  are integer values that describe the mean being used. Thus the Sauter mean diameter,  $D_{32}$ , is defined by the equation:

$$D_{32} = \left[ \frac{\sum d_i^3}{\sum d_i^2} \right] \quad (14)$$

The Sauter mean diameter was selected to represent the mean diameter of droplets within the flotation cell and is particularly relevant to hydrodynamics and mass transfer, since both drag and reaction rates are proportional to the droplet area.

### 3. Results

#### 3.1. Computational model validation

Particle deposition efficiencies have been reported in the literature for particles released into the nasal cavity (Cheng et al., 2001; Kelly, Asgharian, Kimbell, & Wong, 2004; Shi, Kleinstreuer, & Zhang, 2007). The deposition of particles as a function of the inertial parameter, ( $d_a^2 Q$ ) is shown in Fig. 4, which displays the characteristic curve associated with inertial deposition. It can be seen among the experimental deposition data in between Cheng et al. (2001) and Kelly et al. (2004) that there is a discrepancy of up to 4X (80% and 20% at IP=10000) which could be due to the subject variability between the nasal cavity models obtained by Kelly et al. (2004) (53-year-old Caucasian male) and the model used in the present study (25-year-old Asian male), while Häußermann, Bailey, Bailey, Etherington, and Youngman (2001) also states that nasal cavity replicate casts with wider airways can cause less deposition due to secondary flow. The DRW model significantly overestimates particle deposition for an inertial parameter (IP) < 10,000. The modification to the model improves the deposition efficiency for better agreement with the reported data for IP < 10,000. In order to gain confidence in our numerical setup, a simple geometry in the form of a 90° bend pipe was also used to investigate the particle tracking model. The 90° bend pipe is useful as the nasal cavity exhibits similar bends at the nostril inlet (anterior) and the nasopharynx (posterior) ends. In this test the data of Pui, Romay-Novas, and Liu (1987) is used (Fig. 5). The results show that the DRW model over-predicts particle deposition for low Stokes number (< 0.1). The DRW with the near wall correction shows that there is a definite improvement to the turbulent tracking model and this provides some confidence to implement the same setup for the nasal cavity model.

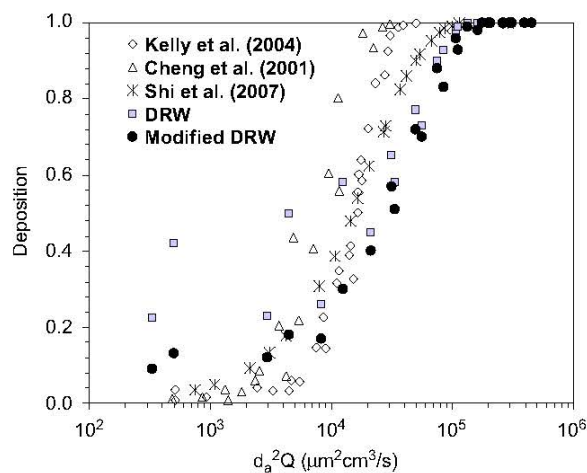


Fig. 4. Inertial deposition efficiency for micron particles in the left cavity side of human nasal cavity compared with the reported data.

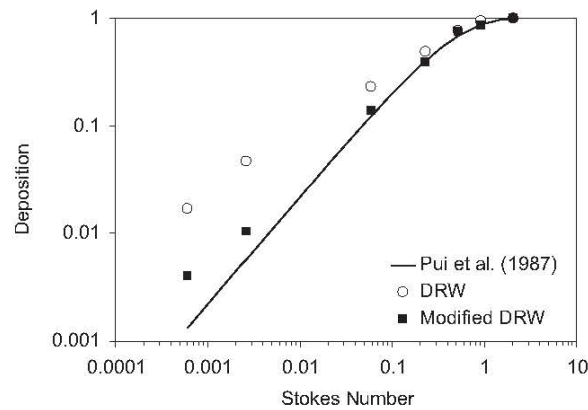


Fig. 5. Particle deposition in a 90° pipe bend for  $Re=10,000$ . The depositions by the DRW process and the modified DRW are shown.

Table 1

Mass flow rates induced through a pressure difference between the pharynx ( $P_i$ ) and the nostril inlets ( $P=0$  Pa).

$P_i$ (Pa)	Nose model			Nose model with spray		
	Left (L/min)	Right (L/min)	Total (L/min)	Left (L/min)	Right (L/min)	Total (L/min)
5	3.81	4.92	8.73	2.87	5.10	7.97
10	5.81	7.22	13.03	4.44	7.50	11.94
15	7.41	9.01	16.42	5.70	9.37	15.06
20	8.73	10.50	19.22	6.73	10.93	17.67
30	10.97	13.13	24.10	8.55	13.74	22.28
40	12.85	15.37	28.23	10.09	16.05	26.14
60	16.11	19.13	35.24	12.73	19.95	32.68

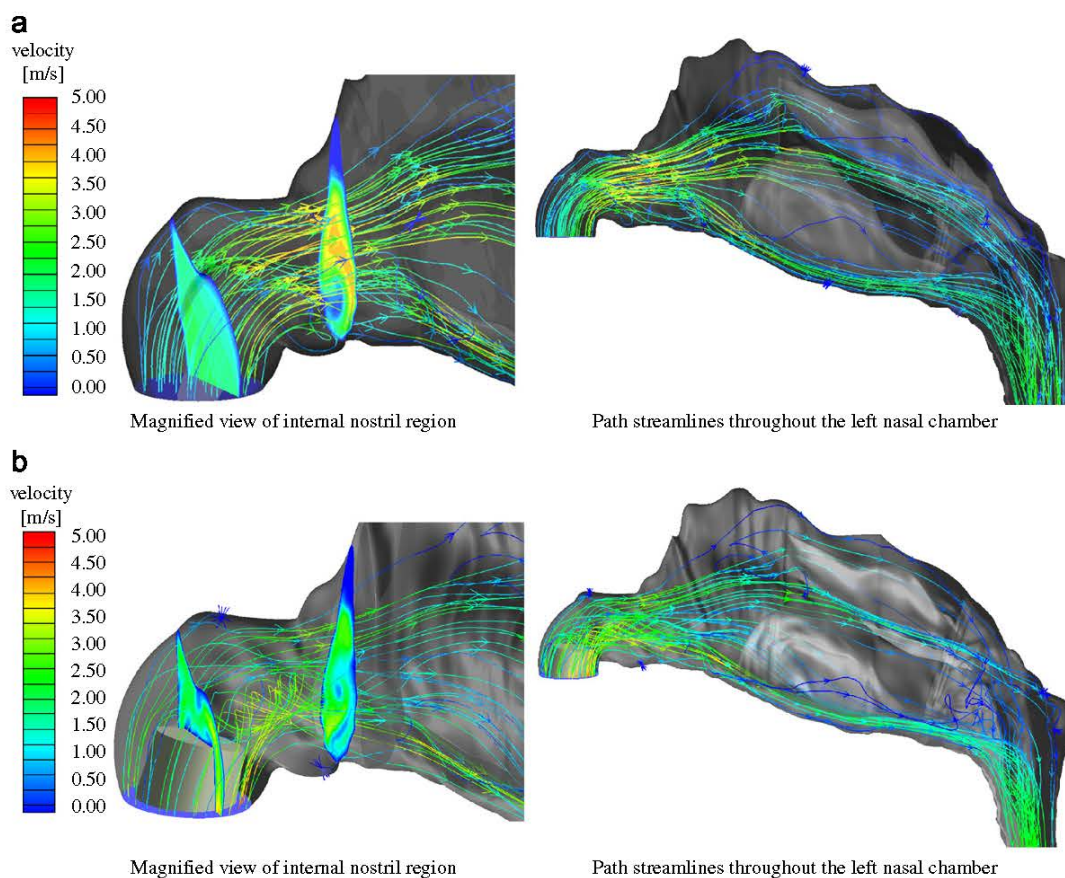
### 3.2. Airflow field

Table 1 shows the mass flow rate obtained from the average pressure drop between the nostril and the pharynx ranging from 5 to 60 Pa. At these pressure drops, the corresponding range of Reynolds numbers at the inlets is 981–3951. In both cases the right nasal chamber shows a greater proportion of flow distribution. Further calculations show that the volume of left cavity is smaller by about 13% than the right cavity, which explains the biased distribution between the left and the right airway, which is 44–56% without the nasal spray and 32–68% with the presence of the nasal spray.

Path streamlines that track the fluid motion from the nostril inlet are shown in Fig. 6(a) for a plain nasal cavity model and (b) a nasal cavity including the spray device. For the plain nasal model, the flow streamlines are generally undisturbed as it flows from the nostril inlet and into the nasal valve. The main feature of the flow appears in the nasal valve region where the flow accelerates through the narrowest cross-section of the airway. This region of flow also exhibits some vortical flow proximal to the airway floor as the flow changes direction from a vertical to a horizontal direction due to the 90°-like bend at the nostril. The bulk flow passes mainly through the middle of the cross-section and then partitions into the upper, middle, and lower flow. The presence of the spray device, taking up space in the nasal vestibule, shows an increase in disturbance within the flow. The effective area of the nostril to the open air is reduced and within the narrow air spaces, the flow accelerates through. At the top of the spray, the streamlines separate and swirl through the nasal valve region. Contours of velocity magnitude with streamwise and crossflow velocities superimposed were applied to cross-sectional slices (Fig. 7) taken at the three locations ( $x=0.6$ , 1.6, and 2.5 cm from the nose tip) as depicted in Fig. 1. The presence of the spray device causes high velocities in the confined space of the nostril periphery as shown in the path streamlines. At the spray head, the flow field experiences separation and two recirculating vortices are found at the edge of the spray device. At the cross-section B,  $x=1.6$  cm, vortices are present in the lower corners due to the elevation of the geometry. The streamlines show the flow still rising vertically. At cross-section C,  $x=2.5$  cm, the flow patterns are quite different for the two models, which suggests that the influence of the spray nozzle inside the nasal cavity is prevalent up to  $x=2.5$  cm.

### 3.3. Sprayed particle characteristics

Using a traversing system, a camera with a field of view (FOV) of 3.082 mm  $\times$  3.853 mm is moved to ten different positions to capture the entire range of the spray field (Fig. 8a). In the near nozzle region the nasal spray produces a continuous liquid



**Fig. 6.** Path streamlines in the anterior region of the nasal cavity affected by the presence of the nasal spray device. Two cross-sections are shown, one at the spray nozzle and the other at the nasal valve region. (a) Plain nasal cavity model and (b) nasal cavity model with spray device.

stream. The liquid appears to oscillate and roll downstream in waves (Fig. 8b). Further downstream the liquid becomes critically unstable and breaks up into ligaments. The two separate snapshots in time show the destructive change on the liquid sheet as a consequence of the unstable wave on the liquid surface. This initial stage of breakup is called the primary breakup of atomisation. The distance at which clearly formed particles are observed is called the breakup length, which occurs just after the ligament breakup region (between the second and the third row in Fig. 8a). At this location, the particles are dispersed over the spray diameter. This is important for CFD models since the introduction of particles into the computational model needs to be defined at a breakup length rather than as a point source from the nozzle exit (which has traditionally been the case). Additional parameters measured for this particular nasal spray include nozzle diameter ( $\sim 0.5$  mm), spray cone angle ( $\sim 30^\circ$ ), initial particle velocity ( $\sim 15$  m/s), and breakup length ( $\sim 5$  mm).

The Sauter mean diameter,  $D_{32}$ , was also measured for the bottom two rows of images (Fig. 8a) (the first two rows were not able to be analysed because of the dense liquid region). Eight mean diameters, three along the fourth row and five across the fifth row, are shown in Fig. 9. Larger Sauter mean diameters are located centrally in the bulk spray flow region. In the centre panel at  $x=0$  mm,  $y=7.705$  mm, the largest statistically significant diameter (having at least 0.1% number count) measured was 291–301  $\mu\text{m}$ , while the smallest diameter was 11–21  $\mu\text{m}$ . Further downstream the diameters continue to breakup into smaller particles. This stage of breakup is called the secondary atomisation breakup. In the outer periphery smaller diameters are found. These measurements provide a perspective when setting a range of values for the initial particle boundary conditions in CFD models. In addition a more effective parametrical study can be performed and analysed to provide better guidance in the development stages of nasal sprays for drug delivery. The spray device was included in the model by placing it in the left nasal chamber at an insertion angle of  $10^\circ$  to the vertical axis. The dispersion of the particles is represented by the spray cone angle that was set at an angle of  $30^\circ$ , and the swirl fraction was 0.5, which is only applicable for a hollow spray cone type. Initial tests of particles with nominal mean diameters suggested by the experimental data (e.g.  $> 80$   $\mu\text{m}$ ) found that all the particles are deposited immediately in the anterior nasal cavity region because of its high inertia. Sprayed particles were introduced into the nasal cavity from a breakup length,  $L_{bu}$ , of 4 mm. The spray cone diameter at the breakup length,  $d_{bu}$ , was 3 mm, while the initial particle velocity was 15 m/s.

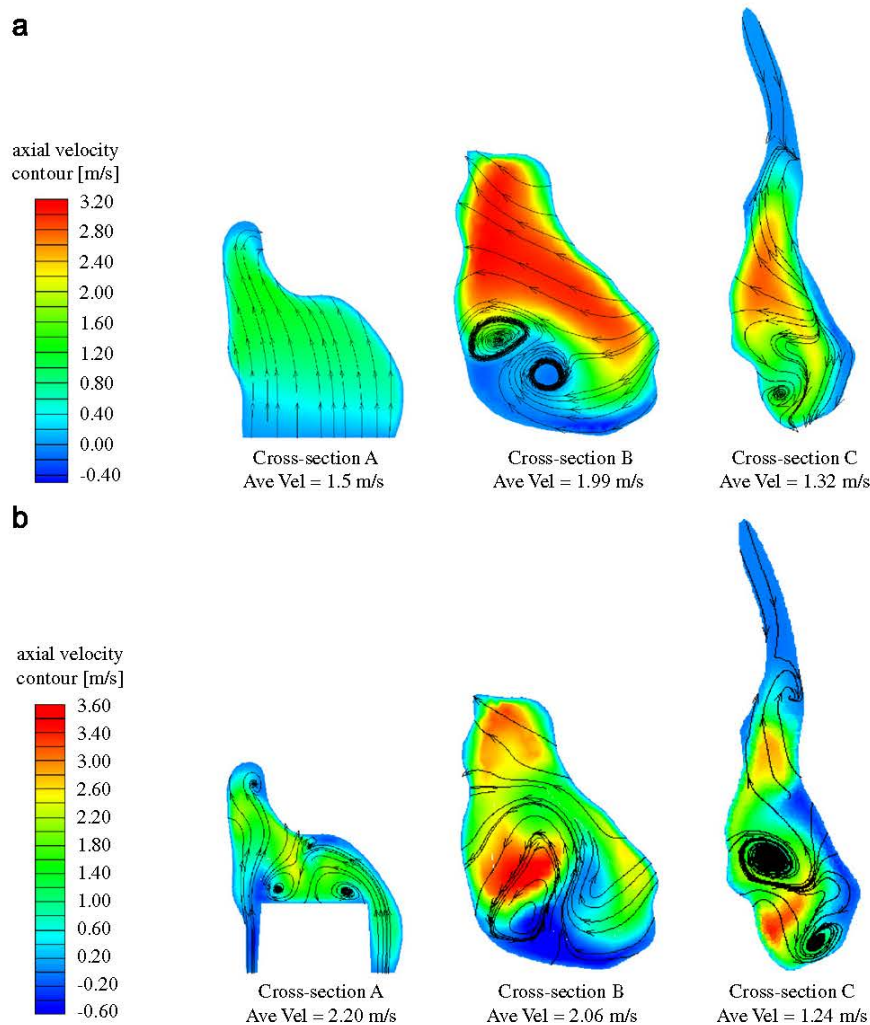
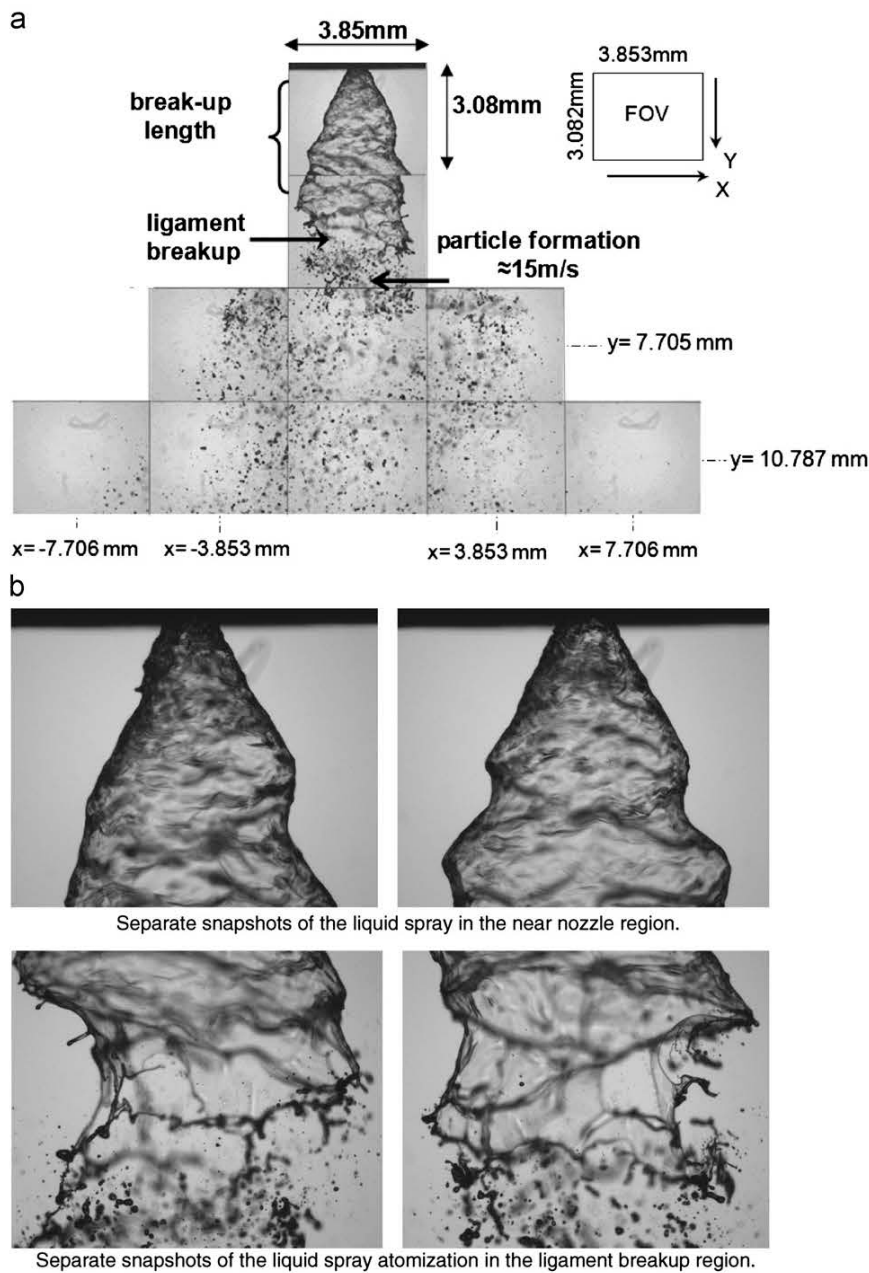


Fig. 7. Crossflow streamlines superimposed onto contours of velocity magnitudes at different coronal cross-sections as defined in Fig. 1. (a) Plain nasal cavity model and (b) nasal cavity model with spray device.

#### 3.4. Particle deposition

Sprayed particle deposition in each region (A—anterior region; M—middle region; and P—posterior region) from the two spray types (solid and hollow cones) is shown in Fig. 10. In general there are small differences between the hollow and the solid spray cones. For both the 5 and 15  $\mu\text{m}$  particles hollow spray cones provide greater deposition in the middle nasal region, which may be due to the radial distribution of the particles caused by the swirling component. As the particle size increases so does the particle inertia. For 15  $\mu\text{m}$  particles, the atomised hollow spray achieves 11% deposition in the middle region of the nasal cavity, whereas a solid sprayed cone achieves 100% deposition in the anterior region, and therefore 0% in the middle region. The swirl fraction creates a radial velocity component for hollow spray cones. This helps direct the particles horizontally towards the nasal valve region, leading to increased particle flow through to the middle nasal cavity. For 50  $\mu\text{m}$  particles, maximum deposition occurs in the anterior regions and no particles reach the middle region. For the solid cone spray deposition occurred mainly in the anterior region, while for the hollow cone, more particles were able to deposit in the middle regions. It should also be noted that a large number of 5  $\mu\text{m}$  particles escaped through the pharynx. This will lead to deposition later downstream in the respiratory tract, and may even deposit deep in the lungs, which may have an adverse health response.

The deposition pattern and particle trajectories for the 5 and 15  $\mu\text{m}$  particles are shown in Figs. 11 and 12, respectively. In addition the particle velocity as it impacts the surface walls was recorded and an average value was taken ( $V_{pi} = \sum_{i=0}^N (v_i/N)$ ). Note that this average particle impact velocity, ( $V_{pi}$ ), is not the same as the deposition velocity,  $V^+ = (U_{ave}A/u^*P\Delta x)\log(N_{in}/N_{out})$ ,



**Fig. 8.** (a) Microscope scan of the internal spray atomizer nozzle. (b) Instantaneous images with the field of view (FOV) of 3.853 mm  $\times$  3.082 mm of the external spray characteristics taken at ten locations and collated together. (c) Two sets of images separated by in time showing the spray particle formation at the near-nozzle region and at the ligament breakup region.

used to characterize the rate of deposition, but rather is a way to determine the influence of the initial particle conditions. The 5  $\mu$ m deposition patterns for the two spray types are similar and this is evident in the particle trajectories that show similar flow paths. The small differences between the two sprays include a greater number of particles depositing immediately above the spray nozzle for the solid spray cone, which is reflected by the higher  $V_{pi}$ . This  $V_{pi}$  value suggests that a larger proportion of particles impacts immediately above the nozzle for a solid spray cone. The lower  $V_{pi}$  suggests that more particles become entrained in the airflow. The particle trajectories are coloured by particle residence time, which also highlights the looping motion of some particles near the spray nozzle. Some particles that are directed away from the main nasal passage lose enough of its initial velocity and change its direction and gets closer to the nozzle.

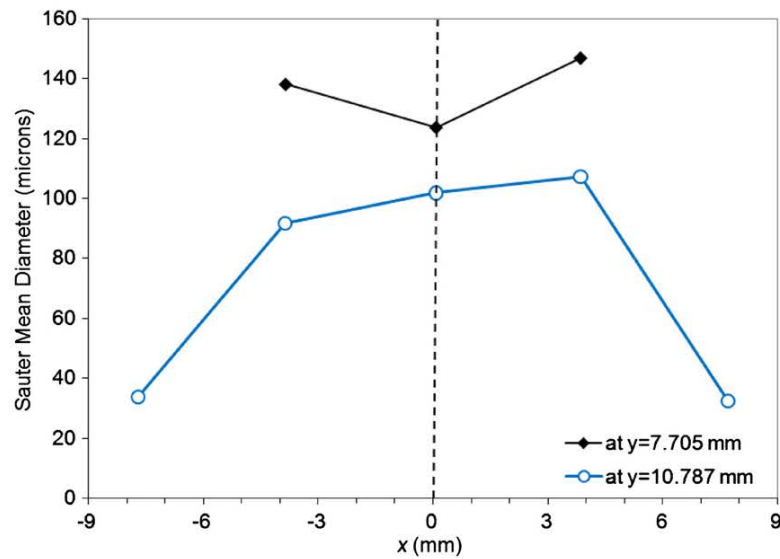


Fig. 9. Sauter mean diameter  $D_{32}$  taken for each FOV section or the fourth ( $y=7.705$  mm) and fifth rows ( $y=10.787$  mm) as depicted in Fig. 9b.

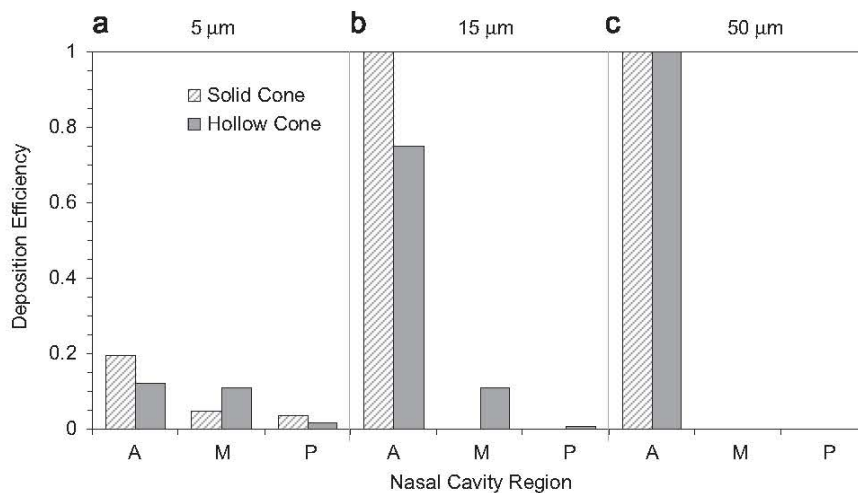
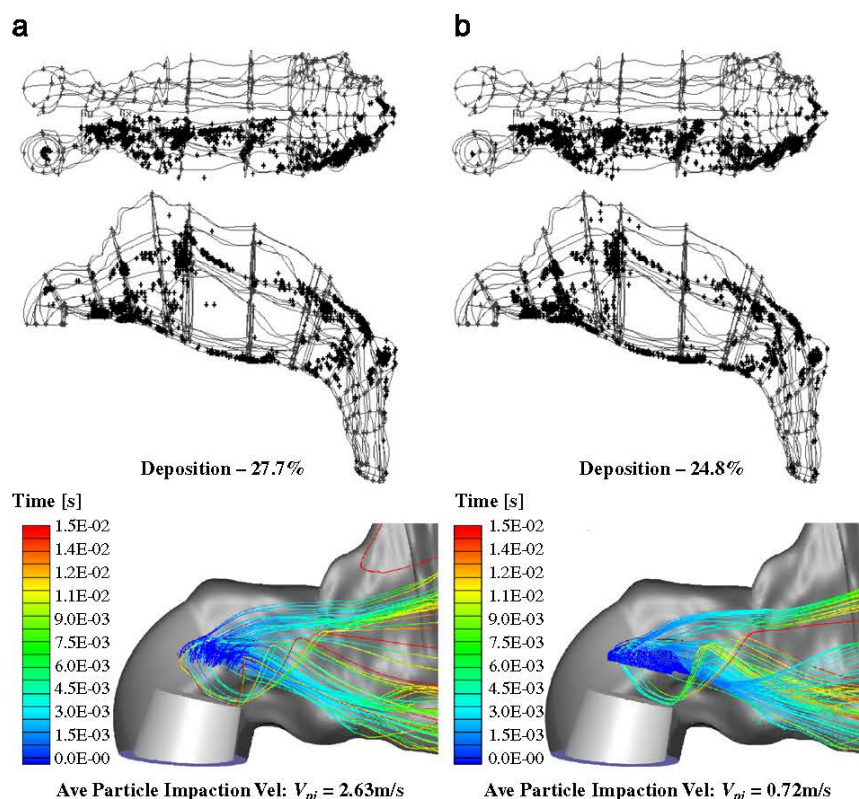


Fig. 10. Sprayed particle deposition from a hollow and a solid spray cone. The x-axis labels, A, M, P represent Anterior, Middle, and Posterior regions, respectively.

15  $\mu\text{m}$  particles have a higher inertial property than a 5  $\mu\text{m}$  particle. The deposition patterns immediately above the nozzle form an outline of the spray type (either solid or hollow spray). While this simulation does not account for particle splattering onto the surface and eventual mucociliary clearance along the nasal walls, it demonstrates the influence of the initial particle conditions (such as the swirl component and the insertion angle) on higher inertial particles. The hollow spray cone allows a small fraction of particles to 'squeeze' through the nasal valve region. It is then inferred that these particles are entrained in the flow before depositing downstream. The  $V_{pi}$  for the solid cone shows that on average the initial particle velocity has decreased from 15 to 9.59 m/s over the small distance from particle injection to the upper walls while for hollow sprays this value is 6.64 m/s.

#### 4. Discussion

Sprayed particle deposition between two computational models of nasal cavity is compared, where the difference between the two models was the presence of a nasal spray device inserted into the left nasal chamber. Firstly the airflow distribution and patterns were compared, which found that the presence of the nasal spray device creates additional



**Fig. 11.** Deposition pattern of  $5\ \mu\text{m}$  in the nasal cavity for solid and hollow spray cones. The particle trajectories are coloured by residence times. (a) Solid cone and (b) hollow cone. (For interpretation of the references to colour in this figure legend, the reader is referred to the web version of this article.)

resistance, obstructing the inhaled air and reducing the flow rate. Furthermore the asymmetrical airflow distribution between the two nasal passages can be attributed to the nasal cycle, which is a result of congestion (swelling) of the erectile tissue (cavernous tissues of the mucosa) in one nasal cavity while at the same time decongestion (shrinking) occurs to the erectile tissue in the other cavity. The airflow through each nasal cavity is then governed by the resistance caused by the cross-sectional area of each airway. Streamlines of secondary flows found that vortices are present in regions of low velocity magnitudes, and in regions of geometry expansion.

Experimental images were then obtained to establish a better understanding of the nasal spray device characteristics. It was deduced that the internal spray atomizer was that of a pressure-swirl type, which is distinguished by the ability to produce greater spray cone angles. The droplet size produced was considerably high having  $D_{32}$  in the order of  $100\ \mu\text{m}$  in the centre plane of the spray, while at the periphery  $D_{32}$  was approximately  $30\ \mu\text{m}$ . The particle size produced is a function of liquid pressure and swirl chamber dimensions, where the smaller the swirl chamber is, the finer the resultant droplets can become, but a greater back pressure is needed to force the liquid through the atomizer. The design of the spray atomizer therefore yields significant influence on the particle trajectories.

It is well recognised that one of the functions of the nose is to filter out foreign particulates during inhalation which was mainly thought to be attributed to cilia movement and nasal hairs within the nose. The curvature in the anterior nose along with the constricting nasal valve region is most significant for therapeutic drug delivery as it prohibits larger particles to penetrate into the middle cavity region for deposition onto the highly vascularised mucosal walls. The initial particle conditions from the experimental data showed that the atomised particles are large in size leading to early deposition in the anterior nasal cavity. The particles that are introduced into the airway therefore need to have its inertia stripped away. The swirling fraction that represents the radial component from the swirl atomizer presents the most effective method to reduce the axial velocity. In addition other parameters such as spray cone angle, insertion angle, particle size distribution, initial particle velocity and the location of injection can play a role in the delivery of drug particles. Improvements to the spray atomizer during its design stage may involve atomising the particles at a slower velocity and achieving a much finer particle size distribution. Also instructions for a patient/user may include aligning the spray device more horizontally to the main nasal passage to increase the chances of deposition downstream from the anterior region. This may involve tilting of the head backwards to allow better alignment.

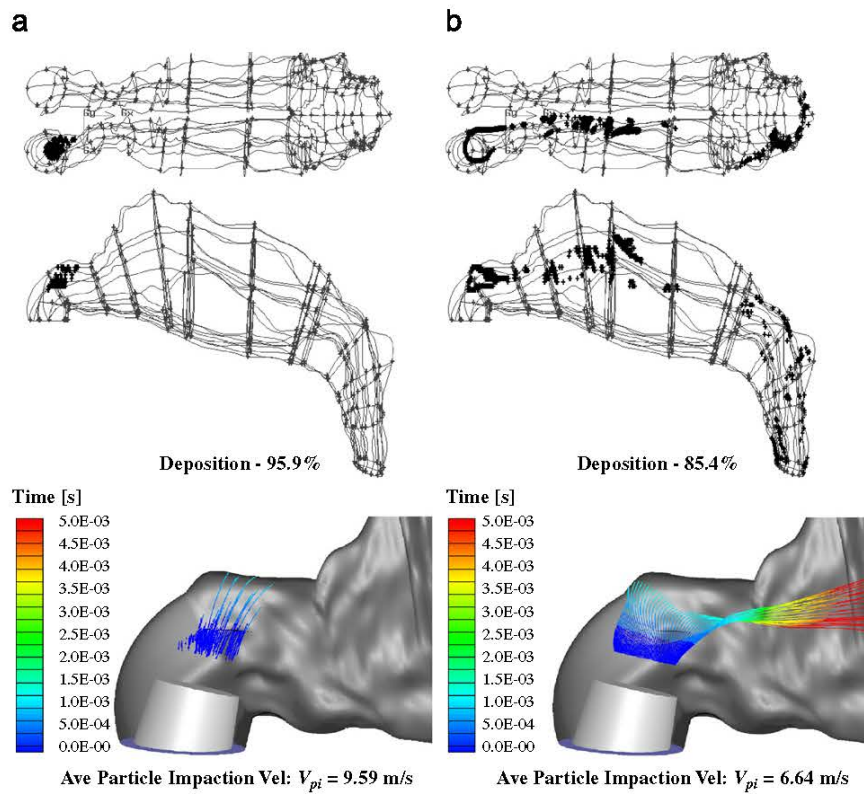


Fig. 12. Deposition of 15  $\mu\text{m}$  in the nasal cavity. The particle trajectories are coloured by residence times. (a) Solid cone and (b) hollow cone. (For interpretation of the references to colour in this figure legend, the reader is referred to the web version of this article.)

Finally, some limitations and improvements of this study need to be noted. In this study one-way coupling is used, which assumes that the flow of particles do not affect the fluid flow. This assumption is valid where the volume fraction of the particles is relatively low ( $< 10\%$ ). This occurs downstream as the particles disperse through the nasal cavity. However near the spray nozzle region (i.e. dense spray region), where the particles are atomising, the volume fraction is much higher. The flow field in this region is therefore expected to be under-predicted in the direction that the spray is aligned ( $10^\circ$  from the vertical). From the spray images the two-way coupling influence for momentum exchange is limited to approximately 6 mm from the spray nozzle. Turbulence modulation is therefore also not included, which requires an additional loop in the numerical iteration within the current methodology. Other assumptions include no particle breakup or coagulation, no particle deformation, and evaporation.

## 5. Conclusion

Two computational models of human nasal cavity were produced from CT-scans, where the difference between the two models was the presence of a nasal spray device. This was coupled with the experimental data that was used to provide realistic initial particle boundary conditions. The experimental data was obtained from PDIA measurements, which provided visualisation of the spray development as well as the Sauter mean diameter at different sections of the spray. Important features of the spray characteristics include the spray cone angle, particle size, and the diameter of the spray cone at a breakup length from the nozzle. The measured values provided a basis for setting appropriate initial particle conditions for the computational model. The two nasal cavity models were first simulated to investigate the differences in the airflow field caused by the presence of the nasal spray head. Increased levels of disturbed flow were found where the spray device was placed in the nasal vestibule. The increase in vortices can have two effects: (i) the swirling vortices that have radial and tangential velocities may in fact slow down the linear velocity of the sprayed particles, thereby reducing the particle inertia and (ii) the dispersion of the particles is increased due to the vortices.

Droplet deposition was found to be high in the anterior regions of the nasal cavity caused by the particle inertia, which is a major hindrance for particles to get through the narrow nasal valve region. Evaluation of the two spray cone types found that hollow spray cones produced more deposition in the middle regions of the nasal cavity for 5 and 15  $\mu\text{m}$  particles. For increased efficacy in nasal drug delivery, design issues such as atomisation for finer particle size distribution and slower



initial particle velocity are suggested. In addition instructing the user to align the spray with the main nasal passage may also help. These results demonstrate the use of CFD to provide insight into design issues related to the spray atomizer performance for nasal drug delivery. In addition this work is a step forward towards a more integrated drug delivery simulation that still lacks additional physics such as unsteady inhalation, and further complex physics such as multiphase turbulence and fluid structure interactions.

## Acknowledgements

The financial support provided by the Australian Research Council (project ID LP0989452) and RMIT University through an Emerging Researcher Grant is gratefully acknowledged.

## References

- Ansys, W. C. (2007). *Fluent User Manual*. USA: Ansys Inc.
- Cheng, Y. S., Holmes, T. D., Gao, J., Guilmette, R. A., Li, S., Surakitbanharn, Y., et al. (2001). Characterization of nasal spray pumps and deposition pattern in a replica of the human nasal airway. *Journal of Aerosol Medicine*, 14, 267–280.
- Gosman, A. D., & Ioannides, E. (1981). Aspects of computer simulation of liquid-fuelled combustors. In: AIAA 19th Aerospace Sciences Meeting, St Louis, MO.
- Graham, D. I., & James, P. W. (1996). Turbulent dispersion of particles using eddy interaction models. *International Journal of Multiphase Flow*, 22, 157–175.
- Häußermann, S., Bailey, A. G., Bailey, M. R., Etherington, G., & Youngman, M. J. (2001). The influence of breathing patterns on particle deposition in a nasal replicate cast. *Journal of Aerosol Science*, 33, 923–933.
- Inthavong, K. (2006). A numerical study into local deposition sites in the nasal cavity for therapeutic and pollutant inhalation. In: Ansys Australasian Users Conference Proceedings 2006.
- Inthavong, K., Tian, Z. F., Li, H. F., Tu, J. Y., Yang, W., Xue, C. L., et al. (2006). A numerical study of spray particle deposition in a human nasal cavity. *Aerosol Science and Technology*, 40, 1034–1045.
- Inthavong, K., Tian, Z. F., Tu, J. Y., Yang, W., & Xue, C. (2008). Optimising nasal spray parameters for efficient drug delivery using computational fluid dynamics. *Computers in Biology and Medicine*, 38, 713–726.
- Inthavong, K., Wen, J., Tian, Z. F., & Tu, J. Y. (2008). Numerical study of fibre deposition in a human nasal cavity. *Journal of Aerosol Science*, 39, 253–265.
- Inthavong, K., Wen, J., Tu, J. Y., & Tian, Z. F. (2009). From CT scans to CFD modelling – fluid and heat transfer in a realistic human nasal cavity. *Engineering Applications of Computational Fluid Mechanics*, 3, 321–335.
- Kelly, J. T., Asgharian, B., Kimbell, J. S., & Wong, B. A. (2004). Particle deposition in human nasal airway replicas manufactured by different methods. Part 1: Inertial regime particles. *Aerosol Science and Technology*, 38, 1063–1071.
- Keyhani, K., Scherer, P. W., & Mozell, M. M. (1995). Numerical simulation of airflow in the human nasal cavity. *Journal Biomechanical Engineering*, 117, 429–441.
- Kleinstreuer, C., & Zhang, Z. (2003). Targeted drug aerosol deposition analysis for a four-generation lung airway model with hemispherical tumours. *Journal of Biomechanical Engineering*, 125, 197–206.
- Li, Z., Kleinstreuer, C., & Zhang, Z. (2007). Simulation of airflow fields and microparticle deposition in realistic human lung airway models. Part I: Airflow patterns. *European Journal of Mechanics B/Fluids*, 26, 632–649.
- Longest, P. W., & Xi, J. (2007). Effectiveness of direct Lagrangian tracking models for simulating nanoparticle deposition in the upper airways. *Aerosol Science and Technology*, 41, 380–397.
- Matida, E. A., Finlay, W. H., Lange, C. F., & Grgic, B. (2004). Improved numerical simulation for aerosol deposition in an idealized mouth-throat. *Journal of Aerosol Science*, 35, 1–19.
- Matida, E. A., Nishino, K., & Torii, K. (2000). Statistical simulation of particle deposition on the wall from turbulent dispersed pipe flow. *International Journal of Heat and Fluid Flow*, 21, 389–402.
- Morsi, S. A., & Alexander, A. J. (1972). An investigation of particle trajectories in two-phase flow systems. *Journal Fluid Mechanics*, 55, 193–208.
- Moser, R. D., Kim, J., & Mansour, N. N. (1999). Direct numerical simulation of turbulent channel flow up to  $Re_\tau=5590$ . *Physics of fluids*, 11, 943–945.
- Pui, D. Y. H., Romay-Novas, F., & Liu, B. Y. H. (1987). Experimental study of particle deposition in bends of circular cross section. *Aerosol Science and Technology*, 7, 301–315.
- Shi, H. W., Kleinstreuer, C., & Zhang, Z. (2007). Modeling of inertial particle transport and deposition in human nasal cavities with wall roughness. *Journal of Aerosol Science*, 38, 398–419.
- Straatsma, J., Van Houwelingen, G., Steenbergen, A. E., & De Jong, P. (1999). Spray drying of food products: 1. Simulation model. *Journal Food Engineering*, 42, 67–72.
- Subramaniam, R. P., Richardson, R. B., Morgan, K. T., Kimbell, J. S., & Guilmette, R. A. (1998). Computational fluid dynamics simulations of inspiratory airflow in the human nose and nasopharynx. *Inhalation Toxicology*, 10.
- Suman, J. D., Laube, B. L., Lin, T. C., Brouet, G., & Dalby, R. (2002). Validity of in vitro tests on aqueous spray pumps as surrogates for nasal deposition. *Pharmaceutical Research*, 19, 1–6.
- Wang, K., Denney, T. S., Morrison, E. E., & Vodyanoy, V. J. (2005). Numerical simulation of air flow in the human nasal cavity. In *Proceedings of the 27th IEEE Annual Conference on Engineering in Medicine and Biology* (pp. 5607–5610). Shanghai, China.
- Wang, Y., & James, P. W. (1999). On the effect of anisotropy on the turbulent dispersion and deposition of small particles. *International Journal of Multiphase Flows*, 25, 551–558.
- Wilcox, D. (1993). *Turbulence Modeling for CFD*. 5354 Palm Drive, La Canada, California: DCW Industries, Inc., 91011.
- Zamankhan, P., Ahmadi, G., Wang, Z., Hopke, P. H., Cheng, Y. S., Su, W. C., et al. (2006). Airflow and deposition of nanoparticles in a human nasal cavity. *Aerosol Science and Technology*, 40, 463–476.



Contents lists available at SciVerse ScienceDirect

## Atmospheric Environment

journal homepage: [www.elsevier.com/locate/atmosenv](http://www.elsevier.com/locate/atmosenv)

## Detailed predictions of particle aspiration affected by respiratory inhalation and airflow

Kiao Inthavong<sup>a</sup>, Qin Jiang Ge<sup>a</sup>, Xiang Dong Li<sup>a</sup>, Ji Yuan Tu<sup>a,b,\*</sup><sup>a</sup>School of Aerospace, Mechanical and Manufacturing Engineering, RMIT University, Australia<sup>b</sup>Department of Building Science, Tsinghua University, Beijing, China

## HIGHLIGHTS

- ▶ Integrated model of human respiratory airway, humanoid, and indoor room is modelled.
- ▶ Flow near the face shows accelerated flow into the nostril during inhalation.
- ▶ Recirculating flow in the wake created behind body can induce pollutants.
- ▶ Particle tracking reveals origin of particles and its fate in respiratory airway.

## ARTICLE INFO

## Article history:

Received 13 June 2012

Received in revised form

23 July 2012

Accepted 30 July 2012

## Keywords:

Air pollution

Particle

Deposition

Nasal cavity

Inhalation

CFD

## ABSTRACT

The effects of air pollution found in the atmosphere and exposure to airborne particles are an important problem in the interest of public health. Exposure to contaminated air under different flow conditions is studied using the latest computational fluid dynamics models. For the first time the upper respiratory airway is integrated into a human body and placed inside a room, facing different airflow speeds ( $0.05 - 0.35 \text{ m s}^{-1}$ ). It was found that the airflow streamlines diverged as it approached the human body, at the torso and accelerated upwards past the face and head before separating at the rear of the head, forming recirculating regions in the wake behind the body. Inhaled particles were tracked backwards to determine its origins. At a plane upstream from the face the locations of particles inhaled form a region known as the critical area, which is presented. This study establishes a better understanding of particle inhalability and provides a step towards a more holistic approach in determining inhalation toxicology effects of exposure to atmospheric particles.

© 2012 Elsevier Ltd. All rights reserved.

## 1. Introduction

The study of the effects of air pollution found in the atmosphere and exposure to these airborne particles is an important problem in the interest of health effects associated with exposure to air pollution. Recently CFD (Computational Fluid Dynamics) simulations have been performed to investigate and visualise the flow patterns and local contaminant concentrations. These studies provide a deeper insight into particle dispersion given that many ventilation system designs are based on the assumption that airborne pollutants in the air are well-mixed within the room, which is not correct (Gadgil et al., 2003).

Studies have shown that localised concentrations and preferential flow regions are primarily caused by the room geometry (Lai et al., 2008; Zhang and Chen, 2006), and ventilation systems (Schlünssen et al., 2001). Particle dispersion studies in a room have been performed by Zhang and Chen (2009) using the Lagrangian particle tracking technique to determine exposure risk of building occupants to particulate matter. Other CFD studies have incorporated a human figure into the room (Poussou et al., 2010) which is a step towards a more integrated and realistic modelling approach to particulate exposure. Hayashi et al. (2002) placed a human occupant in a room to show the effects of contaminant inhalation, although the human face was simplified. It has been shown that inhaled particles from the external surroundings, referred to as the aspiration efficiency is influenced by facial features (Anthony et al., 2005). These studies recommend that CFD simulations should incorporate the complex features of the human face to adequately account for particle aspiration in low velocity environments.

\* Corresponding author. School of Aerospace, Mechanical and Manufacturing Engineering, RMIT University, PO Box 71, Bundoora Vic 3083, Australia. Tel.: +61 3 9925 6191; fax: +61 3 9925 6108.

E-mail address: [jiyuan.tu@rmit.edu.au](mailto:jiyuan.tu@rmit.edu.au) (J.Y. Tu).

As the particles are inhaled, they are transported through the respiratory airways where some are deposited onto surrounding surfaces while some may navigate through the complex geometry and even reach the lung airways, causing deleterious health effects. Internal respiratory studies have been performed by the authors (Inthavong et al., 2009a, 2008, 2011c) among others (Liu et al., 2007; Schroeter et al., 2006) which has found that the transport and deposition of micron sized particles are dominated by its inertial property while submicron and nano sized particles are influenced by diffusion mechanisms. These studies are based on an isolated model of the human nasal cavity or tracheobronchial airway tree and as such the inlet boundary condition imposed at the nostril or trachea inlets are unknown and instead a blunt, parabolic or uniform profile is applied. Based on the aforementioned literature, it is apparent that there is a degree of independence and isolation amongst the cited studies which can be categorized into studies of: i) room and ventilation, ii) aspiration efficiency, iii) and particle deposition efficiencies in the respiratory airway. This leads to some loss in achieving a holistic set of results, which can greatly contribute towards new knowledge in identifying preventative measures for health risk exposure assessment.

Therefore this study presents an integrated CFD model simulation that combines the three aspects of contaminant exposure by including the external room, human occupant with realistic facial features, and the internal nasal–trachea airway. The influences of the external airflow patterns on the transport of indoor particle contaminants are evaluated. Visualisation of the air and particle flow patterns in the freestream and proximal to the nostrils are shown. By using a Lagrangian particle tracking technique, identification of the origins of the upstream particle locations that are inhaled (aspiration efficiency) are found. Furthermore the integrated model has the ability to correlate the contaminant source origin to the fate of the inhaled particle (i.e. particle deposition region in the respiratory airway).

## 2. Method

### 2.1. Computational geometry

A CT scan of the upper respiratory airway consisting of the nasal cavity, pharynx, larynx, and upper trachea from a 51 year old non-smoking Asian male provided the basis for reconstruction of a computational model. Segmentation of the desired airway was performed to extract a contiguous airway path from the nostril inlets to the upper trachea. Details of the segmentation method can be found in Inthavong et al. (2009b). In addition to the nostrils, a partial region of the external nose, proximal to the nostrils was included. A realistic human head was generated as an IGES file from FaceGEN Modeller (Singularity Inversion Inc., 2007) software, based on photographic images taken from a male volunteer. The three-dimensional (3D) head contained detailed facial features, such as shaped eyes, nose, mouth, and ears. Details of the facial features are given in Table 1 and are compared with the 50th percentile of a caucasian male as described in the literature (Huston, 2009; Zhuang et al., 2010). The comparisons show that the CFD model used in this study is slightly smaller than the 50th percentile for caucasian males.

The realistic head was placed onto a simple human body shape, and this was model placed into an empty room to simulate the ambient air. The three submodels (respiratory airway, human body, and surrounding room) were combined by importing the models into a CAD (Computer Aided Design) software modelling program and merged together. The final CAD model in Fig. 1 shows the upstream location (particle release plane) where a uniform concentration of particles is released from, detailed facial features,

**Table 1**  
Body and facial details.

Human occupant details			Facial details		
Dimension	Present study	50th% man <sup>a</sup>	Dimension	Present study	50th% man <sup>b</sup>
Occupant height	170.0	175.9	Head length	18.3	19.5
Mid shoulder height	139.7	144.4	Head circumference	56.3	56.8
Head width	13.5	15.5	Face length	9.1	11.8
Head depth	18.3	19.6	Face width	13.5	14.1
Top of head to chin	19.2	22.1	Nose length	4.13	5.0
Top of head to mouth centre	15.2	18.0	Nose protrusion	1.56	2.1
Top of head to eyes	9.2	11.5	Nose breadth	3.79	3.4

All units are in centimetres [cm].

<sup>a</sup> Huston (2009).

<sup>b</sup> Zhuang et al. (2010).

and the internal nasal-to-trachea respiratory airway cavity that is adjoined to the nostrils. A full human body model is used to include the torso which has been found to influence the particle aspiration (Anderson, 2010).

It is apparent that the model geometry spans over multiple length scales from metre lengths of the room down to centimetres within the airway bronchi. This presents a challenge in producing a quality computational mesh for CFD analysis. This step was also the most exhaustive stage in the CFD simulation process that involved meshing the model sequentially from the internal respiratory airway and outwards into the external room surrounding. Prism layers were applied to the bounding respiratory walls and a tetrahedral unstructured mesh filled the airway passage (Fig. 2a). The respiratory airway alone consisted of 11 million cells. In order to minimise the effects of numerical artificial diffusion (i.e. false diffusion) in the CFD simulation, the fine mesh resolving length scales in centimetres within the respiratory airway was gradually expanded out to length scales of metres to resolve the outer air in the room. Fig. 2b shows the different sections and aspects of the meshing as well as some cross-sectional outlines of the internal respiratory airways. The final number of cells in the mesh incorporating the respiratory airway, human body, and room was 16 million cells which used up 912 Mb in data storage size. Earlier studies by the authors have found that a mesh in excess of 2.0 million provided grid independence for the nasal cavity region (Inthavong et al., 2011a), while a mesh of 1.2 million was sufficient for grid independence for the room with human occupant model (King Se et al., 2010). Due to the large variation in length scales of the flow and geometry there is a greater demand on the computational mesh to minimise false diffusion caused by rapid changes in the mesh elements' size. To ensure quality of results, and a high level of mesh integrity, a mesh independence test was performed by investigating the velocity profiles at a number of different locations (e.g. inside the nasal cavity, in the near breathing region) until the profiles converged. The mesh became convergent at 8 million cells. However to minimise any false diffusion caused by the unstructured mesh a conservative the final computational model using 16 million cells was used. The visualisation and generation of the mesh was possible on a PC computer with 32 Gb Ram 2 Gb video card, and 8 processor cores. The simulations were performed on a High Performance Computing cluster which has 268 processor cores.

### 2.2. Airflow modelling

A steady oncoming freestream of air towards the human occupant was applied in order to investigate the 'worst case scenario' for particle inhalability. This is confirmed by Kennedy and Hinds

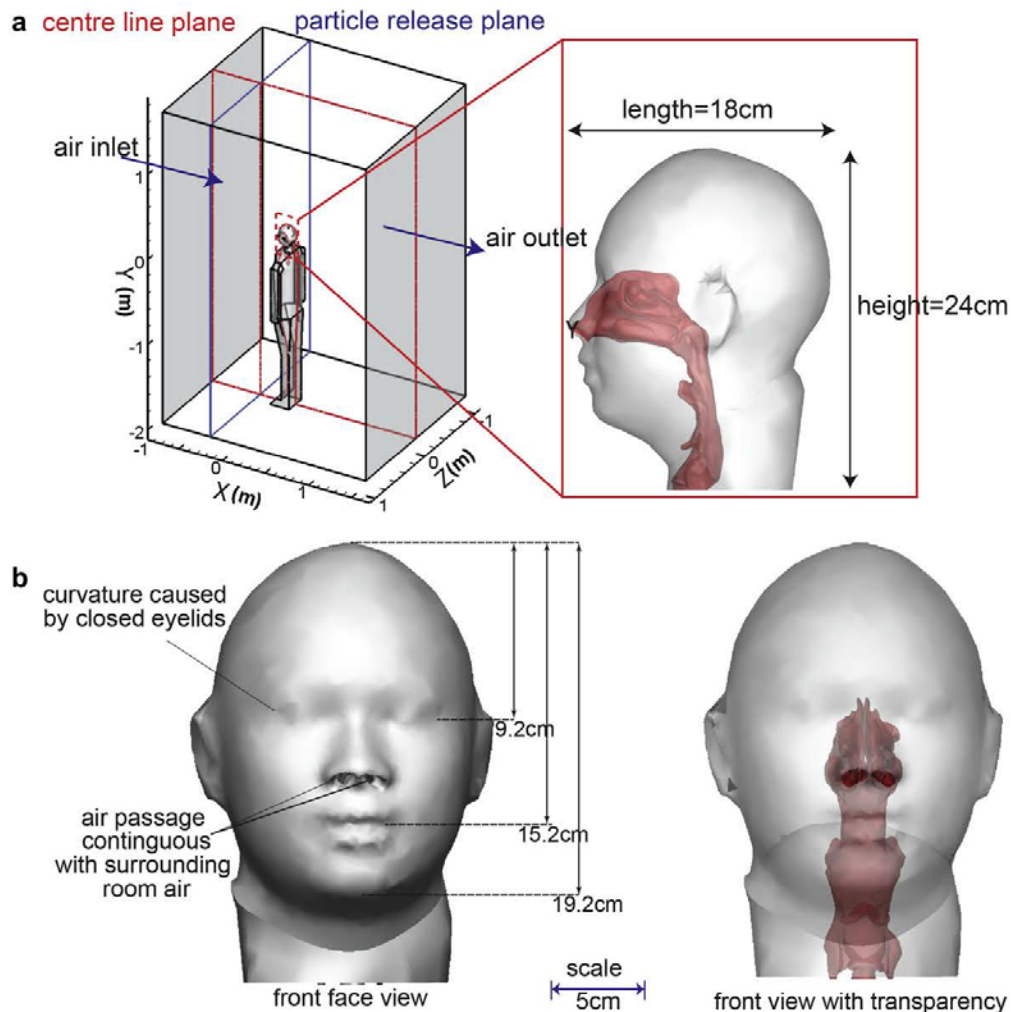


Fig. 1. (a) 3D CAD model incorporating the external surrounding room, human occupant, and the internal nasal–pharynx–larynx–trachea respiratory airway model. (b) Front view showing the detailed facial features. Geometry dimensions and details of the room and human occupant are given in Table 1.

(2002) which showed that the ‘facing-the-wind’ orientation produces an upper limit for inhalability compared with an averaged orientation which is produced by equally weighting particle inhalation over all angles from 0 to 360 orientation. The selection of the ambient airflow was based on the comprehensive survey of airflow speeds in indoor workplaces by Baldwin and Maynard (1998) which found a mean value of  $0.3 \text{ m s}^{-1}$  (ranging from  $0.04$  to  $2.02 \text{ m s}^{-1}$ ) over all workplaces, however this value is skewed by measurements made in a wood drying shed that had a value of  $1.79 \text{ m s}^{-1}$ , and that neglecting this measurement produces a mean of  $0.2 \text{ m s}^{-1}$  (ranging from  $0.04$  to  $0.72 \text{ m s}^{-1}$ ). More specifically for different workplace environments the mean values are: office  $0.011$ – $0.164 \text{ m s}^{-1}$ ; wood turning  $0.064$ – $0.119 \text{ m s}^{-1}$ ; heavy steel industry  $0.063$ – $1.737 \text{ m s}^{-1}$ . Therefore in this study the influence of different indoor airflow velocities ( $0.05$ ,  $0.20$  and  $0.35 \text{ m s}^{-1}$ ) on the respiration and particle locations entering the nasal cavity via the nostrils. Table 2 provides a summary of the inhalation and room flow details.

Reynolds number matching over the head of the humanoid was applied in order to obtain dynamic similarity between the CFD

simulation with existing experimental data in the literature by Anthony et al. (2005). For indoor airflows, reported results have shown much better flow separation and reattachment, which is an expected flow feature of the flow passing over the head, based on the  $k-\epsilon$ -RNG model (Hofmann et al., 2003). But in the human

Table 2  
Inhalation and room flow details.

Inhalation details	Right		Left		Room and ventilation details	
	Area	Perim	Area	Perim	Geometry	Dimension
Nostril openings	Area = $1.52 \text{ cm}^2$	Perim = $4.72 \text{ cm}$	Area = $1.31 \text{ cm}^2$	Perim = $4.62 \text{ cm}$	Length	250 cm
	$D_h = 1.288 \text{ cm}$		$D_h = 1.134 \text{ cm}$		Width	200 cm
					Height	350 cm
Dynamic similarity	Present study		Anthony et al. (2005)			
$Re_{\text{freestream}}$ (room inlet)	48,000		50,250			
$Re_{\text{head}}$	1850		1909			
Head hydraulic diameter	14 cm		9.6 cm			
$V_{\text{freestream}}$ ( $\text{m s}^{-1}$ )	$0.2 \text{ m s}^{-1}$		0.3			

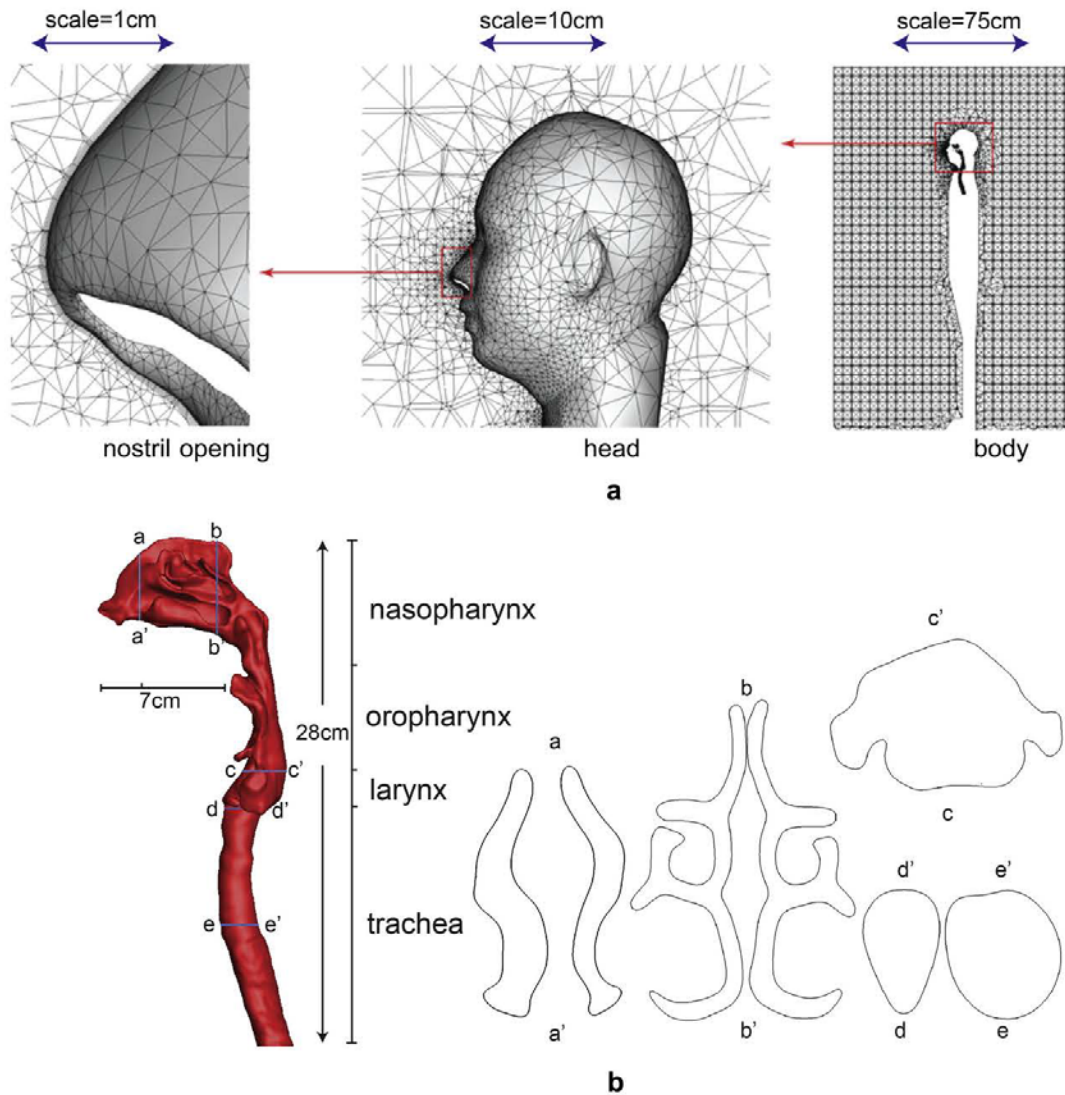


Fig. 2. (a) Mesh outline from close up view of the nostril opening, to the head, to the body inside the room. (b) Cross-sections labelled a–e taken at different locations within the internal upper respiratory airway which consists of the nasal cavity, pharynx, larynx, and trachea.

respiratory system, many researchers have used  $k-\omega$  turbulent model with Shear Stress Transport (SST) developed by Menter et al. (2006) to analyse airflow in the nasal cavity (Wen et al., 2008; Zhang and Kleinstreuer, 2011). For respiratory inhalation, two flow rates of 15 and 40 L per minute (LPM) are presented for the aspiration efficiency through nasal inhalation, which represent light activity and heavy Airflow patterns in the respiratory airways, encounter a rich variety of flow structures existing in all three flow regimes of laminar, transition, and turbulent flow. Recently the four equation SST-transition model, along with an LES and laminar model were evaluated for its performance in predicting all three flow regimes in a constricted pipe and an idealized human oral airway model (Zhang and Kleinstreuer, 2011). The study found that there were no measurable differences between the turbulent models in predicting laminar flows as well as transition to turbulent flow. The SST-transition model is ideal for the internal respiratory flow; however its performance on the indoor airflow is unknown. This raises the

issue of selecting a suitable turbulence model that will accommodate both the flow patterns in the indoor room air and inside the small respiratory airways. Given the successful implementation of the SST-transition model for respiratory airflows by Zhang and Kleinstreuer (2011), the model is first evaluated for indoor airflows against experimental data, a laminar model, and existing models that have proven successful such as the RNG  $k-\epsilon$ , and LES. The continuity and momentum equations are given as:

Continuity equation:

$$\frac{\partial}{\partial x_i} (\rho_g u_i^g) = 0 \quad (1)$$

Momentum equation:

$$\rho_g u_i^g \frac{\partial u_i^g}{\partial x_j} = -\frac{\partial p_g}{\partial x_i} + \frac{\partial}{\partial x_j} \left[ \mu_g \frac{\partial u_i^g}{\partial x_j} \right] \quad (2)$$

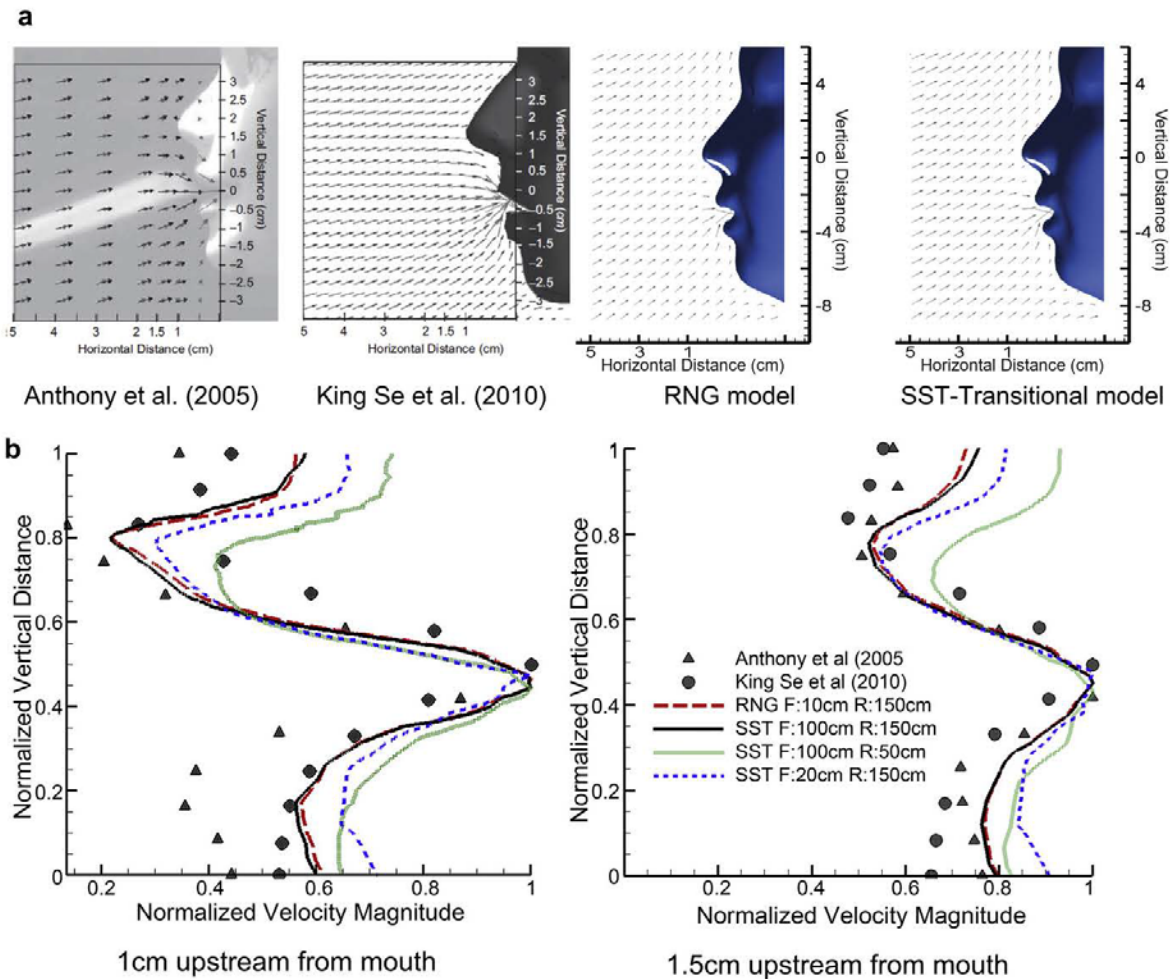


Fig. 3. Velocity vector plots for oral inhalation using (a) CFD and PIV experimental measurements from Anthony et al. (2005). (b) Velocity magnitude profiles at upstream locations of 1 cm and 1 cm from the nose tip.

to be inhaled into the respiratory system. The effect of the vertical flow across the closed mouth region can enhance the inhalability of the particles if breathing through the mouth was also to occur midway through an inhalation cycle. Such a study involving both the nose and mouth inhalation under different breathing situations was not investigated in this paper and is left for future studies.

The velocity profiles in Fig. 4b show a shift in the stagnation regions where the flow bifurcates near the chin is higher for nasal inhalation in comparison with oral inhalation. The comparisons of velocity profiles with data from King Se et al. (2010) show good agreement. In both oral and nasal inhalation, sharp acceleration of the inhaled air occurs as it approaches the mouth or nose, which will contribute additional momentum to inhaled particles, thus greatly enhancing the likelihood of early particle deposition (Fig. 5).

### 3.2. Influence of ambient flow rate

Particle aspiration efficiencies have been defined as the fraction of particles that are inhaled through the nose or mouth during breathing (Vincent et al., 1990), which is also referred to as 'inhalability'. Factors that influence particle aspiration efficiency include

the particle size and the external ambient airflow around the human body. In the cases presented in this study, the human body is facing the oncoming air which transports the particles from upstream towards the breathing region. Fig. 6 shows the oncoming air diverging at the torso as it approaches the body, thus the air that is inhaled comes from underneath the face, rather than above. This implies that airborne particles that are present below the breathing region are more likely to be inhaled. Furthermore the inhalation streamlines show that for a lower ambient airflow rate, a larger region of air (i.e. air 'stream-tube') is inhaled, in comparison to a higher ambient airflow rate. Under both conditions the inhaled air is being pulled from below the breathing region.

The airflow accelerates around the head of the body, the boundary layer separates at the rear, producing a wake, with a recirculation region forming just behind the head. An increase in the ambient airflow rate produces a recirculation region that is further from the body. This study only investigated the inhalability of particles from an upstream source of airflow, however the results of the wake flow shown in Fig. 6 indicate that if the ambient airflow was coming from behind the body, particles from a contaminant source in front of the body may be disturbed and induced into the

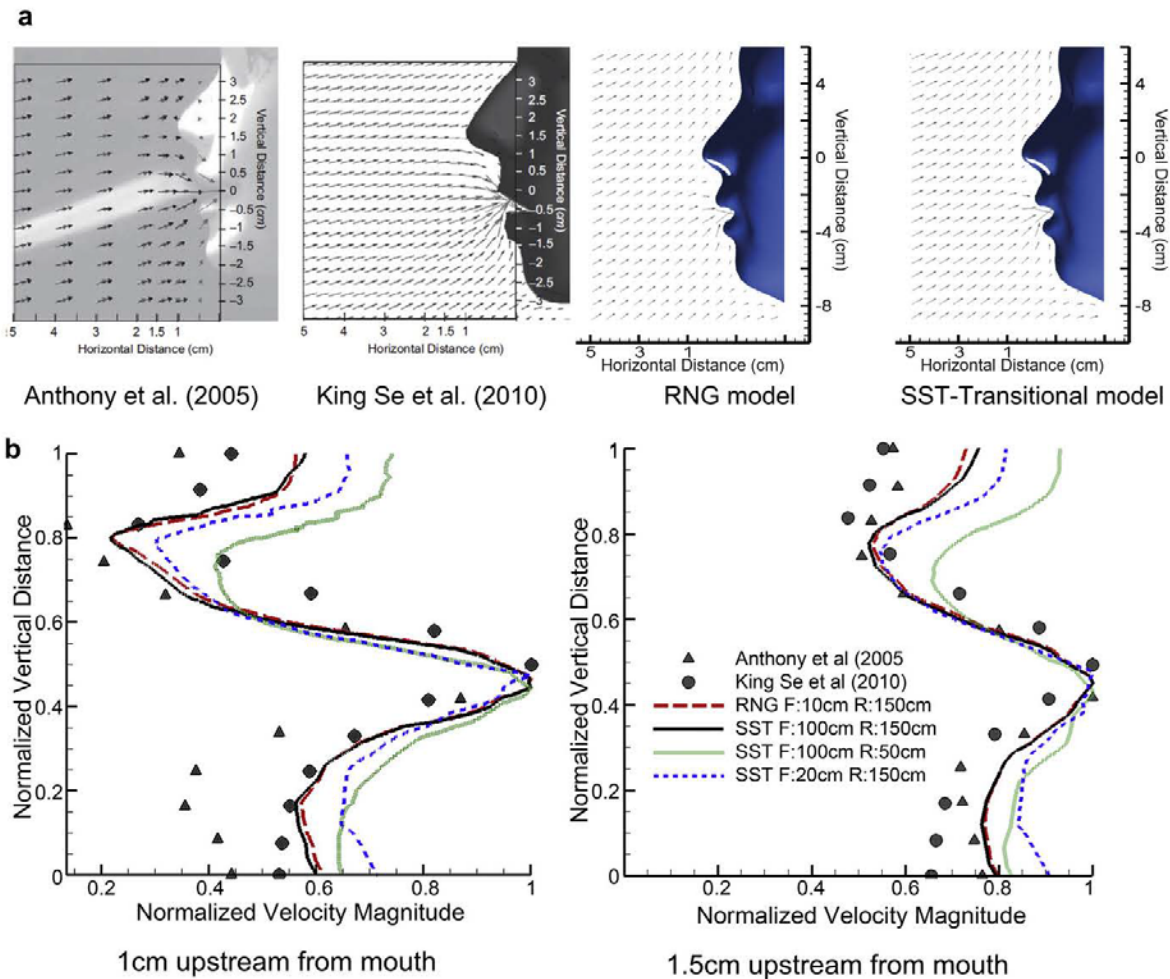


Fig. 3. Velocity vector plots for oral inhalation using (a) CFD and PIV experimental measurements from Anthony et al. (2005). (b) Velocity magnitude profiles at upstream locations of 1 cm and 1 cm from the nose tip.

to be inhaled into the respiratory system. The effect of the vertical flow across the closed mouth region can enhance the inhalability of the particles if breathing through the mouth was also to occur midway through an inhalation cycle. Such a study involving both the nose and mouth inhalation under different breathing situations was not investigated in this paper and is left for future studies.

The velocity profiles in Fig. 4b show a shift in the stagnation regions where the flow bifurcates near the chin is higher for nasal inhalation in comparison with oral inhalation. The comparisons of velocity profiles with data from King Se et al. (2010) show good agreement. In both oral and nasal inhalation, sharp acceleration of the inhaled air occurs as it approaches the mouth or nose, which will contribute additional momentum to inhaled particles, thus greatly enhancing the likelihood of early particle deposition (Fig. 5).

### 3.2. Influence of ambient flow rate

Particle aspiration efficiencies have been defined as the fraction of particles that are inhaled through the nose or mouth during breathing (Vincent et al., 1990), which is also referred to as 'inhalability'. Factors that influence particle aspiration efficiency include

the particle size and the external ambient airflow around the human body. In the cases presented in this study, the human body is facing the oncoming air which transports the particles from upstream towards the breathing region. Fig. 6 shows the oncoming air diverging at the torso as it approaches the body, thus the air that is inhaled comes from underneath the face, rather than above. This implies that airborne particles that are present below the breathing region are more likely to be inhaled. Furthermore the inhalation streamlines show that for a lower ambient airflow rate, a larger region of air (i.e. air 'stream-tube') is inhaled, in comparison to a higher ambient airflow rate. Under both conditions the inhaled air is being pulled from below the breathing region.

The airflow accelerates around the head of the body, the boundary layer separates at the rear, producing a wake, with a recirculation region forming just behind the head. An increase in the ambient airflow rate produces a recirculation region that is further from the body. This study only investigated the inhalability of particles from an upstream source of airflow, however the results of the wake flow shown in Fig. 6 indicate that if the ambient airflow was coming from behind the body, particles from a contaminant source in front of the body may be disturbed and induced into the

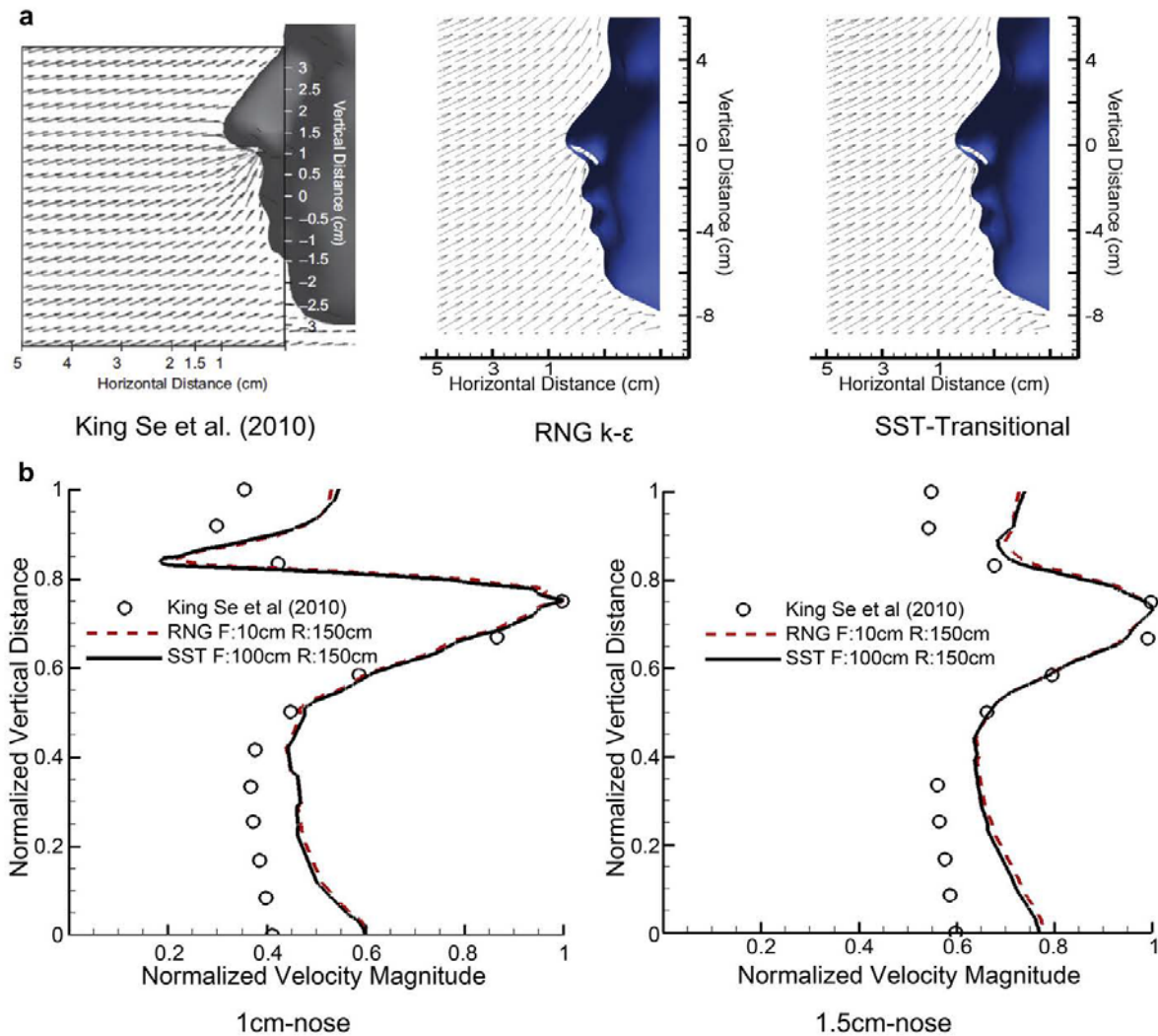


Fig. 4. Velocity vector plots for (a) CFD oral inhalation and (b) PIV experimental measurements from Anthony et al. (2005). (c) CFD nasal inhalation. Ambient surrounding flow rate is  $0.2 \text{ m s}^{-1}$ .

breathing region, and thus enhancing the inhalability of the particles. The wake region can induce a well-mixed scenario through the presence of vortices that can entrain air.

### 3.3. Particle inhalation trajectory

Particle trajectories originating from a plane located at a distance of 0.2 m upstream from the nose tip are shown in Fig. 6 for ambient airflow rates of  $0.05 \text{ m s}^{-1}$  and  $0.35 \text{ m s}^{-1}$ . The results for the airflow rate of  $0.2 \text{ m s}^{-1}$  are not shown as they lie in between the results for airflow rates of  $0.05 \text{ m s}^{-1}$  and  $0.35 \text{ m s}^{-1}$  as expected. The vertical distance coordinate is set to  $y = 0 \text{ m}$  at the nostril level, so that the trajectories of nasal inhaled particles converge to this point. The trajectories show that for  $40 \mu\text{m}$  and  $80 \mu\text{m}$  sized particles, gravitational settling dominates where the particle source originates from a much higher vertical position in relation to the nostril openings. The trajectory of these particles is linear until they reach the nose where acceleration towards the

nostril occurs due to nasal inhalation. This linearity means that the location of the particle source for large particles may be identified for a given upstream distance through extrapolation. The further upstream the distance, the higher the vertical distance should be for the particles to descend towards the nose.

At higher ambient airflow rates the vertical distance needed for  $40 \mu\text{m}$  and  $80 \mu\text{m}$  particles to overcome gravitational settling is reduced significantly from 0.65 m down to 0.05 m due to the horizontal momentum component induced by the airflow. Smaller particles such as  $1\text{--}20 \mu\text{m}$  all possess much lighter masses and therefore its low inertia allows the particles to be influenced by the surrounding flow field. This leads to particles tending to follow the airflow streamlines more and the upstream location of the particle source is now located at a vertical distance of 0.05–0.1 m below the nostrils, since it was shown earlier that the flow streamlines diverge at the torso region as the flow approaches the human body. At the higher ambient airflow rate the trajectories of the smaller particles do not change significantly.



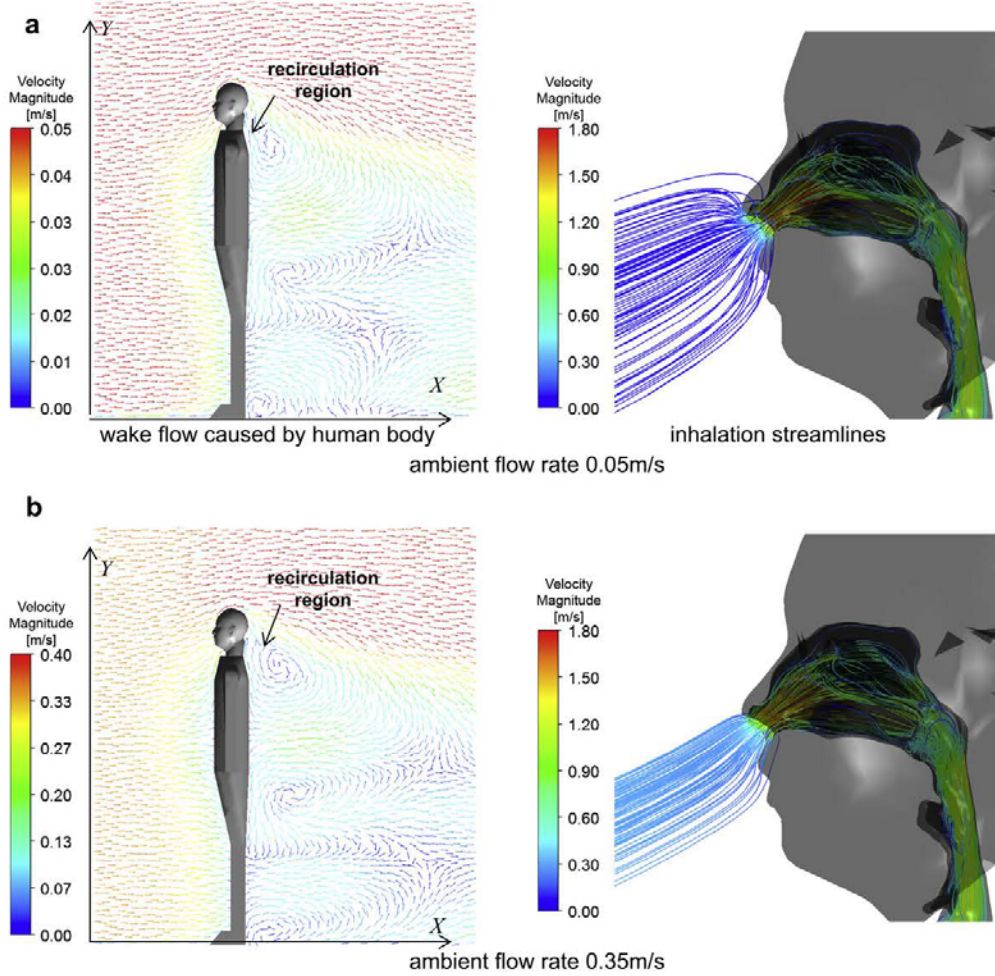


Fig. 5. Velocity vectors in the centreline plane showing the flow field around the humanoid (left). Streamtubes showing the region of air that is inhaled through the nostrils and into the respiratory system (right). The inhalation rate of the nostrils at 15 L min<sup>-1</sup>.

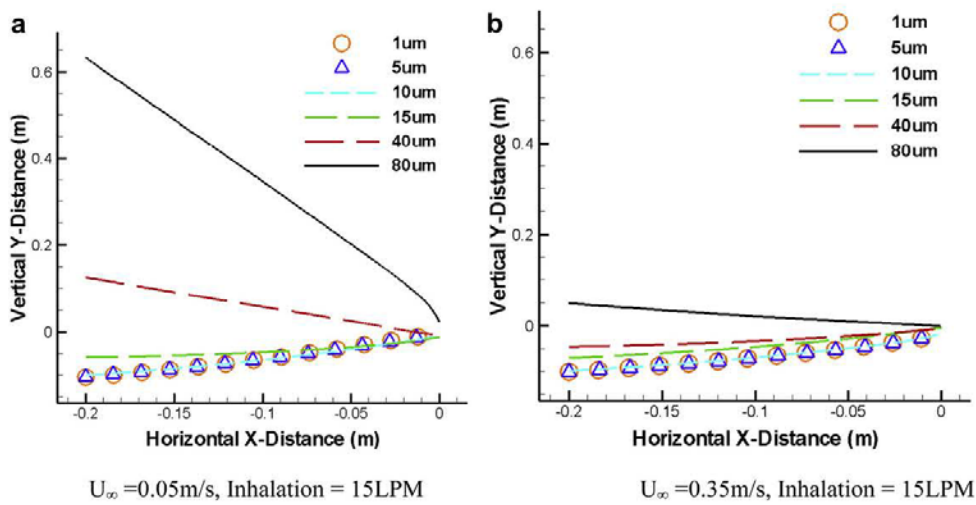


Fig. 6. Sample trajectory of inhaled particles released at 0.2 m upstream for different particle sizes and ambient.

3.4. Particle deposition patterns

The critical area is defined as the region with which particles are inhaled from at a given location upstream from the human body

(Anthony et al., 2005). At the upstream location of 0.2 m from the nostril inlets, the critical areas representing the source of inhaled particles show two distinct regions which is caused by the two different nostril inlets (Fig. 7). The critical areas are viewed from

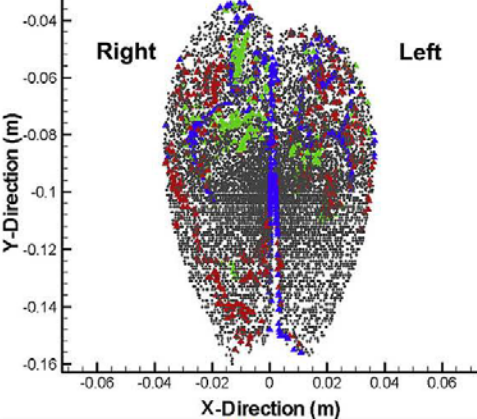

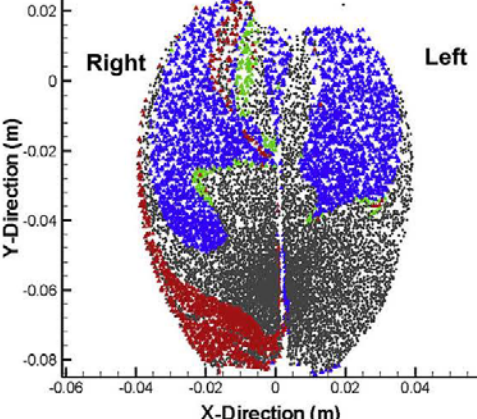

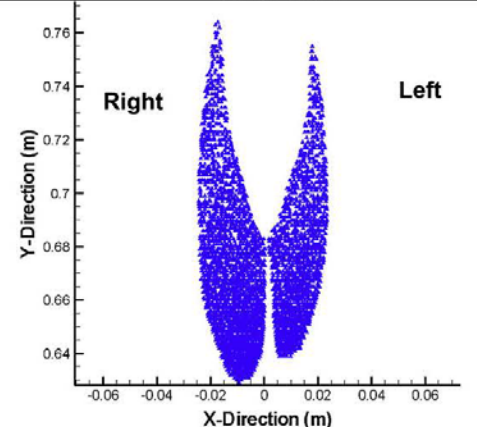

Critical area	Respiratory Deposition	Deposition Efficiency (%)
 <p>Right Left</p> <p>Y-Direction (m)</p> <p>X-Direction (m)</p>		<p><b>1µm</b></p> <p>Nasal region = 3.0%</p> <p>Pharynx = 1.1%</p> <p>Trachea = 1.9%</p> <p>Escape (lung) = 94.0%</p>
 <p>Right Left</p> <p>Y-Direction (m)</p> <p>X-Direction (m)</p>	 <p>high concentration</p>	<p><b>15µm</b></p> <p>Nasal region = 23.2%</p> <p>Pharynx = 1.4%</p> <p>Trachea = 10.8%</p> <p>Escape (lung) = 61.6%</p>
 <p>Right Left</p> <p>Y-Direction (m)</p> <p>X-Direction (m)</p>	 <p>high concentration</p>	<p><b>80µm</b></p> <p>Nasal region = 100%</p> <p>Pharynx = 0%</p> <p>Trachea = 0%</p> <p>Escape (lung) = 0%</p>

Fig. 7. Critical areas for the upstream particle release plane at  $x = 0.20$  m (see 'Particle Release Plane' in Fig. 1) for inhaled particles and its deposition in the upper respiratory airway for ambient airflow rate of  $0.05 \text{ m s}^{-1}$ .

upstream and the labelling convention is to name the left and right critical areas consistent with the same side they sit anatomically with the human body involved. Thus the left critical area is mainly influenced by the left nostril and left nasal chamber that produces the inhalation effort.

Each individual particle that is inhaled through the nostril is tracked via the Lagrangian tracking equation (Eqn. (3)) and the particle deposition onto the respiratory surface is recorded. The accuracy of the particle tracking algorithm was evaluated based on the particle deposition efficiency against the inertial parameter (IP), defined as  $IP = Q \times d^2$ , where  $Q$  is the inhalation flow rate ( $\text{cm}^3 \text{ s}^{-1}$ ), and  $d$  is the aerodynamic particle diameter ( $\mu\text{m}$ ). It was found that using the damping function to correct the turbulent fluctuations in the near wall (Equation (6)) provided sufficiently accurate results which can be found in Inthavong et al. (2011a, 2011b).

The blue coloured particles represent those particles depositing onto the nasal cavity region; the green particles deposit onto the pharyngeal region; the red particles deposit onto the trachea; and the grey particles are those that don't deposit and in fact escape from the respiratory geometry and enter the bronchial regions of the lungs. For  $1 \mu\text{m}$  particles, there is no distinguishable pattern from the critical area that can allow confident predictions of where a particle may deposit within the respiratory airway.

For  $15 \mu\text{m}$  particles nearly all the particles that deposit in the trachea region originate from the left side of the critical area. This suggests that particles that enter the left nasal chamber, and take on that particular pathway will experience and be influenced by a different airflow pattern if the particles had entered the right-hand nasal chamber. During normal nasal physiology, the nasal cavity is asymmetrical where one nasal passage is typically more patent than the other. This asymmetry is referred to as the nasal cycle which is a result of congestion (swelling) of the erectile tissue (cavernous tissues of the mucosa) in one nasal cavity while at the same time decongestion (shrinking) occurs to the erectile tissue in the other cavity. The airflow through each nasal cavity is then governed by the resistance caused by the cross-sectional area of each airway. This asymmetry may explain the bias for those particles that exist in the lower left region of the critical area to deposit in the trachea region.

A second pattern that emerges from the  $15 \mu\text{m}$  critical area is that the blue coloured particles (depositing in the nasal cavity region) exist in the upper half of the critical area, compared with the red coloured particles (depositing in the trachea) which exist in the lower half of the critical area. It has been established that for  $15 \mu\text{m}$  sized particles early deposition in the nasal cavity is attributed to inertial deposition (Inthavong et al., 2006; Wang et al., 2009), where particles that exhibit high momentum will not follow the airflow streamlines. In Fig. 6 it was shown that as the particles accelerated as they approached the nostrils, due to the inhaled air that complements the oncoming airflow. In addition particles originating from above the nostrils are further accelerated by the gravitational pull which becomes more influential as the particles become larger in size. These two contributing factors cause the particles to exhibit higher inertia as they enter the respiratory domain, when compared to those particles that originate from below the nostrils. A further investigation found that a large number of those particles that deposited in the nasal region (total = 23.2%) are concentrated at or near the nostril inlet, and is labelled in Fig. 7 with arrows pointing to these high concentration regions.

For  $80 \mu\text{m}$  particles the larger mass of the particle means that it is highly influenced by gravitational settling, and therefore the critical areas at the upstream location are located at a much higher vertical distance from the nostril inlets. Similar to the  $15 \mu\text{m}$  particles, the  $80 \mu\text{m}$  particles are further accelerated due to the inhaled air that complements the oncoming airflow, thereby increasing its inertial

properties even further. This creates regions of high concentration of particles depositing at or near the nostril inlets (arrows pointing to high concentration region). The shape of the critical area is that of two narrow teardrops where a larger concentration of particles is found near the bottom of the critical area.

#### 4. Conclusion

An integrated CFD model simulation was performed to better understand the air and particle flow patterns in human exposure to indoor air pollutants. A realistic upper respiratory airway model based on CT-scans was created and integrated into a human body. During inhalation, the flow patterns near the face show vertically aligned flow streams which transport the particles towards either the nose during nasal inhalation or mouth during oral inhalation. An influence of the ambient airflow rate on the flow patterns is the increased acceleration of flow that begins as the airflow diverges at the torso. Flow separation occurs at the rear of the human head and there is a shift in the recirculation region, and different wake effects are found. This indicates that if the ambient airflow was coming from behind the body, particles form a contaminant source in front of the body may be disturbed and induced into the breathing region. Trajectories of the inhaled particles found that the source of large inhaled particles (e.g.  $40 \mu\text{m}$  and  $80 \mu\text{m}$ ) that are originating from upstream must be above the nose as gravitational settling is significant for these particles. For the smaller particles ( $1\text{--}20 \mu\text{m}$ ), particles tend to follow the flow streamlines and their original upstream location must be below the nostrils. The critical area shapes were determined by reverse tracking the particles to its origins and colour coding their positions in order to determine if a pattern could be deduced for predictions of local respiratory region deposition. It was found that only the  $15 \mu\text{m}$  particle size produced discernible pattern. This study aimed to establish a better understanding of particle inhalability and to enhance the state of the art CFD modelling towards a holistic simulation for exposure of airborne particles.

#### Acknowledgements

The authors gratefully acknowledge the financial support provided by the National Basic Research Program (973) of China, Grant No. 2012CB720100 and the Australian Research Council (project ID: DP120103958).

#### References

- Anderson, K.R., 2010. Computational Fluid Dynamics (CFD) Study Investigating the Effects of Torso Geometry Simplification on Aspiration Efficiency. Department of Occupational and Environmental Health, The University of Iowa, Iowa.
- Anthony, T.R., Flynn, M.R., Eisner, A., 2005. Evaluation of facial features on particle inhalation. *Annals of Occupational Hygiene* 49, 179–193.
- Baldwin, P.E.J., Maynard, A.D., 1998. A survey of wind speeds in indoor workplaces. *Annals of Occupational Hygiene* 42, 303–313.
- Gadgil, A.J., Lobscheid, C., Abadie, M.O., Finlayson, E.U., 2003. Indoor pollutant mixing time in an isothermal closed room: an investigation using CFD. *Atmospheric Environment* 37, 5577–5586.
- Hayashi, T., Ishizu, Y., Kato, S., Murakami, S., 2002. CFD analysis on characteristics of contaminated indoor air ventilation and its application in the evaluation of the effects of contaminant inhalation by a human occupant. *Building and Environment* 37, 219–230.
- Hofmann, W., Golser, R., Balashazy, I., 2003. Inspiratory deposition efficiency of ultrafine particles in a human airway bifurcation model. *Aerosol Science and Technology* 37, 988–994.
- Huston, R.L., 2009. Principles of Biomechanics. CRC Press. 9780849334948.
- Inthavong, K., Tian, Z.F., Li, H.F., Tu, J.Y., Yang, W., Xue, C.L., Li, C.G., 2006. A numerical study of spray particle deposition in a human nasal cavity. *Aerosol Science and Technology* 40, 1034–1045.
- Inthavong, K., Wen, J., Tian, Z., Tu, J., 2008. Numerical study of fibre deposition in a human nasal cavity. *Journal of Aerosol Science* 39, 253–265.

- Inthavong, K., Tu, J.Y., Ahmadi, G., 2009a. Computational modelling of gas-particle flows with different particle morphology in the human nasal cavity. *Journal of Computational Multiphase Flows* 1, 57–82.
- Inthavong, K., Wen, J., Tu, J.Y., Tian, Z.F., 2009b. From CT scans to CFD modelling – fluid and heat transfer in a realistic human nasal cavity. *Engineering Applications of Computational Fluid Mechanics* 3, 321–335.
- Inthavong, K., Ge, Q., Se, C.M.K., Yang, W., Tu, J.Y., 2011a. Simulation of sprayed particle deposition in a human nasal cavity including a nasal spray device. *Journal of Aerosol Science* 42, 100–113.
- Inthavong, K., Tu, J., Heschl, C., 2011b. Micron particle deposition in the nasal cavity using the v2-f model. *Computers & Fluids* 51, 184–188.
- Inthavong, K., Zhang, K., Tu, J., 2011c. Numerical modelling of nanoparticle deposition in the nasal cavity and the tracheobronchial airway. *Computer Methods in Biomechanics and Biomedical Engineering* 14, 633–643.
- Isabey, D., Chang, H.K., 1981. Steady and unsteady pressure-flow relationships in central airways. *Journal of Applied Physiology* 51, 1338–1348.
- Kennedy, N.J., Hinds, W.C., 2002. Inhalability of large solid particles. *Journal of Aerosol Science* 33, 237–255.
- King Se, C.M., Inthavong, K., Tu, J., 2010. Inhalability of micron particles through the nose and mouth. *Inhalation Toxicology* 22, 287–300.
- Lai, A.C.K., Wang, K., Chen, F.Z., 2008. Experimental and numerical study on particle distribution in a two-zone chamber. *Atmospheric Environment* 42, 1717–1726.
- Liu, Y., Matida, E.A., Junjie, G.U., Johnson, M.R., 2007. Numerical simulation of aerosol deposition in a 3-D human nasal cavity using RANS, RANS/EIM, and LES. *Journal of Aerosol Science* 38, 683–700.
- Menter, F.R., Langtry, R.B., Likki, S.R., Suzen, Y.B., Huang, P.G., Volker, S., 2006. A correlation-based transition model using local variables – part I: model formulation. *Journal of Turbomachinery* 128, 413–422.
- Morsi, S.A., Alexander, A.J., 1972. An investigation of particle trajectories in two-phase flow systems. *Journal Fluid Mechanics* 55, 193–208.
- Poussou, S.B., Mazumdar, S., Plesniak, M.W., Sojka, P.E., Chen, Q., 2010. Flow and contaminant transport in an airliner cabin induced by a moving body: model experiments and CFD prediction. *Atmospheric Environment* 44, 2830–2839.
- Schlünssen, V., Vinzents, P.S., Mikkelsen, A.B., Schaumburg, I., 2001. Wood dust exposure in the Danish furniture industry using conventional and passive monitors. *Annals of Occupational Hygiene* 45, 157–164.
- Schroeter, J.D., Kimbell, J.S., Asgharian, B., 2006. Analysis of particle deposition in the turinate and olfactory regions using a human nasal computational fluid dynamics model. *Journal of Aerosol Medicine* 19, 301–313.
- Vincent, J.H., Mark, D., Miller, B.G., Armbruster, L., Ogden, T.L., 1990. Aerosol inhalability at higher windspeeds. *Journal of Aerosol Science* 21, 577–586.
- Wang, S.M., Inthavong, K., Wen, J., Tu, J.Y., Xue, C.L., 2009. Comparison of micron- and nanoparticle deposition patterns in a realistic human nasal cavity. *Respiratory Physiology and Neurobiology* 166, 142–151.
- Wen, J., Inthavong, K., Tu, J.Y., Wang, S., 2008. Numerical simulations for detailed airflow dynamics in a human nasal cavity. *Respiratory Physiology & Neurobiology* 161, 125–135.
- Zhang, Z., Chen, Q., 2006. Experimental measurements and numerical simulations of particle transport and distribution in ventilated rooms. *Atmospheric Environment* 40, 3396–3408.
- Zhang, Z., Chen, Q., 2009. Prediction of particle deposition onto indoor surfaces by CFD with a modified Lagrangian method. *Atmospheric Environment* 43, 319–328.
- Zhang, Z., Kleinstreuer, C., 2011. Laminar-to-turbulent fluid-nanoparticle dynamics simulations: model comparisons and nanoparticle-deposition applications. *International Journal for Numerical Methods in Biomedical Engineering* 27, 1930–1950.
- Zhuang, Z., Landsittel, D., Benson, S., Roberge, R., Shaffer, R., 2010. Facial anthropometric differences among gender, ethnicity, and age groups. *Annals of Occupational Hygiene* 54, 391–402.